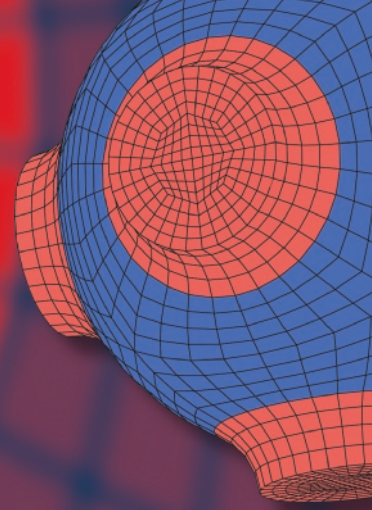


Advanced Structured Materials

Muhamad Husaini Abu Bakar
Faizatul Azwa Zamri
Andreas Öchsner *Editors*



Progress in Engineering Technology II

 Springer


Advanced Structured Materials

Volume 131

Series Editors

Andreas Öchsner, Faculty of Mechanical Engineering, Esslingen University of Applied Sciences, Esslingen, Germany

Lucas F. M. da Silva, Department of Mechanical Engineering, Faculty of Engineering, University of Porto, Porto, Portugal

Holm Altenbach , Faculty of Mechanical Engineering, Otto von Guericke University Magdeburg, Magdeburg, Sachsen-Anhalt, Germany

Common engineering materials reach in many applications their limits and new developments are required to fulfil increasing demands on engineering materials. The performance of materials can be increased by combining different materials to achieve better properties than a single constituent or by shaping the material or constituents in a specific structure. The interaction between material and structure may arise on different length scales, such as micro-, meso- or macroscale, and offers possible applications in quite diverse fields.

This book series addresses the fundamental relationship between materials and their structure on the overall properties (e.g. mechanical, thermal, chemical or magnetic etc.) and applications.

The topics of *Advanced Structured Materials* include but are not limited to

- classical fibre-reinforced composites (e.g. glass, carbon or Aramid reinforced plastics)
- metal matrix composites (MMCs)
- micro porous composites
- micro channel materials
- multilayered materials
- cellular materials (e.g., metallic or polymer foams, sponges, hollow sphere structures)
- porous materials
- truss structures
- nanocomposite materials
- biomaterials
- nanoporous metals
- concrete
- coated materials
- smart materials

Advanced Structured Materials is indexed in Google Scholar and Scopus.

More information about this series at <http://www.springer.com/series/8611>

Muhamad Husaini Abu Bakar ·
Faizatul Azwa Zamri · Andreas Öchsner
Editors

Progress in Engineering Technology II

 Springer

Editors

Muhamad Husaini Abu Bakar
Malaysian Spanish Institute
Universiti Kuala Lumpur
Kulim, Kedah, Malaysia

Faizatul Azwa Zamri
Malaysian Spanish Institute
Universiti Kuala Lumpur
Kulim, Kedah, Malaysia

Andreas Öchsner
Faculty of Mechanical Engineering
Esslingen University of Applied Sciences
Esslingen, Baden-Württemberg, Germany

ISSN 1869-8433

Advanced Structured Materials

ISBN 978-3-030-46035-8

<https://doi.org/10.1007/978-3-030-46036-5>

ISSN 1869-8441 (electronic)

ISBN 978-3-030-46036-5 (eBook)

© The Editor(s) (if applicable) and The Author(s), under exclusive license to Springer Nature Switzerland AG 2020

This work is subject to copyright. All rights are solely and exclusively licensed by the Publisher, whether the whole or part of the material is concerned, specifically the rights of translation, reprinting, reuse of illustrations, recitation, broadcasting, reproduction on microfilms or in any other physical way, and transmission or information storage and retrieval, electronic adaptation, computer software, or by similar or dissimilar methodology now known or hereafter developed.

The use of general descriptive names, registered names, trademarks, service marks, etc. in this publication does not imply, even in the absence of a specific statement, that such names are exempt from the relevant protective laws and regulations and therefore free for general use.

The publisher, the authors and the editors are safe to assume that the advice and information in this book are believed to be true and accurate at the date of publication. Neither the publisher nor the authors or the editors give a warranty, expressed or implied, with respect to the material contained herein or for any errors or omissions that may have been made. The publisher remains neutral with regard to jurisdictional claims in published maps and institutional affiliations.

This Springer imprint is published by the registered company Springer Nature Switzerland AG
The registered company address is: Gewerbestrasse 11, 6330 Cham, Switzerland

Contents

1	Micro-Power Energy Harvester Using Piezoelectric for Acoustic Sound Wave Energy Harvesting	1
	Haris Fazilah Hassan and Rosemizi Abd Rahim	
1.1	Introduction	2
1.2	Experimental Setup	3
1.3	Result and Discussion	3
1.4	Conclusion	5
	References	6
2	Damage Diagnosis of a Structural Steel Plate Using Wavelet Packet Transform	7
	Pranesh Krishnan, Sazali Yaacob, M. P. Paulraj, and Mohd Shukry Abdul Majid	
2.1	Introduction	8
2.2	Methods	9
2.3	Feature Extraction	11
2.3.1	Wavelet Packet Decomposition (WPC)	12
2.4	Damage Classification	13
2.5	Classification Results	13
2.6	Conclusions	14
	References	14
3	A Study on the Influence of Temperature on Steel Corrosion Over Time	17
	Sharmiwati-Mohammed-Sharif and Wan Noreaman Wan Zuharuddin	
3.1	Introduction	17
3.2	Methods	18
3.2.1	Material	18
3.2.2	Temperature	19
3.2.3	Thermal Imaging	19

3.3	Results and Discussion	20
3.4	Conclusion	22
	References	22
4	Binding Friction of NiTi Archwires at Different Size and Shape in 3-Bracket Bending Configuration	25
	Mohd Nizam Ahmad, Abdus Samad Mahmud, Muhammad Fauzinizam Razali, and Norehan Mokhtar	
4.1	Introduction	26
4.2	Materials and Method	26
4.3	Results and Discussion	28
4.4	Conclusion	31
	References	31
5	Design of a Child Restraint System for Motorcycles	33
	Zulkarnain Abdul Latiff and Fazidah Saad	
5.1	Introduction	33
	5.1.1 Problem Statement	34
	5.1.2 Objectives	34
5.2	Literature Review	37
5.3	Methodology	37
	5.3.1 CAD Modelling	39
	5.3.2 Finite Element Analysis	39
	5.3.3 Material Selection	39
5.4	Results and Discussions	39
5.5	Conclusions	42
	References	43
6	Drowsiness Detection Using Electroencephalogram Anomaly Based on Spectral Entropy Features and Linear Classifier	45
	Pranesh Krishnan, Sazali Yaacob, and Annapoorni Pranesh Krishnan	
6.1	Introduction	46
6.2	Methods	48
6.3	Feature Extraction	49
6.4	Results	53
6.5	Conclusion	53
	References	54
7	Close Loop Feedback Direct Current Control in Driving Mode of a Four Quadarns Drive Direct Current Chopper for Electric Vehicle Traction Controlled Using Fuzzy Logic	57
	Saharul Arof, Noramlee M. Noor, R. Mohamad, Emilia Noorsal, P. A. Mawby, and H. Arof	
7.1	Introduction	58
7.2	Literature	58

- 7.2.1 Four Quadrants Drive DC Chopper 59
- 7.2.2 Fuzzy Logic 62
- 7.3 Methodology 64
 - 7.3.1 Simulation Model with MATLAB/Simulink 68
- 7.4 Result and Discussion 68
- 7.5 Conclusions 70
- References 71

- 8 Digital Proportional Integral Derivative (PID) Controller for Closed-Loop Direct Current Control of an Electric Vehicle Traction Tuned Using Pole Placement 73**
 Saharul Arof, N. M. Noor, M. F. Alias, Emilia Noorsal, Philip Mawby, and H. Arof
- 8.1 Introduction 74
- 8.2 Literature Review 74
 - 8.2.1 Direct Current Control During Driving Mode 75
 - 8.2.2 Mathematical Equation in Driving Mode 76
- 8.3 Methodology 78
 - 8.3.1 System Stability Using Root Locus 78
 - 8.3.2 PID Controller 79
 - 8.3.3 Tuning the PID Using MATLAB/Simulink SISOTOOL 80
 - 8.3.4 Conversion to Discrete Model 81
 - 8.3.5 PID Controller Design by Pole Assignment 82
 - 8.3.6 Simulation Model with MATLAB/Simulink 84
- 8.4 Results and Discussion 85
- 8.5 Conclusion 88
- References 88

- 9 Numerical Analysis of Multiphase Electrolyte Flows in an Al-Air Battery Using Smoothed Particle Hydrodynamics 91**
 Faizah Osman and Muhamad Husaini Abu Bakar
- 9.1 Introduction 91
- 9.2 Methodology 92
 - 9.2.1 Pre-processing 92
 - 9.2.2 Processing 93
 - 9.2.3 Post-processing 94
- 9.3 Results and Discussion 94
 - 9.3.1 Pressure Distribution 94
 - 9.3.2 Velocity Profile 95
 - 9.3.3 Velocity Contour 97
- 9.4 Conclusions 99
- References 99

10	Discrete-Time Linear System of New Series Motor Four-Quadrant Drive Direct Current Chopper Numerically Represented by Taylor Series	101
	Saharul Arof, E. D. Sukiman, N. H. N. Diyanah, N. M. Noor, Emilia Noorsal, Philip Mawby, and H. Arof	
10.1	Introduction	102
10.2	Literature Review	102
10.2.1	FQDC in Driving Mode	104
10.2.2	Numerical Representation	105
10.2.3	Taylor Series Numerical Solution	105
10.3	Methodology	106
10.3.1	Algorithm of Taylor Series	107
10.3.2	Simulation of the Model Using MATLAB/Simulink Function	109
10.4	Result and Discussion	109
10.5	Conclusion	110
	References	111
11	Cooking Oil Turbidity Analysis	113
	Marina Borhan, Muhammad Safwan Che Ab Aziz, Aiman Rafique Mohd Nasir, Muhamad Husaini Abu Bakar, and Liyana Isamail	
11.1	Introduction	113
11.2	Experimental	114
11.2.1	Cooking Oil	114
11.2.2	Turbidity Sensor	115
11.2.3	NodeMCU	115
11.2.4	Serial I2C LCD Display Adapter	116
11.2.5	ThingSpeak	117
11.3	Results and Discussion	118
11.4	Conclusions	118
	References	118
12	Series Motor Four-Quadrant Direct Current Chopper: Reverse Mode, Steering Position Control with Double-Circle Path Tracking and Control for Autonomous Reverse Parking of Direct Current Drive Electric Car	121
	Saharul Arof, M. S. Said, N. H. N. Diyanah, N. M. Noor, N. M. Yaakop, Philip Mawby, H. Arof, and Emilia Noorsal	
12.1	Introduction	122
12.1.1	Literature Review	122
12.1.2	Automatic Parking Review	122
12.1.3	Electric Power Steering	123
12.1.4	Path Tracking	125

- 12.2 Methodology 126
 - 12.2.1 Position Control of Steering 128
 - 12.2.2 Tuning PID Using SISO Tool 130
 - 12.2.3 Simulation Model 131
- 12.3 Results and Discussion 133
- 12.4 Conclusion 133
- References 135

- 13 Series Motor Four-Quadrant DC Chopper: Reverse Mode, Direct Current Control, Triple Cascade PIDs, and Ascend-Descend Algorithm with Feedback Optimization for Automatic Reverse Parking** 137
 - Saharul Arof, M. S. Said, N. H. N. Diyanah, N. M. Noor, J. A. Jalil, Philip Mawby, H. Arof, and Emilia Noorsal
 - 13.1 Introduction 138
 - 13.1.1 Literature Review 138
 - 13.1.2 Review of Automatic Parking 139
 - 13.2 Methodology 140
 - 13.2.1 Control Strategy During Reverse Mode 140
 - 13.2.2 Direct Current Control in Driving and Reverse Mode 142
 - 13.2.3 Vehicle Movement Control with Cascade PIDs 143
 - 13.2.4 Ascend-Descend Algorithm 144
 - 13.2.5 Simulation Model with MATLAB/Simulink 145
 - 13.3 Results and Discussion 146
 - 13.4 Conclusions 148
 - References 149

- 14 The Image Processing Technique of Defect Detection in Metal Materials Using Active Infrared Thermography** 151
 - Nor Liyana Maskuri, Muhamad Husaini Abu Bakar, and Ahmad Kamal Ismail
 - 14.1 Introduction 152
 - 14.2 Methodology 152
 - 14.2.1 Experimental Setup 152
 - 14.2.2 Image Acquisition and Processing 154
 - 14.2.3 Image Representation in the Red Green Blue Scale 154
 - 14.3 Results and Discussion 155
 - 14.3.1 Image Data 155
 - 14.3.2 Image Filtering and Enhancement 155
 - 14.3.3 Image Segmentation and Analysis 157
 - 14.4 Conclusions 159
 - References 159

15	Alternator Performance Analysis of a Micro-Turbogenerator in Automotive Application	161
	Khairul Shahril, Muhammad N. A. Hamid, Mohamad Zulfikar, Adli Tajul, and Shahril. N. Soid	
15.1	Introduction	162
15.2	Literature Review	162
15.3	Experimental Set-Up	165
15.3.1	Result Measurement	165
15.4	Results and Discussion	167
15.5	Conclusion	169
	References	169
16	Experimental Study of the Engine Performance Enhancement by Using a Micro-turbocharger System	171
	Khairul Shahril, S. N. Soid, Khairul Akmal, Muhammad N. A. Hamid, and W. Faradiana	
16.1	Introduction	172
16.2	Literature Review	172
16.3	Experimental Setup	174
16.3.1	Motorcycle Engine	174
16.3.2	Turbocharger (Spinning Turbine)	174
16.3.3	Test Rig	175
16.3.4	Project Setup Overview	176
16.4	Results and Discussion	177
16.4.1	Fuel Consumption	178
16.4.2	Engine Power, Torque and Brake Mean Effective Pressure	179
16.4.3	Specific Fuel Consumption	182
16.5	Conclusions	183
	References	184
17	Solving the Production Bottleneck Through Minimizing the Waste of Motion for Manual Assembly Processes	185
	Mohd Norzaimi Che Ani and Ishak Abdul Azid	
17.1	Introduction	186
17.2	A Review of Solving the Production Bottleneck	187
17.3	Research Framework	189
17.4	Data Collection and Analysis	190
17.4.1	Phase 1: Process Familiarization and Time Study Analysis	190
17.4.2	Phase 2: Bottleneck Analysis and Waste Optimization	193
17.4.3	Phase 3: Validation, Verification, and Implementation	194

17.5	Discussions	195
17.6	Conclusions	196
	References	197
18	Investigation the Impact of 5S Implementation Toward Accident-Free Manufacturing Industries	199
	Muhammad Syafiq Ridha Mutaza, Mohd Norzaimi Che Ani, and Azmi Hassan	
18.1	Introduction	200
18.2	5S Review	201
18.3	Research Approach	201
18.4	Result and Discussion	202
18.5	Conclusion	202
	References	204
19	Effect of Maleic Anhydride Polypropylene on the Properties of Spear Grass Fiber in Reinforced Polypropylene and Ethylene Propylene Diene Monomer Composites	205
	Muhammad Azree Ifwat Adnan, Faizatul Azwa Zamri, Mohamad Sabri Mohamad Sidik, and Siti Rohana Ahmad	
19.1	Introduction	206
19.2	Methodology	206
	19.2.1 Preparation of PP/EPDM/SGF Composites	206
	19.2.2 Water Absorption Test	208
	19.2.3 Tensile Test	209
19.3	Result and Discussion	209
	19.3.1 Water Absorption	209
	19.3.2 Tensile Properties	210
19.4	Conclusion	211
	References	212
20	Effect of Acid Acrylic on Mechanical Properties and Swelling Behavior of Spear Grass Fiber Filled Polypropylene Composites	213
	Nuramalena Abdul Latif, Muhammad Afiq Mohd Nabin, Mohamad Sabri Mohamad Sidik, and Nurashikin Sawal	
20.1	Introduction	214
20.2	Experimental	214
	20.2.1 Materials	214
	20.2.2 Mixing Procedure	214
	20.2.3 Filler Treatment	216
	20.2.4 Compression Molding	216
	20.2.5 Mechanical Tensile Test	216
	20.2.6 Water Absorption Test	216

20.3 Results and Discussion 217

 20.3.1 Tensile Strength 217

 20.3.2 Young’s Modulus 217

 20.3.3 Elongation at Break 218

 20.3.4 Water Absorption 219

20.4 Conclusion 220

References 220

21 Parametric Optimization of Electrical Discharge Machining of SiSiC Ceramic Through the Taguchi Design Approach 223

Abdul’Azeez A. Aliyu, Ahmad Majdi Abdul Rani,
Muhammad Al’Hapis Abdul Razak, and Sadaqat Ali

21.1 Introduction 224

21.2 Experimentation 224

 21.2.1 Materials 224

 21.2.2 Procedure and Methods 225

 21.2.3 Taguchi Approach 227

21.3 Results and Analysis 228

21.4 Verification Runs 231

21.5 Conclusions 233

References 233

22 The Impact of Sintering Dwell Time on Nitrogen Absorption, Densification and Microhardness of 316L Stainless Steel Using Powder Metallurgy 235

Sadaqat Ali, Ahmad Majdi Abdul Rani,
Muhammad Al’Hapis Abdul Razak, Abdul Azeez Abdu Aliyu,
and Krishnan Subramaniam

22.1 Introduction 236

22.2 Materials and Methods 237

22.3 Results and Discussion 238

22.4 Conclusion 241

References 242

23 Kinematic and Dynamic Analysis of a Stephenson III Six-Bar Linkage for Amplified Rectilinear Motion: Application to Globe Valve Control Mechanism 243

Farooq I. Azam, Haizum Aimi Zaharin, Ahmad Majdi Abdul Rani,
and Muhammad Al’Hapis Abdul Razak

23.1 Introduction 244

23.2 Kinematic Synthesis 245

23.3 Kinematic Analysis 247

23.4 Force Analysis 250

23.5 Conclusion and Future Implications 251

References 254

- 24 Influence of Porous Designs on Mechanical Properties of Ti6Al4V for Biomedical Applications 255**
Haizum Aimi Zaharin, Farooq I. Azam, Ahmad Majdi Abdul Rani, and Muhammad Al’Hapis Abdul Razak
- 24.1 Introduction 256
- 24.2 Literature Review 256
 - 24.2.1 Bone Mechanical Properties 257
 - 24.2.2 Aseptic Loosening and Stress Shielding 258
 - 24.2.3 Scaffold Porous Structures 259
- 24.3 Methodology 260
- 24.4 Results 262
- 24.5 Conclusion and Future Implications 269
- References 269

Chapter 1

Micro-Power Energy Harvester Using Piezoelectric for Acoustic Sound Wave Energy Harvesting



Haris Fazilah Hassan and Rosemizi Abd Rahim

Abstract The advancement of portable electronic devices and the ever-increasing integrated functions which have become a necessity in smartphones, tablets and similar devices have prompted the industry to look for portable power supplies to enhance the lifetime and the usage of portable electronic devices. Therefore, harvesting free energy from the surroundings to provide usable electrical energy could be an interesting solution toward this requirement. In this paper, sound waves energy which is in the form of a pressure wave is investigated to be as a source of free energy which is abundant in our surroundings. The piezoelectric type called PZT 5A bimorph cantilever was introduced as a sound energy harvester during an experimental work. The piezoelectric was tested to extract sound energy produced by the loudspeaker at several predetermined distances from the loudspeaker. The result shows that the maximum voltage of $83 \text{ mV}_{\text{peak}}$ was obtained with the sound intensity of 102.6 dB at a resonant frequency of 374 Hz, and the maximum power of $3.445 \mu\text{W}$ was produced at 1 k Ω of optimal load resistance.

Keywords Piezoelectric bimorph cantilever · Sound waves energy resonant frequency · Maximum power

H. F. Hassan (✉)

Electrical, Electronics and Automation Section, Universiti Kuala Lumpur-Malaysian Spanish Institute, 09000 Kulim, Kedah, Malaysia

e-mail: harisfazilah@unikl.edu.my

R. Abd Rahim

Advanced Communication Engineering Centre, School of Computer and Communication Engineering, University Malaysia Perlis, Perlis, Malaysia

e-mail: rosemizi@unimap.edu.my

© The Editor(s) (if applicable) and The Author(s), under exclusive license to Springer Nature Switzerland AG 2020

M. H. Abu Bakar et al. (eds.), *Progress in Engineering Technology II*,

Advanced Structured Materials 131,

https://doi.org/10.1007/978-3-030-46036-5_1

1.1 Introduction

To date, most of the portable electronic devices such as electronic communication devices and wireless sensor electronic devices are battery-powered. Thus, it will require a continuous battery replacement or battery charging due to its limited lifetime. Due to this limitation, the utilization of free energy from the surroundings to replace the dependency on battery will be an interesting solution. Furthermore, harvesting free energy as a source of electrical power will be capable to improve the lifetime and the usage of portable electronic devices.

Recently, many researchers show their interest in the field of energy harvesting technology to develop self-powered electronic devices by utilizing the environmental energy. For instance, harvesting energy from thermal [1, 2], solar [3, 4], wind [5, 6] and mechanical vibration [7–9] has been explored to utilize this energy in powering low power consumption electronic devices.

One of the abundant sources in our surroundings and good to be utilized as a source of energy is the sound wave energy. It is sustainable and easy to obtain and will provide a great advantage to be a potential source in energy harvesting application. In sound wave energy harvesting, the main issue that has been highlighted is the low-level energy density available in the surroundings [10, 11]. Therefore, it is imperative that the acoustic energy harvester must be designed to be able to capture the maximum energy density at a resonant frequency in order to produce maximum electrical energy. Many studies have been presented in enhancing the acoustic energy harvesting in different techniques. Generally, these techniques can be classified into resonant matching techniques, harvesting techniques and circuit optimization techniques.

In the case of resonant matching technique, there was a study to perform experimental investigations on acoustic energy harvesting utilizing a piezoelectric (PVDF composite) cantilever integrated with a Helmholtz resonator [12]. The result has conclusively shown that the maximum energy conversion efficiency occurred when the resonant frequency of the cantilever and acoustic noise resonant frequency from the Helmholtz resonator were matched. A maximum harvested voltage of 0.22 V was produced at 865 Hz of resonant frequency.

In the case of harvesting technique, a study discovered that the maximization of harvested power efficiency for multiple PVDF piezoelectric cantilever beam can be optimized by configuring its array placement such as the aligned and the zigzag configurations [13]. The results showed that the PVDF beams placed in the zigzag configuration were able to produce more 36.7% of harvested voltage and 45% of harvested power as compared to the aligned configuration. The significant increases in the harvested voltage and power are due to more paths for the acoustic air particles' motion which occurred in the zigzag configuration.

1.2 Experimental Setup

In principle, a sound wave can be classified as a longitudinal wave created by the vibration of the object. For instance, the sound wave that travels through the air will cause vibration and pressure along the direction of wave motion due to changes in density of the wave. As a result, it will create vibration energy which is conveyed through a medium. With this phenomenon, this energy is looking to have a great potential to be as a source of energy for energy conversion from sound energy to electrical energy.

In this study, harvesting sound energy and converting it into electrical energy will be performed by a piezoelectric generator. A piezoelectric material is an active material which will generate an electrical charge under mechanical stress. It has good properties such as a simple structure, higher output voltage and higher conversion efficiency.

In this section, a PZT 5A bimorph cantilever is employed to act as an energy extractor and generator. The piezoelectric generator will extract the sound wave energy from a loudspeaker. The loudspeaker is used to generate sound wave energy from the motion of the diaphragm and produces a longitudinal sound wave motion which is in the form of a pressure wave. Then, the energy carried by the pressure wave will hit the cantilever and cause the deformation of the cantilever structure. As a result, the deformation of the cantilever structure will produce an electrical charge which is in the form of a sine wave voltage. During the experiment, the amplitude voltage of the loudspeaker is set at 10 mV_{p-p}, and the frequency is varied at different values until the resonant frequency of the cantilever is determined. The resonant frequency of the PZT 5A bimorph cantilever is obtained by referring to the highest output voltage achieved at certain values of the varied frequencies.

In this work, the piezoelectric generator is separated at 1 cm, 3 cm and 5 cm distance, respectively, to the loudspeaker during the experimental work. The signal generator is used to generate the loudspeaker at certain frequency and the amplitude of voltage. Finally, the voltage generated by the piezoelectric generator is measured by using an oscilloscope, and for sound intensity measurement, a sound-level meter is used in this work. The overall experimental setup is illustrated in Fig. 1.1.

1.3 Result and Discussion

The performance of the PZT-5A harvester is evaluated based on the ability to produce maximum sinusoidal voltage at resonant condition. By using the frequency matching technique whereby, the frequency of the sound generated from the source is tuned to match the frequency of PZT-5A harvester. The measurement of the maximum voltage amplitude generated from PZT-5A harvester was measured in open-circuit condition, and the result is presented in Fig. 1.2.

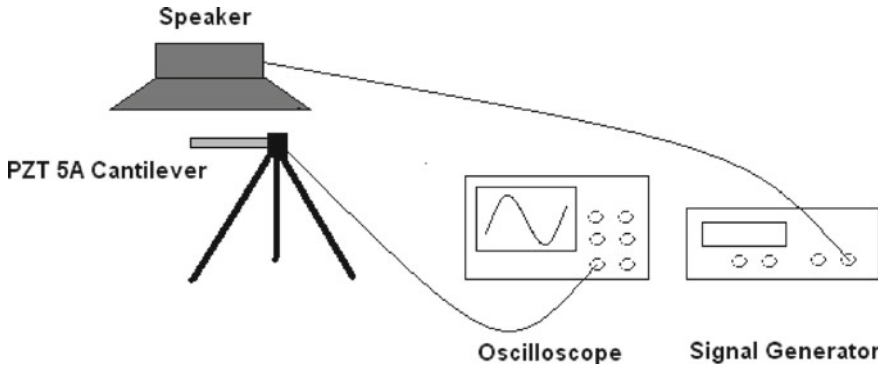


Fig. 1.1 Schematic of the sound wave energy harvesting experimental setup

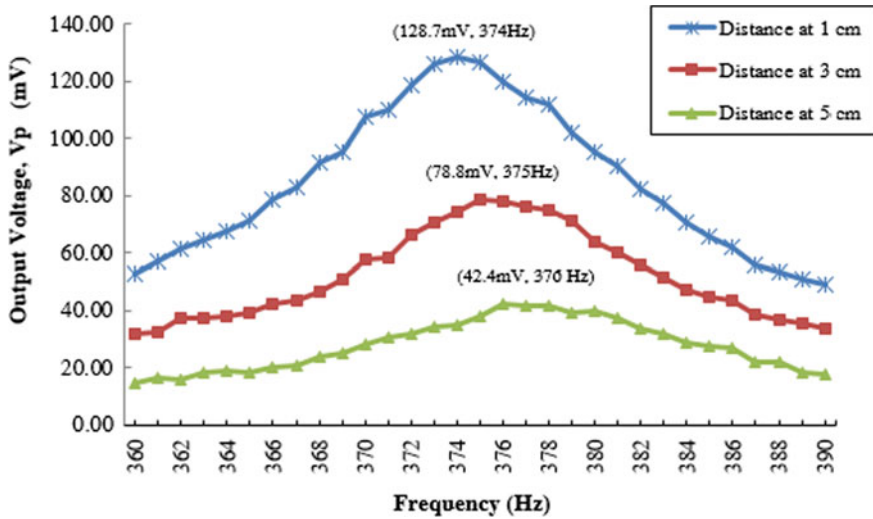


Fig. 1.2 PZT-5A open-circuit output voltage measurement at different distances

Figure 1.2 illustrates the measurement result where it shows that the maximum voltage of 128.7 mV_p in open-circuit condition occurs at 374 Hz of resonant frequency. Simultaneously, in conjunction with the resonant frequency of 374 Hz, the SPL value was measured and found to be 102.6 dB. The result of the measurement is summarized in Table 1.1.

Another pertinent study was also carried out to evaluate the maximum power generated by the PZT-5A. By applying the impedance matching technique, the maximum power is determined by applying different values of resistive load. The results of the experimental works were obtained by varying the value of the resistive load and the output voltage was then measured at resonant condition.

Table 1.1 PZT-5A open-circuit output voltage measurement at resonant frequency

Distance (cm)	Resonant frequency (Hz)	SPL (dB)	Output voltage (mV _p)
1	374	102.6	128.7
3	375	99.6	78.8
5	376	95.6	42.4

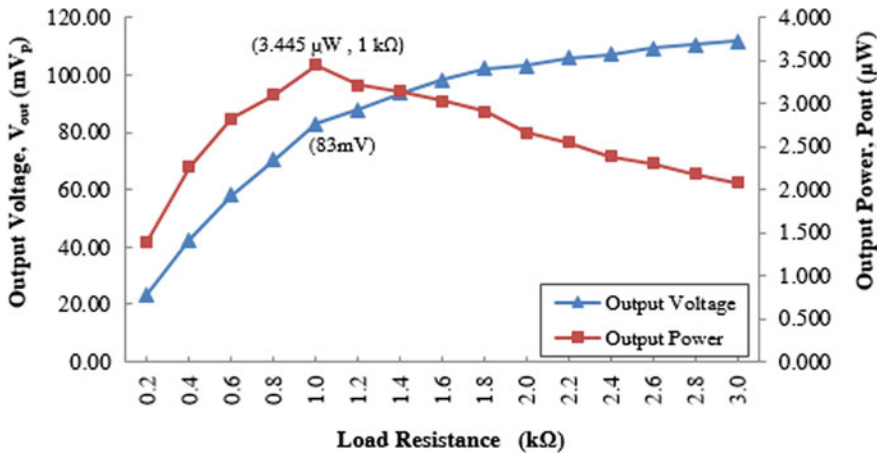


Fig. 1.3 PZT-5A maximum output power measurement

From Fig. 1.3, it has been found that both impedances between internal resistance of the PZT-5A harvester and load resistance matched at 1 kΩ. The corresponding voltage of 83 mV_p at 1 kΩ optimal load resistance was then used to calculate the maximum power output from the PZT-5A harvester which was found to be 3.445 µW.

1.4 Conclusion

In this work, the experimental work of sound wave energy harvesting using a piezoelectric bimorph cantilever was presented. The technique employed clearly demonstrates energy harvesting between the sound source and piezoelectric generator in both closed-contact and opened-contact states, thus justifying the feasibility of sound as a source of energy in piezoelectric energy harvesting applications. It is clearly shown that the maximum power produced by the PZT-5A generator was found to be 3.445 µW and the corresponding voltage of 83 mV_p at 1 kΩ optimal load resistance was obtained with the sound intensity of 102.6 dB at resonant frequency of 374 Hz. The result also verifies and successfully demonstrates the usage of piezoelectric generators in a cantilever structure to harvest the sound energy.

References

1. Yang, S.M., Lee, T.: Development of a thermoelectric energy harvester with thermal isolation cavity by standard CMOS process. *Sens. Actuator A Phys.* **153**(2), 244–250 (2009)
2. Ferrari, M., Ferrari, V., Guizzetti, M., Marioli, D., Taroni, A.: Characterization of thermoelectric modules for powering autonomous sensors. In: *Instrumentation and measurement technology conference (IMTC '07)*, Warsaw, Poland, pp. 1–6 (2007)
3. Guilar, N., Chen, A., Kleeburg, T., Amirtharajah, R.: Integrated solar energy harvesting and storage. In: *International symposium on low power electronics and design—2006 (ISLPED '06)*, Tegernsee, Germany, pp. 20–24 (2006)
4. Guilar, N.J., Kleeburg, T.J., Chen, A., Yankelevich, D.R., Amirtharajah, R.: Integrated solar energy harvesting and storage. *IEEE Trans. Very Large Scale Integr. (VLSI) Syst.* **17**(5), 627–637 (2009)
5. Myers, R., Vickers, M., Kim, H.: Small scale windmill. *Appl. Phys. Lett.* **90**(054106), 3 (2007)
6. Sodano, H.A., Park, G., Inman, D.J.: A review of power harvesting from vibration using piezoelectric materials. *Shock Vibration Digest* **36**(3), 197–205 (2004)
7. Beeby, S.P., Tudor, M.J., White, N.M.: Energy Harvesting vibration sources for Microsystems applications. *Meas. Sci. Technol.* **17**, R175–195 (2006)
8. Roundy, S., Wright, P.K., Rabaye, J.: A study of low level vibrations as a power source for wireless sensor nodes. *Comput. Commun.* **26**, 1131–1144 (2003)
9. Roundy, S., Wright, P.K.: A piezoelectric vibration based generator for wireless electronics. *Smart Mater. Struct.* **13**, 1131–1142 (2004)
10. Li, B., You, J.H.: Harvesting ambient acoustic energy using acoustic resonators. In: *Proceedings of Meetings on Acoustics* vol. 12, No. 1, p. 065001. Acoustical Society of America (2011)
11. Cunefare, K.A., Skow, E.A., & Erturk, A.: Transduction as energy conversion; harvesting of acoustic energy in hydraulic systems. In: *Proceedings of Meetings on Acoustics*. vol. 19, No. 1, p. 030070. Acoustical Society of America (2013)
12. Noh, S., Lee, H., Choi, B.: A study on the acoustic energy harvesting with Helmholtz resonator and piezoelectric cantilevers. *Int. J. Precision Eng. Manuf.* **14**(9), 1629–1635 (2013)
13. Li, B., Laviage, A.J., You, J.H., Kim, Y.J.: Harvesting low-frequency acoustic energy using quarter-wavelength straight-tube acoustic resonator. *Appl. Acoust.* **74**(11), 1271–1278 (2013)

Chapter 2

Damage Diagnosis of a Structural Steel Plate Using Wavelet Packet Transform



**Pranesh Krishnan, Sazali Yaacob, M. P. Paulraj,
and Mohd Shukry Abdul Majid**

Abstract Cracks and physical damages are a threat to the strength of structures. Non-destructive test (NDT) measures are used to detect the damages at the earlier phase to avoid any major damage to the structures. Vibration signal processing is one of the NDT methods to determine the damage based on the experimental modal analysis. In this study, an experimental setup is devised to freely suspend a steel plate of size 30 cm by 60 cm. Based on the experimental modal analysis, the steel structure is struck using an impact hammer and the dispersed mechanical energy is bagged as vibration response using an accelerometer. The damages of size 512–1852 μm were manually simulated at arbitrary locations on the surface of the steel structure. The data acquisition procedure is repeated before and after the simulation of damage. The vibration signals are then processed, and the wavelet packet transform is applied to extract the dominant features from both the normal and fault data. The feature set is normalized between 0 and 1 are then mapped toward the condition of the plate to formulate the final dataset. Using a K-fold cross-validation technique, the dataset is trained and tested using support vector machine (SVM) and K-nearest neighbor (KNN) classifiers. The results are compared and discussed.

P. Krishnan (✉) · S. Yaacob

Intelligent Automotive Systems Research Cluster, Electrical Electronics and Automation Section, Malaysian Spanish Institute Universiti Kuala Lumpur, Kulim Hi-Tech Park, 09000 Kulim, Kedah, Malaysia

e-mail: pranesh@unikl.edu.my

S. Yaacob

e-mail: sazali.yaacob@unikl.edu.my

M. P. Paulraj

Sri Ramakrishna Institute of Technology, Coimbatore, Tamil Nadu, India

e-mail: paulraj.pandian@yahoo.com

M. S. Abdul Majid

School of Mechatronic Engineering, Universiti Malaysia Perlis, 02600 Arau, Perlis, Malaysia

e-mail: shukry@unimap.edu.my

© The Editor(s) (if applicable) and The Author(s), under exclusive license to Springer Nature Switzerland AG 2020

M. H. Abu Bakar et al. (eds.), *Progress in Engineering Technology II*,

Advanced Structured Materials 131,

https://doi.org/10.1007/978-3-030-46036-5_2

Keywords Damage detection · Experimental modal analysis · Non-destructive testing · Wavelet packet transform

2.1 Introduction

Unidentified damages can put human safety at risk, cause long-term machine downtimes, interruption in the production and subsequently increase the production cost. Early damage detection and possible location of the faults from the vibration measurements is one of the primary tasks of condition monitoring. Vibration-based condition monitoring has been in practice since the late 1970s. Several approaches have been used in the literature which are categorized as: (a) Natural frequency based, (b) mode shape based, (c) mode shape curvature or strain mode shape based, (d) dynamic measured flexibility based, (e) matrix update based, (f) the non-linear method based, (g) neural network based, and other methods. Carden and Fanning [2] conducted a detailed review of the vibration-based condition monitoring techniques. Their review emphasized on the structural engineering applications. They discussed various pattern recognition models. Yan et al. [8] summarized the state-of-the-art and development of vibration-based structural damage detection methods. They discussed the traditional type (frequency response function, change in natural frequency, change in structural stiffness) and modern type (neural network, wavelet analysis, genetic algorithm) vibration-based damage detection. Further, Fan and Qiao [3] extended the review on the vibration-based damage identification methods. They summarized the damage identification algorithms developed for beam type and plate type structures. They also highlighted the limitations of the existing damage detection methods. They finally addressed the need for robust multiple damage detection methods, quantification methods for damage magnitude, and viable damage identification methods. Zhou et al. [10] used a vibration exciter and Fiber Bragg Gratings (FBG) sensors to detect damage from a steel plate. They employed a multiple scale entropy and a support vector machine to detect the presence of the damage. Zhang et al. [9] conducted a simulation study on the shear crack on steel plates. Rus et al. [7] developed an optimization technique for steel plate damage detection based on the noisy impact test. They designed an optimal filter to reduce the effect of noise. Gao et al. [4] conducted an experimental study to detect the multi-damage in steel plates based on the non-modal method. They presented a damage localization index (IFS flexibility). They also discussed on the effect of boundary condition and damage magnitude. Alavi et al. [1] presented a method for crack growth detection in steel plates. Damage growth was studied using data fusion of multiple sensors and damage progression was studied using individual sensors. Zima and Rucka [11] investigated the damage detection using the guided wave propagation technique. They used a continuous wavelet transform to find the reflected waves in the Lamb wave signals. Several researchers have adopted the vibration-based damage diagnosis in the fields of rotating machinery, civil engineering, and structural health monitoring.

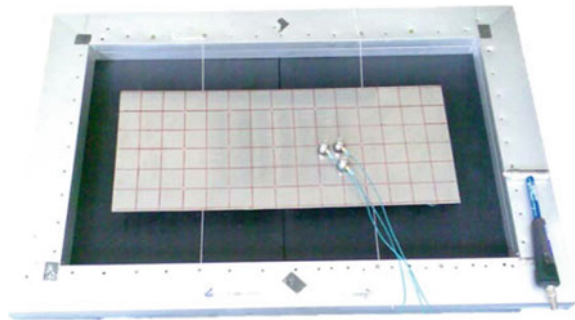
In this work, the existence of damage is identified using the support vector machine (SVM) model developed using the spectral features extracted from the vibration response. Based on the experimental modal analysis, a protocol is designed to excite a freely suspended steel structure. The distribution of the vibration response is captured using accelerometers. The excitation point and the placement of accelerometers are changed to record the data throughout the structure. Damages are simulated and the experiment is repeated in the damaged condition. The vibration signal is further trimmed and segmented into frames. The spectral features are further extracted from each frame to constitute the feature set. The feature vectors are normalized and the condition of the steel structure is labeled accordingly to form the final dataset. A support vector modal is constructed and trained based on the K-fold cross-validation method. The network model is tested and the classification accuracy is reported.

2.2 Methods

For this study, a stainless-steel plate of 60 cm by 30 cm was considered. An experimental framework was designed to loosely support the steel plate. The selection of the steel structure, the dimensions, numbering format, and the details of the procedure have been discussed in detail in the author's previous papers [5, 6] (Fig. 2.1).

Data Collection: The cells are evenly divided and only 36 chambers at the center of the plate are considered for the experiment. The data collection protocol is designed by changing the locations of the impact points and accelerometers (a combination of roving hammer and roving accelerometer tests). The details of the data acquisition are detailed in the earlier publication by the author [5, 6]. The impact test is carried out for the 36 locations by changing the locations of the impact and the accelerometer which constitutes of 144 samples. Each sample contains four signals (1 impact hammer signal and three accelerometer signals). The dispersion of energy and the protocol are represented in Figs. 2.2, 2.3, 2.4 and 2.5. The impact experiment is conducted on 10 similar steel plates under normal condition which forms 1440 normal samples.

Fig. 2.1 Experimental support for a loosely supported steel plate



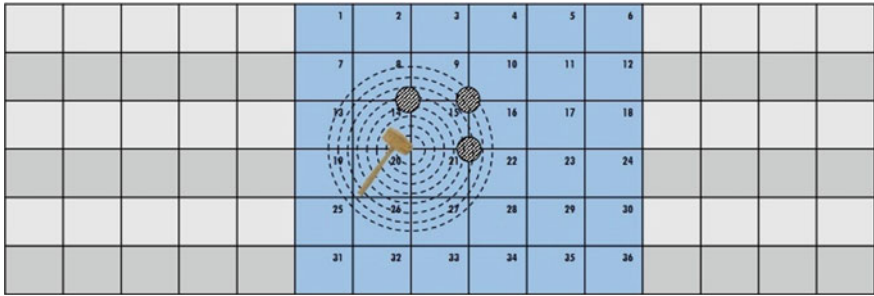


Fig. 2.2 Accelerometer localization (protocol 1)

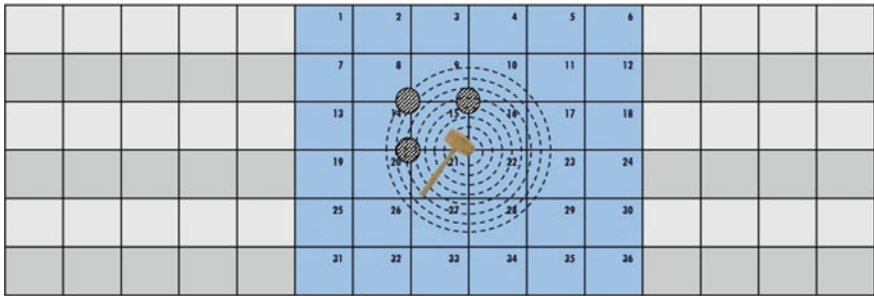


Fig. 2.3 Accelerometer localization (protocol 2)

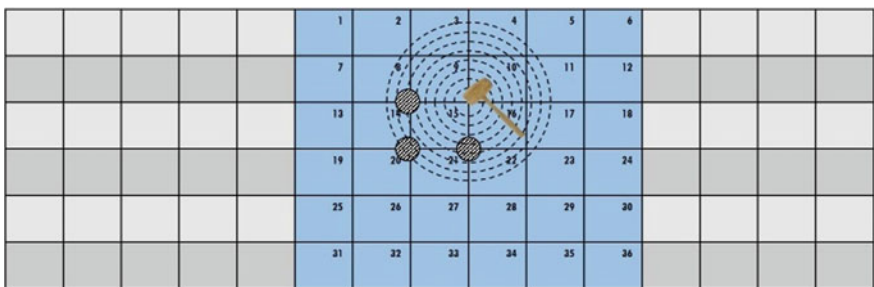


Fig. 2.4 Accelerometer localization (protocol 3)

Damage simulation: Damages were simulated using drill bits on the surface of the steel plate at arbitrary locations for all the 10 plates. The depth of the damage was measured using a surface electron microscope. The average depths of the simulated damages were 1182 μm . The experiment is repeated after the damage simulation for all the 144 locations in the 10 plates to form 1440 damaged samples.

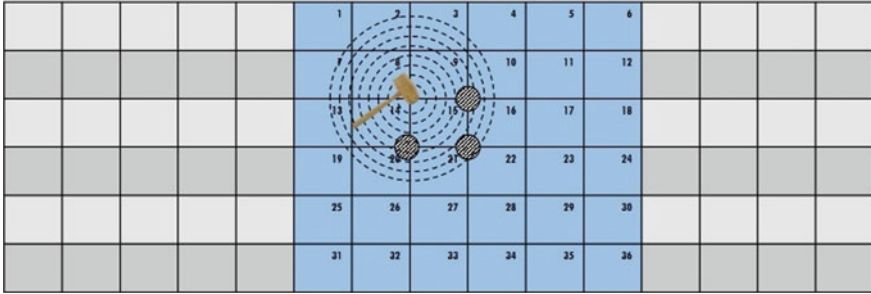


Fig. 2.5 Accelerometer localization (protocol 4)

2.3 Feature Extraction

Features carry dominant characteristics of the signal by reducing the dimensionality without losing the information. The vibration signal represents an exponential decay of the energy dispersed through the structure after the impact with respect to time. The signal spans for 20 s, however, the time of strike of the impact hammer on the steel plate is inconsistent throughout the experiment. Also, the exponential decay is not consistent throughout all the locations of the structure. The raw signal is the signal that is trimmed and is represented in Fig. 2.6. Fast Fourier transform (FFT) is computed over the raw signal and represents the frequency components of the signal. Figure 2.7 shows the FFT plot of the complete signal.

To effectively study the features, the vibration signal is segmented into frames of 1024 samples.

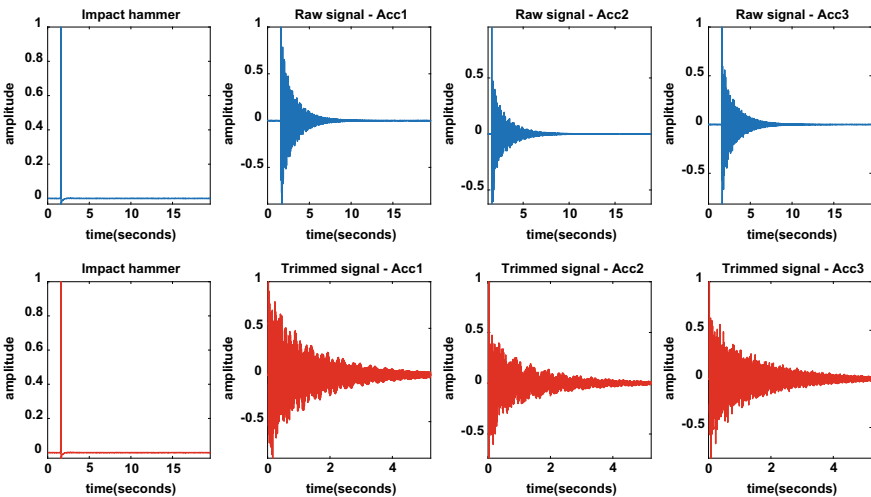


Fig. 2.6 Raw and trimmed accelerometer signals

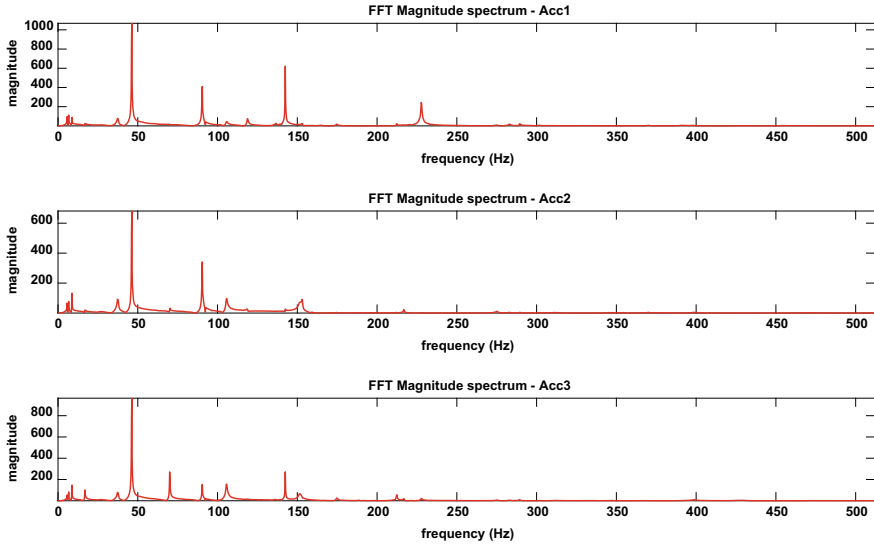


Fig. 2.7 FFT magnitude spectrum of a typical signal

2.3.1 Wavelet Packet Decomposition (WPC)

Wavelet transform is a mathematical tool that transforms the sequential data in time axis to spectral data in both time and frequency domain. In regular wavelet analysis, the decomposition occurs only to the approximation component of each level using the dyadic filter bank. However, the necessary frequencies can be achieved by implementing the wavelet packet transform to further decompose the signal. For n level decomposition, there are $n + 1$ possible ways to decompose or encode the signal. In wavelet packet analysis, the details as well as the approximation can be split. This yields more than different ways to encode the signal.

Each component in the wavelet packet tree can be viewed as a filtered component with a bandwidth of a filter decreasing with increasing level of decomposition and the whole tree can be viewed as a filter bank.

A wavelet packet is represented as a function, ' ψ ', where ' i ' is the modulation parameter, ' j ' is the dilation parameter and ' k ' is the translation parameter.

$$\psi_{j,k}^i(t) = 2^{-j/2} \psi^i(2^{-j}t - k) \quad (2.1)$$

where $i = 1, 2, 3 \dots jn$ and ' n ' is the level of decomposition in the wavelet packet tree. The wavelet is obtained by the following recursive relationship

$$\psi^{2i}(t) = \frac{1}{\sqrt{2}} \sum_{k=-\infty}^{\infty} h(k) \psi^i\left(\frac{t}{2} - k\right) \quad (2.2)$$

2.4 Damage Classification

Data preprocessing is referred to the set of procedures used to process the raw data for further processing such as classification or clustering. The dataset derived from the features does not follow a uniform data distribution. Hence, the feature set is rescaled between a certain range to enhance the performance of the classifier. The spectral features derived from the vibration signals are rescaled between '0' and '1' and associated with the class to form the dataset for classification.

Support vector machine (SVM) model is a machine learning algorithm based on the statistical learning. The SVM model is chosen in this study to classify the presence of damage. In this method, we plot each data as a point in the n -dimensional space with the value of each feature being the value of the particular coordinate. The classification is performed by finding the hyperplane that differentiates between the two classes. Hence, finding the right hyperplane becomes very crucial in SVM. By maximizing the distance, also known as the margin between the nearest data point and the hyperplane will determine the right hyperplane. The kernel method is used to transform the low-dimensional input space to a higher dimensional space in a non-linear separation problem. The 'fitcsvm' function in MATLAB is used to model the SVM. 'Radial basis function' kernel is used to classify between drowsy and alert classes.

K-Nearest neighbor algorithm (kNN) is one of the simplest and easy to implement a supervised machine learning algorithm. The K factor is very crucial in determining the class boundaries. The boundaries become smooth with increased values of K . The training error rate and the validation error rate are the two parameters used to access for the values of K . The 'fitcknn' function in MATLAB is used to model the KNN classifier. The 'Minkowski' method is used as a distance metric, and the number of neighbors value is chosen to be 3 in this classification method.

2.5 Classification Results

The wavelet packet transform features extracted from the vibration signals. Support vector machine and KNN classifiers were used to train the feature matrix. The K-fold cross-validation method is used to process the dataset into training and testing. The average classification accuracy, sensitivity, specificity, true positive rate, false positive rate for the KNN, and SVM classifiers are calculated and the results are tabulated in Table 2.1.

The results show that KNN outperforms SVM in accuracy, the sensitivity of the network is high.

Table 2.1 Classification results

Classifier	Accuracy	Sensitivity	Specificity	TPR	TFR
SVM	92.6	94.2	86.3	95.0	53.8
KNN	95.0	95.6	96.8	94.3	42.8

2.6 Conclusions

To conclude, the presence of damage is detected using the support vector machine (SVM) model developed using the spectral features extracted from the vibration response. Based on the experimental modal analysis, a protocol is designed to excite a freely suspended steel structure. The distribution of the vibration response is captured using the accelerometers. The excitation point and the placement of accelerometers are changed to record the data throughout the structure. Damages are simulated and the experiment is repeated in the damaged condition. The vibration signal is further trimmed and segmented into frames. The wavelet packet transform features are further extracted from each frame to constitute the feature set. The feature vectors are normalized and the condition of the steel structure is labeled accordingly to form the final dataset. SVM and KNN models are constructed and trained based on the K-fold cross-validation method. The network model is tested and the classification accuracy is reported. KNN model outperforms with an accuracy of 95%.

References

1. Alavi, A.H., Hasni, H., Lajnef, N., Chatti, K.: Damage growth detection in steel plates: numerical and experimental studies. *Eng. Struct.* **128**, 124–138 (2016). <https://doi.org/10.1016/j.engstruct.2016.09.026>
2. Carden, E.P., Fanning, P.: Vibration-based condition monitoring. *Mech. Mach. Sci.* **11**, 431–477 (2004). https://doi.org/10.1007/978-94-007-6422-4_11
3. Fan, W., Qiao, P.: Vibration-based damage identification methods: a review and comparative study. *Struct. Health Monit.* **10**(1), 83–111 (2011). <https://doi.org/10.1177/1475921710365419>
4. Gao, H., Guo, X., Zhao, Y.: Experimental study of multi-damage detection in a plate based on non-modal method. *Exp. Tech.* **38**(6), 6–15 (2014). <https://doi.org/10.1111/j.1747-1567.2012.00845.x>
5. Paulraj, M.P., Yaacob, S., Abdul Majid, M.S., Kazim, M.N.F.M., Krishnan, P.: Structural steel plate damage detection using nondestructive testing, frame energy based statistical features and artificial neural networks. *Procedia Eng.* **53**, 376–386 (2013)
6. Paulraj, M.P., Yaacob, S., Abdul Majid, M.S., Krishnan, P.: Application of frame energy based DCT moments for the damage diagnosis in steel plates using FLNN. In: 2012 IEEE Student Conference on Research and Development (SCORED), pp. 120–123 (2012). <https://doi.org/10.1109/SCORED.2012.6518623>
7. Rus, G., Lee, S.Y., Chang, S.Y., Wooh, S.C.: Optimized damage detection of steel plates from noisy impact test. *Int. J. Numer. Methods Eng.* **68**(7), 707–727 (2006). <https://doi.org/10.1002/nme.1720>

8. Yan, Y.J., Cheng, L., Wu, Z.Y., Yam, L.H.: Development in vibration-based structural damage detection technique. *Mech. Syst. Sig. Process.* **21**(5), 2198–2211 (2007). <https://doi.org/10.1016/j.ymssp.2006.10.002>
9. Zhang, S.Q., Jiao, S.H., Ding, J.H., Zhang, Q.F., Jiang, H.S.: Simulation study on shear crack of steel plate. *Mater. Sci. Forum* **941**, 480–485 (2018). <https://doi.org/10.4028/www.scientific.net/msf.941.480>
10. Zhou, Z., Peng, B., Wei, Q., Liu, Q., Jiang, X., Ai, Q.: Damage detection based on multi-scale entropy and support vector machine. In: *Proceedings of the 2014 International Conference on Innovative Design and Manufacturing (ICIDM)*, pp. 28–33. IEEE (2014)
11. Zima, B., Rucka, M.: Application of wavelet transform in analysis of guided wave propagation signals for damage detection in a steel plate. *Diagnostyka* **16**(2), 43–48 (2015)

Chapter 3

A Study on the Influence of Temperature on Steel Corrosion Over Time



Sharmiwati-Mohammed-Sharif and Wan Noreaman Wan Zuharuddin

Abstract Corrosion is the main factor for steel failure. It is a natural process, which converts a refined metal to a more chemically stable form, such as its oxide, hydroxide or sulphides. It's the gradual destruction of material (usually metals) by chemical and/or electrochemical reaction with the environment. For this study, the influence of temperature on the corrosion surface of the steel evaluated under the temperature that has been applied ranging between 40 and 110 °C for 2 min for the heat released by the material. The study of temperature absorption was conducted under low temperature between -17 °C until 15 °C for 2 min. This investigation of the experiment showed that the application of corrosion temperature behaviour of steel can be used or applied as the renewable application or purpose in the sector of engineering.

Keywords Corrosion · Temperature · Mild steel

3.1 Introduction

Steel in service often has lasting effects and long lifetime, but all materials except gold are unstable, that is, a material that is unstable in air and saturated water at ambient temperature, and for the most part, is also unstable in air-free water [6]. It is a natural process, which transforms fine metals into more stable forms of chemicals, such as oxides, hydroxides or sulphides, and it will cause a significant factor in steel failure [7]. Thus, almost all environments reveal hostile conditions for steels and their application in engineering and commercial success, and the application depends on the protection mechanism [5].

Sharmiwati-Mohammed-Sharif · W. N. Wan Zuharuddin (✉)
Universiti Kuala Lumpur Malaysian Spanish Institute, Kulim Hi-Tech Park, 09000 Kulim,
Kedah, Malaysia
e-mail: wannoreaman@gmail.com

Sharmiwati-Mohammed-Sharif
e-mail: sharmiwati@unikl.edu.my

© The Editor(s) (if applicable) and The Author(s), under exclusive license
to Springer Nature Switzerland AG 2020
M. H. Abu Bakar et al. (eds.), *Progress in Engineering Technology II*,
Advanced Structured Materials 131,
https://doi.org/10.1007/978-3-030-46036-5_3

In some steel/environment systems, the metal protected by passive, naturally formed surface conditions prevents reactions. In other arrangements, metal surfaces remain active, and some form of protection must be provided by the design [2]. It applies mainly to ordinary iron and low alloy steel and mild steel, which are the most productive, most expensive and versatile steel material [1].

Corrosion happens when the protection mechanism has been ignored, damaged or fatigued leaving the material exposed to the attack [4]. Problems related to practical corrosion often encountered in engineering contexts and allied disciplines, where such an approach may be hindered by certain uncertainty combinations of electrochemistry, metallurgy and physics that must be brought to light bear if a satisfactory solution found [8]. This overview shows the relevance of various disciplines and some relationships between them.

Besides that, there is a no. of application of corrosion to the society. Mostly, corrosion prevented from occurring on any material with any kind of method that involves anti-corrosion [3]. The corrosion surface or materials commonly were eliminated without knowing their renewable application or function in the engineering sector.

3.2 Methods

3.2.1 Material

Material that selected in this research was mild steel. The material has been prepared by using the method of preparation of metallographic test specimens. There were two types of specimens produced, and for one of them, corrosion occurred as shown in Figs. 3.1 and 3.2.

Fig. 3.1 Mild steel specimen with non-corrosion surface

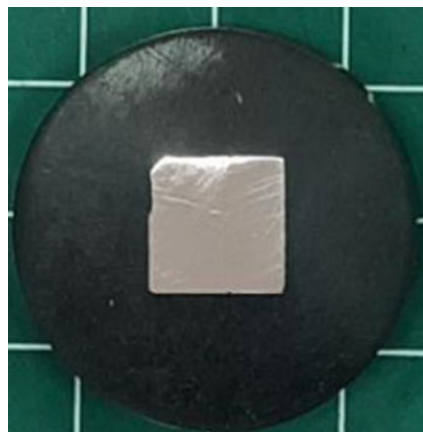
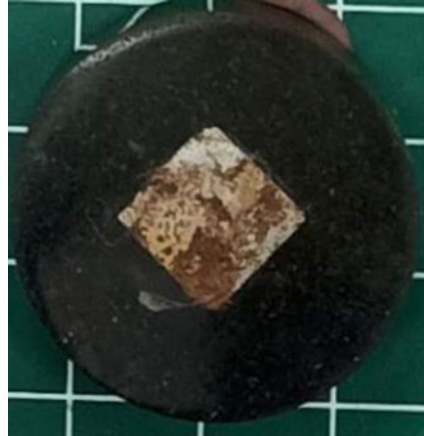


Fig. 3.2 Mild steel specimen that occurs with corrosion surface



3.2.2 *Temperature*

In this study, low and high temperatures were used to conduct the experiment. By using this type of temperature range, it can represent the environment temperatures that occur for several steel types to produce a corrosion situation and produce the steel failure. To gain low temperature, ice cube mixing with sea salt was used and act as agent for the temperature of the specimen to drop lower than 10 °C. These situations are applied on both specimens corrosion and non-corrosion surface, of the mild steel. During the process, both samples were contacted or exposed to the temperature agent for 2 min. For the specimen that has been exposed to high temperature was by using boiling water that has been heated up using an induction stove. To gain high temperature, we used the same method as in the case of the low temperature, i.e. by adding sea salt. Sea salt acts as an agent to increase or decrease the temperature in this experiment. Both the specimens were exposed to the high temperature for 2 min.

3.2.3 *Thermal Imaging*

A thermal imaging camera (TIC) is a type of thermometer camera used in the engineering sector. By providing infrared radiation as visible light, the camera enables the operator or user to see hot spots through smoke, darkness or heat-resistant obstacles. It is built using a hot and waterproof housing and is textured to withstand the dangers of land operations. It also can view low temperature as well. Temperature distributions of both specimens were recorded by using the TIC equipment to gain the results.

3.3 Results and Discussion

This part of the discussion will present the temperature distributions of corrosion and non-corrosion surface on the mild steel after being exposed to low and high temperature. Based on Fig. 3.3, it represents the value of the temperature absorption on both specimens that exposed to a temperature of 87.9 °C for 2 min. For the corrosion surface, the temperature absorption was 44.4 °C, but when compared with the non-corrosion surface, it gained 36.7 °C for the absorption process.

After the specimen was removed from the high-temperature agent, it was set in rest for 6 min on two periods to monitor the temperature behaviour release on both samples. As shown in Fig. 3.4, it represents the temperature release behaviour for the corrosion and non-corrosion surface of the material. For the corrosion surface, the temperature release speed that occurred was 0.03 °C/s, but when compared with the non-corrosion surface the result that was gained was 0.006 °C/s. Based on the finding that has been gained, corrosion surface is faster in terms of speed release temperature that occurs with high temperature.

For the lower temperature situation, a different type of result situation occurred for the specimens when compared to the high-temperature situation. The result of the experiment can be seen in Fig. 3.5 that specimen has been exposed with -16.5 °C for 2 min. After this process of 2 min duration, the sample is removed from the low-temperature source. For the corrosion surface, it provided the result based on the TIC method as 15.3 °C but for the non-corrosion surface as 19.9 °C of the temperature absorption process. The result has shown that the corrosion surface can absorb more temperature than the non-corrosion surface.

After the specimen was separated from the low-temperature agent, it was set to rest for 6 min on two periods to monitor the temperature behaviour on both specimens, the same procedure as in the case of the high-temperature condition. As shown in Fig. 3.6, it represents the temperature release behaviour for the corrosion and non-corrosion surface of the material. For the corrosion surface, the temperature release

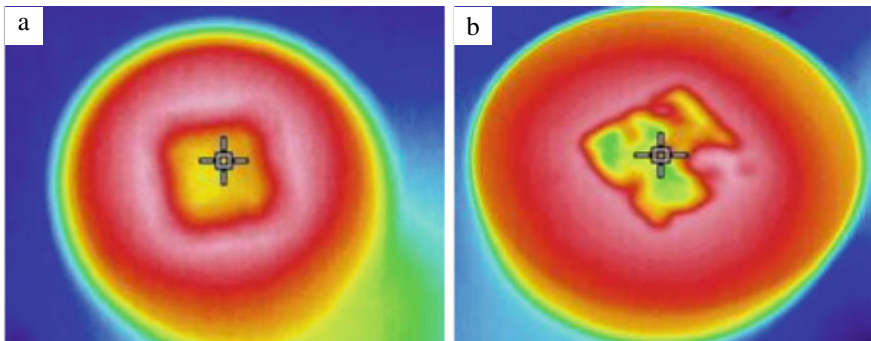


Fig. 3.3 a Non-corrosion surface temperature absorption 36.7 °C, b corrosion surface temperature absorption 44.4 °C

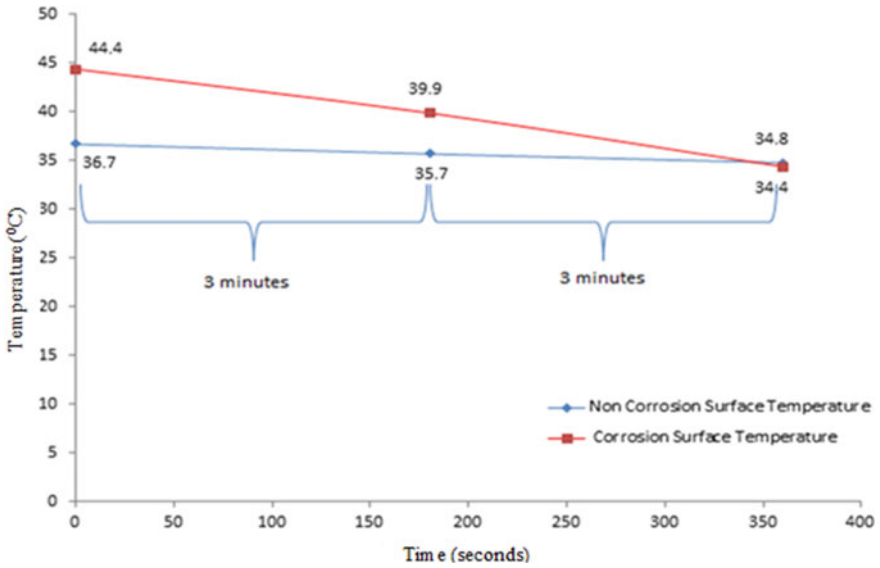


Fig. 3.4 Temperature change over time of the mild steel surfaces at high-temperature conditions

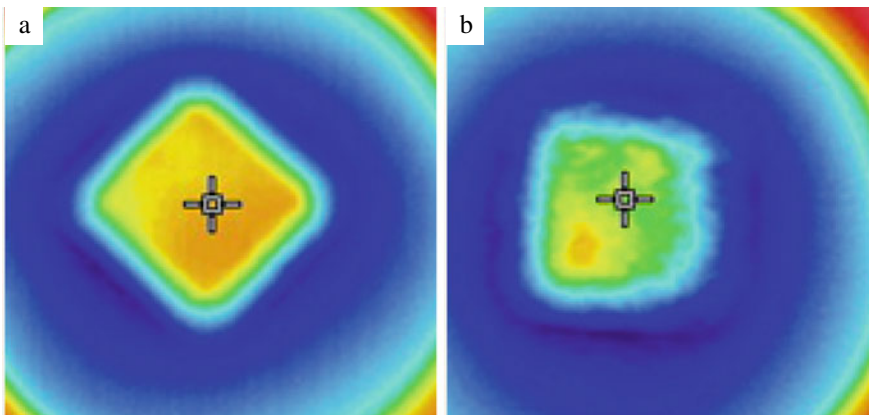


Fig. 3.5 **a** Non-corrosion surface temperature absorption 19.9 °C, **b** corrosion surface temperature absorption 15.3 °C

speed that occurred was 0.0023 °C/s, but when compared with the non-corrosion surface result that has been gained was 0.0021 °C/s. Based on the finding that has been gained, the non-corrosion surface is slower in terms of temperature release speed that occurs at low temperature.

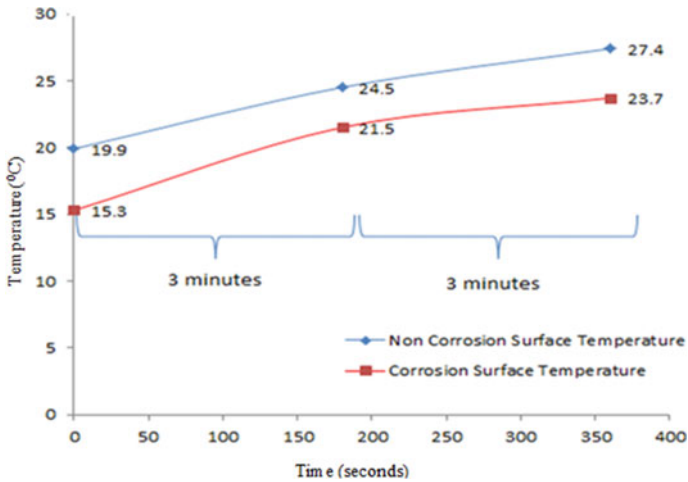


Fig. 3.6 Temperature change over time of the mild steel surfaces at low-temperature conditions

3.4 Conclusion

This research has found some results for the absorption and release temperature on the non-corrosion and corrosion surfaces. Based on the data that been gain, the corrosion surface provides better temperature in terms of absorption for both conditions when compared with the non-corrosion surface. For the temperature release process, in the situation of high temperature, the corrosion surface is faster, but when occurring with low temperature, the non-corrosion surface provides a higher release speed of the temperature. Both specimens give different results for different situations.

Acknowledgements First and foremost, praise to God, without His blessing, this research would not be able to complete. All thanks to Almighty Allah, the compassionate and merciful, who knows about whatever is there in the universe, hidden and evident, and has enabled me to elucidate a drop from the existing ocean of knowledge. However, this research would not be completed without the kind support and help from Universiti Kuala Lumpur Malaysian Spanish Institute members and most of all Dr. Sharmiawati Binti Mohamed Shariff. Thanks to her for all the support and knowledge that has been given.

References

1. Chen, Q., Wang, C., Sun, X., Cao, Y., Guo, T., Chen, J.: Evaluation and prediction for effect of conductive gussasphalt mixture on corrosion of steel bridge deck. *Constr. Build. Mater.* **228**, 116837 (2019). <https://doi.org/10.1016/j.conbuildmat.2019.116837>
2. Dhole, G.S., Gunasekaran, G., Ghorpade, T., Vinjamur, M.: Progress in Organic Coatings Smart acrylic coatings for corrosion detection. *Prog. Org. Coat.* **110**(January), 140–149 (2017). <https://doi.org/10.1016/j.porgcoat.2017.04.048>

3. Gonzalez, M., Nithiyantham, U., Carbó-argibay, E., Bondarchuk, O., Grosu, Y., Faik, A.: Solar energy materials and solar cells graphitization as efficient inhibitor of the carbon steel corrosion by molten binary nitrate salt for thermal energy storage at concentrated solar power. *Sol. Energy Mater. Sol. Cells* **203**(September), 110172 (2019). <https://doi.org/10.1016/j.solmat.2019.110172>
4. Liu, H., Cao, F., Song, G., Zheng, D., Shi, Z., Dargusch, M.S., Atrens, A.: Review of the atmospheric corrosion of magnesium alloys. *J. Mater. Sci. Technol.* **35**(9), 2003–2016 (2019). <https://doi.org/10.1016/j.jmst.2019.05.001>
5. Loto, R.T., Olukeye, T., Okorie, E.: Synergistic combination effect of clove essential oil extract with basil and atlas cedar oil on the corrosion inhibition of low carbon steel. *S. Afr. J. Chem. Eng.* **30**, 28–41 (2019). <https://doi.org/10.1016/j.sajce.2019.08.001>
6. Song, D., Hao, J., Yang, F., Chen, H., Liang, N., Wu, Y., Zhang, J., Ma, H., Klu, E.E., Gao, B., Jiang, J.: Corrosion behavior and mechanism of Cr e Mo alloyed steel: role of ferrite/bainite duplex microstructure. *J. Alloy. Compd.* **809**, 151787 (2019). <https://doi.org/10.1016/j.jallcom.2019.151787>
7. Talbot, D.E.J., Talbot, J.D.R.: *Corrosion Science and Technology*, 3rd edn. Plenum Press, Boca Raton (2018). <https://doi.org/10.1201/9781351259910>
8. Wicker, M., Alduse, B.P., Jung, S.: Author's accepted manuscript detection of hidden corrosion in metal roofing shingles utilizing infrared thermography. *J. Build. Eng.* **20**, 201–207 (2018). <https://doi.org/10.1016/j.job.2018.07.018>

Chapter 4

Binding Friction of NiTi Archwires at Different Size and Shape in 3-Bracket Bending Configuration



Mohd Nizam Ahmad, Abdus Samad Mahmud,
Muhammad Fauzinizam Razali, and Norehan Mokhtar

Abstract During orthodontic treatment, the force released by the bent of a NiTi archwire is influenced by the friction developed in the bracket system. This in vitro study investigated the amount of friction encountered by the NiTi archwire in a 3-brackets configuration. Five different sizes within two shapes of NiTi archwire were considered for the bending test at different deflection magnitudes of 2, 3 and 4 mm. The binding friction was measured by comparing the force-deflection curve of the NiTi archwire with the use of polytetrafluoroethylene (Teflon) bracket and stainless steel brackets. The force result from the Teflon bracket was considered as a control test, utilizing its frictionless character. This investigation revealed that the binding friction is affected by the archwire size and shape. The NiTi archwire experienced higher binding friction during activation and slightly lower during the wire recovery at deactivation. The magnitude of the binding friction gradually increased with the increase of the archwire size and shape, with the largest binding friction of 7.6 N recorded from the 0.457 mm × 0.635 mm rectangular archwire and the smallest binding friction was recorded from the 0.356 mm round archwire.

Keywords Binding friction · 3-brackets bending test · Teflon bracket · NiTi archwire · Orthodontic leveling treatment

M. N. Ahmad (✉)
Engineering Section, Universiti Kuala Lumpur Malaysian Spanish Institute, Kulim Hi-Tech Park,
09000 Kulim, Kedah, Malaysia
e-mail: mohdnizam@unikl.edu.my

M. N. Ahmad · A. S. Mahmud · M. F. Razali
Nanofabrication and Functional Materials Research Group, School of Mechanical Engineering,
Engineering Campus, Universiti Sains Malaysia, 14300 Nibong Tebal, Penang, Malaysia
e-mail: abdus@usm.my

M. F. Razali
e-mail: mefauzinizam@usm.my

N. Mokhtar
Craniofacial and Biomaterial Science Cluster, Advanced Medical and Dental Institute, Universiti
Sains Malaysia, Bertam, 13200 Kepala Batas, Penang, Malaysia
e-mail: norehanmokhtar@usm.my

4.1 Introduction

In orthodontic leveling treatment, a tooth is protruded to align with adjacent teeth by inducing a force onto the subjected tooth. The force is generated by bending an archwire on brackets that are glued to multiple teeth. The effective force magnitude to induce tooth movement for leveling is around 1–3 N [1]. A higher force magnitude can damage the gum tissue, while a lower force magnitude does not encourage tooth movement or prolong the treatment time [2].

NiTi shape memory alloy orthodontic archwire is widely used in current practice because they provide a constant force over a huge deflection magnitude. Also, their unique superelasticity behavior allows large strain recovery of approximately 6–8% strain without permanent deformation [3, 4]. In orthodontic treatment procedure, it is the recovery force of the archwire that induces a tooth movement [3–5]. However, the contact between the archwire and bracket produces unwanted friction. This friction restrains the deflected archwire from retraction, thus tooth movement is hindered.

The friction at the contact area between the archwire and bracket can be classified into sliding and binding resistances. Sliding friction exists from the sliding motion of the archwire on the bracket and binding friction develops when the archwire is bent at the tip/lip of the bracket slot [5]. The magnitude of sliding friction is dependent on the friction coefficient between the archwire and bracket [6]. If elastomeric ligature is used to secure the archwire on brackets, the magnitude of sliding friction may increase substantially. Binding friction is also dependent on the friction coefficient, but the magnitude increases as the bent angle decrease, or in other words, as the deflection of the archwire increases [7–9]. In this regard, binding friction is also influenced by the archwire size and shape.

In normal case practice, different sets of archwire sizes are used during treatment, depending on the displacement distance and angle of the tooth that to be treated. In most of the cases, round archwires with diameter of 0.356–0.457 mm are used and a rectangular archwire of 0.406×0.559 mm is used at the final stage of treatment [10–12]. Selection of archwire size and shape is guided by the deflection force of archwire provided by the manufacturers. The force is measured from a 3-point bending test, and thus, friction values are not included. The objective of this work is to measure the binding friction of orthodontic archwires in 3-bracket configuration at leveling treatment.

4.2 Materials and Method

The friction measurement was done from the force-deflection behavior of the NiTi archwire bent in 3-brackets configuration. The bending jig is illustrated in Fig. 4.1a. The middle indenter resembles the subjected tooth to be moved in leveling treatment, and the two columns at each side resemble the teeth for anchoring the archwire. The

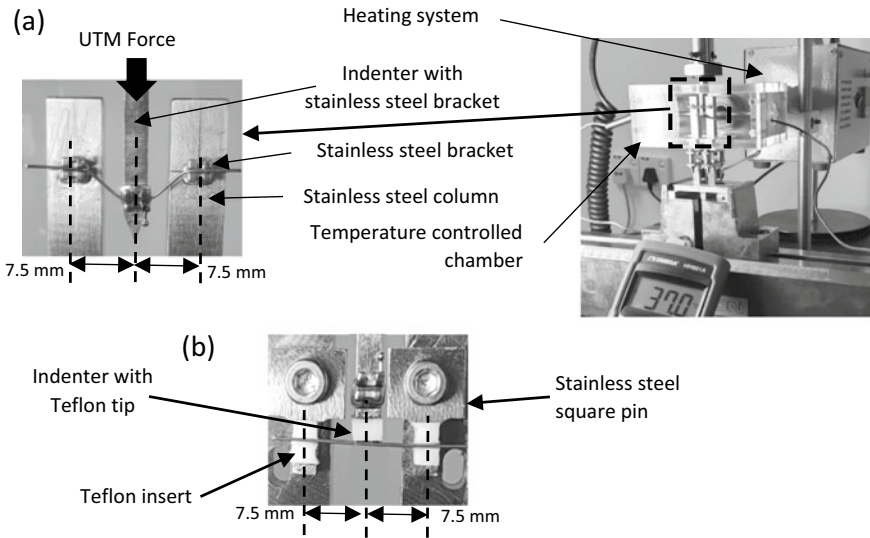


Fig. 4.1 Experimental setup of friction measurement

commercial NiTi archwires (G&H Orthodontics) were used together with a commercial stainless steel bracket, mini MBT prescription (Natural Orthodontics) with 0.559 mm slot height. The brackets were glued to the stainless steel columns by using cyanoacrylate adhesive (Supa Glue, Selleys). In this test, ligature was not used for eliminating the potential friction it might contribute. The indenter was mounted onto the load cell of the universal tensile machine (Instron 3367) to provide force to deflect the archwire. The force resolution of this tensile machine is 0.01 N. The bending span was 15 mm to resemble a common adult Asian tooth pitch at dentition. The bending test was done in a temperature-controlled chamber set at the oral temperature of 37 °C. The chamber was able to maintain the temperature at ± 1 °C accuracy.

Teflon brackets were used to demonstrate frictionless behavior during the bending test. The Teflon brackets were fabricated by cutting a Teflon bar into a small insert, then press-fitted into the slot of a stainless steel square pin, as shown in Fig. 4.1b. Teflon bracket was bolted to the stainless steel column. During the bending test, the indenter with Teflon tip is providing the force to bend archwire. The width of the Teflon pin is the same as the stainless steel bracket width, to standardize the contact surface during bending.

Bending of the archwire was done at crosshead speed of 1 mm per minute in universal tensile machine. The archwires were deflected to three different distances of 2, 3 and 4 mm at each test. Five commercial NiTi archwires were used in this bending tests. Table 4.1 shows the archwire size and shape used at different brackets types.

Table 4.1 Brackets type and NiTi archwire used

Bracket	NiTi archwire size (mm)	
	Round	Rectangular
Teflon	0.356, 0.406, 0.457	0.406 × 0.559, 0.457 × 0.635
Stainless steel	0.356, 0.406, 0.457	0.406 × 0.559, 0.457 × 0.635

During the bending test, the activation phase is when the indenter is moving downward to bend the archwire to the required deflection distance. The deactivation phase is the archwire recovery to its original position, thus the force measured by the load cell is the recovery force produced by the archwire. The activation phase resembles the installation of the archwire by the orthodontist, while the deactivation phase resembles the effective force produced by the bent archwire on its way to recovery, thus induces tooth movement.

4.3 Results and Discussion

Figure 4.2a shows the force-deflection curve of the 0.406 mm round NiTi archwire at 4 mm deflection with the use of stainless steel and Teflon brackets. In general, the NiTi archwire behaved differently with respect to the material type of the bracket. It is seen that in the presence of the stainless steel bracket, the NiTi archwire exhibited the activation and deactivation force over a gradient curve. The archwire deformation initiated with a linear elastic behavior for the first 1 mm deflection. The deflection behavior exhibited a gradient force curve when the archwire was further bent to 4 mm deflection. This implies a non-constant force of stress-induced martensitic phase transformation (SIMT) of the NiTi shape memory alloy. This gradient force trend indicates the increase of friction magnitude at the archwire-bracket surfaces as the deflection increases. On the other hand, the recovery of the archwire during the deactivation cycle initiated at a lower force magnitude. This implies that the friction encountered by the archwire while sliding in the bracket slot has reduced the deactivation force strength, thus delays the reverse phase transformation to a lower force level. As the deactivation cycle continued, the archwire force gradually increased in relation to the decreasing of friction.

On the other hand, the archwire exhibited a constant bending force in a plateau trend whenever the Teflon bracket was considered. This signifies the ability of the NiTi archwire to exert force in a constant manner in a frictionless bracket system.

Referring to Fig. 4.2a, the force slopes of the stainless steel curve and Teflon curve in the elastic region are different due to the bracket geometry. The size of the Teflon bracket is slightly different as compared to the stainless steel bracket. This happened due to machining variation in the fabrication of the Teflon bracket. Any difference in bracket width affects the bending span. The Teflon bracket with a slightly bigger bending span has produced a lower force slope as compared to the stainless steel

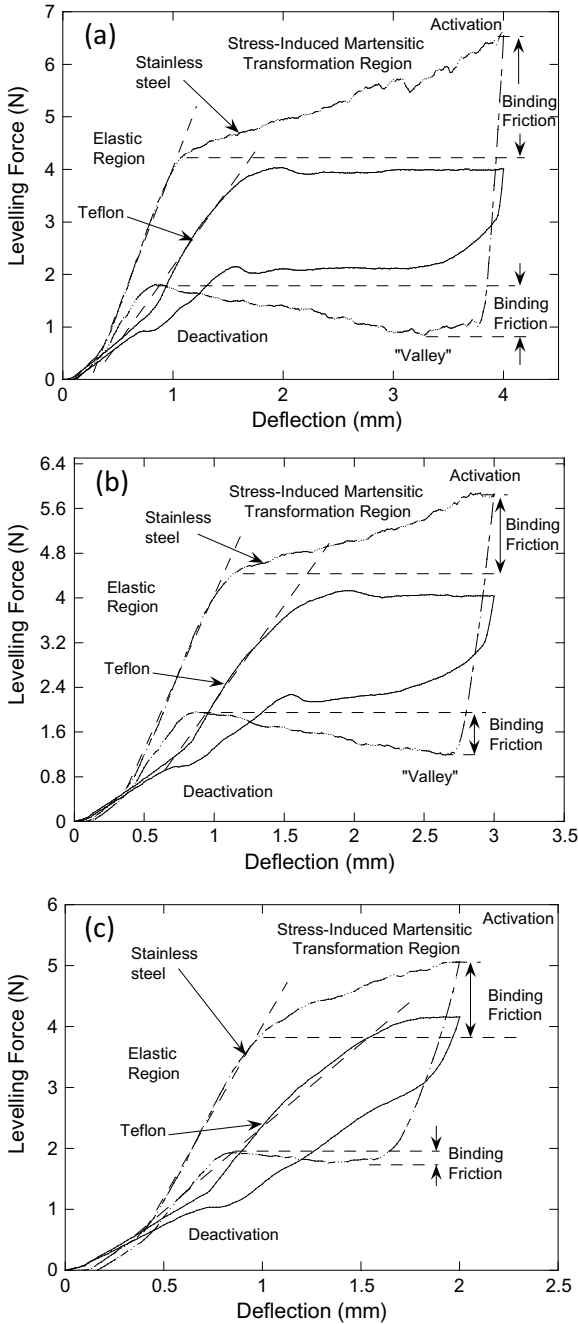


Fig. 4.2 Force-deflection curve of 0.406 mm NiTi archwire on stainless steel bracket and Teflon bracket; **a** 4 mm deflection, **b** 3 mm deflection, **c** 2 mm deflection

bracket. Teflon is relatively soft, thus small deformation happens at the bracket tip during archwire bending and this can affect the bending span.

The difference of the force magnitude at SIMT region of the force-deflection curve is considered as binding friction. Referring to the SIMT region of the force-deflection curve of stainless steel during activation, if no friction occurs, the magnitude of the force is constant along the archwire bending. This is clearly demonstrated by the flat plateau of the force-deflection curve on the Teflon bracket. The same method was done to measure the binding friction during deactivation. If no friction occurs during deactivation, the magnitude of the force is also constant along the archwire recovery. Figure 4.2a–c illustrate the force-deflection curves at 4 mm deflection, 3 mm deflection and 2 mm deflection, respectively. From these force-deflection curves, binding frictions were measured at three deflections, which refer to the magnitude of force differences at every deflection, on both activation and deactivation. The deflection of the archwire is directly influenced by the binding friction. From the force-deflection curves, binding friction during archwire activation increased from 2 mm deflection to 4 mm deflection; however, the binding friction during archwire deactivation decreased from 4 mm deflection to 2 mm deflection.

The binding frictions measured on five NiTi archwires during activation and deactivation phase at three deflections are summarized in Table 4.2. From this table, the binding friction also increases with the increases of the archwire size. Bigger archwires produced higher binding friction as compared to smaller archwires. At 4 mm deflection, during activation, 1.215 N of binding friction was measured from the 0.356 mm round archwire while 7.601 N of binding friction was measured from the 0.457 mm round archwire. During deactivation phase, the binding friction also increased as the archwire size increased, but the magnitude difference was smaller. A similar trend of binding force increment with respect to the archwire size was also observed from a rectangular archwire.

Table 4.2 shows that the archwire shape also affects the binding friction. The round archwires produced relatively lower binding frictions on both activation and deactivation phases as compared to rectangular archwires, for all deflection magnitudes. For the 4 mm deflection, the 0.406 mm round archwire produced almost 54% lower binding friction on activation as compared to the 0.406 mm × 0.559 mm

Table 4.2 Binding friction measured on five NiTi archwires at three deflections

Deflections (mm)	Loading phase	Binding friction (N) at round archwire			Binding friction (N) at rectangular archwires (mm)	
		0.356	0.406	0.457	0.406 × 0.559	0.457 × 0.635
2	Activation	0.665	0.914	1.690	2.787	3.008
3		1.102	1.680	3.178	4.355	5.499
4		1.215	2.544	3.765	5.569	7.601
2	Deactivation	0.607	0.698	1.235	1.371	2.441
3		0.776	1.223	1.668	2.052	3.371
4		0.936	1.270	1.851	2.463	4.590

rectangular archwire. While on deactivation, the friction was about 48% lower. This higher binding friction of the rectangular archwire is clearly due to its larger area moment of inertia as compared to round archwires.

The binding friction table generated in this work can help orthodontist to select the appropriate archwire size and shape for orthodontic leveling treatment. Based on binding friction results of five NiTi archwires, the 0.406 mm round archwire is more suitable because it produces small binding friction and at the same time produces sufficient magnitude of force to induce tooth movement during deactivation. Although the smaller round archwire can produce a smaller binding friction, the deactivation force produced on archwire recovery phase can be insufficient to induce the tooth movement effectively.

4.4 Conclusion

The friction measurement technique introduced in this work has successfully measured binding frictions on five different sizes and shapes of NiTi archwires in a 3-brackets bending system. The findings show that the archwire size and shape affected the binding frictions at leveling treatment. Binding frictions measured on bigger archwire size were higher than the smaller archwire size. Similarly, the rectangular archwires produced higher binding friction which was due to its bigger magnitude of area moment of inertia. Unlike sliding friction of which the magnitude is constant over the deflection range, the magnitude of the binding friction is directly proportional to the magnitude of the archwire deflection, thus the value is not constant.

Acknowledgements The authors are grateful for the financial support provided by Universiti Sains Malaysia under the grant USMRUI:1001/PMEKANIK/8014068.

References

1. Yee, J.A., Türk, T., Elekdağ-Türk, S., et al.: Rate of tooth movement under heavy and light continuous orthodontic forces. *Am. J. Orthod. Dentofac. Orthop.* **136**(2), 1–9 (2009)
2. Cobourne, M.T., DiBiase, A.T.: *Handbook of Orthodontics*. Elsevier (2010)
3. Nosalik, K., Maciej, K.: Contemporary NiTi archwires—mechanical properties. *Dent. Med. Probl.* **49**(3), 433–437 (2012)
4. Otsuka, K., Ren, X.: Physical metallurgy of Ti-Ni-based shape memory alloys. *Prog. Mater. Sci.* **50**(5), 511–678 (2005)
5. Fernandes, D.J., Peres, R.V., Mendes, A.M., Elias, C.N.: Understanding the shape-memory alloys used in orthodontics. *ISRN Dent.* **2011**, 1–6 (2011)
6. Kusy, R.P., Whitley, J.Q.: Influence of archwire and bracket dimensions on sliding mechanics: derivations and determinations of the critical contact angles for binding. *Eur. J. Orthod.* **21**(2), 199–208 (1999)

7. Ahmad, M.N., Mahmud, A.S., Razali, M.F., et al.: Force-deflection behaviour of NiTi archwires in a polytetrafluoroethylene (Teflon) bracket system. *Mater. Sci. Eng. Technol.* **50**(3), 289–294 (2019)
8. Burrow, S.J.: Friction and resistance to sliding in orthodontics: a critical review. *Am. J. Orthod. Dentofac. Orthop.* **135**(4), 442–447 (2009)
9. Razali, M.F., Mahmud, A.S., Mokhtar, N.: Force delivery of NiTi orthodontic arch wire at different magnitude of deflections and temperatures: a finite element study. *J. Mech. Behav. Biomed. Mater.* **77**, 234–241 (2018)
10. Murayama, M., Namura, Y., Tamura, T., et al.: Relationship between friction force and orthodontic force at the leveling stage using a coated wire. *J. Appl. Oral Sci.* **21**(6), 554–559 (2013)
11. Bantleon, H.P.: The mechanical background of binding in a three bracket-relationship simulating a premolar, canine and lateral incisor in levelling. *Orthod. Waves* **70**(2), 53–58 (2011)
12. Phermsang-ngarm, P., Charoemratrote, C.: Comparison of the load-deflection characteristics of superelastic nickel titanium wires. *Othod. Waves.* 6–12 (2018)

Chapter 5

Design of a Child Restraint System for Motorcycles



Zulkarnain Abdul Latiff and Fazidah Saad

Abstract In developing countries, children riding on a motorcycle as a pillion or driver are very common despite restriction by law for the driver. Children as motorcycle pillioners or riders are more vulnerable. They are vulnerable to hazard on lower limb and falling from the motorcycle due to a lack of stability. This paper is focused on designing a child restraint system for motorcycles with an engine capacity of 100–150 cc that can secure the safety of the child passenger from aged 2 to 5 years old and being able to support a maximum child passenger of 20 kg weight. The methodology used in designing this product includes house of quality, morphological chart, weighted objective analysis, sketching, concept design, CAD modelling, finite element analysis and prototyping. The result of the design is able to withstand the child maximum weight of 20 kg and was successfully installed at a Modenas KRIS.

Keywords Child pillion · Child restraint system · Motorcycle

5.1 Introduction

In developing countries, particularly in Asia, motorcycle use has been dramatically growing, and motorcycles are one of the most important means of transportation because of rapid economic development, convenience in congested traffic and ease of parking on narrow streets. For instance, motorcycles comprise 95% of registered motor vehicles in Vietnam, 67% in Taiwan, 63% in China and 60% in Malaysia. A

Z. Abdul Latiff

Manufacturing Section, Malaysian Spanish Institute, Universiti Kuala Lumpur, Kulim Hi-Tech Park, 09000 Kulim, Kedah, Malaysia

e-mail: zulkarnain@unikl.edu.my

F. Saad (✉)

Engineering Section, Malaysian Spanish Institute, Universiti Kuala Lumpur, Kulim Hi-Tech Park, 09000 Kulim, Kedah, Malaysia

e-mail: fazidah@unikl.edu.my

© The Editor(s) (if applicable) and The Author(s), under exclusive license to Springer Nature Switzerland AG 2020

M. H. Abu Bakar et al. (eds.), *Progress in Engineering Technology II*,

Advanced Structured Materials 131,

https://doi.org/10.1007/978-3-030-46036-5_5

large proportion of motorcycles in developing countries are scooters with a smaller engine capacity [1].

The main reason for using motorcycles is the economical mode of transportation. Most families prefer using a lightweight motorcycle, one with an engine capacity below 125 cc [2].

Table 5.1 shows the total motor vehicles by type and state of Malaysia by the date of 31 March 2016. It is clearly seen that motorcycle is the most used by Malaysian with 12,220,072 units.

According to Table 5.2, by the year of 2014, motorcycles with an engine capacity of 101–150 cc are the most used by Malaysian with 436,896 units compared to other engine capacities.

With both data given, it is true that motorcycles are an economical mode of transportation and engine capacity below 125 cc.

In developing countries, children riding on a motorcycle as a pillion or driver are very common despite restrictions by law for the driver. Children as motorcycle pillions or riders are more vulnerable. They should be protected by their family and by society [3].

5.1.1 Problem Statement

The safety of the young pillion on a motorcycle is insecure without using proper restraint system. The possibility of falling from the motorcycle is imminent due to their lack of stability in early ages.

Children under five years do not have a strong grip to hold a driver and always lose their concentration. Hence, when they sit behind the driver, a sudden change of direction or velocity without restraint may cause them to fall off. A sleepy child or a child losing concentration can also easily fall off the motorcycle.

Children, 4–6 years old, have the highest rate of bone lengthening compared to other age groups in pre-pubertal children. However, their legs are not long enough to be supported by most motorcycles' footrests. The unprotected lower limb has the highest frequency serious injuries of surviving motorcyclist [6].

5.1.2 Objectives

To design a child restraint system for motorcycles with an engine capacity of 100–150 cc that can secure the safety of a child passenger from age 2 to 5 years old.

The child restraint system should be able to support a maximum child passenger of 20 kg weight.

Table 5.1 Total motor vehicles by type and state, Malaysia, 31 March 2016—road transport department

Negeri State	Motosikal Motorcycle	Motokar Motorcar	Bas Bus	Teksi Taxi	Kereta Sewa Pandu Sendiri Hire and Drive car	Kebudayaan Barang-Barang Goods vehicle	Lain-Lain Others	Jumlah Total
Perlis	79,425	24,060	177	126	79	2003	2287	108,157
Kedah	907,446	321,870	2957	2332	1389	40,232	31,009	1307,235
Pulau Pinang	1356,113	1084,796	5181	3805	1740	78,696	39,753	2570,084
Perak	1318,148	737,673	4733	3666	878	76,542	60,374	2202,014
Selangor	1358,343	1088,737	6871	15,529	2238	190,064	139,959	2801,741
Wilayah Persekutuan	1783,751	3734,766	19,093	55,885	46,976	269,834	239,109	6149,414
Negeri Sembilan	536,067	330,743	2487	1934	565	49,009	16,500	937,305
Melaka	453,991	329,468	1694	1558	434	28,553	14,193	829,891
Johor	1802,042	1424,718	8778	12,698	2762	151,305	98,308	3500,611
Pahang	575,201	366,707	1968	1892	982	46,651	29,065	1022,466
Terengganu	373,402	199,729	1072	929	328	22,307	13,469	611,236
Kelantan	529,851	291,819	2026	1522	587	30,016	16,687	872,508
Sabah	367,437	617,695	7191	4639	3978	123,808	99,625	1224,373
Sarawak	760,965	750,952	3122	2438	1716	95,534	101,347	1716,074
Portal Rakan Niaga Malaysia	17,890	702,249	0	44	19	1431	102	721,735
	12,220,072	12,005,982	67,350	108,997	64,671	1205,985	901,787	26,574,844

Sumber Jabatan Pengangkutan Jalan
Source Road Transport Department

Table 5.2 New registered motorcycle for individual/company vehicles by engine capacity and state, Malaysia, 2014—road transport department

Negeri state	Kenderaan Persendirian Individual vehicles						Kenderaan Berpendaftaran Syarikat Company registered vehicles					
	<i>Kuasa Enjin Engine capacity (c.c)</i>											
	≤100 cc	101–150 cc	151–250 cc	251–500 cc	>500 cc	≤100 cc	101–150 cc	151–250 cc	251–500 cc	>500 cc		
Perus	319	4126	121	9	28	3	1	0	0	0	0	
Kedah	2656	36,965	885	126	346	5	33	0	0	0	0	
Pulau Pinang	2721	41,091	1985	210	1181	0	12	0	0	0	0	
Perak	5153	34,959	1028	86	350	7	20	0	0	2	2	
Selangor	9597	55,307	3549	458	1888	15	16	0	0	0	0	
W.P. Kuala Lumpur	9338	59,986	6069	732	4440	5	145	0	0	8	8	
Negeri Sembilan	2341	14,764	994	78	391	22	0	0	0	1	1	
Melaka	1863	41,057	642	29	193	6	10	0	0	0	0	
Johor	8108	63,077	3357	233	1231	10	17	0	0	2	2	
Pahang	3098	19,131	684	65	366	0	13	0	0	0	0	
Terengganu	1487	14,948	235	17	131	0	28	0	0	2	2	
Kelantan	3864	22,778	435	64	170	0	11	0	0	1	1	
Sabah	8209	23,378	713	73	342	7	6	0	0	2	2	
Sarawak	10,040	32,329	836	82	436	13	11	0	0	0	0	
Malaysia	68,794	436,896	21,533	2262	11,493	93	323	–	–	18	18	

Sumber: Jabatan Pengangkutan Jalan

Source: Road Transport Department

5.2 Literature Review

With an increase in the number of motorcycle riders and pillion riders, the incidence of motorcycle-associated injuries has also increased. This problem is not limited only to developing countries. A study in Australia showed that the incidence of motorcycle-related injuries requiring hospital emergency room treatment in children and adolescents in Victoria had increased by almost 10% per year [3].

The injured region of highest frequency in the seriously injured but surviving motorcyclists was the lower limbs, particularly fractures. Tibia ranked the highest in terms of fractures, followed by fractures of the femur [4].

Children as motorcycle passengers or riders are more vulnerable. They should be protected by their family and by society [5].

There are three groups of children safety listed by the World Health Organization (WHO):

Infants: at birth to 1 year old

Toddlers and preschoolers: 2–5 years old

Children 6 to 15 years old.

Every category has their maximal safety features that need to be followed. But there is a possible option for minimally acceptable safety that can be used. Table 5.3 shows the maximal safety and the minimal safety required.

Toddlers have relatively short legs and a long trunk, with lumbar lordosis and protruding abdomens. At 24 months, weight increases by 2 kg from 12 months of age, and height increases by 12 cm. By 24 months, children are about ½ of their ultimate adult height. After four years, the torso slims as the legs lengthen. Children, 4–6 years, old have the highest rate of bone lengthening compared to other age groups in pre-pubertal children. However, their legs are not long enough to be supported by most motorcycles' footrests [6].

Children under five years do not have a strong grip to hold a driver and always lose their concentration. Hence, when they sit behind the driver, a sudden change of direction or velocity without restraint may cause them to fall off. A sleepy child or a child losing concentration can also easily fall off the motorcycle [5].

Safety equipment aimed to restrain a child while riding on a motorcycle might prevent fall injuries. There are two kinds of uncommon restraint equipment for children on motorcycles of which there is no research evidence yet supporting their efficacy and effectiveness. An example is the mounted child seat. However, no special child seat for a motorcycle pillion has been developed by any country [7].

5.3 Methodology

The methodology that was used is house of quality, morphological chart, weighted objective analysis, sketching, conceptual design, CAD modelling using Catia V5

Table 5.3 Maximal safety for children—World Health Organization

	Maximal safety	Possible option for minimally acceptable safety
<p>Infants: at birth to 1 years old</p>	<ul style="list-style-type: none"> • Do not allow infants on motorcycles • Do more bio-mechanical research for appropriate helmet, infant seat, and infant sling related to speed limitation for future safety recommendations 	<ul style="list-style-type: none"> • Design a motor-tricycle which has a protective passenger space and a restraint system which is compatible with a child seat • A baby of nine months and older should wear an age-appropriate standardized helmet as additional safety equipment (a bicycle helmet is available for children of 9 months and older)
<p>Toddlers and preschoolers: 2–5 years</p>	<ul style="list-style-type: none"> • Do not allow toddlers and preschoolers under 6 years on a motorcycle as a passenger • It should be prohibited by law • Do more bio-mechanic research for appropriate helmet, and child seat (comparing benefit and risk of increasing momentum) related to speed limitation for future safety recommendations 	<ul style="list-style-type: none"> • Children 2–5 years old must use all available protective gear when being carried on a motorcycle <ul style="list-style-type: none"> – Mounted seat: Children 2–5 years old whose feet cannot reach the footrest must be transported on a motorcycle passenger – Crash helmet: Achild pillion passenger must wear his/her own standardized crab helmet which fits his/her head – Clothing: A pair of pants is necessary because it can protect his/her legs in case of a crash, that skirts or shorts would not do – Footwear: Rubber or leather footwear would prevent foot injuries in case of a crash or foot entrapment • Only motorcyclists who have passed an additional motorcycle test for carrying a child passenger can carry children under 12 year • Use motor-tricycle as a safer mode of transport instead of a motorcycle. Child passengers aged 2–5 years or weight <20 kg could be transported in a protective passenger space with a child seat

R21 software and finite element analysis in the same software. The sequences of activities are shown in Fig. 5.1.

5.3.1 CAD Modelling

The conceptual design is drawn by using a CAD software to be able to represent more details in the drawing. The software used is CATIA R5 R21 version. The 3D modelling is shown in Fig. 5.2.

5.3.2 Finite Element Analysis

The purpose of the analysis is to determine the maximum stress that can be applied to the specific part, backrest and pillar. A static analysis was carried out for this child restraint with two different loads applied: a load of 300 N and load of 1000 N. This is because the child mass is assumed to be around 30 kg. From the maximum stress obtained, a safety factor of the product can be calculated. In this analysis, a few steps are taken to make sure the reading is correct.

- (i) Both brackets are clamped to avoid movement.
- (ii) Backrest and both pillars are subjected to the load.

5.3.3 Material Selection

The materials used for this analysis are steel (brackets and pillars) and plastic (backrest).

5.4 Results and Discussions

Figure 5.3 shows the first analysis done with a force of 300 N applied to the backrest. Both brackets are clamped. The results show that the applied maximum stress of $6.25e + 007 \text{ N/m}^2$ does not exceed the steel's yield strength of $2.5e + 008 \text{ N/m}^2$ and the polypropylene's yield strength of $3.69e + 008 \text{ N/m}^2$. Thus, the product does not fail under this load force. The safety factor for the backrest is 6 while for the pillar is 4.

Figure 5.4 shows the second analysis done with a force of 1000 N applied to the backrest. Both brackets are clamped. The applied maximum stress of $3.06e + 008 \text{ N/m}^2$ exceeds the steel's yield strength of $2.5e + 008 \text{ N/m}^2$ and is slightly below

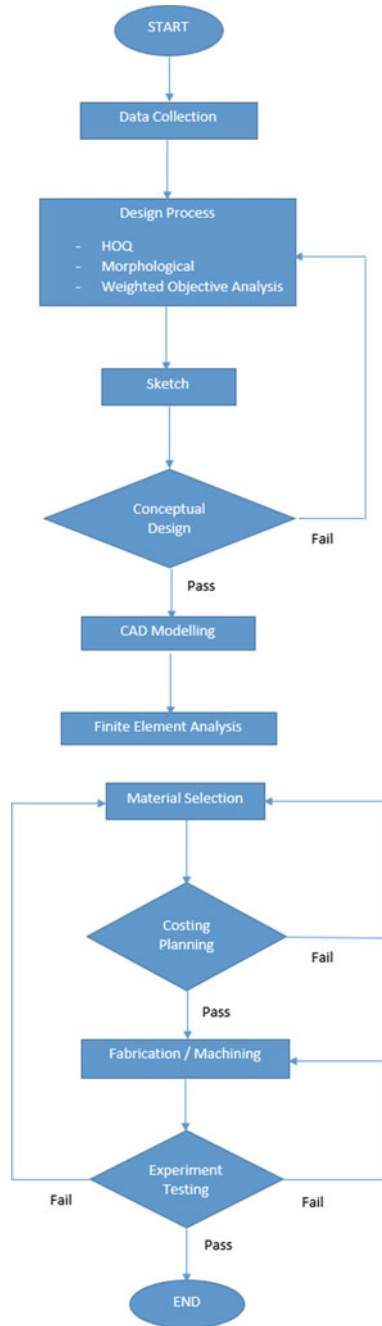


Fig. 5.1 Flowchart of project methodology

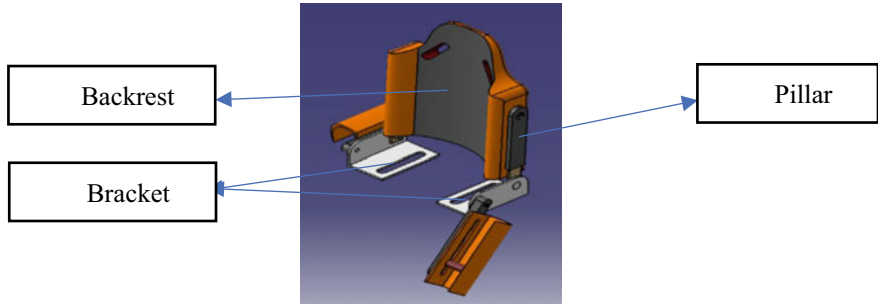


Fig. 5.2 3D modelling of the child restraint system

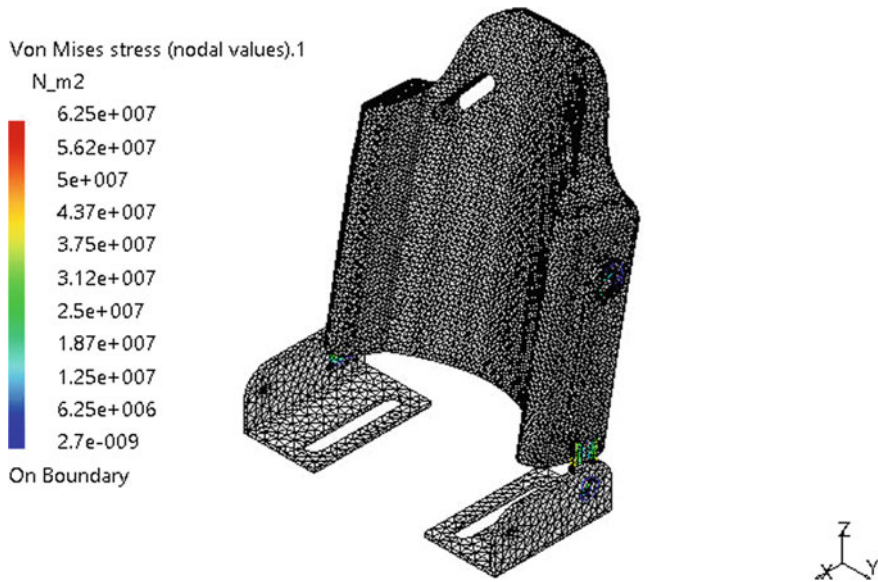


Fig. 5.3 First analysis with a load of 300 N

the polypropylene's yield strength of $3.69e + 008 \text{ N/m}^2$. Thus, the product fails for the pillars part under this load force. The pillar may break, and the backrest plastic material undergoes as lightly deformation. The safety factor for backrest is 1.2 while pillar is 0.8. Table 5.4 shows the mechanical properties used during the analysis.

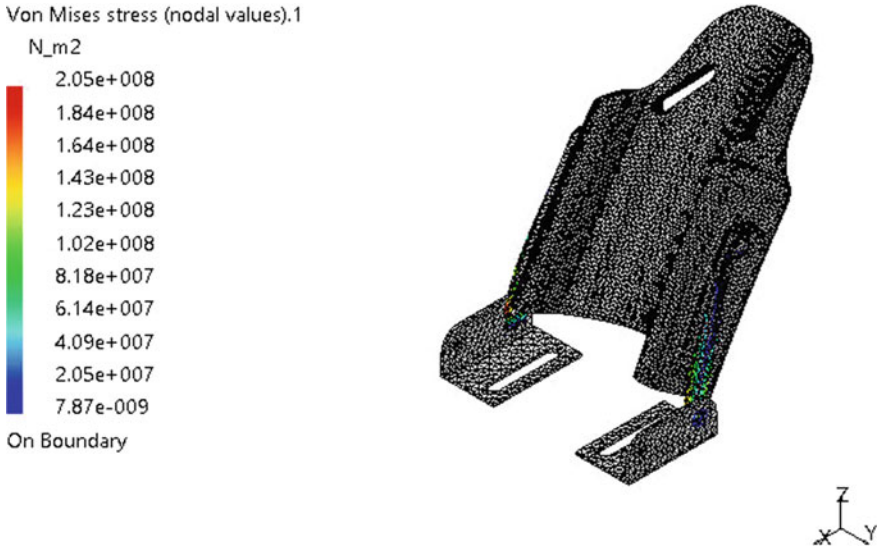


Fig. 5.4 s analysis with a load of 1000 N

Table 5.4 Mechanical properties of material used [8]

Mechanical properties	AISI 6000 steel (Bracket, Pillars)	Polypropylene (Backrest)
Young’s Modulus, E (GPa)	205.0	1.340
Shear Modulus, G (GPa)	80.0	0.4
Poisson’s ratio, ν	0.290	0.392
Density, ρ (Kg/m ³)	7850	775.1
Yield strength, S_y (MPa)	824	40
Shear strength, S_s (MPa)	992	22.3

5.5 Conclusions

Finite element analysis proves that the design is able to withstand a weight of 20 kg and an applied 300 N/30 kg force, with the safety factor is 6 for the backrest and 4 for the pillar. The prototype made is able to be mounted on the motorcycle Modenas KRISS and suitable to use for children 2–5 years old.

The ability to secure children with this product is still not tested as the project is still in an early prototype design.

References

1. Guide, B.P.: Vehicle ergonomics best practice guide. Highways Agency (2007)
2. Katz, G.: Quality function deployment and the house of quality. In: The PDMA ToolBook 3 for New Product Development, pp. 41–69. <https://doi.org/10.1002/9780470209943.ch2> (2008)
3. Kulcsar, R.M., Borozan, I.S., Argesanu, V., Madaras, L.: Car seats ergonomic evaluation. Ann. Faculty Eng. Hunedoara Int. J. Eng. **11**(2), 141–146 (2013)
4. Legislation, S.W., Observation, R., & Trend, S.W.: Safety seatbelt wearing among vehicle occupants in Malaysia : status of 5—years implementation of rear seatbelt regulations background seatbelt wearing legislation seatbelt wearing trend way forward, May 2008–2009 (2014)
5. Lin, M.R., Kraus, J.F.: A review of risk factors and patterns of motorcycle injuries. *Accid. Anal. Prev.* **41**(4), 710–722 (2009). <https://doi.org/10.1016/j.aap.2009.03.010>
6. Roslan, A., Sarani, R., Hashim, H.H., & Saniran, N.: Motorcycle ADSA fact sheet. In: Malaysian Institute of Road Safety Research (Miros), vol. 2, pp. 1–4 (2011)
7. Smith, G., Richardson, J., Summers, J.D., Mocko, G.M.: Concept exploration through morphological charts: an experimental study. *J. Mech. Des.* **134**(5), 51004 (2012). <https://doi.org/10.1115/1.4006261>
8. <http://www.matweb.com>

Chapter 6

Drowsiness Detection Using Electroencephalogram Anomaly Based on Spectral Entropy Features and Linear Classifier



Pranesh Krishnan, Sazali Yaacob, and Annapoorni Pranesh Krishnan

Abstract Sleeping on the wheels due to drowsiness is one of the significant causes of death tolls all over the world. The primary reason for sleepiness is due to the lack of sleep and irregular sleep patterns. Several methods such as unobtrusive sensors, vehicle dynamics and obtrusive physiology sensors are suggested to diagnose drowsiness of drivers. However, the unobtrusive sensors detect drowsiness in the later stage, whereas the physiological methods use obtrusive sensors such as electroocular, electromyogram and electroencephalograms and produce high accuracy in the early detection of drowsiness, which makes them a preferable solution. The objective of this research article is to classify drowsiness with alertness based on the electroencephalographic (EEG) signals using band power and log energy entropy features. The publicly available ULg DROZY database was used in this research. The five EEG channels from the raw multimodal signal are extracted. By using a band-pass filter with the cut-off frequencies of 0.1 and 50 Hz the high-frequency components were removed. Another band-pass filter bank is designed to slice the raw signals into eight sub-bands, namely delta, theta, low alpha, high alpha, low beta, mid beta, high beta and gamma. The preprocessed signals were segmented into an equal number of frames with a frame duration of 2 s using a rectangular time windowing approach with an overlap of 50%. Spectral entropy features were extracted for each frame in the sub-bands. The extracted feature sets were further normalized between 0 and 1 and labeled as drowsy and alert and then combined to form the final dataset. The K-fold cross-validation method is used to divide the dataset into training and testing sets. The processed dataset is then trained using, K-nearest neighbor network, and

P. Krishnan (✉) · S. Yaacob · A. P. Krishnan

Intelligent Automotive Systems Research Cluster, Electrical Electronics and Automation Section, Malaysian Spanish Institute Universiti Kuala Lumpur, Kulim Hi-Tech Park, 09000 Kulim, Kedah, Malaysia

e-mail: pranesh@unikl.edu.my

S. Yaacob

e-mail: sazali.yaacob@unikl.edu.my

A. P. Krishnan

e-mail: annapoorai.mani@s.unikl.edu.my

© The Editor(s) (if applicable) and The Author(s), under exclusive license to Springer Nature Switzerland AG 2020

M. H. Abu Bakar et al. (eds.), *Progress in Engineering Technology II*,

Advanced Structured Materials 131,

https://doi.org/10.1007/978-3-030-46036-5_6

support vector machine classifiers, and the results are compared. The KNN classifier produces 95% classification accuracy.

Keywords Spectral entropy · DROZY database · Frame analysis · Drowsiness

6.1 Introduction

Road accidents are certainly a growing concern in most of the nations because of its increase in the cause of death tolls. Reports from the World Health Organization (WHO) state that road accidents are the 9th leading cause of death globally [1]. Sleep-associated vehicle accidents have the highest share of traffic accidents. 30% of all fatalities and injuries have been caused by sleepiness worldwide.

The US National Highway Traffic Safety Administration (NHTSA) projected that drowsy driving is the reason for 40,000 injuries and 1500 demises in car crashes per year [2]. These deaths could be avoided if driver drowsiness was observed correctly, and drivers were certainly alarmed. Sleepiness is a physiological phenomenon signifying a lack of energy and motivation. There are various issues such as inadequate sleep, extended mental or physical work, long periods of stress and anxiety that generate fatigue in humans. Driver drowsiness has gained importance in the last 80 years. According to statistics, there is a huge requirement to build a system for monitoring the drivers and gauging their level of attention, which is also called as advanced driver assistant systems (ADAS). There are several techniques to detect driver drowsiness, which are broadly categorized into vehicle based, behavior based and physiology based.

In the vehicle-based methods, the parameters such as pressure on the acceleration pedal, lane deviation and steering angle position are used to determine whether the driver is under the influence of drowsiness or not. Nowadays, modern vehicle manufactures implement one or all of the above methods in the driver assistant systems as a safety measure. However, the driving environment, road marking, climatic conditions and driving skill make this method difficult to evaluate the state of the driver [2].

Another technique is to continually monitor and record the driver's motion, namely eye closure, eye blink, yawning and head movements through a fixed camera with an intelligent system to discriminate between the state of the vigilance and drowsiness. Nevertheless, the critical limitation in this method is due to the reduced recognition rate under the dim lighting background and the stage at which the drowsiness is detected. The behavioral method detects drowsiness only after the driver is entirely influenced by sleep.

Among the various drowsiness detection techniques, the physiology-based process involves electroencephalogram (EEG), electromyogram (EMG), electrocardiogram (ECG) and electrooculogram (EOG). The EEG method yields high accuracy and is referred to as the gold standard. Thus, the physiology-based method produces high efficiency and reliability in detecting drowsiness at an early stage with high

efficiency. Yet, the EEG signal, which is the most preferred physiological signal, has the closest association with drowsiness. The drawbacks of the EEG signals are that as they have high temporal resolution and can be easily interfered by EMG, eye blink and electromagnetic noise [2].

Drowsy driving is a vital issue and hence need to be identified at the earliest. Drowsiness has subsequent effects: (a) driver's reduced attention to surroundings, (b) considerable delay in reaction time and (c) affecting the driver's capability to make decisions. The literature study attempts to review all the previous approaches in detecting drowsiness. Drivers involved in sleep-related crashes reported that the quality of their sleep was either poor or fair [3]. Missing an hour of sleep can lead to car crash risk. The only antidote for drowsiness is sleep [4].

Li et al. [5] used Fp1 and O1 EEG channels to discriminate between alert and drowsy. Pranoto et al. [6] detected drowsiness in truck drivers using a speed limiter integrated fatigue analyzer. The system is based on the Arduino UNO, sensing the driver's body temperature and heart rate. Ribeiro et al. [7, 8] developed an EEG-based drowsiness detection system based on the Sleep-EDF database and used Hjorth coefficients, power spectral density and average power to classify drowsiness. Albalawi and Li [9] developed a real-time drowsiness detection based on a single channel EEG signal using eight frequency bands. They computed the relative power and classified the drowsy and alert state with the support vector machine (SVM) classifier. They compared the results of the developed system with the MIT-BIH polysomnographic database. Leger et al. [10] developed an inflight vigilance state detection system, which used a single EEG channel for pilots. Pathak and Jayanthi [11, 12], Da Silveira et al. [13], Picot et al. [14, 15] and Ogino and Mitsukura [16] researched on the use of a single EEG channel to classify alert and drowsy states of drivers. Hu [17] compared the different features and classifiers for driver drowsiness detection based on a single EEG channel [18]. Alluhaibi et al. [19] discussed the various driver behavior detection methods, their advantages and disadvantages. Mu et al. [20] detected driver fatigue using combined entropy features from the EEG signals. Belakhdar et al. [21–23] used a single channel EEG signal to classify drowsiness based on the average power of the delta and alpha waves. They compared the ANN and SVM classifiers for the best accuracy. They used the MIT-BIH polysomnographic dataset. Correa et al. [24, 25] extracted features using spectral and wavelet decomposition methods to classify the drowsy and alert state.

In this work, we have considered the ULg multimodality drowsiness database. The database contains multimodal signals, namely five EEG channels, two EOG channels, one EMG and one ECG channel along with the psychomotor vigilance test (PVT) and video data. We have considered only the five EEG signals for analysis and to classify between the alert and drowsy state. We have used the framing method to segment the signal into equal frames of 2 s using a rectangular window with an overlap of 50%. The raw signal is trimmed using a band-pass filter to a maximum cut-off frequency of 50 Hz. Further, each frame is segmented into eight sub-bands using a band-pass filter bank. We have extracted the log energy entropy and band power features for each of the frames. The feature set is then rescaled using a bipolar normalization method. The feature set is labeled as drowsy and alert, and then, all

the alert and drowsy data are combined to form the final dataset. The K-fold cross-validation technique is used. The dataset is trained using K-nearest neighbor network, and support vector machine classifiers, and the results are compared.

The remaining of the paper is ordered as follows. The details from the literature and the proposed methodology are explained in the second part of the introduction section. The multimodality drowsiness database, data acquisition protocol and the channel selection are explained in the first part of the methods section. The second part details the preprocessing, sub-band filtering and feature extraction procedures used in this approach. The data preprocessing section details dimensionality reduction and data preparation for the six classification models. The results section projects the results followed by the discussion section, which discusses the outcome of this research. The final conclusion section details the contributions and concludes the paper.

6.2 Methods

DROZY database: The publicly available ULg multimodality drowsiness (DROZY) database is considered in this research as it contains a multimodal approach. The complete details of the multimodal data collection, data description and the protocol are represented in Fig. 6.1 [1].

In this research, it is planned to use the ULg multimodality drowsiness database. The database contains physiology related signals, i.e., EEG, EOG, ECG and EMG. By using the Embla Titanium system, the signals were recorded from EEG channels C3, C4, Cz, Pz and Fz referenced at A1 in the international 10-20 system. The vertical and horizontal EOG signals, ECG and EMG signals were also recorded at a sampling frequency of 512 Hz. Along with these signals, video signals were also recorded. The drowsiness and alert signals were recorded from 14 male and female subjects. The test was conducted in a controlled environment in three trials. Before the first trial, the subjects were asked to have a good sleep pattern for the past week. In the first trial, the subjects were asked to perform an action watching the screen. After the first trial, the subjects were asked to stay awake for 36–38 h to keep them sleep deprived. In the second and third trials, the subjects performed the same previous

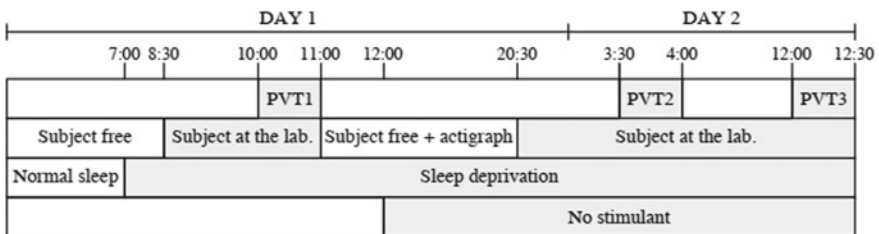


Fig. 6.1 Protocol design during the data collection. Adapted from [1]

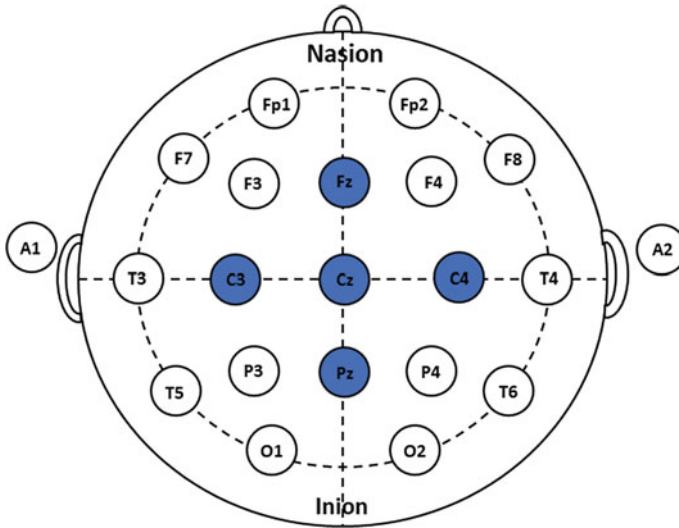


Fig. 6.2 EEG electrode placement conforming to the international 10-20 system

experiment. At the end of the final test, the subjects were arranged for a sound sleep before leaving the laboratory.

Channel selection: The experiment was conducted in three trials in two days, as mentioned in the protocol. The authors conducted an extensively used tool to measure the performance impairments due to drowsiness using a 10-min psychomotor vigilance test (PVT). This test gives the reaction time to visual or auditory stimuli that occur at random inter-stimulus intervals.

The database contains PSG signals from 11 electrophysiological signals (five EEG, two EOG, one ECG and one EMG). The five EEG channels are recorded from C3, C4, Cz, Pz and Fz locations present in the central lobe of the brain. The placement of the EEG channels is depicted in Fig. 6.4. The sensors are placed around C3, C4 and Cz locations and deal with the sensory and motor functions [26]. This research uses monopolar montage with C3 as a reference. The vertical and horizontal EOG signals are recorded from above and at the side of the right eye to capture the eye blinks. An ECG channel is recorded from the electrode placed on the chest, and an EMG signal is recorded from the electrode placed on the neck of the participant. The placement of electrodes is pictorially represented in Fig. 6.2.

6.3 Feature Extraction

Dimensionality reduction plays a vital role in classifier performance. Dimensionality reduction is achieved either by feature extraction or feature selection. For both feature extraction and feature selection approach, the feature evaluation criterion,

dimensionality of the feature space and optimization procedure are required. Feature extraction is the conversion of the raw data to a dataset with the selected number of variables which contains the most discriminatory evidence. Feature extraction, on the other hand, considers the whole original data and maps the useful information into a lower-dimensional space. The following section explains the signal processing and feature extraction process (Fig. 6.3).

EEG signal processing: EEG signals are the non-invasive physiological means of recording brain activity. It has the closest association with drowsiness. The EEG has neural domain signal information which has a high temporal resolution but can be easily interfered by EMG, eye blink and electromagnetic noise [27]. The EEG, along with the EMG, ECG and EOG signals, remains the European data format (EDF). A MATLAB function is used to extract only the EEG signals, which are of interest in this research. The experiment was conducted for 10 min, and the EEG signal contains information up to 600 s. The signals are recorded at 512 Hz sampling frequency. The signals include both EOG and EMG, which contribute toward the drowsiness detection. Hence, the eye blink artifacts and the EMG artifacts which are removed in conventional biosignal processing is avoided in this research. The raw signal is processed directly without any artifacts removal. However, a Butterworth low-pass filter with a cut-off frequency of 50 Hz is designed to attenuate the high-frequency components.

Sub-band filtering: The EEG signal is conventionally divided into alpha, beta, theta, gamma and delta waves based on their rhythms. These waves are further subdivided into low, medium and high and are extracted using a suitable band-pass filter based on their frequencies [9]. A Butterworth band-pass filter bank with eight

Fig. 6.3 Multimodal electrode placement during the experiment

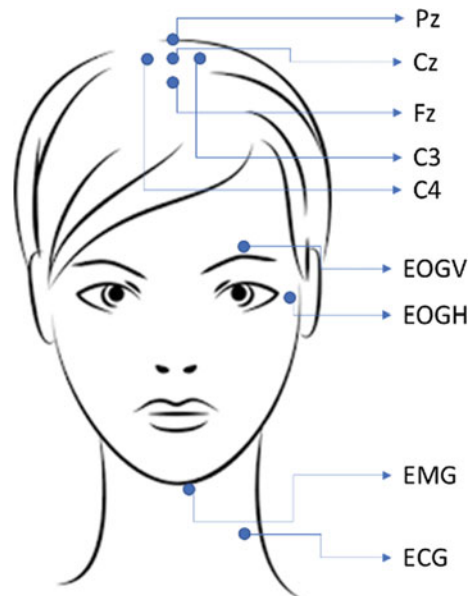


Table 6.1 EEG sub-band filtering

Wave	Frequency range (Hz)	μV	Nature	Optimal
Delta	0.1–4	20–200	Very slow	Deep sleep
Theta	4–8	20–100	Slow	Depressants
Low alpha	8–9	20–60	Moderate	Relaxation
High alpha	9–12	20–60	Moderate	Relaxation
Low beta	12–16	2–20	High	Conscious
Mid beta	16–20	2–20	High	Blinking
High beta	20–30	2–20	High	Alertness
Gamma	30–50	3–5	Very high	Cognition

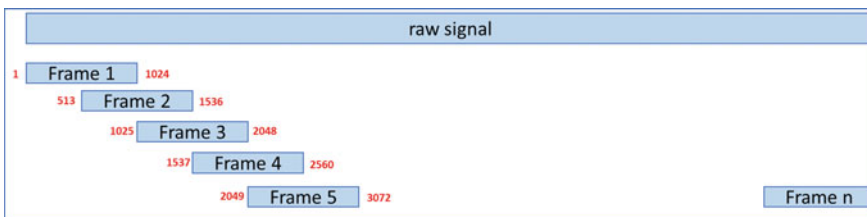
frequency bands is designed and used to extract the sub-bands of the EEG signals. Table 6.1 details the cut-off frequencies for all the eight sub-bands.

Frame blocking, windowing and overlap: The raw signal is recorded for 10 min. It is difficult to apply any feature extraction methods to the whole signal. Hence, the signal is divided into specific time windows (signal epochs) from the continuous EEG signal. On a trial and error method, the duration of the time windows is selected based on the performance metrics. In this case, the 2-s window is chosen to segment the raw EEG signal. An overlap of 50% is applied during the process of windowing (Fig. 6.4).

During each trial of the experiment, data are recorded for an average time of 10 min, which is approximately 600 s. All the signals are read, and the maximum length of the signal is computed and taken as reference, for those signals where the length is short, zeros are padded at the end of the signal to make all signals even. The raw EEG signal is segmented into 2 s pulses. After segmenting the signals into frames of 2 s with the windowing technique, the original raw signal grows to 300 per each subject per each trial, thereby enhancing the data.

Spectral Centroid

The spectral centroid is widely used in speech research to identify the robust and dominant frequency. The spectral centroid for the vibration signal is calculated using Eq. (6.1) as shown below.

**Fig. 6.4** Frame blocking

$$SC = \frac{\int kX(k)dk}{\int X(k)dk} \quad (6.1)$$

where $X(k)$ represents the FFT output, and k represents the number of FFT components.

Spectral Centroid frequency

The spectral centroid frequency is computed as the average of amplitude weighted frequencies, divided by the total amplitude. The spectral centroid frequency for the vibration signal is computed based on Eq. (6.2) as shown below

$$SCF_i = \frac{\sum_{n=1}^M f * S[f]w_i[f]}{\sum_{n=1}^M S[f]w_i[f]} \quad (6.2)$$

where M is the number of frequency bins.

Classification: Data preprocessing is referred to the set of procedures used to process the raw data for further processing such as classification or clustering. The dataset derived from the features does not follow a uniform data distribution. Hence, the feature set is rescaled between a certain range to enhance the performance of the classifier. The spectral features derived from the vibration signals are rescaled between '0' and '1' and associated with the class to form the dataset for classification.

The support vector machine (SVM) model is a machine learning algorithm based on the statistical learning. The SVM model is chosen in this study to classify the presence of damage. In this method, we plot each data as a point in the n -dimensional space with the value of each feature being the value of the particular coordinate. The classification is performed by finding the hyperplane that differentiates between the two classes. Hence, finding the right hyperplane becomes very crucial in SVM. By maximizing the distance, also known as the margin between the nearest data point and the hyperplane will determine the right hyperplane. The kernel method is used to transform the low-dimensional input space into a higher-dimensional space in a nonlinear separation problem. The 'fitsvm' function in MATLAB is used to model the SVM. 'Radial basis function' kernel is used to classify between drowsy and alert classes.

K-nearest neighbor algorithm (KNN) is one of the simplest and easy to implement a supervised machine learning algorithm. The K -factor is very crucial in determining the class boundaries. The boundaries become smooth with increased values of K . The training error rate and the validation error rate are the two parameters used to access for the values of K . The 'fitknn' function in MATLAB is used to model the KNN classifier. The 'minkowski' method is used as a distance metric, and the number of neighbor's value is chosen to be 3 in this classification method.

Table 6.2 Classification results

Classifier		Accuracy	Sensitivity	Specificity	TPR	TFR
SVM	Dataset 1	91.6	92.2	89.3	98.0	43.8
	Dataset 2	93.5	94.9	88.6	96.7	48.1
KNN	Dataset 1	93.2	94.6	96.8	96.3	39.8
	Dataset 2	95.9	96.7	94.2	93.5	40.2

6.4 Results

The spectral features namely spectral centroid, and spectral centroid frequency are extracted for each frame of the EEG signals. Support vector machine is used to train the feature matrix. The K-fold cross-validation method is used to process the dataset into training and testing. The average classification accuracy, for the KNN and SVM classifiers, is calculated, and the results are tabulated in Table 6.2.

The results show that KNN outperforms SVM in accuracy, and the sensitivity of the network is high.

6.5 Conclusion

This study performed the detection and classification of drowsiness, between the alert and drowsy state using the five EEG channels. We have used the framing method to segment the signal into equal frames of 2 s using a rectangular window with an overlap of 50%. The raw signal is trimmed using a band-pass filter to a maximum cut-off frequency of 50 Hz. Later, each frame is segmented into eight sub-bands using a band-pass filter bank. The log energy entropy and band power for each of the frames were extracted as features. The feature set is then rescaled using a bipolar normalization method. The feature set is labeled as drowsy and alert, and then, all the alert and drowsy data are combined to form the final dataset. From the three trials, the feature sets for the drowsy class extracted from the trial 2 and trial 3 were labeled as '0', and the alert feature set extracted from trial 1 was marked as '1'. The extracted feature sets were further normalized and tagged as drowsy and alert and then combined to form the final dataset. The K-fold cross-validation method is used. The dataset was trained using the two classifier models: K-nearest neighbor network, and support vector machine. The trained models were validated using the test dataset, and the performance of the classifiers on the two datasets was compared. Overall, the KNN classifier achieves 95.2 and 94.6% by outperforming the other classifiers. The proposed frame-based approach can be used for other classification applications as well. The developed model can be applied for driver drowsiness classification and other drowsiness research.

References

1. Massoz, Q., et al.: The ULg multimodality drowsiness database (called DROZY) and examples of use. In: 2016 IEEE Winter Conference on Applications of Computer Vision (WACV). IEEE (2016)
2. Ha, U., Yoo, H.J.: A multimodal drowsiness monitoring ear-module system with closed-loop real-time alarm. In: 2016 IEEE Biomedical Circuits and Systems Conference, BioCAS, 2016, pp. 536–539 (2016)
3. Stutts, J.C., Wilkins, J.W., Vaughn, B.V.: Why Do People Have Drowsy Driving Crashes: Input From Those Who Just Did, pp. 1–81 (1999)
4. Leefeldt, E.: Losing an hour of sleep can heighten car crash risk: AAA warns. CBC News, 2019 [Online]. Available: <https://www.cbsnews.com/news/daylight-saving-time-losing-an-hour-of-sleep-can-heighten-your-car-crash-risk-aaa-says/>. Accessed 28 June 2019
5. Li, W., He, Q.C., Fan, X.M., Fei, Z.M.: Evaluation of driver fatigue on two channels of EEG data. *Neurosci. Lett.* **506**(2), 235–239 (2012)
6. Pranoto, H., Leman, A.M., Sukmajati, D., Hanum, B., Baba, I.: Drivers drowsiness detection with speed limiter integrated fatigue analyzer (SLIFA) on fuel tank truck. *Int. J. Integr. Eng.* **10**(2), 66–70 (2018)
7. Ribeiro, D., Cardoso, A., Teixeira, C.: Online demonstration of an EEG-based drowsiness detector. In: Proceedings of 2017 4th Experiment International Conference, pp. 93–94 (2017)
8. Ribeiro, D., Teixeira, C., Cardoso, A.: EEG-based drowsiness detection platform to compare different methodologies. In: Proceedings of 2017 4th Experiment International Conference, pp. 318–322 (2017)
9. Albalawi, H., Li, X.: Single-channel real-time drowsiness detection based on electroencephalography. In: Proceedings of the Annual International Conference of the IEEE Engineering in Medicine and Biology Society, EMBS, July 2018, pp. 98–101 (2018)
10. Leger, D., et al.: In-flight automatic detection of vigilance states using a single EEG channel. *IEEE Trans. Biomed. Eng.* **61**(12), 2840–2847 (2014)
11. Pathak, M., Jayanthi, A.K.: Designing of a single channel EEG acquisition system for detection of drowsiness. In: 2017 International Conference on Wireless Communications, Signal Processing and Networking (WiSPNET), pp. 1364–1368 (2017)
12. Pathak, M., Jayanthi, A.K.: Development of a real-time single channel brain-computer interface system for detection of drowsiness. *Biomed. Eng. Appl. Basis Commun.* **29**(03), 1750019 (2017)
13. Da Silveira, T.L.T., Kozakevicius, A.J., Rodrigues, C.R.: Automated drowsiness detection through wavelet packet analysis of a single EEG channel. *Expert Syst. Appl.* **55**, 559–565 (2016)
14. Picot, A., Charbonnier, S., Caplier, A.: On-line detection of drowsiness using brain and visual information. *IEEE Trans. Syst. Man Cybern. Part A Syst. Humans* **42**(3), 764–775 (2012)
15. Picot, A., Charbonnier, S., Caplier, A.: On-line automatic detection of driver drowsiness using a single electroencephalographic channel. In: 2008 30th Annual International Conference of the IEEE Engineering in Medicine and Biology Society, pp. 3864–3867 (2008)
16. Ogino, M., Mitsukura, Y.: Portable drowsiness detection through the use of a prefrontal single-channel electroencephalogram. *Sensors (Switzerland)* **18**(12), 1–19 (2018)
17. Hu, J.: Comparison of different features and classifiers for driver fatigue detection based on a single EEG channel. *Comput. Math. Methods Med.* **2017** (2017)
18. Mehreen, A., Anwar, S.M., Haseeb, M., Majid, M., Ullah, M.O.: A hybrid scheme for drowsiness detection using wearable sensors. *IEEE Sens. J.* **19**(13), 1 (2019)
19. Alluhaibi, S.K., Al-Din, M.S.N., Moyaid, A.: Driver behavior detection techniques: a survey. *Int. J. Appl. Eng. Res.* **13**(11), 8856–8861 (2018)
20. Mu, Z., Hu, J., Min, J.: Driver fatigue detection system using electroencephalography signals based on combined entropy features. *Appl. Sci.* **7**(2), 150 (2017)

21. Belakhdar, I., Kaaniche, W., Djmel, R., Ouni, B.: Detecting driver drowsiness based on single electroencephalography channel. In: 13th International Multi-Conference on Systems, Signals & Devices, SSD 2016, pp. 16–21 (2016)
22. Belakhdar, I., Kaaniche, W., Djmel, R., Ouni, B.: A comparison between ANN and SVM classifier for drowsiness detection based on single EEG channel. In: 2nd International Conference on Advanced Technologies for Signal and Image Processing, ATISIP, 2016, pp. 443–446 (2016)
23. Belakhdar, I., Kaaniche, W., Djmal, R., Ouni, B.: Single-channel-based automatic drowsiness detection architecture with a reduced number of EEG features. *Microprocess. Microsyst.* **58**, 13–23 (2018)
24. Correa, A.G., Leber, E.L.: An automatic detector of drowsiness based on spectral analysis and wavelet decomposition of EEG records. In: 2010 Annual International Conference of the IEEE Engineering in Medicine and Biology Society, EMBC'10, pp. 1405–1408 (2010)
25. Garcés Correa, A., Orosco, L., Laciari, E.: Automatic detection of drowsiness in EEG records based on multimodal analysis. *Med. Eng. Phys.* **36**(2), 244–249 (2014)
26. Kasabov, N.K.: *Time-Space, Spiking Neural Networks and Brain-Inspired Artificial Intelligence*. Springer, Heidelberg (2019)
27. Ha, U., Yoo, H.J.: An EEG-NIRS ear-module SoC for wearable drowsiness monitoring system. In: 2016 IEEE Asian Solid-State Circuits Conference, A-SSCC 2016 Proceedings, pp. 193–196 (2017)

Chapter 7

Close Loop Feedback Direct Current Control in Driving Mode of a Four Quadrants Drive Direct Current Chopper for Electric Vehicle Traction Controlled Using Fuzzy Logic



Saharul Arof, Noramlee M. Noor, R. Mohamad, Emilia Noorsal, P. A. Mawby, and H. Arof

Abstract The direct current (DC) series motor is the highest starting torque motor compared to other motors with the same kilowatt power. The conventional speed controller that is used in an electric vehicle utilizes the series motor that can cause jerk and slip during start-up. This paper discusses the usage of a direct current control (DCC) in the four quadrants direct current chopper (FQDC) application to overcome the start-up problem. The series motor current is controlled in a closed-loop fashion using the fuzzy logic technique. The DCC is a current control method using a lookup table (LUT) with a predetermined reference current. The system is tested using MATLAB/Simulink. The simulation results using MATLAB/Simulink show that the current can be controlled using a fuzzy logic technique.

S. Arof (✉) · N. M. Noor · R. Mohamad
Malaysian Spanish Institute Kulim Hi-Tech Park, Universiti Kuala Lumpur, 09000 Kulim,
Kedah, Malaysia
e-mail: saharul@unikl.edu.my

N. M. Noor
e-mail: noramlee@unikl.edu.my

R. Mohamad
e-mail: mrosyidi@unikl.edu.my

S. Arof · E. Noorsal
Faculty of Electrical Engineering, Universiti Teknologi MARA Cawangan Pulau Pinang, 13500,
Permatang Pauh, Pulau Pinang, Malaysia
e-mail: emilia.noorsal@uitm.edu.my

P. A. Mawby
University of Warwick School of Engineering, Coventry CV47AL, UK
e-mail: p.a.mawby@warwick.ac.uk

H. Arof
Engineering Department, Universiti Malaya, Jalan Universiti, 50603 Kuala Lumpur, Malaysia
e-mail: ahamzah@um.edu.my

Keywords Direct current (DC) drive · DCC · Fuzzy logic · Four quadrants chopper · LUT controller · Current control · EC

7.1 Introduction

The emission of hydrocarbons not only pollutes the environment but also contributes to global warming which melts the icebergs and increases the sea level. Using efficient electric vehicles (EV) for transportation is one of the solutions to reduce global hydrocarbon emission. The price of EV is expensive making it unattainable to many people, especially those living in poor countries. Thus, there is a need for researchers to look for an alternative EV that can reduce the cost, thus making it more economical and affordable such as direct current (DC) drive EV.

7.2 Literature

Interest in research for economical DC drive EV started in 2009 at the Oak Research National Laboratory (ORNL) [1]. The USA had successfully designed a brushed motor with high power output (55 kW) and high efficiency (92%) that can operate in low operating voltages (13 V). In conjunction with the research in a DC drive motor, a new series motor, four quadrants DC chopper, was designed and the proposed chopper has multiple operations [2]. Several studies cover several areas related to the DC drive EV and its incorporated battery charger [3] for the FQDC. These investigations were extended to the attempt to study different types of DC drive motor such as separately excited motor has been conducted [4]. To improve the FQDC performance, optimization tools such as artificial intelligence are introduced to control the proposed FQDC chopper [5–7]. Detailed investigations on the chopper operation modes led to the establishment of a simulation model to test the DC chopper for electric car and light rail transit (LRT) [8]. Further investigations on each of the chopper operations on the voltage, current, torque and speed of the FQDC have been carried out [9]. For DC series motor traction EV application, the speed control and torque control have been successfully done and implemented with direct current control (DCC) [10]. For power regeneration, the FQDC offers the generator mode of the FQDC with several techniques of regenerated power as studied and discussed in [11]. In order for the FQDC to be applied in the real world, it needs a controller with a running control algorithm embedded in the system. The controller and its control algorithm were studied using processor in the loop (PIL) technique [12]. Each operation of FQDC mode can improve its performance using AI optimization tools such as genetics algorithm [13].

In this paper, a closed-loop feedback current control using fuzzy logic for a DC series motor in driving mode of FQDC is discussed.

7.2.1 Four Quadrants Drive DC Chopper

Figure 7.1 depicts the driving mode of the FQDC which offers seven modes of operations including the forward and reverse driving, field weakening, parallel driving, generating, regenerative braking and resistive braking capabilities. The closed-loop feedback current control of the DC series motor in driving mode of the FQDC is also shown in Fig. 7.1.

For a traction motor, the torque is used to move a vehicle from a standstill, and when the vehicle has started moving, it already has some inertia; thus, a lower torque is required to propel the vehicle. The series motor has the highest starting torque compared to other types of motors. This is good for other types of the applications except for motor traction. The high starting torque will cause jerks during start-up

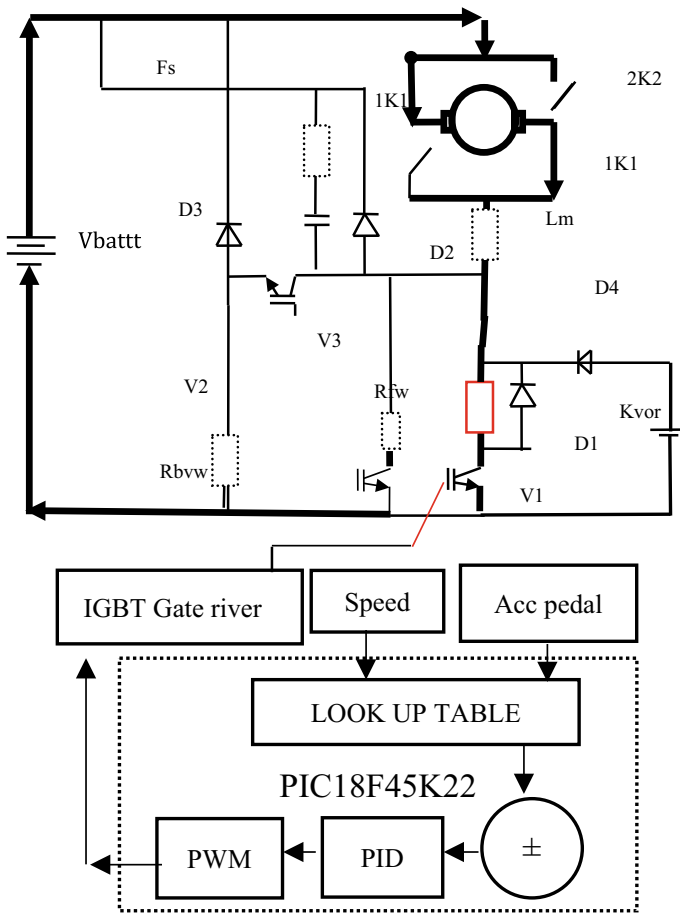


Fig. 7.1 Driving mode of the FQDC

which are unwanted. To overcome the jerk effect while start-up, the torque of a series motor has to be reduced during start-up. The blue color line in Fig. 7.2 represents the normal torque–speed characteristic of a DC series motor. To achieve a better start-up, the torque versus speed characteristics line has to be altered as shown by the red line in Fig. 7.2.

After the cut-off, the final expected torque–speed characteristics curve is shown in Fig. 7.2. For the DC series motor, the torque and current have a significant relationship, which can be seen if they are plotted together as shown in Fig. 7.3. Both torque and current produce a similar trend of speed except with different strength [10].

The flow of the current in driving mode is shown in Fig. 7.4.

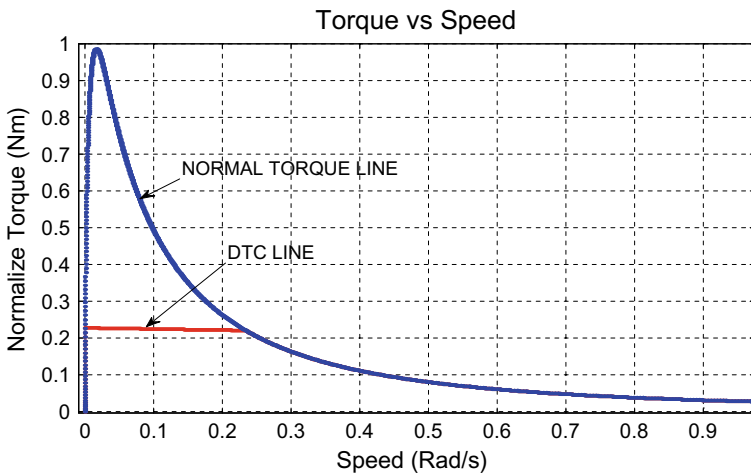


Fig. 7.2 Torque versus speed curve under load

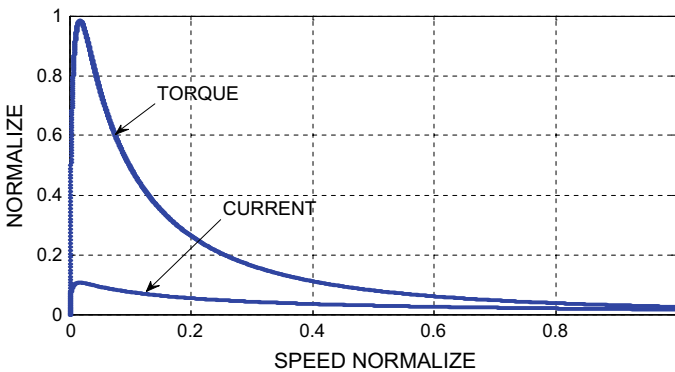
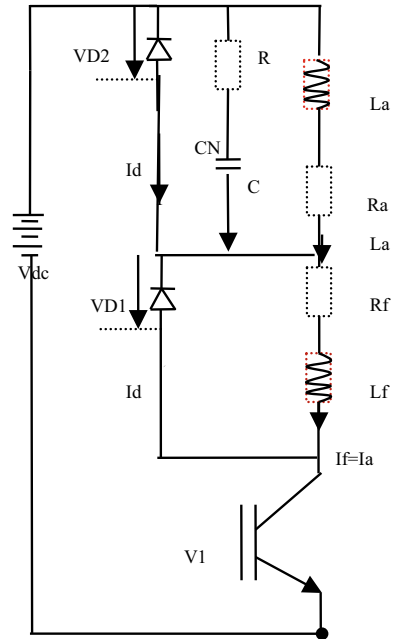


Fig. 7.3 Current versus normalized speed

Fig. 7.4 Driving mode



As a result, a lookup table (LUT) can be set as input reference to the closed-loop feedback control of the current [10].

The following general equations describe the voltage and current for the chopper. Equations (7.1)–(7.4) are general equations that are applicable to all chopper operation modes. B_{emf} is the back emf of the motor, V_a and V_f are the armature and field voltages, K_b is the back emf constant, K_t is the torque motor constant, I_f is the field current, R_a and R_f are the motor coil resistances, I_a is the armature current, ω is the angular speed, and T_d is the motor torque.

$$I_a = \frac{V_{batt} - I_a(R_a + R_f) - B_{emf}}{L_a + L_f} \quad (7.1)$$

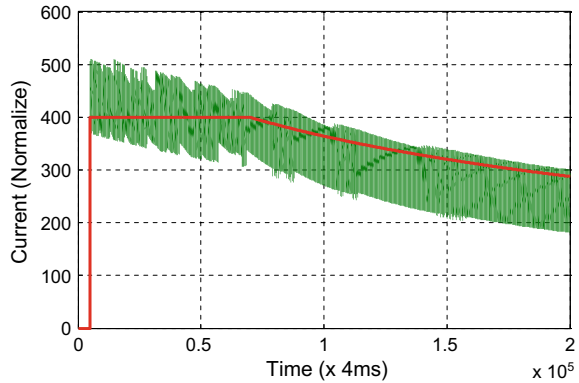
$$B_{emf} = K_v I_f \omega \quad (7.2)$$

$$T_d = K_t I_f I_a \quad (7.3)$$

$$\omega = \int \frac{T_d - (T_L + B_w)}{J} \quad (7.4)$$

In driving mode, the direct current control is applied based on the armature current. While the motor is running, the armature current depends on the back emf, and the back emf depends on the field current. The motor speed and current were tested using

Fig. 7.5 Direct current control



a digital PID controller as shown in Fig. 7.5. In the beginning, the speed is linearly increased and that is the indication of direct current control.

7.2.2 Fuzzy Logic

Lofti Zadeh is the founder and the key contributor to fuzzy logic (FL) and its applications [14–16]. The basic architecture of FL is based on the concept of a ‘crisp’ input and ‘crisp’ output. Crisp means the actual data or parameter being used, which is described in either quantitative or qualitative parameters. The full architecture of FL is shown in Fig. 7.6.

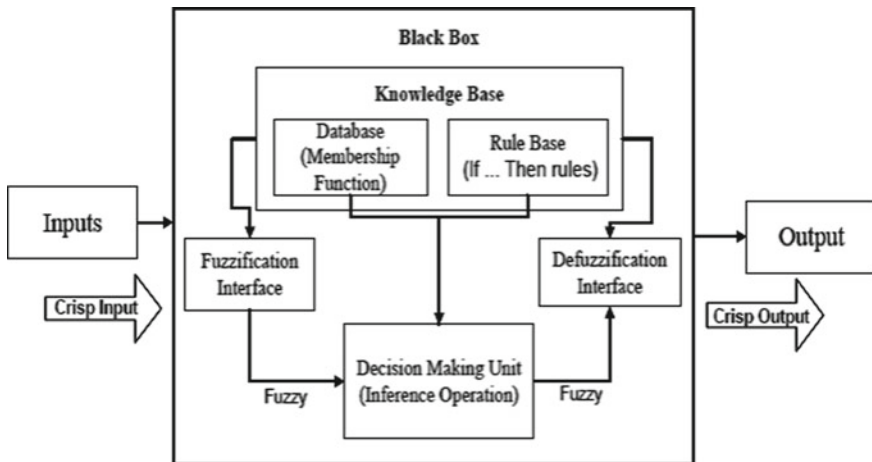


Fig. 7.6 Architecture of FL

7.2.2.1 Fuzzification Interface

Fuzzification involves rule evaluation and aggregation, which is done mostly in the knowledge base block. There are two common techniques which are used in this process: the Mamdani method and the Sugeno method. Unlike Sugeno, the advantage of the Mamdani method is in capturing expert knowledge in its entirety, whereas the Sugeno uses singleton rule output, which only works well with linear techniques [16]. In deciding this, the set will be based on the inputs and outputs of the system being modeled. The three most popular membership functions (MFs) are known as the triangular, Gaussian and trapezoidal functions [16]. The usage of triangular and trapezoidal MF can speed up the performance rate, but lower the level of accuracy. This process and implementation are performed in the database block. The function of the rule-based block is to determine the rules relationship for each of the inputs and the outputs. This is where the inference system is used, specifically based on ‘If...then...rules’ or Bayesian rules [16] given below:

IF x is A_i and IF y is B_i then z is C_i

The design of these rules usually depends on the inputs and each of the membership functions. As also described in [16], rule evaluation in the fuzzy inference system model is based on either an ‘AND’ function or an ‘OR’ function, in terms of the fuzzy operation as an algebraic product of algebraic sum, which is used to compare the inputs. The level of the truth value of the antecedent is then determined, and the consequent membership function is either clipped (correlation minimum) or scaled (correlation product) [16]. This fuzzy operator will compare each of the inputs, and this operation takes place between the fuzzification interface and knowledge base, and will be processed in the decision-making unit as shown in Fig. 7.6.

7.2.2.2 Defuzzification Interface

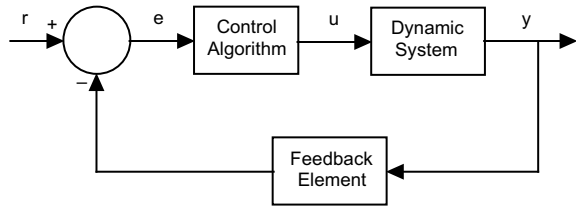
The final step is to convert all of the fuzzy values to crisp values. This is done by defuzzification or aggregation of the rule output. The examples of the defuzzification methods are center of gravity or centroid, the maximum membership principle, the weighted average method, the mean-max membership method, the center of sum method, the center of largest area method and the first (or last) maxima method [16]. The most commonly used defuzzification technique is the centroid method.

7.2.2.3 Closed-Loop Feedback Control Using Fuzzy Logic

A typical fuzzy logic controller for a closed-loop feedback control system is shown in Fig. 7.7. Equations (7.5) and (7.6) describe the relationship between the change of control ($u(k)$) on the one hand and the error ($e(k)$) and change in the error.

$$\Delta e(k) = e(k) - e(k - 1). \quad (7.5)$$

Fig. 7.7 Basic structure of a fuzzy logic closed-loop feedback system



$$\Delta rerr(k) = rerr(k) - rerr(k - 1). \tag{7.6}$$

7.3 Methodology

The two inputs to the fuzzy logic controller are the motor current error as shown in Fig. 7.8 and the rate of motor current error as shown in Fig. 7.9. The single fuzzy output is shown in Fig. 7.10, which is the PWM output signal to fire the IGBT, so more or less current can enter the chopper circuit. The reference for the input current of the closed-loop feedback control is obtained from the LUT [12]. The Sugeno style of fuzzy logic is chosen due to its simplicity and linearity, and it is suitable for a linear system. The membership function is first set and the degree of membership function is set after several trial and errors during the open-loop trials.

The two inputs of fuzzy sets (error and rate of error), which use the triangular membership function and one output set to represent the final output signal, are established. The types of error membership functions are negative, zero, small and

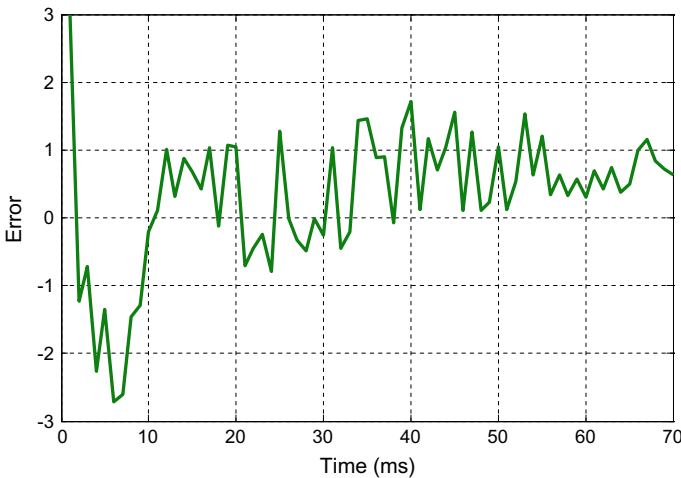


Fig. 7.8 Error signal

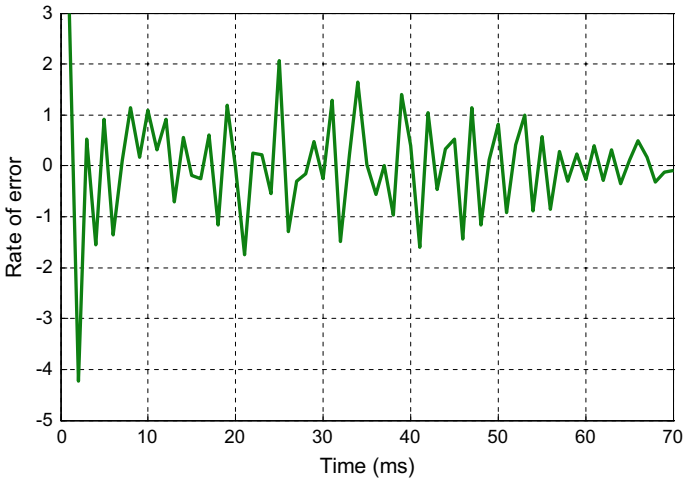


Fig. 7.9 Rate of error (RERR) versus time

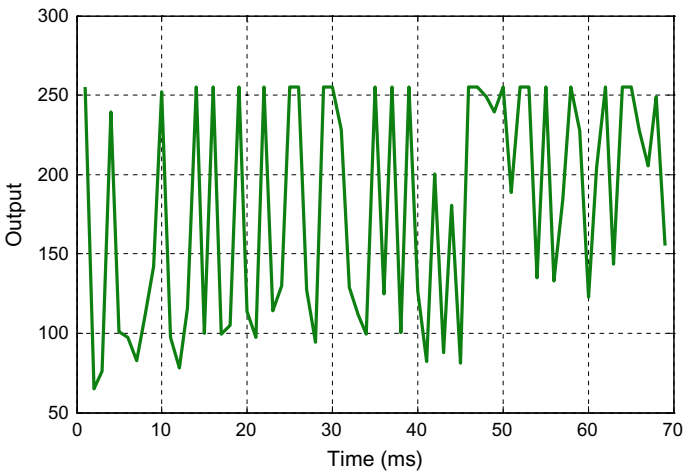


Fig. 7.10 Fuzzy output (PWM) versus time

big as indicated in Fig. 7.11. The rate of error membership function is negative big, negative small, zero, small and big as shown in Fig. 7.12. The membership function boundary for both fuzzy sets is equally divided. The boundaries are set according to error and rate of error under the influence of the system transient response and timing delay of the system.

The output of fuzzy with Sugeno method as shown in Fig. 7.13 is set after several trial-and-error tests during open-loop and closed-loop tests before it can be finally set up. The singleton output of Sugeno is set according to the error and rate of error

Fig. 7.11 Fuzzy logic membership function for error

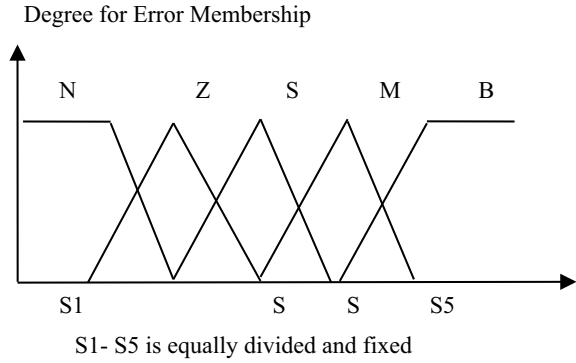


Fig. 7.12 Fuzzy logic membership function for rate of error

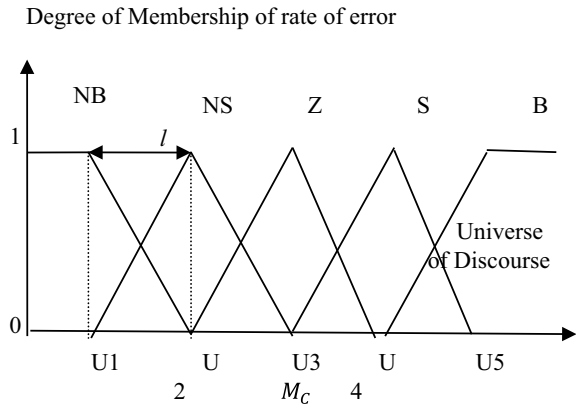
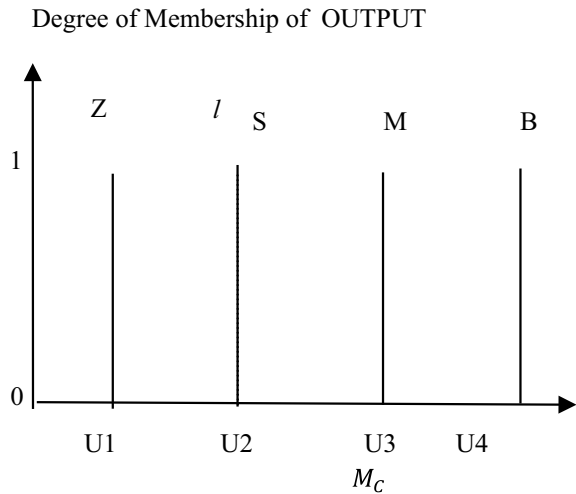


Fig. 7.13 Fuzzy logic singleton output



output under the influence of the system’s transient response and time delay of the system.

The rules for input and output of the fuzzy logic are listed in Table 7.1. The rules are set according to the system transient response and influenced by the time delay of the systems.

Two inputs of fuzzy logic which are the error of the current and rate of the error of the current are fed to the fuzzy logic controller for the closed-loop feedback control of direct current control as shown in Fig. 7.14. The input reference (the expected current) is taken from LUT which has undergone several interpolations before the

Table 7.1 Set of rules

ERR	RERR	OUTPUT
ZERO	HIGH	ZERO
ZERO	MED	ZERO
ZERO	LOW	ZERO
ZERO	ZERO	ZERO
ZERO	NHIGH	LOW
ZERO	NMED	MED
ZERO	NLOW	HIGH
LOW	HIGH	LOW
LOW	MED	LOW
LOW	LOW	LOW
LOW	ZERO	LOW
LOW	NHIGH	LOW
LOW	NMED	MED
LOW	NLOW	HIGH
MED	HIGH	MED
MED	MED	MED
MED	LOW	MED
MED	ZERO	MED
MED	NHIGH	LOW
MED	NMED	MED
MED	NLOW	HIGH
HIGH	HIGH	HIGH
HIGH	MED	HIGH
HIGH	LOW	HIGH
HIGH	ZERO	HIGH
HIGH	NHIGH	LOW
HIGH	NMED	MED
HIGH	NLOW	HIGH
NEG	-	ZERO

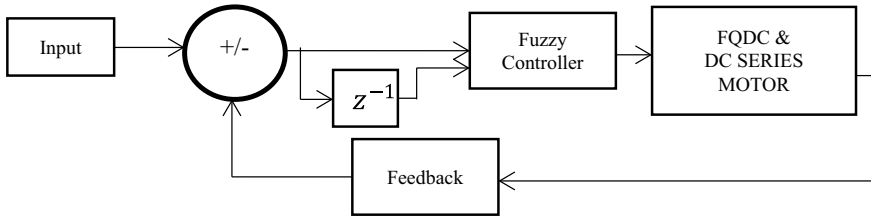


Fig. 7.14 Fuzzy logic in closed-loop feedback control

final value is obtained [12]. The expected input reference current value is according to the speed of the motor [12].

7.3.1 Simulation Model with MATLAB/Simulink

A simulation model using MATLAB/Simulink is established by using mathematical Eqs. (7.1)–(7.4) which are transformed into a physical-based model as shown in Fig. 7.15. The simulation model is used to observe the system's performance and tune fuzzy logic controller controlling the FQDC with direct current control technique. From the obtained results, the controller performance is observed, tuned and improved.

7.4 Result and Discussion

The result of the fuzzy logic closed-loop feedback control FQDC incorporated with a DC series motor armature current and motor speed in driving mode is shown in Fig. 7.16. The speed of the motor is normalized. During the first stage of the direct current control, it is observed that the motor speed increases linearly.

The fuzzy logic controller usually is not able to operate correctly in the first attempt. It is common then to redesign and to do many attempts before a successfully operated controller is built. After the completion of the development of the controller's model, a software tool is used to simulate the model in order to obtain observable simulation data. These data reflect the degree of the controller's performance. Based on the data, some changes are then made to the initial model if redesign is necessary. This adjustment process on the model is known as tuning.

By tuning, the optimal operating point of the controller can be searched and maintained to make sure that good performance is achieved at the required level [15, 16]. There are two ways to tune a fuzzy logic controller: modifying the membership functions and changing the set of rules applied [15, 16]. Usually, both methods of tuning are done based on heuristic knowledge of experienced operators. Often, experts carry out trial-and-error experiments for tuning. Sometimes, they have to

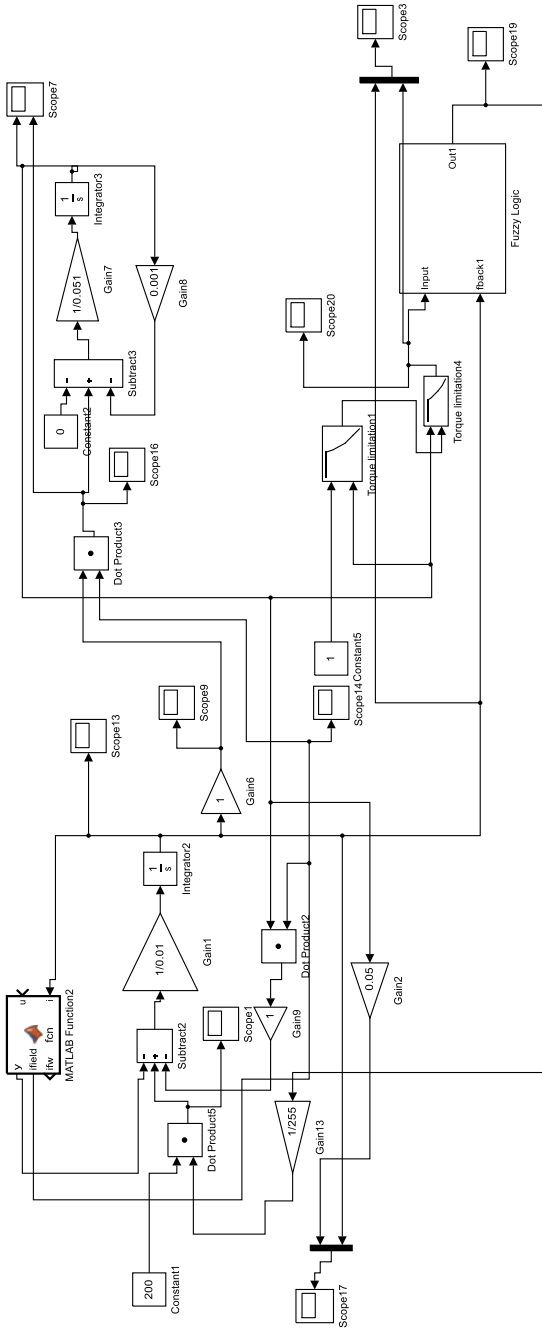


Fig. 7.15 Simulation model with fuzzy logic in closed-loop feedback control

Fig. 7.16 Speed and current of the FQDC DC series motor controlled by fuzzy logic in closed-loop feedback control

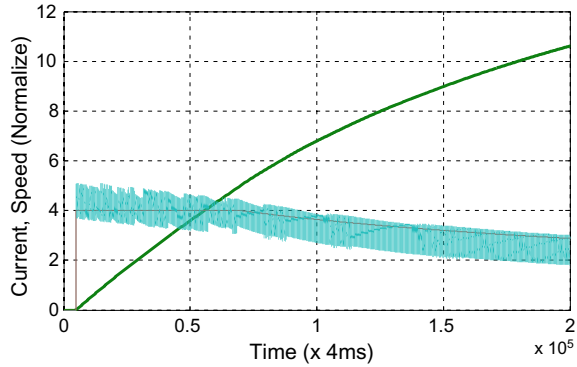
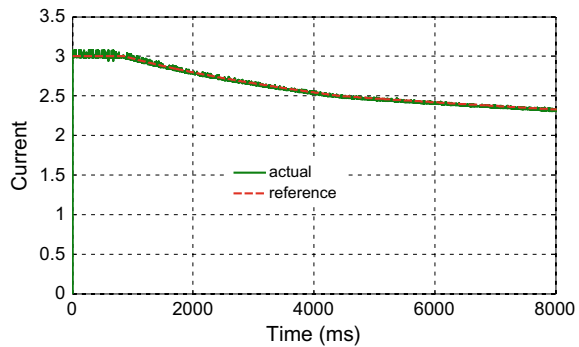


Fig. 7.17 Current control by fuzzy logic after fine-tuning



undergo a number of trials before arriving at the results needed. During each trial, some parameters are changed and a modified model is built and simulated to get the output for a specific operating condition of the system. The final result is shown in Fig. 7.17.

7.5 Conclusions

The proposed fuzzy logic control successfully controls the armature current in direct current control mode of a closed-loop feedback and can be used as a control algorithm for controlling the armature current of a four quadrants DC chopper of series motor for the application as a DC drive electric car.

References

1. Oak Ridge National Laboratory: Advanced Brush Technology for DC Motors (2009). Available: <http://peemrc.ornl.gov/projects/emdc3.jpg>
2. Arof, S., Jalil, J.A., Yaakop, N.M., Mawby, P.A., Arof, H.: (2014) Series motor four quadrants drive DC chopper part 1: overall. In: International Conference on Power Electronics. <https://doi.org/10.1109/PECON.2014.7062468>
3. Arof, S., Diyanah, N.N.H., Mawby, P., Arof, H., Mohd Yaakop, N.: Low Harmonics Plug-in Home Charging Electric Vehicle Battery Charger Utilizing Multi-level Rectifier, Zero Crossing and Buck Chopper: Part 1: General Overview. *Prog. Eng. Technol.* **119**, 103–108 (2019). https://doi.org/10.1007/978-3-030-28505-0_9
4. Arof, S., Diyanah, N.H.N., Noor, N.M., Jalil, J.A., Mawby, P.A., Arof, H.: A new four quadrants drive chopper for separately excited DC motor in low cost electric vehicle. *Prog. Eng. Technol.* **119**, 119–138 (2019). https://doi.org/10.1007/978-3-030-28505-0_10
5. Arof, S., Muhd Khairulzaman, A.K., Jalil, J.A., Arof, H., Mawby, P.A.: Self tuning fuzzy logic controlling chopper operation of four quadrants drive DC chopper for low cost electric vehicle. In: 6th International Conference on Intelligent Systems, Modeling and Simulation, IEEE computer Society, pp. 40–45 (2015)
6. Arof, S., Zaman, M.K., Jalil, J.A., Mawby, P.A., Arof, H.: Artificial intelligence controlling chopper operation of four quadrants drive DC chopper for low cost electric vehicle. *Int. J. Simul. Syst. Sci., Technol.* (2015). <https://doi.org/10.5013/ijssst.a.16.04.03.2015>
7. Arof, S., Diyanah, N.H., Mawby, P.A., Arof, H.: Study on implementation of neural network controlling four quadrants direct current chopper: part 1: using single neural network controller with binary data output. *Adv. Eng. Process. Technol.* 37–57 (2019). https://doi.org/10.1007/978-3-030-05621-6_4
8. Arof, S., Hassan, H., Rosyidi, M., Mawby, P.A., Arof, H.: Implementation of series motor four quadrants drive DC chopper for dc drive electric car and LRT via simulation model. *J. Appl. Environ. Biol. Sci.* **7**(3S), 73–82 (2017)
9. Arof, S., Noor, N.M., Alias, F., Mawby, P.A., Arof, H.: Investigation of chopper operation of series motor four quadrants DC chopper. *J. Appl. Environ. Biol. Sci.* **7**(3S), 49–56 (2017)
10. Arof, S., Jalil, J.A., Kamaruddin, N.H., Yaakop, N.M., Mawby, P.A., Arof, H.: Series motor four quadrants drive DC chopper part 2: driving and reverse with direct current control. In: International Conference on Power Electronics, pp. 775–780. 978-1-5090-2547-3/16 (2016). <https://doi.org/10.1109/pecon.2016.7951663>
11. Arof, S., Diyanah, N.H.N., Noor, N.M.N., Md. Radzi, J., Jalil, A., Mawby, P.A., Arof H.: Series motor four quadrants drive DC chopper: part 4: generator mode. *Prog. Eng. Technol.* **119**, 155–167 (2019). https://doi.org/10.1007/978-3-030-28505-0_12
12. Arof, S., Diyanah, N.H., Yaakop, M., Mawby, P.A., Arof, H.: Processor in the loop for testing series motor four quadrants drive direct current chopper for series motor driven electric car: part 1: chopper operation modes testing. *Adv. Eng. Process. Technol.*, pp. 59–76 (2019). https://doi.org/10.1007/978-3-030-05621-6_5
13. Arof, S., Diyanah, N.H.N., Noor, N.M., Rosyidi, M., Mawby, P.A., Arof H.: Genetics algorithm for setting up look up table for parallel mode of new series motor four quadrants DC chopper. *Prog. Eng. Technol.* **119**, 155–167 (2019). https://doi.org/10.1007/978-3-030-28505-0_12
14. Jamaludin, J., Rahim, N.A.: An elevator control group system with a self tuning fuzzy logic group controller. *IEEE Trans. Ind. Electron* **57**(12) (2010)
15. Jamaludin, J., Rahim, N.A.: Development of self tuning fuzzy logic controller for intelligent control of elevator system. *Eng. Appl. Artif. Intell.* **22**(8)
16. Negnevitsky, M.: *Artificial Intelligence, a Guide to Intelligent System*, 3rd edn. Addison Wesley, Pearson Education, UK (2011)

Chapter 8

Digital Proportional Integral Derivative (PID) Controller for Closed-Loop Direct Current Control of an Electric Vehicle Traction Tuned Using Pole Placement



Saharul Arof, N. M. Noor, M. F. Alias, Emilia Noorsal, Philip Mawby, and H. Arof

Abstract Direct current (DC) series motors have a higher starting torque compared to other types of motors, and their power is in the kilowatt range. The standard speed is applied for electric vehicles (EVs) with a series motor, and four quadrants direct current chopper (FQDC) can cause jerk and slip during the start-up. DC control (DCC) is one of the solutions applied to FQDC to overcome this start-up problem. The DCC is the current control strategy that employs a lookup table with a predetermined reference current. The current has to be controlled in a closed loop with feedback. An inefficient feedback controller with wrongly tuned parameters can cause ripples in current and torque. This paper describes the modeling and the control of a proposed DCC using a PID controller with the pole placement technique. The system is tested using MATLAB/Simulink which shows that the current can be controlled using the digital PID utilizing the pole placement technique.

S. Arof (✉) · N. M. Noor · M. F. Alias
Universiti Kuala Lumpur, Malaysian Spanish Institute, Kulim Hi-Tech Park, 09000 Kulim,
Kedah, Malaysia
e-mail: saharul@unikl.edu.my

N. M. Noor
e-mail: noramlee@unikl.edu.my

M. F. Alias
e-mail: fauzialias@unikl.edu.my

S. Arof · E. Noorsal
Faculty of Electrical Engineering, Universiti Teknologi MARA Cawangan Pulau Pinang, 13500
Permatang Pau, Pulau Pinang, Malaysia
e-mail: emilia.noorsal@uitm.edu.my

P. Mawby
University of Warwick School of Engineering, Coventry CV47AL, UK
e-mail: p.a.mawby@warwick.ac.uk

H. Arof
Engineering Department, Universiti Malaya, Jalan Universiti, 50603 Kuala Lumpur, Malaysia
e-mail: ahamzah@um.edu.my

Keywords DC drive · Series motor · Four quadrants chopper · DCC · Current control · Closed-loop control · Digital PID controller · Pole placement · Driving · EV

8.1 Introduction

The emission of hydrocarbons not only pollutes the environment but also contributes to global warming, which melts the icebergs and increases the sea level. Using efficient electric vehicles (EV) for transportation is one of the solutions to reduce the global hydrocarbon emission. Unfortunately, the price of EV is expensive, making it unattainable to many people, especially those living in developing countries.

8.2 Literature Review

In 2009, Oak Ridley National Laboratory (ORNL), USA, unveiled a new type of DC brushed motors with a high-power output (55 kW) and high efficiency (92%) but operating at a low operating voltage (13 V) [1]. Attempt to improve the conventional H-Bridge chopper by an increased number of operations or to allow motor reverse action has been continuously carried out. But ever since the discovery of the new DC motor by the ORNL, a new series motor, four quadrants DC chopper shown in Fig. 8.1, was designed and the proposed chopper has more operations compared to the earlier versions [2]. Several other studies related to DC drive EV led to research on EC battery charger [3], and different types of DC drive brushed such as the separately excited motor that can be used for motor traction for DC EV have been done [4]. A detailed investigation into the chopper operation modes led to the establishment of a simulation model to test the chopper operations for the application as electric car and light rail transit (LRT) [5]. This simulation model led to further detailed investigations into each of the chopper operations and on the specific pattern of the motor voltage, current, torque, speed of the series motor and FQDC running for DC drive EC application have been continuously carried out [6]. For DC series motor traction of EC application, the speed and the torque control for the series motor, in an attempt to reduce jerk and tire slip, have been successfully done and implemented with the direct current control technique [7]. For power regeneration, the FQDC offers the generator mode with several techniques of starting the regenerated power and the voltage control is studied and discussed in [8]. In order for the FQDC to be applied in real world, it needs controllers running the control algorithm in the embedded system. The controller and its control algorithm are studied and tested using processor in the loop (PIL) technique [9]. To improve the new FQDC performance, optimization tools such as artificial intelligence (AI) are introduced to control all the operations of the proposed FQDC chopper [10, 11]. Among the three AI controllers, ANFIS shows the best performance followed by neural network and the self-tuning fuzzy

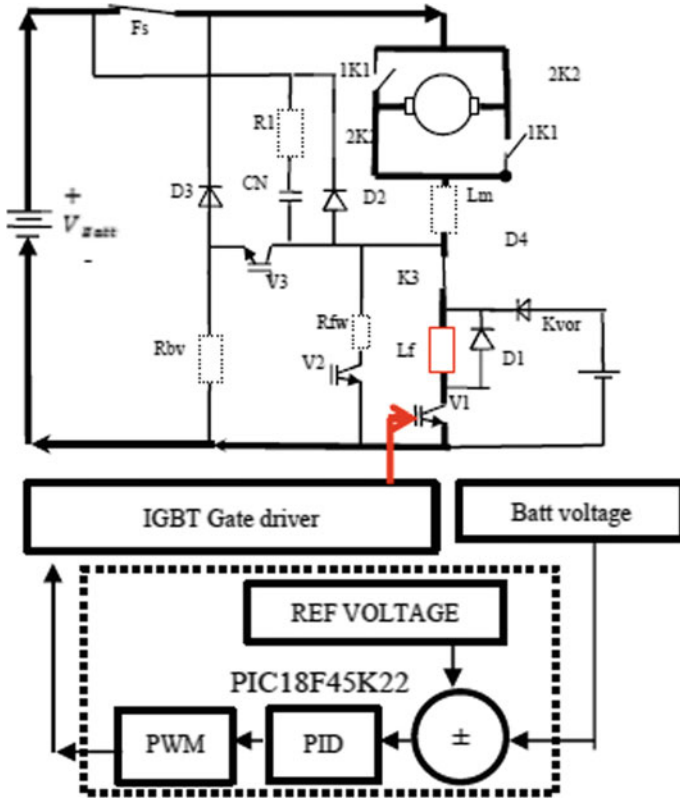


Fig. 8.1 Series motor four quadrants DC chopper

logic controller. A study on neural network controller to uncover the best method of tuning has been carried out and the single controller with binary output has been investigated in detail [12]. On each specific FQDC chopper operation mode, the single performance can be further improved using AI optimization tools such as the genetics algorithm to set up a specific lookup table for the field current [13].

8.2.1 Direct Current Control During Driving Mode

In driving mode, the FQDC can be represented as a diagram as shown in Fig. 8.1.

A series motor has the highest starting torque compared to the other types of motors. This is good for different types of applications except for the motor traction. The high starting torque will cause jerks during start-up, and it is unwanted. From that reason, in order to remove the jerk effect during start-up, the torque of a series motor has to be reduced. In Fig. 8.2, the blue color line represents the example of

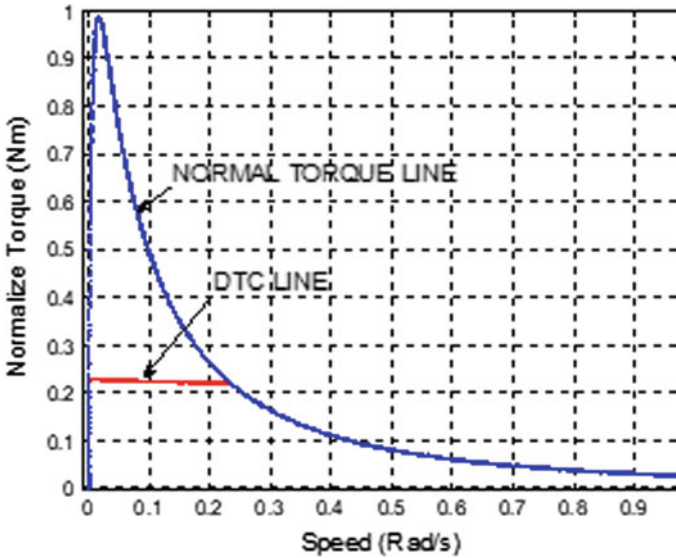


Fig. 8.2 Torque versus speed curve under load

normal torque–speed characteristics of a DC series motor. To achieve a better start-up, the torque versus speed characteristics line during start-up has to be cut off as shown by the red line.

For the DC series motor, the torque and current have a significant relationship, and this is plotted together in Fig. 8.3. Torque and current show the same pattern, but the current is on a much smaller scale. Thus, the armature current can be used instead of the torque as an input reference for the closed-loop feedback control [7].

A lookup table of the armature current versus speed [7] can be created, and this lookup table can be used as a reference as shown in Fig. 8.4 for the closed-loop feedback control of the direct current control in driving mode [7].

8.2.2 Mathematical Equation in Driving Mode

The following general equations describe the voltage and current for the chopper. Equations (8.1)–(8.3) are general equations for the motor. B_{emf} is the back emf of the motor, V_a and V_f are the armature and field voltages, K_b is the back emf constant, K_t is the torque motor constant, I_f is the field current, R_a and R_f are the motor coil resistances, I_a is the armature current, ω is the angular speed, and T_d is the motor torque [2].

$$e_g = K_{bemf} i_f \omega \quad (8.1)$$

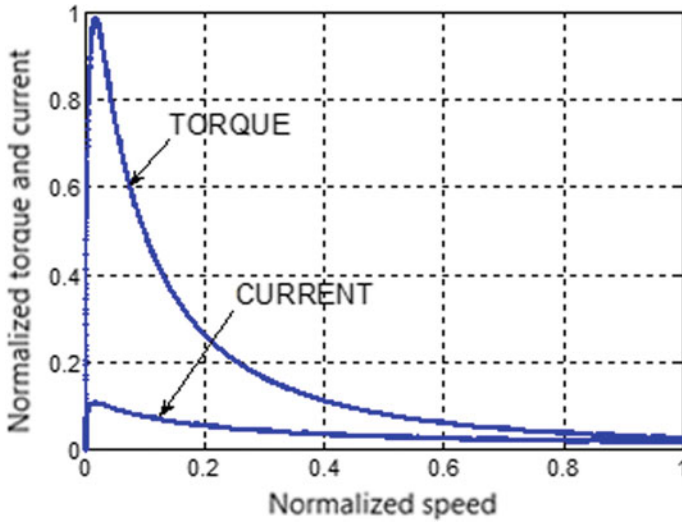


Fig. 8.3 Normalized torque and current versus normalized speed

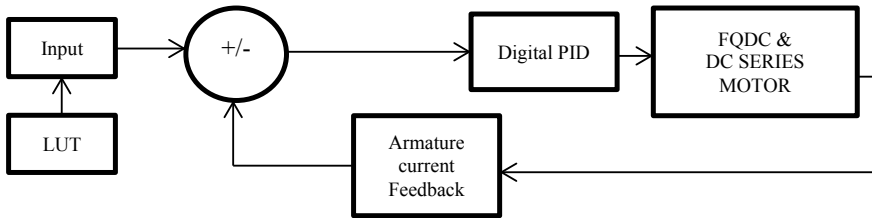


Fig. 8.4 Closed-loop feedback control of the direct current control

$$T_d = K_t i_a i_f \tag{8.2}$$

$$T_d = J \frac{d\omega}{dt} + B\omega + T_L \tag{8.3}$$

The linear differential equations are shown in Eqs. (8.4)–(8.6).

$$V_{dc} = E_g + I_a R_a + I_f R_f + (L_f + L_f) \frac{di_f}{dt} \tag{8.4}$$

$$\frac{di_f}{dt} = \frac{di_a}{dt} \tag{8.5}$$

$$\frac{d}{dt}[I_a] = \left[\frac{-(R_a+R_f)}{L_a+L_f} \right] [I_a] \left[\frac{1}{L_a+L_f} \right] [V_{\text{batt-Eg}}] \quad (8.6)$$

In driving mode, the direct current control is applied based on the armature motor current.

8.3 Methodology

8.3.1 System Stability Using Root Locus

Equations (8.1)–(8.4) are converted to a transfer function model, as shown in Eqs. (8.7)–(8.9). Equation (8.9) is equated to Eq. (8.10), and finally, the value of s is determined.

$$G_s = \frac{K}{s(S(L_f + L_a) + (R_f + R_a))} \quad (8.7)$$

In closed loop

$$T(s) = \frac{K}{s^2(L_f + L_a) + (R_f + R_a)s + K} \quad (8.8)$$

The characteristics equation is

$$s^2(L_f + L_a) + (R_f + R_a)s + K = 0 \quad (8.9)$$

Using

$$\frac{-b \pm \sqrt{b^2 - 4ac}}{2a} \quad (8.10)$$

we obtain the following solution: $s = 0, -2495.4, -4.6$.

For the root locus graph as shown in Fig. 8.5, when K is zero, it starts from 0 (more dominant than -4.6) on the right-hand side and -2500 at the left-hand side. As K increased, these two values are move to each other, and at value of 1250, whose values for $\zeta\omega_n$, they meet. As K moves further, one will be upward, and the other will be moving downward. The system is always stable.

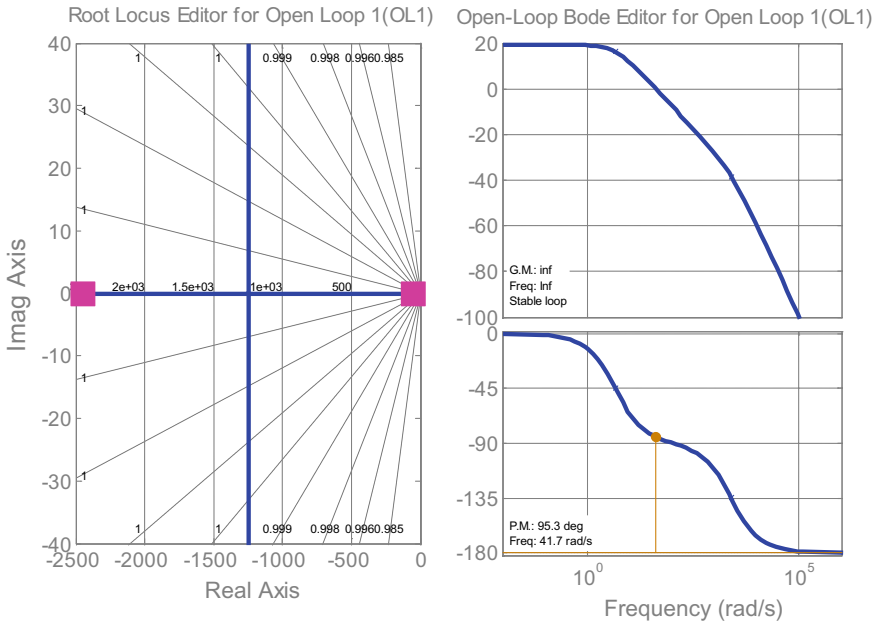


Fig. 8.5 Root locus and Bode plot

8.3.2 PID Controller

The PID controller equation is

$$K_p + \frac{K_i}{s} + K_d s = \frac{K_p s + K_i + K_d s^2}{s} \tag{8.11}$$

8.3.2.1 PI Controller

The PI algorithm can be expressed in the continuous time domain as:

$$u(t) = K_p e(t) + K_i \int_{\tau=0}^t e(\tau) d\tau \tag{8.12}$$

where $u(T)$ is the control input signal, $e(t)$ is the error signal, t is the continuous time domain, τ is the calculus variable of integration, K_p is the proportional mode control gain, K_i is the integral mode control gain.

The implementation of this algorithm in an embedded system like a microcontroller requires a transformation into the discrete time domain. The trapezoidal sum

approximation is used to transform the integral term into the discrete time domain. The proportional term does not require approximation.

$$P \text{ term: } K_p e(t) = K_p e(k)$$

$$I \text{ term: } K_i \int_{\tau=0}^t e(\tau) d\tau \cong K_i \sum_{i=0}^k \frac{h}{2} [e(i) + e(i-1)] \quad (8.13)$$

Time relationship: $t = k * h$

where h is the sampling period, k is the discrete time index: $k = 0, 1, 2, \dots$

The storage memory variable “sum” is needed to calculate the full summation in each time step, the summation is expressed as a running sum as follows

$$\text{sum}(k) = \text{sum}(k-1) + [e(k) + e(k-1)] \quad (8.14)$$

$$u(k) = K_p e(k) + K_i' \text{sum}(k) \quad (8.15)$$

8.3.3 Tuning the PID Using MATLAB/Simulink SISOTOOL

If the transfer function is loaded to the MATLAB/Simulink SISO tool with auto tuning, the PID compensator equation is given as

$$C = 2.6738e6 \times \frac{(1 + 0.38s)}{s}$$

whereby $K_p = 2.6738e6$, $z = \frac{1}{0.38}$, $z = 2.6315$, $K_i = K_p z$, $K_i = 7,036,315.7$.

The step response result of the PID controller is tuned using the SISO tool, as shown in Fig. 8.6.

The previous discussion on the PID controller modeling and control is done with an analogue/continuous system and with an analogue PID controller. However, these current days, the analogue is no longer used and replaced by the digital/discrete controller. The continuous system is considered as a discrete system if a delay is added into the circuit. Figure 8.7 shows the result when a delay is added. The result contains a steady-state error.

Fig. 8.6 Transient response closed-loop control

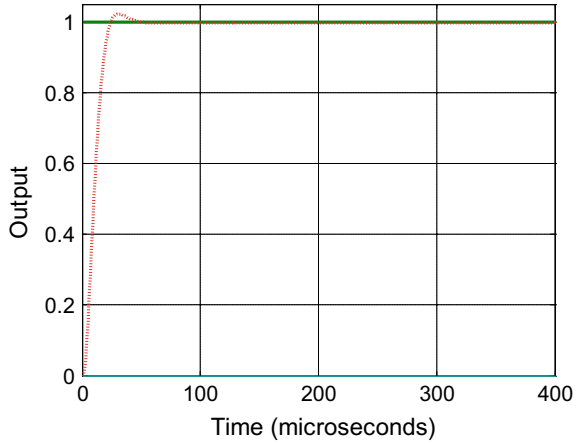
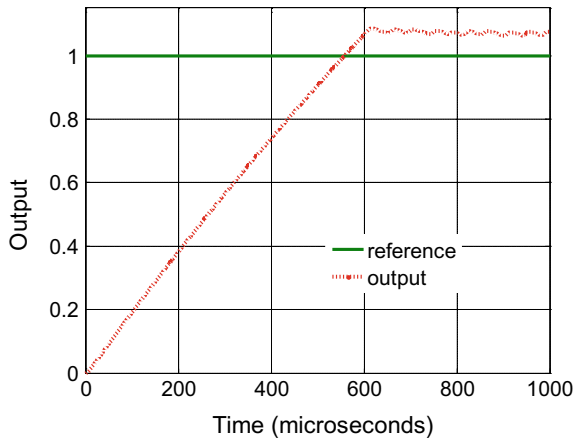


Fig. 8.7 Steady-state error closed-loop control



8.3.4 Conversion to Discrete Model

The transfer function of the armature current in the driving mode can be represented as a first-order system using the MATLAB system identification tool as the equations given below:

$$G(s) = \frac{1}{s + 167}$$

$$G(z^{-1}) = Z\{G_{\text{zoh}}(s)G(s)\} = Z\left\{\frac{1 - e^{-Ts}}{s} \frac{K}{1 + \tau_m s}\right\}$$

$$G(z^{-1}) = Z(1 - z^{-1}) \frac{\frac{K}{\tau_m}}{s\left(\frac{1}{\tau_m} + s\right)}$$

$$\begin{aligned}
 G(z^{-1}) &= K \left(\frac{z-1}{z} \right) Z \left(\frac{c}{s(c+s)} \right) \\
 G(z^{-1}) &= K \left(\frac{z-1}{z} \right) \left(\frac{z}{z-1} \right) \left(\frac{1-e^{-cT}}{z-e^{-cT}} \right) \\
 G(z^{-1}) &= K \left(\frac{1-e^{-cT}}{z-e^{-cT}} \right)
 \end{aligned}
 \tag{8.16}$$

where $c = 1/\tau_m$.

8.3.5 PID Controller Design by Pole Assignment

A PID controller can be cast in the following discrete time form.

$$u(t) = \frac{r(t)(g_0 + g_1 + g_2) - (g_0 + g_1z^{-1} + g_2z^{-2})y(t)}{1 - z^{-1}}
 \tag{8.17}$$

The coefficients g_0, g_1, g_2 are related to K_p, K_d, K_i the proportional, derivative and integral gain setting by

$$\begin{aligned}
 K_p &= -g_1 - 2g_2 \\
 K_d &= g_2 \\
 K_i &= g_0 + g_1 + g_2
 \end{aligned}$$

The closed-loop feedback of the digital PID controller and the discrete system in discrete form are shown in Fig. 8.8.

$$\begin{aligned}
 \frac{y(t)}{r(t)} &= \frac{\frac{Z^{-d}BG}{AF}}{1 + \frac{Z^{-d}BG}{AF}} \\
 \frac{y(t)}{r(t)} &= \frac{Z^{-d}BG}{AF + Z^{-d}BG}
 \end{aligned}$$

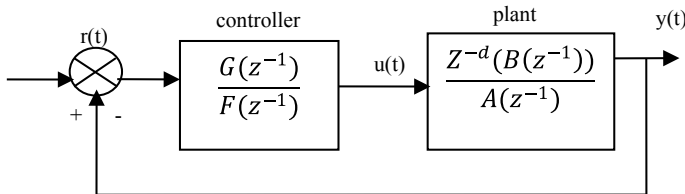


Fig. 8.8 Discrete closed-loop control

The characteristic equation is $AF + Z^{-d}BG = 0$

Let,

$$AF + Z^{-d}BG = T$$

where

$$T = 1 + t_1Z^{-1} + t_2Z^{-2} + \dots + t_nZ^{-n}$$

T = sampling time, τ_m = time constant.

Assuming $d = 0$, the controller transfer function is:

$$G_c(z^{-1}) = \frac{u(t)}{e(t)}$$

$$G_c(z^{-1}) = \frac{G}{F} = \frac{g_0 + g_1z^{-1} + g_2z^{-2}}{1 - z^{-1}} \quad (8.18)$$

$$u(t)[1 - z^{-1}] = e(t)[g_0 + g_1z^{-1} + g_2z^{-2}]$$

$$u(t) - u(t - 1) = g_0e(t) + g_1e(t - 1) + g_2e(t - 2)$$

So

$$u(t + 2) = u(t + 1)g_0e(t + 2) + g_1e(t + 1) + g_2e(t)$$

And the plant transfer function is:

$$G_p(z^{-1}) = \frac{y(t)}{u(t)}$$

$$G_p(z^{-1}) = \frac{B}{A} = \frac{b_1z^{-1}}{1 + a_1z^{-1} + a_2z^{-2}}$$

$$u(t)[b_1 - z^{-1}] = y(t)[1 + a_1z^{-1} + a_2z^{-2}]$$

$$b_1u(t - 1) = y(t) + a_1y(t - 1) + a_2y(t - 2)$$

So,

$$y(t + 2) = -a_1y(t + 1) - a_2y(t) + b_1u(t + 1)$$

Hence, $AF + BG = T$

$$1 + a_1z^{-1} + a_2z^{-2})(1 - z^{-1}) + b_1z^{-1}(g_0 + g_1z^{-1} + g_2z^{-2})$$

$$= 1 + t_1 z^{-1} + t_2 z^{-2}$$

Equating the coefficient we get,

$$g_0 = \frac{t_1 + (1 - a_1)}{b_1}$$

$$g_1 = \frac{t_2 + (a_1 - a_2)}{b_1}$$

$$g_2 = \frac{a_2}{b_1}$$

From the equation of the closed-loop system,

$$\frac{y(t)}{r(t)} = \frac{Z^{-d}BG}{AF + Z^{-d}BG}$$

Hence, $AF + BG = T$

$$(1 + a_1 z^{-1} + a_2 z^{-2})(1 - z^{-1}) + b_1 z^{-1}(g_0 + g_1 z^{-1} + g_2 z^{-2}) = 1 + t_1 z^{-1}$$

where $t_1 = \exp\left(\frac{-T}{\tau_m}\right)$

For the PID controller software programming, the value of K_p , K_i and K_d is determined by,

$$K_p = -g_1 - 2g_2$$

$$K_p = 110 = 12.24, \quad K_i = g_0 + g_1 + g_2, \quad K_i = 230$$

$$K_d = g_2, \quad K_d = 0$$

8.3.6 Simulation Model with MATLAB/Simulink

Simulation of a model using the software can monitor the result and performance of the proposed FQDC under the closed-loop feedback control. The MATLAB/Simulink and mathematical model used for studying the driving mode operation with the direct current control technique in closed-loop feedback with discrete PID controller tuning with the pole placement method is shown in Figs. 8.9 and 8.10.

The experimental hardware setup shown in Fig. 8.11 is used to verify the simulation and mathematical model.

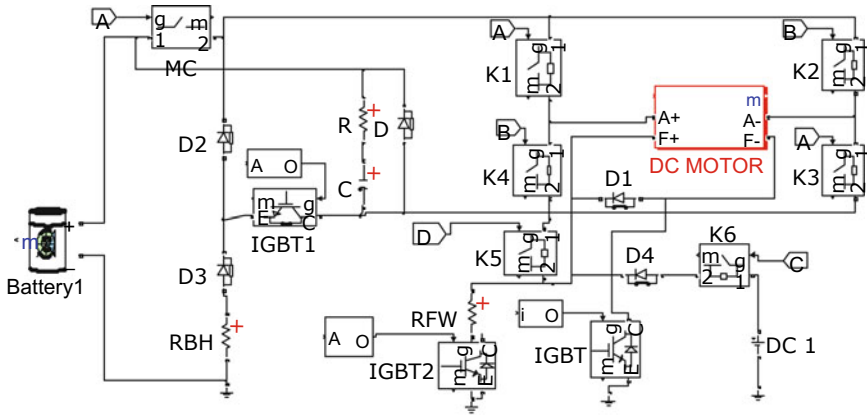


Fig. 8.9 Simulation model

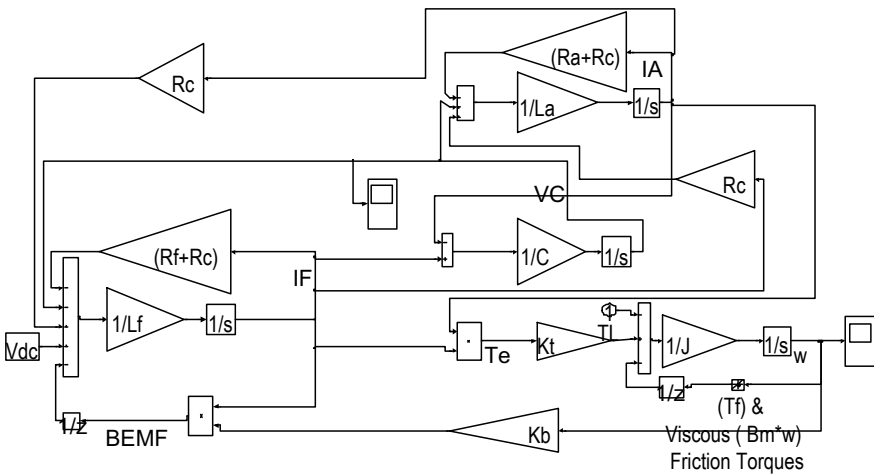


Fig. 8.10 Physical-based model of DC motor with DCC

8.4 Results and Discussion

The system was tested with a PID controller, and the first test was on the current control at a constant speed. The result is shown in Fig. 8.12.

The second test is the current control when the motor speed changes, and the result is shown in Fig. 8.13. The variation of the current (normalized) is observable. But the actual performance did not represent the DCC and PID tuned by the pole placement. It is because of the result after A/D . Thus, the result has been amplified almost twenty times.

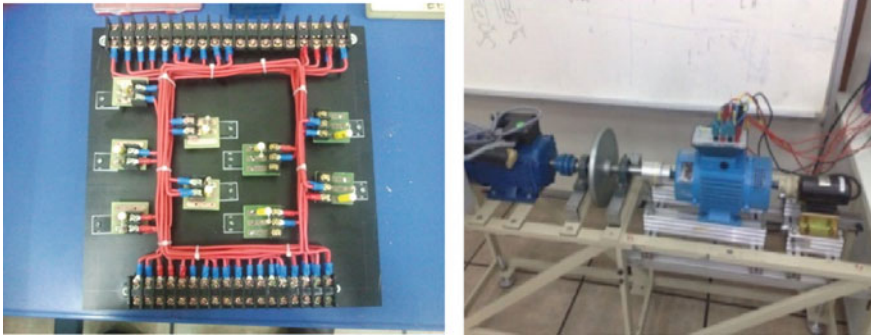


Fig. 8.11 Experimental setup

Fig. 8.12 Transient response closed-loop control

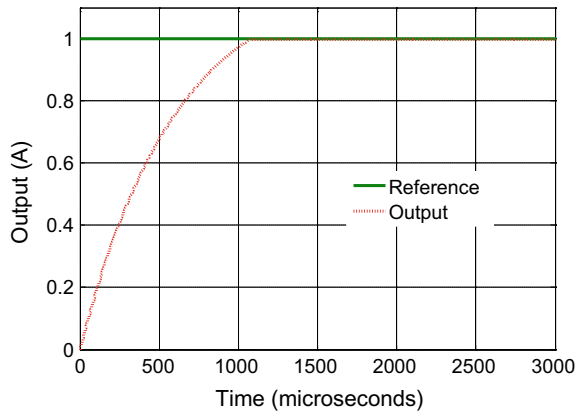
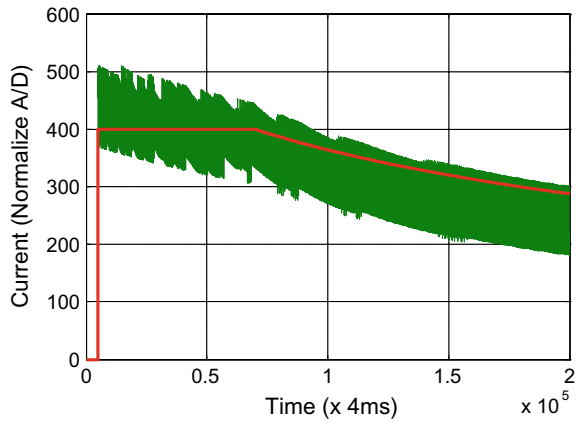


Fig. 8.13 Transient response closed-loop control of current at speed changes



A complete test of the motor speed (normalized) and current (normalized) using DCC applied is shown in Fig. 8.14. In the beginning, when the current is maintained, the motor speed increases linearly due to the DCC. But when the current is lowered, the motor speed increases slowly before reaching a final value.

A comparison through the simulation model is made to compare motor speed and current with DCC and speed control methods, as shown in Fig. 8.15. The speed control shows a rapid increase in motor speed, and this causes tire slip and the jerking effect while the DCC presents the linear increase in speed. Notice at the end the speed will be the same for both methods.

The experimental results of the DCC and feedback control tuned with pole placement are shown in Fig. 8.16. The simulation and mathematical model results are also shown for comparison purposes. It is observed that the current can be controlled as per the requirement of the DCC.

Fig. 8.14 Transient response closed-loop control of current

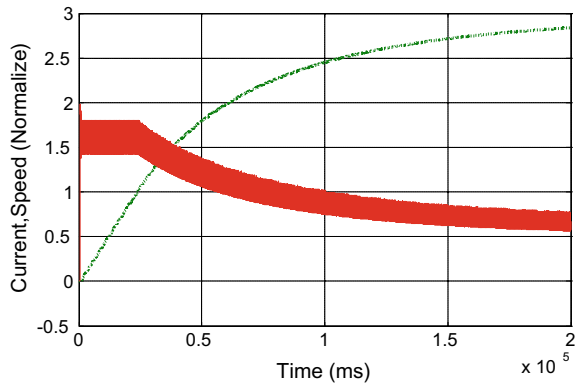


Fig. 8.15 Simulation result of speed control and DCC

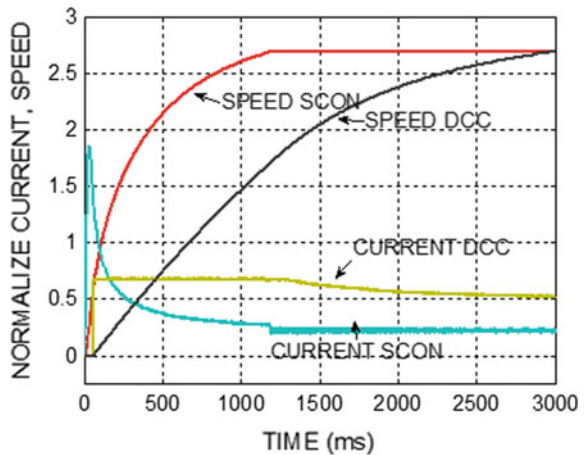
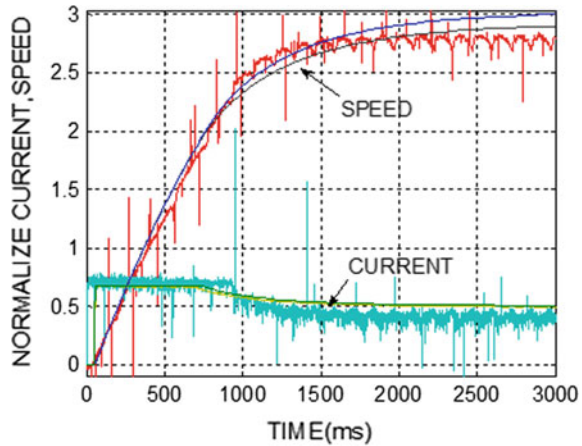


Fig. 8.16 Simulation result and experiment DCC



8.5 Conclusion

The DCC method can control the DC series motor current via FQDC chopper. The pole placement method is used to tune the digital PID for closed-loop feedback control of the current with DCC to eliminate jerking and tire slip during start-up.

References

1. Oak Ridge National Laboratory: Advanced Brush Technology for DC Motors. Available: <http://peemrc.ornl.gov/projects/emdc3.jpg> (2009)
2. Arof, S., Jalil, J.A., Yaakop, N.M., Mawby, P.A., Arof, H.: Series motor four quadrants drive DC chopper part 1: overall. In: International Conference on Power Electronics (2014)
3. Arof, S., Diyanah, N.H., Mawby, P., Arof, H., Yaakop, N.M.: Low harmonics plug-in home charging electric vehicle battery charger utilizing multi-level rectifier, zero crossing and buck chopper: part 1: general overview. In: Progress in Engineering Technology, pp. 103–108 (2019). https://doi.org/10.1007/978-3-030-28505-0_9
4. Arof, S., Diyanah, N.H.N., Noor, N.M., Jalil, J.A., Mawby, P.A., Arof, H.: A new four quadrants drive chopper for separately excited DC motor in low cost electric vehicle. In: Progress in Engineering, pp. 119–138 (2019). https://doi.org/10.1007/978-3-030-28505-0_10
5. Arof, S., Hassan, H., Rosyidi, M., Mawby, P.A., Arof, H.: Implementation of series motor four quadrants drive DC chopper for DC drive electric car and LRT via simulation model. J. Appl. Environ. Biol. Sci. 7(3S), 73–82 (2017)
6. Arof, S., Noor, N.M., Elias, F., Mawby, P.A., Arof, H.: Investigation of chopper operation of series motor four quadrants DC chopper. J. Appl. Environ. Biol. Sci. 7(3S), 49–56 (2017)
7. Arof, S., Jalil, J.A., Kamaruddin, N.H., Yaakop, N.M., Mawby, P.A., Arof, H.: Series motor four quadrants drive DC chopper part 2: driving and reverse with direct current control. In: International Conference on Power Electronics, pp. 775–780 (2016). <https://doi.org/10.1109/pecon2016.7951663>. 978-1-5090-2547-3/16
8. Arof, S., Diyanah, N.H.N., Noor, N.M.N., Radzi, M., Jalil, J.A., Mawby, P.A., Arof, H.: Series motor four quadrants drive DC chopper: part 4: generator mode. In: Progress in Engineering, pp. 155–167 (2019). https://doi.org/10.1007/978-3-030-28505-0_12

9. Arof, S., Diyanah, H.N., Yaakop, M., Mawby, P.A., Arof, H.: Processor in the loop for testing series motor four quadrants drive direct current chopper for series motor driven electric car: part 1: chopper operation modes testing. In: *Advanced Engineering for Processes and Technologies*, pp. 59–76 (2019). https://doi.org/10.1007/978-3-030-05621-6_5
10. Arof, S., Muhd Khairulzaman, A.K., Jalil, J.A., Arof, H., Mawby, P.A.: Self tuning fuzzy logic controlling chopper operation of four quadrants drive DC chopper for low cost electric vehicle. In: *6th International Conference on Intelligent Systems, Modeling and Simulation*, IEEE Computer Society, pp. 40–24 (2015)
11. Arof, S., Zaman, M.K., Jalil, J.A., MAwby, P.A., Arof, H.: Artificial intelligence controlling chopper operation of four quadrants drive DC chopper for low cost electric vehicle. *Int. J. Simul. Syst. Sci. Technol.* (2015). <https://doi.org/10.5013/ijssst.a.16.04.03>
12. Arof, S., Diyanah, N.H., Mawby, P.A., Arof, H.: Study on implementation of neural network controlling four quadrants direct current chopper: part 1: using single neural network controller with binary data output. In: *Advanced Engineering for Processes and Technologies*, pp. 37–57 (2019)
13. Arof, S., Diyanah, N.H.N., Noor, N.M., Rosyidi, M., Mawby, P.A., Arof, H.: Genetics algorithm for setting up look up table for parallel mode of new series motor four quadrants DC chopper. In: *Progress in Engineering*, pp. 155–167 (2019). https://doi.org/10.1007/978-3-030-28505-0_12

Chapter 9

Numerical Analysis of Multiphase Electrolyte Flows in an Al-Air Battery Using Smoothed Particle Hydrodynamics



Faizah Osman and Muhamad Husaini Abu Bakar

Abstract The aluminium–air (Al-air) battery is one of the demanded batteries as it is safe and efficient to power up an electronic device. However, the corrosion behaviour due to the hydrogen gas released from the aluminium anodes is a critical issue that must be considered in the Al-air battery development. This paper is aimed to establish an Al-air battery single-cell model and to simulate the hydrogen gas release by using the smoothed particle hydrodynamics (SPH) method. As a result, the pressure distribution and velocity profile inside the Al-air battery are being studied. These two measured parameters are closely significant indicators towards the corrosion behaviour. Controlling the fluid behaviour inside the Al-air battery by using the SPH method is another way to improve the performance of the battery.

Keywords Aluminium–air battery · Corrosion rate · SPH · Hydrogen gas

9.1 Introduction

The growing development of advanced electronic devices and electric vehicles (EVs) results in a great requirement for high energy density storage systems [1]. Metal–air batteries such as lithium–air (Li-air) batteries, aluminium–air (Al-air) batteries, and zinc–air batteries are considered as the most promising alternatives for the power source of EVs due to their high energy density [2]. However, the practical application of metal–air batteries is still challenging, especially in Al-air batteries. Alternatively, many strategies have been purposed and explored, which promoted the development of Al-air batteries. This is because the battery systems suffer from low voltage and specific energy, and extremely high corrosion rates under open circuit condition

F. Osman (✉) · M. H. Abu Bakar
System Engineering and Energy Laboratory, Universiti Kuala Lumpur—Malaysian Spanish
Institute, Kulim Hi-Tech Park, 09000 Kulim, Kedah, Malaysia
e-mail: faizah.osman23@s.unikl.edu.my

M. H. Abu Bakar
e-mail: muhamadhusaini@unikl.edu.my

© The Editor(s) (if applicable) and The Author(s), under exclusive license
to Springer Nature Switzerland AG 2020
M. H. Abu Bakar et al. (eds.), *Progress in Engineering Technology II*,
Advanced Structured Materials 131,
https://doi.org/10.1007/978-3-030-46036-5_9

[3]. The generated hydrogen due to corrosion in the electrolyte also decreases the potential of the battery due to abnormal chemical efficiencies of the electrolyte. Thus, it is considered as multiphase flows, and the flow behaviour during operation of the battery remains to be investigated.

One way to analyse the electrolyte flows inside the Al-air batteries is by using smoothed particle hydrodynamics (SPH). SPH is a mesh-free, Lagrangian particle method for simulating the dynamics of continuum media, such as in solid mechanics and fluid flows [4]. It is a method where the coordinates move with the fluid, which carries physical properties such as density, mass, viscosity, velocity, and pressure. It has been used due to several benefits over traditional grid-based techniques such as the finite element method and the finite volume method [5]. Recently, SPH has been used widely in solving problems related to fluid flows, especially in multiphase flows [6–8]. With numerous applications within engineering industries, there is a great interest in using this SPH method inside the battery [9].

To summarize, the electrolyte flow behaviour inside Al-air batteries plays a crucial role to determine the performance of the battery system. This paper is aimed to develop the understanding of multiphase flows between the electrolyte and hydrogen gas released from the aluminium anode. Through the numerical approach, the pressure distribution and the velocity profile of certain areas have been stimulated to ensure the smoothness of the electrolyte flow in sharp monitoring. By understanding the flow behaviour, the optimum condition for Al-air batteries can be achieved.

9.2 Methodology

9.2.1 Pre-processing

To investigate the corrosion rate and the electrolyte flow inside the Al-air battery, a setup of initial parameters is needed. A simple two-dimensional model is considered, consisting of two cathodes (blue colour), an anode (grey colour) at the centre, and two bubble columns (orange colour) immersed in sodium hydroxide electrolyte (dash lines) as shown in Fig. 9.1. The thickness for the anode, cathode, and bubble is 0.1 mm. The bubble thickness sizing is based on experimental values and equal to 0.1 mm. The hydrogen gas volume collected from the experiments [10] is reconstructed in the simulations. The results are collected at points h_1 , h_2 , and h_3 which are at heights 0.13 mm, 0.43 mm, and 0.73 mm located from the ground.

Hydrogen bubbles flow from the bottom of the tank to upwards. The flow simulation is based on the free-surface method, and the interface between the gas and liquid is moving the boundary. The behaviour of two different fluids (hydrogen gas and sodium hydroxide solution) with different physical properties is stimulated. Table 9.1 shows the physical properties for both fluids inclusive of density, isentropic factor, and surface tension.

Fig. 9.1 Simulation parameter

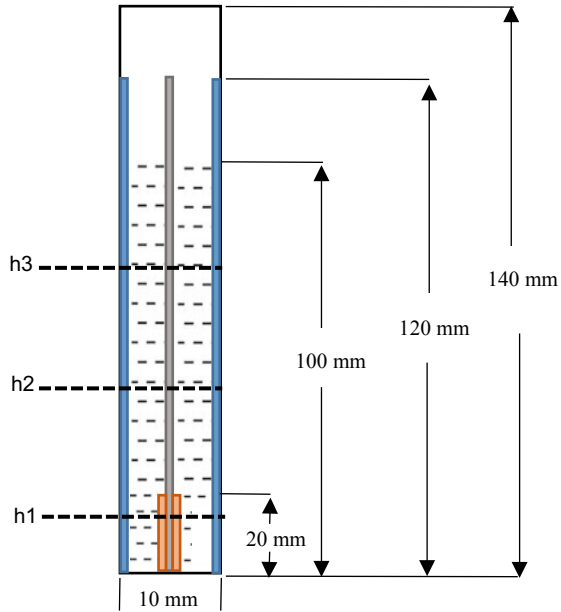


Table 9.1 Physical properties of the hydrogen gas and sodium hydroxide solution in the simulation

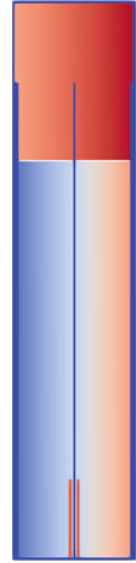
Phase	Density (kg/m ³)	Isentropic factor	Surface tension (N/m)
Sodium hydroxide solution	1515	7	0.071
Hydrogen gas	1.4	1.41	–

9.2.2 Processing

In the processing section, a program named GenCase is included to define the initial configuration of the simulation and the parameters of the execution. GenCase employs a three-dimensional Cartesian mesh to locate particles and it builds any object using particles. The mesh node around the single Al-air battery is defined. The particles are created within the mesh node of the three-dimensional Cartesian mesh.

Figure 9.2 shows a single cell of the Al-air battery that has been generated by the particles using GenCase. The *distance particle* used for this geometry is 0.0003 m or 0.3 mm, and the particles generated for this geometry are 48 788.

Fig. 9.2 Generation of a 2D Al-air battery formed by particles using GenCase



9.2.3 Post-processing

Once the simulation is finished, there are two parts that can be post-processed: the visualization part and the numerical measurement part. For the visualization part, the output files are in VTK file and the results of the simulation are plotted using the ParaView software and the velocity contour can be visualized, whereas, for the numerical measurement part, the output files are in CSV file. Files in the CSV format can be exported from programs and stored as data in tables in a spreadsheet software. In multiphase flow simulations, the pressure and velocity data for the particles are in this file.

9.3 Results and Discussion

9.3.1 Pressure Distribution

Figure 9.3 presents the pressure distribution at $h1$, $h2$, and $h3$ of a single-cell Al-air battery throughout the 3 s of simulation. The pressure distribution is given in the unit Pascal. In general, the pressure has risen significantly over the entire period at all positions. As can be seen, the $h1$ position had the highest-pressure distribution among other positions. At time 1 s, the pressure at $h1$ was 9442.67 Pa, and by time 2 and 3 s, the pressure increased to 10,087.5 and 10,545.7 Pa. It appears that the pressure continuously rose to around 500 Pa per time.

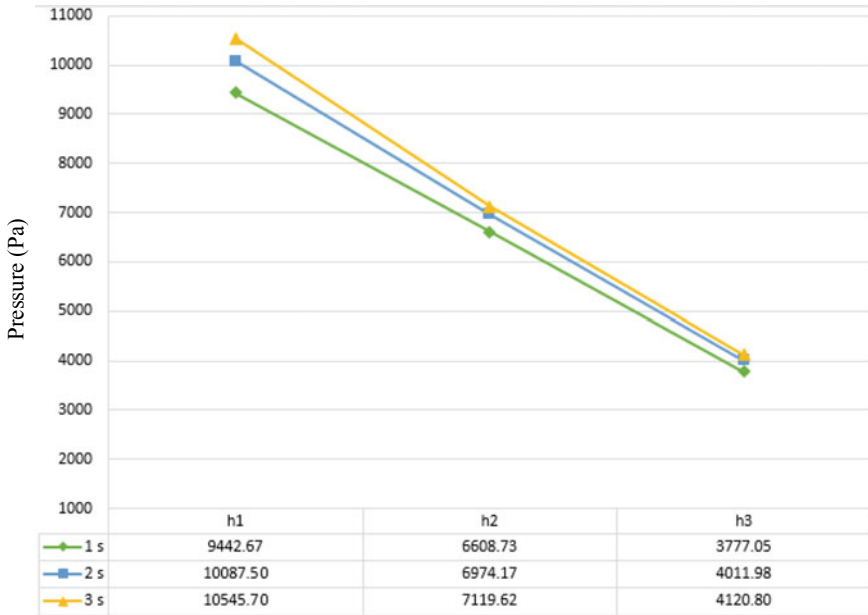


Fig. 9.3 Pressure distribution at h_1 , h_2 and h_3 for 1 s, 2 s, and 3 s

There seem to be hydrogen gas bubbles rising at h_1 from 1 to 3 s, and this affects the drag coefficient resulting in a high pressure in the observed results. On the other hand, the pressure distribution at h_2 and h_3 positions increased slowly and remains steady until the end. But the lowest increment of pressure was at h_3 position where approximately 100–200 Pa was only observed. This is because the gas holdup might not be arrived at the h_3 position yet by the time of 3 s. The system pressure increases with increasing gas holdup.

9.3.2 Velocity Profile

Figure 9.4 illustrates the velocity profile at h_1 position for 1–3 s for the Al-air battery system. At the beginning of 1 s, the velocity at 0.04 m coordinate had the lowest velocity among the other coordinates. Soon, it rose to the highest value at point 0.06 m coordinate given the value of 0.019 m/s. Shortly after, it decreased extensively at point 0.07 m.

Aside from that, at the t_2 line, the velocity begun around 0.002 m/s and started to drop at coordinate 0.03 m. At coordinate 0.04 m, the velocity showed a little bit higher value compared to the 0.03 m coordinate. The velocities at t_2 line showed the accelerated significantly started from coordinated 0.04 m. The highest pressure at 2 s line was close to 0.014 m/s.

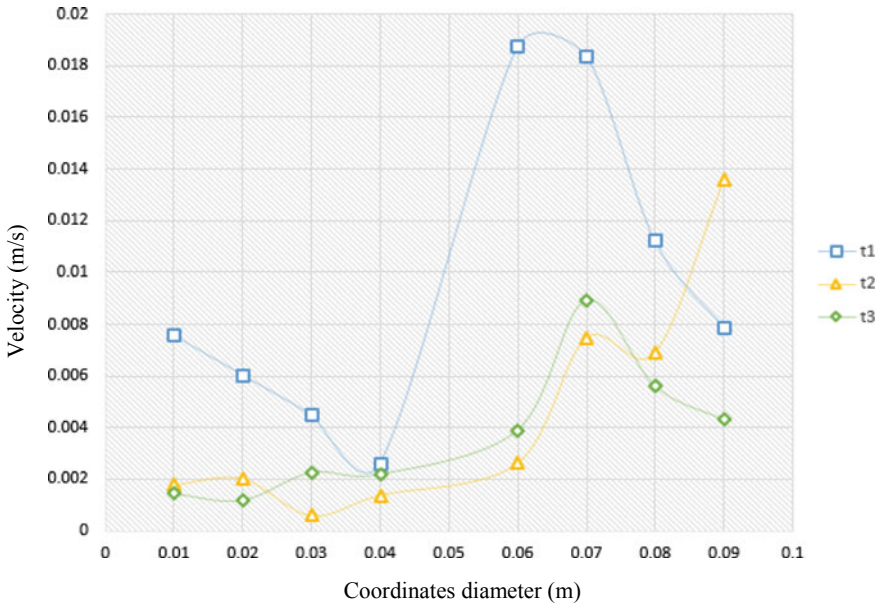


Fig. 9.4 Velocity profile at $h1$ for 1, 2, and 3 s

Besides that, initially at $t3$ line, velocities started around 0.002 m/s. At the coordinates of 0.03 m, the velocity value was approximately in the middle between the $t1$ and $t2$ lines. Later, it rose until 0.009 m/s at the 0.07 m coordinate. Eventually, it began to drop at 0.004 m/s.

Velocities at the $h2$ position for 1–3 s for the Al-air battery system are shown in Fig. 9.5. Earlier of 1 s, the velocity started at 0.01 m near 0.004 m/s. While around 0.011 m/s at the coordinates of 0.02 m, it given the highest velocities value in $t1$ line.

The highest velocity achieved was at the 0.06 m coordinate at the $t2$ line. This coordinate actually reflects the position of hydrogen gas bubbles which were near the anode. However, the 0.01 and 0.09 m coordinates were the most distant from the following hydrogen gas. Thus, this is the reason why the coordinates hold the lowest velocities in the graph.

Figure 9.6 displays velocities at the $h3$ position for 1–3 s for the Al-air battery system. In general, coordinates 0.02 and 0.08 m have the highest values compared to the other coordinates. In contrast to the $t2$ line at coordinate 0.08 m, the velocity value was low, while during 3 s time, the velocity showed roughly 0.011 m/s.

The internals caused a higher velocity at the centre of the geometry and a stronger downward flow in the region. This axial velocity produced a strong global recirculation that pulled the bubbles down near the column’s wall. Besides that, the fluctuation from the bubble rising within the sodium hydroxide electrolyte causes the velocities occasionally changing from time to time.

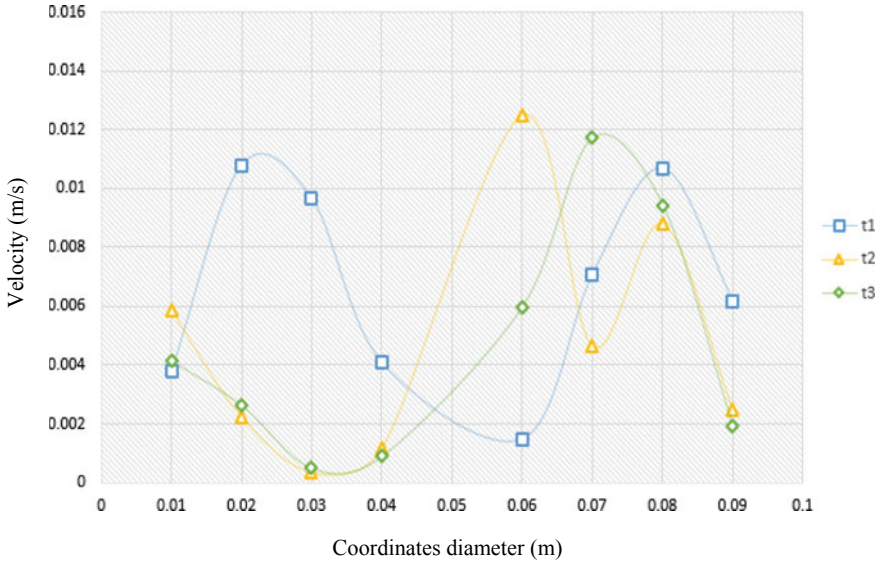


Fig. 9.5 Velocity profile at h2 for 1, 2, and 3 s

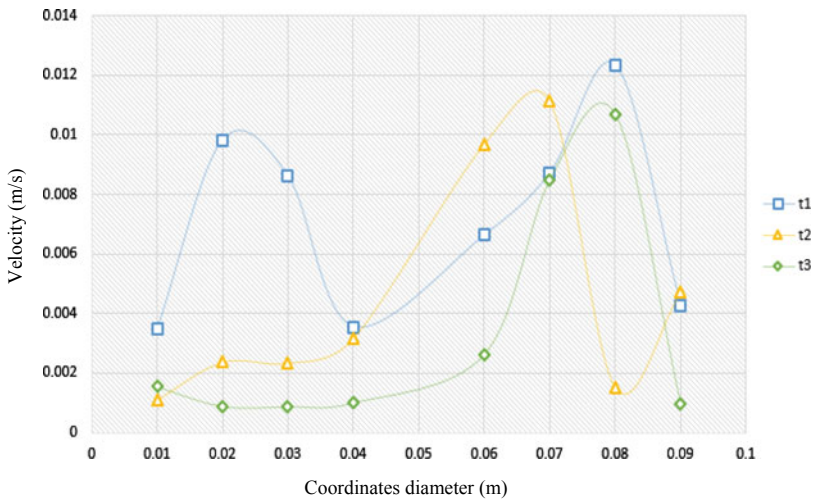


Fig. 9.6 Velocity profile at h3 for 1, 2, and 3 s

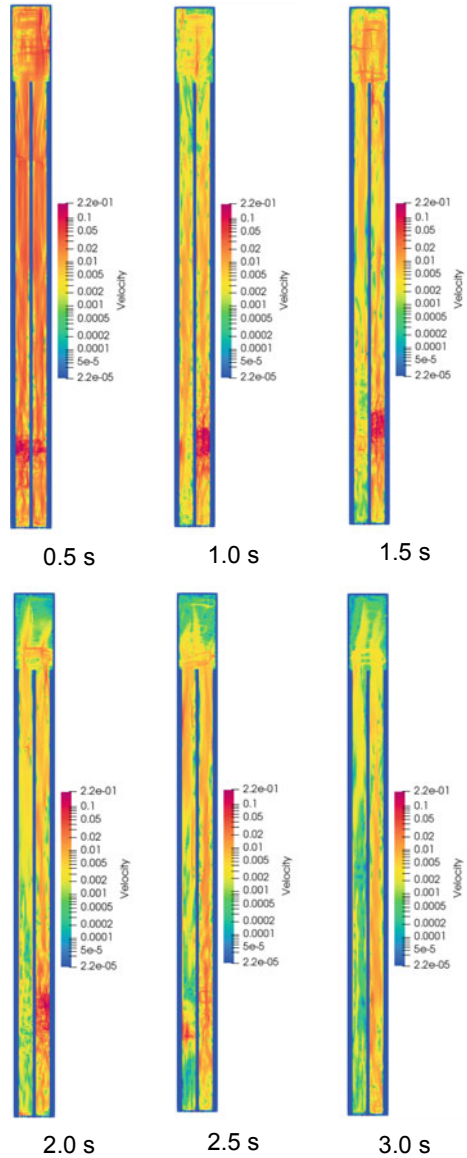
9.3.3 Velocity Contour

The velocity contour is also one of the important parameters that can be discussed in the battery. From these contours, the behaviour of the battery system can be analysed.

Velocity contours of a single-cell Al-air battery are shown in Fig. 9.7. The contours shown are from 0.5 to 3.0 s with a 0.5 s time interval.

At time 0.5 s, most of the entire battery geometry shows the red colour meaning that the velocity profile was very high among other times. By time 1 s, the velocities decreased but only certain areas had high velocity. At time 1.5 s, the velocity increases in the upper region of the battery casing. It could be explained by the fluctuation

Fig. 9.7 Velocity contour at different time



occurred at the right-hand bottom of the casing. The particles started to collide with each other and this produced the high number of pressures as stated in Fig. 9.3.

At time 2.0 s, the velocities begun to drop slowly as the bubble moved upwards. By the time 2.5 s, it begun to fade away which allowed the anode to fully do the chemical reaction with the sodium hydroxide. In 3.0 s, the battery tank slightly had the optimum moment in time to do chemical reaction without any interference of the left hydrogen bubble.

9.4 Conclusions

In conclusion, the SPH method can be used for evaluating the multiphase flows inside a single-cell Al-air battery. As far as known, the SPH method gives high accuracy in results throughout the entire process of the simulation. From this research, the pressure distribution and the velocities at three different positions in the battery casing were obtained. It can be concluded that, when the corrosion process happened, the chemical reaction between the anode and sodium hydroxide solution produced hydrogen bubbles. These bubbles will accumulate surrounding the anode surface, and the anode will have difficulties to achieve the maximum chemical reaction and this affects the battery performance.

Acknowledgements The authors gratefully acknowledge the financial support for this research work by Yayasan Tengku Abdullah Scholarship (YTAS), Universiti Kuala Lumpur Malaysian Spanish Institute (UniKL MSI) and System Engineering and Energy Laboratory (SEELab).

References

1. Wagner, F.T., Lakshmanan, B., Mathias, M.F.: Electrochemistry and the future of the automobile. *J. Phys. Chem. Lett.* (2010). <https://doi.org/10.1021/jz100553m>
2. Mokhtar, M., Talib, M.M., Majlan, E.H., et al.: Recent developments in materials for aluminum-air batteries. *J. Ind. Eng. Chem.* (2015). <https://doi.org/10.1016/j.jiec.2015.08.004>
3. Gelman, D., Shvartsev, B., Wallwater, I., et al.: An aluminum–ionic liquid interface sustaining a durable Al-air battery. *J. Power Sources.* (2017). <https://doi.org/10.1016/j.jpowsour.2017.08.014>
4. Liu, G.G.R., Liu, M.B.: Smoothed Particle Hydrodynamics: A Meshfree Particle Method (2003). <https://doi.org/10.1142/9789812564405>
5. Violeau, D., Rogers, B.D.: Smoothed particle hydrodynamics (SPH) for free-surface flows: past, present and future. *J. Hydraul. Res.* (2016). <https://doi.org/10.1080/00221686.2015.1119209>
6. Zubeldia, E.H., Fourtakas, G., Rogers, B.D., Farias, M.M.: Multi-phase SPH model for simulation of erosion and scouring by means of the shields and Drucker-Prager criteria. *Adv. Water Resour.* (2018). <https://doi.org/10.1016/j.advwatres.2018.04.011>
7. Yang, X., Kong, S.C.: Smoothed particle hydrodynamics method for evaporating multiphase flows. *Phys. Rev. E* (2017). <https://doi.org/10.1103/PhysRevE.96.033309>

8. Douillet-Grellier, T., De Vuyst, F., Calandra, H., Ricoux, P.: Simulations of intermittent two-phase flows in pipes using smoothed particle hydrodynamics. *Comput. Fluids* (2018). <https://doi.org/10.1016/j.compfluid.2018.10.004>
9. Zeng, J., Wu, W., Jiang, F.: Smoothed particle hydrodynamics prediction of effective transport coefficients of lithium-ion battery electrodes. *Solid State Ionics* (2014). <https://doi.org/10.1016/j.ssi.2014.03.016>
10. Osman, F., Harith, M.Z., Sidik, M.S.M., Bakar, M.H.A.: Development of an aluminum-air battery using T6-6061 anode as electric vehicle power source (2019). https://doi.org/10.1007/978-3-030-28505-0_19

Chapter 10

Discrete-Time Linear System of New Series Motor Four-Quadrant Drive Direct Current Chopper Numerically Represented by Taylor Series



Part 1: Driving Mode Operation

Saharul Arof, E. D. Sukiman, N. H. N. Diyanah, N. M. Noor, Emilia Noorsal, Philip Mawby, and H. Arof

Abstract This paper proposes a numerical method using Taylor series in representing a new series motor of a four-quadrant drive direct current chopper (FQDC) in driving mode operation for electric vehicle's application. The representation has three main purposes which are for troubleshooting, error correction and optimization. The Taylor series will be used to imitate the real system of a FQDC, but it is running in an embedded system such as a PIC microcontroller. Through this representation system, we can do a fault diagnose, error correction and system tuning without disturbing the

S. Arof (✉) · E. D. Sukiman · N. H. N. Diyanah · N. M. Noor
Malaysian Spanish Institute, Universiti Kuala Lumpur, Kulim Hi-Tech Park, 09000 Kulim,
Kedah, Malaysia
e-mail: saharul@unikl.edu.my

E. D. Sukiman
e-mail: edrinsukiman@gmail.com

N. H. N. Diyanah
e-mail: diyanahhisham94@gmail.com

N. M. Noor
e-mail: noramlee@unikl.edu.my

S. Arof · E. Noorsal
Faculty of Electrical Engineering, Universiti Teknologi MARA Cawangan Pulau Pinang, 13500
Permatang Pauh, Pulau Pinang, Malaysia
e-mail: emilia.noorsal@uitm.edu.my

P. Mawby
University of Warwick School of Engineering, Coventry CV47AL, UK
e-mail: p.a.mawby@warwick.ac.uk

H. Arof
Engineering Department, Universiti Malaya, Jalan Universiti, 50603 Kuala Lumpur, Malaysia
e-mail: ahamzah@um.edu.my

real system on running. Once the optimization via representation is obtained, it can be applied to the real system. The representation system using Taylor series is tested using MATLAB/Simulink. The simulation results using MATLAB/Simulink show that the Taylor series computation algorithm successfully represents the FQDC in driving mode.

Keywords Numerical method · Taylor series · DC drive · Four-quadrant chopper · System representation · EV

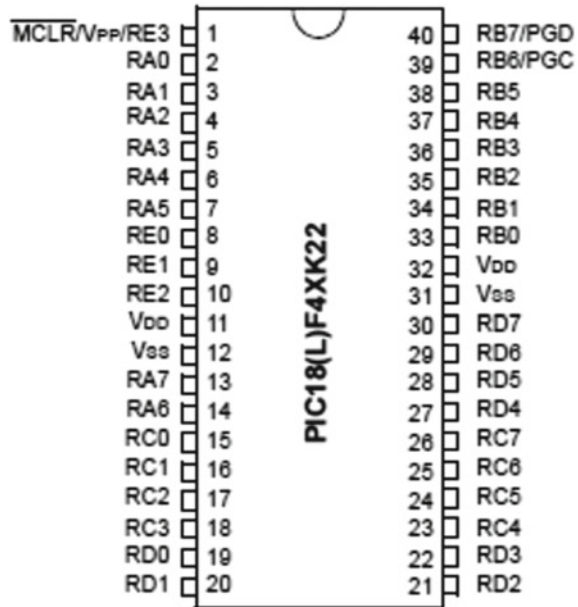
10.1 Introduction

Environmental concerns and energy issues have resulted in a massive transfer of effort in the automotive industry from an internal combustion engine (ICE) to an electric vehicle (EV) as the primary source of transport. The transportation sector generates the most significant contribution, with approximately 28.9% of greenhouse gas emissions. The effects of fossil fuels and their rising prices have increased the interest in EVs significantly. The advantages of EVs which are clean and silent technology, better efficiency and cheaper source of energy than fuel make the EVs better than ICE vehicles.

10.2 Literature Review

The Oak Ridge National Laboratory (ORNL) [1], USA in 2009, had succeeded in designing a DC-brushed motor with high-power output 55 kW, high efficiency (92%) that can operate in low-operating voltages (13 V). This development has started the interest to embark research toward DC drive EC. Attempts to improve the conventional h-Bridge chopper for series motor by an increased number of operations or to reverse rotation have been continuously carried out. But ever since the discovery of the new DC motor by the ORNL, a new series motor four-quadrant DC chopper as in Fig. 10.1, was designed, and the proposed chopper has more operations compared to the standard versions [2]. Other studies related to the DC drive EV led to the research on different types of DC drive brushed motors such as the separately excited DC motor that can be used for motor traction for DC EV [3]. A detailed investigation of the chopper operation modes led to the establishment of a simulation model to test the chopper operations for the application as an electric car and light rail transit (LRT) [4]. This simulation model led to further detailed investigations on each of the chopper operations, and on the specific pattern of the motor voltage, current, torque, speed, of the series motor and FQDC running for DC drive EC application have been continuously carried out [5]. For series motor traction of EC application, the speed and the torque control for the series motor, in an attempt to reduce jerk and tire

Fig. 10.1 PIC microcontroller



slip, have been successfully done and implemented with the direct current control technique [6]. For power regeneration, the FQDC offers the generator mode with several methods of starting the regenerated power, and the voltage control is studied and discussed in [7]. In order for the FQDC to be applied in the real world, it needs controllers running the control algorithm in the embedded system. The controller and its control algorithm are studied and tested using the processor in the loop (PIL) technique [8]. To improve the new FQDC performance, optimization tools such as artificial intelligence (AI) are introduced to control all the operations of the proposed FQDC chopper [9, 10]. Among the three AI controllers, ANFIS shows the best performance followed by a neural network and the self-tuning fuzzy logic controller. A study on the neural network controller to uncover the best method of tuning has been carried out, and the single controller with binary output has been investigated in detail [11]. On each specific FQDC chopper operation mode, the performance can be further improved using AI optimization tools such as the genetics algorithm to set up a particular lookup table for the field current in parallel mode operations [12]. Several other studies related to DC drive EV led to research on EC battery charger that offers low harmonics [13]. This battery charger uses zero cross, multilevel rectifier and buck chopper.

Black box model, online fault diagnoses, system correction and online optimization are important and crucial to the system of EVs, and this causes an increasing interest in research in system on a research study in the system representation with numerical methods. Once represented the system, which is turned to a discrete-time

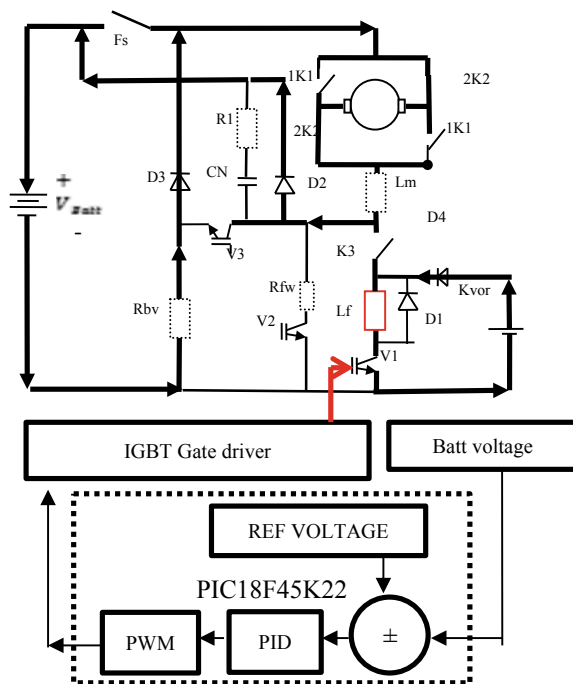
linear system, it is present as an algorithm in an embedded system such as a microcontroller as shown in Fig. 10.1. A numerical representation which imitates the real system, but running in an embedded system, allows that the system tuning can be done without disturbing the real system. Once the system optimization is obtained, the result can be applied to the real system. Fault diagnosis also can be made by comparing the imitated system and the actual/real system. For certain applications, system correction can be done by correcting the actual system using reference from the imitated system. The adjustment is done and tested in the imitated system before the final adjustment is made to the actual system. This paper intends to study the numerical representation of a series motor FQDC in driving mode operation using Taylor series in which the algorithm can be run in an embedded system such as a PIC microcontroller for DC drive electric vehicles (EVs) application.

10.2.1 FQDC in Driving Mode

In driving mode, the FQDC can be represented as a diagram in Fig. 10.2.

Equations (10.1)–(10.5) are general equations that apply to all chopper operation modes. B_{emf} is the back emf of the motor, V_a and V_f are the armature and field voltages, K_b is the back emf constant, K_t is the torque motor constant, I_f is the field

Fig. 10.2 FQDC in driving mode operation



current, R_a and R_f are the motor coil resistances, I_a is the armature current, ω is the angular speed and T_q is the motor torque.

$$B_{\text{cmf}} = K_b i_f \omega \quad (10.1)$$

$$T_q = K_t i_a i_f \quad (10.2)$$

$$T_q = j \frac{d\omega}{dt} + B\omega + T_L \quad (10.3)$$

$$V_{\text{dc}} = E_g + I_a R_a + I_f R_f + (L_f) \frac{di_f}{dt} \quad (10.4)$$

$$\frac{di_f}{dt} = \frac{di_a}{dt} \quad (10.5)$$

10.2.2 Numerical Representation

Numerical methods for the solution of differential equations have been studied since the end of the last century. A large number of integration formulas have been published especially for solving specialized systems of differential equations [14]. A numerical representation is a digital representation method that allows describing a real or unreal (2D or 3D) through a sampling of some points that discretize the initial shape into a mesh. This representation either is created on the computer or by converting preexisting work into digital work [15].

Several numerical methods can be used for the numerical solution such as the Euler method, Runge–Kutta, Taylor Series, Adams-Bashforth, Mile, etc. [16]. Each numerical formula is applied successively for solving systems of homogeneous linear differential equations with time-dependent coefficients and constant coefficients and for solving non-linear differential equations.

10.2.3 Taylor Series Numerical Solution

In mathematics, a Taylor series is a representation of a function as an infinite sum of terms which are calculated from the values of the function's derivatives at a single point. The approximation accuracy increase as the number of terms in the expansion is increasing [17, 18].

Where is this of Taylor series, Let, $\frac{dy}{dx} = f(x, y)$ be a differential equation whose solution is $y = f(x)$ and $y(x_0) = y_0$ is the initial condition. By using Taylor's series of one variable for the expansion of the function $f(x)$ at $x = x_0$, we obtain

$$f(x) = f(x_0) + \frac{(x - x_0)}{1!} f'(x_0) + \frac{(x - x_0)^2}{2!} f''(x_0) + \dots \tag{10.6}$$

Putting $x = x_1 + h$, we get the general equation as follows,

$$Y_{n+1} = y_n + \frac{h}{1!} y_n' + \frac{h^2}{2!} y_n'' + \frac{h^3}{3!} y_n''' + \dots \tag{10.7}$$

10.3 Methodology

In this paper, the Taylor series method is chosen as the most suitable method for numerical representation of the series motor of as FQDC. Even though the Runge–Kutta method is a more advanced approach to numerical integration of differential equations, this method is not suitable for linear differential equations [19]. Furthermore, the calculation method is much more complicated compared to the Taylor series method, and thus, the error estimation is not easy to compute. Equations (10.1)–(10.5) are converted into the Physical Based Model form such as shown in Fig. 10.3, and the process of the conversion is shown in Fig. 10.4.

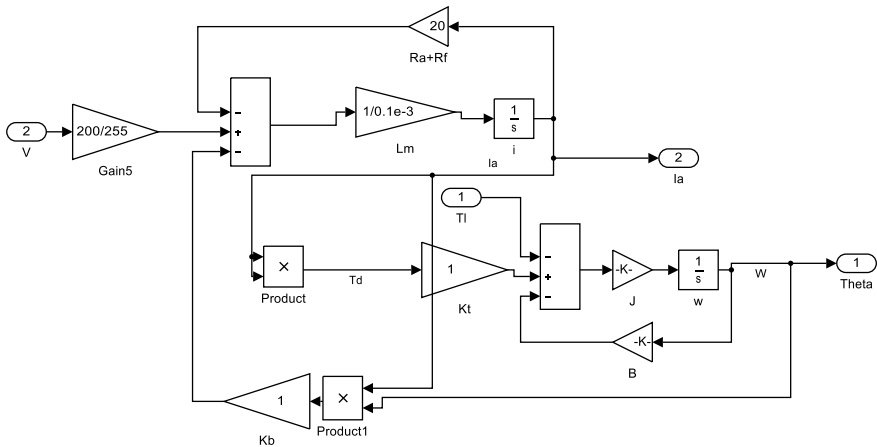


Fig. 10.3 Physical-based model of Eqs. (10.1)–(10.5)

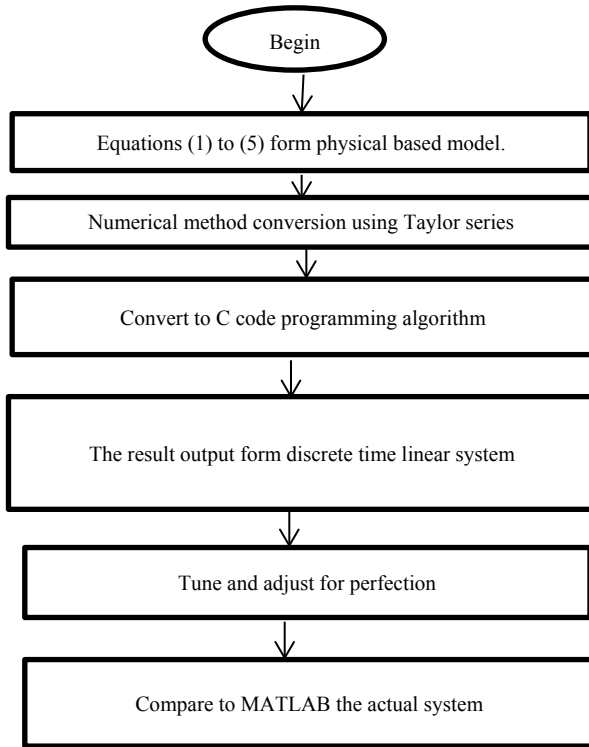


Fig. 10.4 Block diagram of the operation

10.3.1 Algorithm of Taylor Series

For the algorithm of the Taylor series method, specify the following quantities [19]:

$$x_0, x_n, y_0, h$$

where, x_0, y_0 is the initial point, x_n is the point where the solution is required and is the step length to be used in the process of the calculation. Repeat the computation of:

$$f(x_i, y_i), f'(x_i, y_i), f''(x_i, y_i) \dots \tag{10.8}$$

$$y(x_i + h) = y(x_i) + \frac{h}{1!} f'(x_i, y_i) + \frac{h^2}{2!} f''(x_i, y_i) + \frac{h^3}{3!} f'''(x_i, y_i) + \dots \tag{10.9}$$

where, $x_i = x_i + h$ until $x_i = x_n$.

The MATLAB/Simulink software with MATLAB functions is used to implement the numerical Taylor series algorithm. Equations (10.1)–(10.5) are converted to the programming algorithm. Modern compilers such as available in MATLAB/Simulink can solve mathematical equations without transforming to different algorithms. This makes easy to straight input the mathematical equation by writing them in the MATLAB function. Only Eqs. (10.3) and (10.4) need to have h values according to the Taylor series method, and the values are included in the code. The h values are determined by trial and error, and they depend on the time. Fixed variables such as the voltage supply, armature resistance, armature inductance, torque constant, the field winding resistance, field inductance and back emf constant are declared as fixed variables.

As there are (5) equations being used, the algorithm is separated into five steps or stages/state. Equation (10.4) and followed by Eq. (10.5) then Eq. (10.2), Eq. (10.3) and finally, Eq. (10.1), and the process is continued.

Equation (10.3) is for the motor angular speed, and it is transformed into

$$\omega = \omega + \left(\frac{T_d - (B_w + T_l)}{J} * h \right) \quad (10.10)$$

Equation (10.4) is for calculating the armature current, and it is transformed into

$$I_a = I_a + \left(\frac{V_{dc} - (b_{emf} + I_a R_a + I_f R_f)}{L} * h \right) \quad (10.11)$$

where ω is the angular speed and I_a is the armature current, and h is the Taylor series coefficient.

The C programming technique with “switch case” is used to perform the stages. Predetermined time interval value is included, and it has two important roles. First, it is attached to a positive edge trigger; it provides a timing sequence to execute the next instruction in this case equations. The second function is to create a delay which is functioning like a normal timer delay which is used to provide a time delay before the process moves to the next or increases the state/stages sequences. At each stage, one equation that has been transformed into an algorithm is solved. When the stage increases and stage five is reached, it turns back to state one and is continuously repeated. At each stage, one equation is solved. The solved value is carried out to the next stages. At each stage, a proper time delay can be added before the process moves to the next stage. The exact time delay is determined and implemented in the case of the imitated system, and it is used to have the same transient response as the actual system. A memory is used to store each information of back emf, speed, current, torque and state so that these values will be used in the next state or when the five sequences are over and restart these values will be used to complete a new stage.

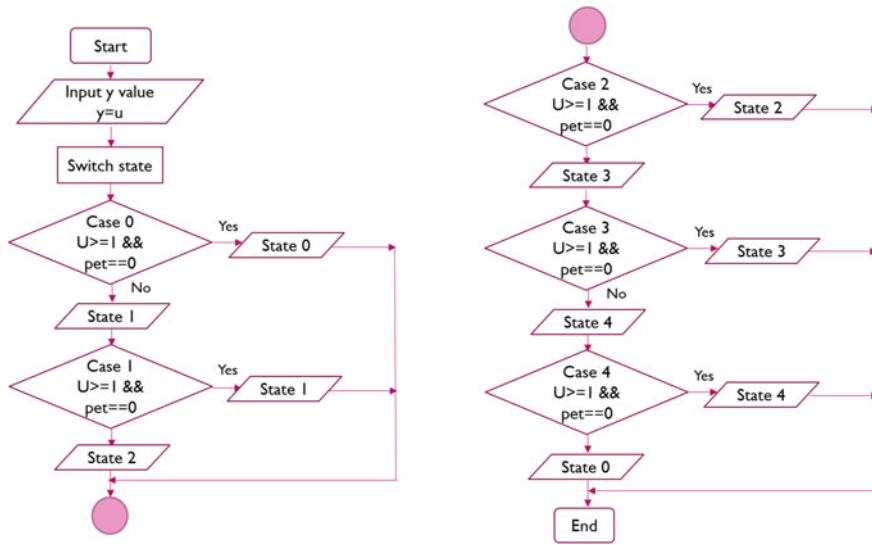


Fig. 10.5 Flow diagram

By using the switch state in the algorithm, the simulation result of the state graph is switched for every case. After the program finished stage 4, it goes back to process for state 0 again. This program flow continues as shown in Fig. 10.5. By using the numerical method of Taylor series in the program algorithm, the speed is incremented for every state until it reaches the steady state.

10.3.2 Simulation of the Model Using MATLAB/Simulink Function

A MATLAB/Simulink model using MATLAB function is used to represent the embedded system whereby Taylor’s series-based algorithm is running represents the FQDC running in driving mode. Figure 10.6 exhibits the MATLAB/Simulink simulation model.

10.4 Result and Discussion

In Fig. 10.7a, a state which represents the sequence of polling the code is shown that the state is continuously repeated. In Fig. 10.7b, the speed of the series motor is shown. The algorithm shows the transient response. The speed increases like a first-order system to the maximum speed and then remains constant. In Fig. 10.7c, the

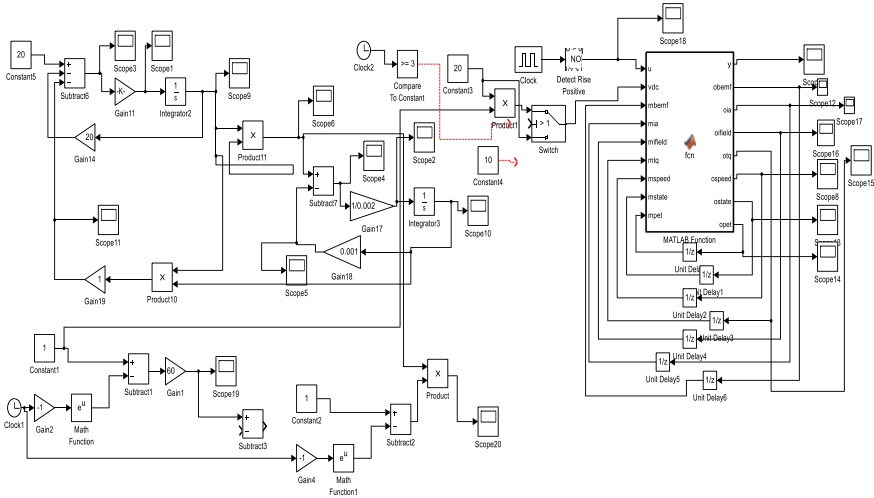


Fig. 10.6 MATLAB/Simulink simulation model

motor torque is shown. The torque is high at the beginning of the motor operation which is true for DC series motors and decreases as the back emf of the motor increases. The back emf is low at an initial lower speed of the series motor, which is the exact B_{emf} pattern of the motor as in Eq. (10.1), and then increases to the maximum at high speed and remains constant. Finally, the current or the armature and field current is shown in the figure *e* and *f*. Motor current follows the pattern of a torque which is high at the beginning and low as the speed increases due to the back emf as in Eq. (10.4). The armature and field current are the same because they are connected in series for DC series motor in a driving mode of FQDC as in Eq. (10.5).

10.5 Conclusion

The proposed numerical representation method with Taylor series has successfully imitated the DC series motor of a FQDC running in driving mode. The imitated system can be used for optimization, correction and fault diagnose of series motor FQDC in driving mode operation of an EV. The series motor and FQDC can be used as main components of DC drive EV as an alternative to AC drive EV.

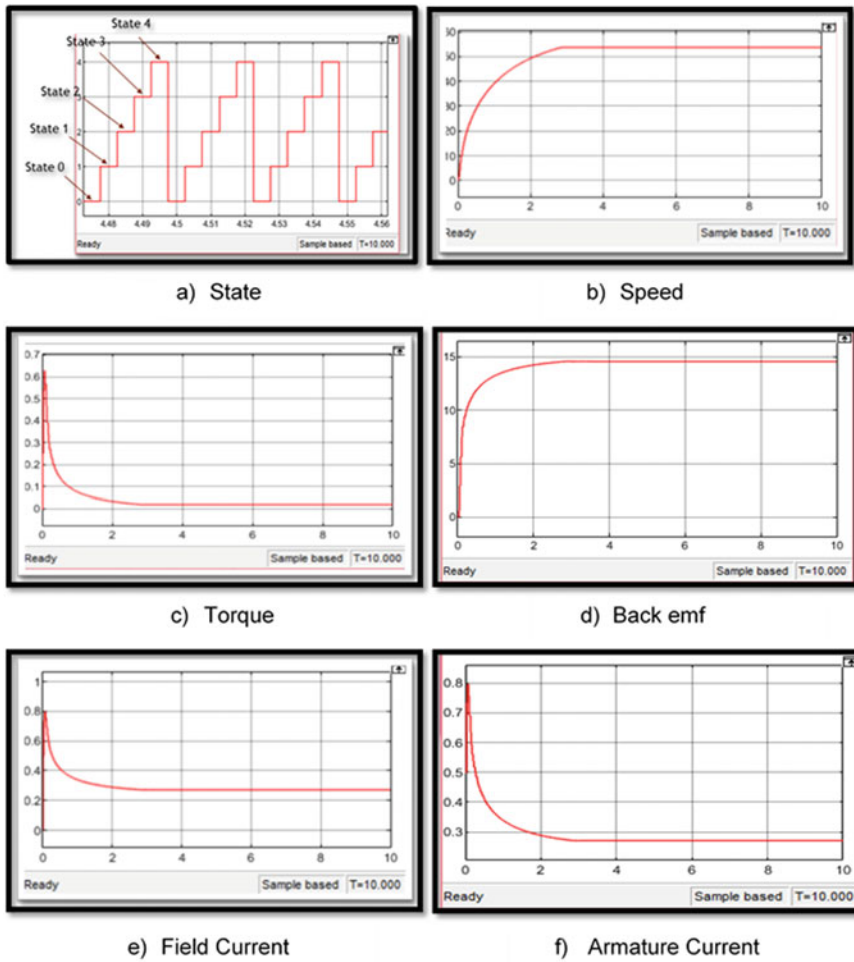


Fig. 10.7 Output of the simulation model

References

1. Oak Ridge National Laboratory: Advanced Brush Technology for DC Motors (2009). Available: <http://peemrc.ornl.gov/projects/emdc3.jpg>
2. Arof, S., Jalil, J.A., Yaakop, N.M., Mawby, P.A., Arof, H.: Series motor four quadrants drive DC chopper part 1: overall. In: International Conference on Power Electronics. IEEE, 2015 (2014)
3. Arof, S., Diyanah, N.H.N., Noor, N.M., JalilP. J.A., Mawby, A., Arof. H.: A new four quadrants drive chopper for separately excited DC motor in low cost electric vehicle. Prog. Eng. 119–138 (2019). https://doi.org/10.1007/978-3-030-28505-0_10
4. Arof, S., Hassan, H., Rosyidi, M., Mawby, P.A., Arof, H.: Implementation of Series motor four quadrants Drive dc chopper for dc drive electric car and LRT via simulation model. J. Appl. Environ. Biol. Sci., 7(3S), 73–82 (2017)

5. Arof, S., Noor, N.M., Elias, F., Mawby, P.A., Arof, H.: Investigation of chopper operation of series motor four quadrants DC chopper. *J. Appl. Environ. Biol. Sci.*, **7**(3S), 49–56 (2017)
6. Arof, S., Jalil, J.A., Kamaruddin, N.H., Yaakop, N.M., Mawby, P.A., Arof, H.: Series motor four quadrants drive DC chopper part 2: driving and reverse with direct current control. In: *International Conference on Power Electronics*, pp. 775–780 (2016). [978-1-5090-2547-3/16. https://doi.org/10.1109/pecon.2016.7951663](https://doi.org/10.1109/pecon.2016.7951663)
7. Arof, S., Diyanah, N.H.N., Noor, N.M.N., Radzi, J.M., Jalil, A., Mawby, P.A., H. Arof, H.: Series motor four quadrants drive DC chopper: Part 4: generator mode. *Prog. Eng.* 155–167 (2019). https://doi.org/10.1007/978-3-030-28505-0_12
8. Arof, S., Diyanah, N.H.N., Yaakop, M., Mawby, P.A., Arof, H.: Processor in the loop for testing series motor four quadrants drive direct current chopper for series motor driven electric car: part 1: chopper operation modes testing. *Adv. Eng. Process. Technol.* 59–76 (2019). https://doi.org/10.1007/978-3-030-05621-6_5
9. Arof, S., Muhd Khairulzaman, A.K., Jalil, J.A., Arof, H., Mawby, P.A.: Self tuning fuzzy logic controlling chopper operation of four quadrants drive DC chopper for low cost electric vehicle. In: *6th International Conference on Intelligent Systems, Modeling and Simulation*, IEEE computer Society, pp. 40–45 (2015)
10. Arof, S., Zaman, M.K., Jalil, J.A., Mawby, P.A., Arof, H.: Artificial intelligence controlling chopper operation of four quadrants drive DC chopper for low cost electric vehicle. *Int. J. Simul., Syst. Sci., Technol.* (2015). <https://doi.org/10.5013/ijssst.a.16.04.03,2015>
11. Arof, S., Diyanah, N.H., Mawby, P.A., Arof, H.: Study on implementation of neural network controlling four quadrants direct current chopper: part 1: using single neural network controller with binary data output. *Adv. Eng. Process. Technol.* 37–57 (2019)
12. Arof, S., Diyanah, N.H.N., Noor, N.M., Rosyidi, M., Mawby, P.A., Arof, H.: Genetics algorithm for setting up look up table for parallel mode of new series motor four quadrants dc chopper. *Prog. Eng.* 155–167 (2019) https://doi.org/10.1007/978-3-030-28505-0_12
13. Arof, S., Diyanah N.H.N., Mawby, P., Arof, H., Yaakop, N.M.: Low harmonics plug-in home charging electric vehicle battery charger utilizing multi-level rectifier, zero crossing and buck chopper: part 1: general overview. *Prog. Eng. Technol.* 103–108 (2019). https://doi.org/10.1007/978-3-030-28505-0_9
14. Hassan, M., Mohd, T.A.T.: Mathematical modeling and simulation of an electric vehicle. *J. Mech. Eng. Sci. (JMES)* (2015)
15. Chau, K.T., Chan, C.C., Liu, C., Lin, F.: Fault diagnosis of power components in electric vehicles. *J. Asian Electr. Veh.* **11**(2), (2013)
16. Xianjin, H., Yannan, Y., Chen, X., Jie, L., Liwei, Z.: Summarize of electric vehicle electric system fault and fault-tolerant technology. **12**(2), 1094–1099 (2014)
17. Kunovsky, J.: *Modern Taylor Series Method* (2015)
18. Nilsson, P., Shaik, A.U.R., Gangarajaiah, R., Hertz, E.: *Hardware Implementation of the Exponential Function Using Taylor Series* (2014)
19. Weirich, M.R., Paim, G., da Costa, E.A., Bampi, S.: *A Fixed-Point Natural Logarithm Approximation Hardware Design Using Taylor Series* (2018)

Chapter 11

Cooking Oil Turbidity Analysis



**Marina Borhan, Muhammad Safwan Che Ab Aziz,
Aiman Rafique Mohd Nasir, Muhamad Husaini Abu Bakar,
and Liyana Ismail**

Abstract Recycling cooking oils in daily life is a common thing to do for some people to reduce the costs. However, this habit will lead to an unhealthy lifestyle. Reheating oil undergoes a series of chemical changes such as oxidation and hydrolysis, which will produce some harmful substances that will generate lipid peroxidation that could possibly be dangerous to human health. This experiment is conducted on how to detect the turbidity of the oil by using a simple experimental setup.

Keywords Recycling cooking oil · Reheating cooking oil · Turbidity · Health

11.1 Introduction

Cooking oil is an essential product used in everyday cooking. The oil can be used in many different ways to enhance the flavor and give a particular texture on the taste. Most of the household reuse the oil to minimize wastage and reduce costs. By reheating the same oil, thermal oxidation of the cooking oil will generate free radicals and dietary consumption which results in harmful health effects [1]. The easiest way to determine is by the turbidity. Turbidity of the oil will change when the oil has been used for several times.

M. Borhan · M. S. Che Ab Aziz · A. R. Mohd Nasir · M. H. Abu Bakar · L. Ismail (✉)
System Engineering and Energy Laboratory, Universiti Kuala Lumpur Malaysian Spanish
Institute, Kulim Hi-Tech Park, 09000 Kulim, Kedah, Malaysia
e-mail: liyanaisamail@gmail.com

M. Borhan
e-mail: marina.borhan@s.unikl.edu.my

M. S. Che Ab Aziz
e-mail: msafwan.aziz@s.unikl.edu.my

A. R. Mohd Nasir
e-mail: aiman.nasir31@s.unikl.edu.my

M. H. Abu Bakar
e-mail: muhamadhusaini@unikl.edu.my

© The Editor(s) (if applicable) and The Author(s), under exclusive license
to Springer Nature Switzerland AG 2020
M. H. Abu Bakar et al. (eds.), *Progress in Engineering Technology II*,
Advanced Structured Materials 131,
https://doi.org/10.1007/978-3-030-46036-5_11

Turbidity is the non-transparency of a fluid caused by sizeable individual particles, and it is unseen to the naked eye. For example, turbidity in sunflower oil can be caused by the high-waxes, free fatty acids and minor amounts of hydrocarbons, sterols and their esters, as well as fatty alcohols [2–6]. However, in Asia palm oil is commonly used, and it contains 50% unsaturated fat and 50% saturated fat [7, 8]. Consuming repeatedly heated oil is the affect factor of atherosclerosis leading to cardiovascular diseases [8–10].

In Kuala Lumpur, Malaysia, a study had been conducted to figure out the level of knowledge, attitude and practice of night market food about the usage of repeatedly heated cooking oil. Based on the 100 respondents, the majority of respondents had only limited (53%) or small (18%) level of knowledge regarding this issue [11].

11.2 Experimental

11.2.1 *Cooking Oil*

In this experiment, there were three sets of cooking oil that were used (Fig. 11.1). The oil that never had been used, oil that has been used for the first time (see Fig. 11.2)

Fig. 11.1 New oil



Fig. 11.2 Oil that has been used for the first time





Fig. 11.3 Oil has been used three times

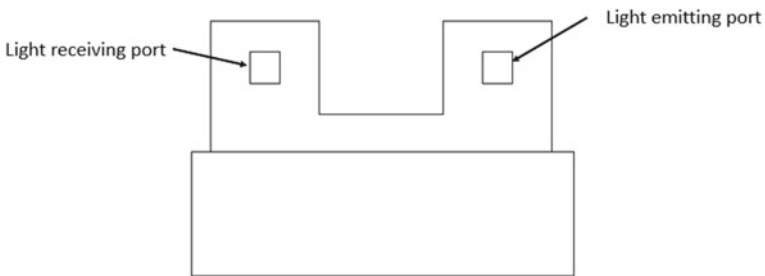


Fig. 11.4 Turbidity sensor diagram

and oil that has been used three times (see Fig. 11.3). The turbidity sensor was put in the oil, and the measurement was taken.

11.2.2 Turbidity Sensor

A turbidity sensor is used to determine the concentration of suspended particles in a sample by checking the incident light scattered from the sample, see Figs. 11.4 and 11.5. The dispersed light will be picked up by a photodiode and will be converted to turbidity.

11.2.3 NodeMCU

NodeMCU is an open-source IoT platform (see Fig. 11.6) which includes firmware that runs on the ESP8266 Wi-Fi SoC. It is used to receive the data from the turbidity sensor, display it on the LCD screen and send the data via Wi-Fi to the ThingSpeak.

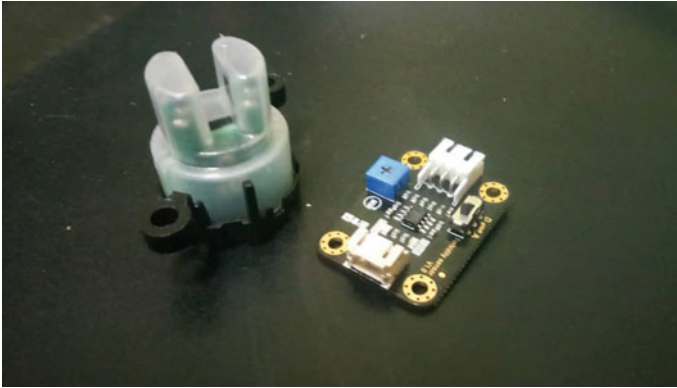


Fig. 11.5 Turbidity sensor and its adapter

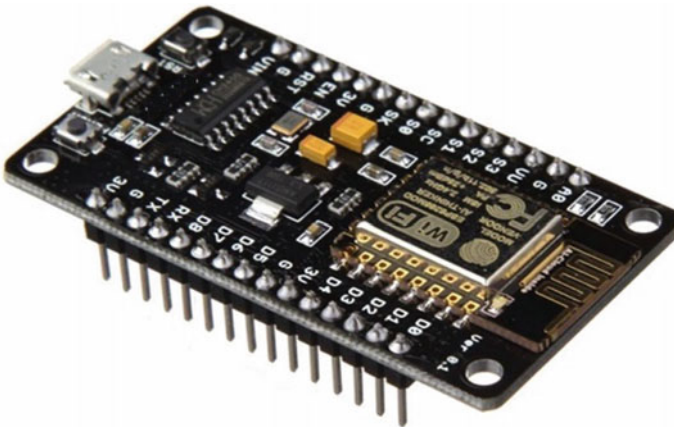


Fig. 11.6 NodeMCU

11.2.4 Serial I2C LCD Display Adapter

The serial I2C LCD display adapter is used (see Fig. 11.7) because only a fewer pin would be needed with a regular 16×2 LCD display which is VCC, GND, SDA and SCL. The contrast of the LCD can be adjusted via the on-board potentiometer and the backlight can be turned on or off via a jumper wire. The adapter is connected to the LCD display, and it will display the value of the measured turbidity, see Fig. 11.8.

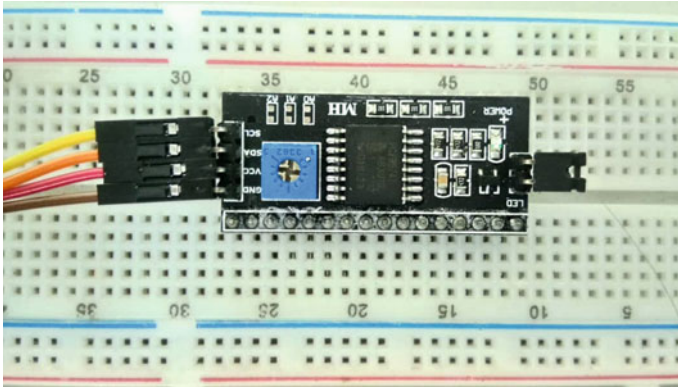


Fig. 11.7 Serial I2C LCD display adapter



Fig. 11.8 LCD display

11.2.5 ThingSpeak

In this project, ThingSpeak is used to visualize live data streams in the cloud. The data that has been captured by the sensor will be sent to the ThingSpeak via NodeMCU, see Fig. 11.9.

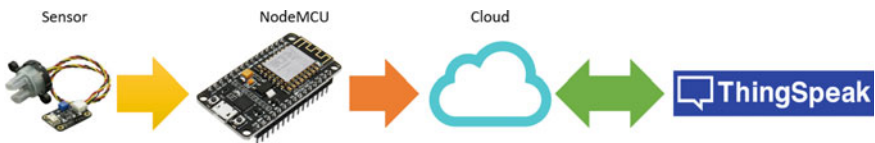
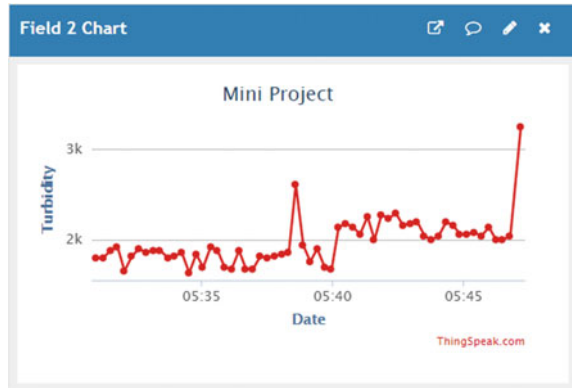


Fig. 11.9 Connection of the sensor to the ThingSpeak channel

Fig. 11.10 Turbidity result

11.3 Results and Discussion

In this experiment, three cooking oil samples have been taken. The results have shown that the turbidity value of the cooking oil increases when the oil is used repeatedly. Cooking oil that has never been used gives the reading of 1000 NTU and below 2000 NTU. The number is increasing to 2000 NTU as the oil has been used for the first time, and it increases rapidly as the oil is used three times (Fig. 11.10).

11.4 Conclusions

The usage of recycled cooking oil has shown that the quality of oil turbidity will change by the time it has been used. Other than that, the viscosity of the oil also changes as the color starts to turn dark. By conducting this experiment, it can help to spread awareness regarding the habit of using recycled cooking oil.

Acknowledgements The authors would like to thank the System Engineering and Energy Laboratory (SEELab).

References

1. Venkata, R.P., Subramanyam, R.: Evaluation of the deleterious health effects of consumption of repeatedly heated vegetable oil (2016). <https://doi.org/10.1016/j.toxrep.2016.08.003>
2. Leibovitz, Z., Ruckenstein, C.: Winterization of sunflower oil (1984). <https://doi.org/10.1007/BF02542153>
3. Bianchi, G., Avato, P.: Surfaces waxes from grain, leaves and husks of maize. *Cereal Chem.* **61**, 45–47 (1984)
4. Hu, X., Daun, J.K., Scarth, R.: Characterization of wax sediments in refined canola oils (1993). <https://doi.org/10.1007/BF02542589>

5. Przybylski, R., Biliaderis, C.G., Eskin, N.A.M.: Formation and partial characterization of canola oil sediment (1993). <https://doi.org/10.1007/BF02543028>
6. Baltanás, M.A., Molina, H., Silva, C.: Rapid methods for predicting the appearance of turbidity in sunflower oil and their comparison with cold tests (1998). <https://doi.org/10.1007/s11746-998-0054-3>
7. Dutta, A., Dutta S.K.: Vitamin E and its role in the prevention of atherosclerosis and carcinogenesis: a review (2013). <https://doi.org/10.1080/07315724.2003.10719302>
8. Xian, T.K., et al.: Reheated palm oil consumption and risk of atherosclerosis : evidence at ultrastructural level (2012). <https://doi.org/10.1155/2012/828170>
9. Odia, O.J., Ofori, S., Maduka, O.: Palm oil and the heart: a review (2015). <https://doi.org/10.4330/wjc.v7.i3.144>
10. Adam, S.K., Das, S., Jaarin, K.: A detailed microscopic study of the changes in the aorta of experimental model of postmenopausal rats fed with repeatedly heated palm oil (2009). <https://doi.org/10.1111/j.1365-2613.2009.00658.x>
11. Azman, A., et al.: Level of knowledge, attitude and practice of night market food outlet operators in Kuala Lumpur regarding the usage of repeatedly heated cooking oil. *Med. J. Malaysia* **67**, 91–101 (2012)

Chapter 12

Series Motor Four-Quadrant Direct Current Chopper: Reverse Mode, Steering Position Control with Double-Circle Path Tracking and Control for Autonomous Reverse Parking of Direct Current Drive Electric Car



Saharul Arof, M. S. Said, N. H. N. Diyanah, N. M. Noor, N. M. Yaakop, Philip Mawby, H. Arof, and Emilia Noorsal

Abstract This paper focused on the steering position control for automatic reverse parking of a direct current (DC) drive electric car. The steering position control was integrated into a vehicle cornering algorithm using a two-turn/double-circle concept. The control technique was simulated using MATLAB/Simulink; the results showed that the technique successfully met the objective of steering position control for

S. Arof (✉) · M. S. Said · N. H. N. Diyanah · N. M. Noor · N. M. Yaakop
Universiti Kuala Lumpur Malaysian Spanish Institute, Kulim Hi-Tech Park, 09000 Kulim, Kedah, Malaysia
e-mail: saharul@unikl.edu.my

M. S. Said
e-mail: msazali@unikl.edu.my

N. H. N. Diyanah
e-mail: diyanahhisham94@gmail.com

N. M. Noor
e-mail: noramlee@unikl.edu.my

S. Arof · P. Mawby
University of Warwick School of Engineering, Coventry CV47AL, UK
e-mail: p.a.mawby@warwick.ac.uk

H. Arof
Engineering Department, Universiti Malaya, Jalan Universiti, 50603 Kuala Lumpur, Malaysia
e-mail: ahamzah@um.edu.my

E. Noorsal
Faculty of Electrical Engineering, Universiti Teknologi MARA Cawangan Pulau Pinang, 13500 Permatang Pau, Pulau Pinang, Malaysia
e-mail: emilia.noorsal@uitm.edu.my

reverse parking. Therefore, it is suitable to be implemented in an autonomous DC drive electric car.

Keywords DC drive · Reverse parking · Steering control · Double circle · Four quadrants DC chopper · Series motor · Position and speed · Torque control · EV

12.1 Introduction

One of the primary reasons for the introduction of electric cars into the market is the concern due to greenhouse gas emission and its contribution to global warming. The purpose of creating electric cars that reduce or eliminate exhaust emissions is to help combat this issue [1]. Unfortunately, the price of electric vehicle (EV) and hybrid electric vehicle (HEV) is expensive, making them unattainable to many people, especially those living in poor countries. This has led to the study on the possibility for direct current drive EV [1], which is known to be economical.

12.1.1 Literature Review

The study on DC drive EV includes the design of new DC motors, low harmonics EV battery charger and four-quadrant chopper to improve the performance and extend its capability, such as by adding the mode of chopper operations, as shown in Fig. 12.1 [1–4]. Further investigation of four-quadrant DC chopper (FQDC) hardware and simulation model includes the feedback control using direct current control and optimisation using artificial intelligence (AI) to optimise all operations to works as complete electric vehicle (EV) while running in different earth profiles [5–13].

12.1.2 Automatic Parking Review

Automatic parking is important when a vehicle driver happens to deal with environmental constraints, whereby higher attention and skills are required [14, 15]. To carry out automatic parking, it requires a coordinated control of the steering angle and the surrounding to avoid collision [16]. The parking assistance system has been developed using image assistance by Mercedes, Volvo, and BMW. A particular drawback is the current technology which captures an image signal influenced by the environmental brightness. A commercial version of automatic parking assistance was first introduced by Toyota Motor Corporation during their production of the Toyota Prius in 2004. Similarly, Lexus 2007 LS also has the Advanced Parking Guidance System.

Automatic parking consists of parking trajectory, vehicle location detection, parking space detection, turning, and reverse position control [17, 18]. The parking space

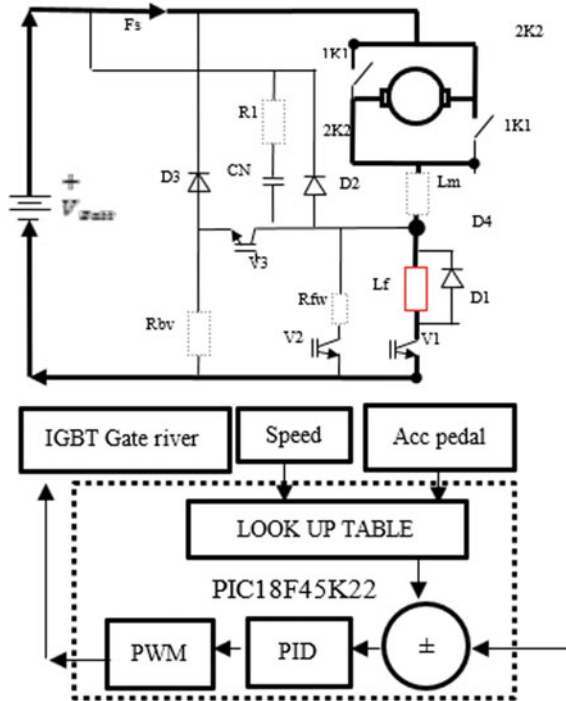


Fig. 12.1 Current paths in reverse mode

detection is used to check the availability of the space for parking, whereby such details are not included in this paper.

12.1.3 Electric Power Steering

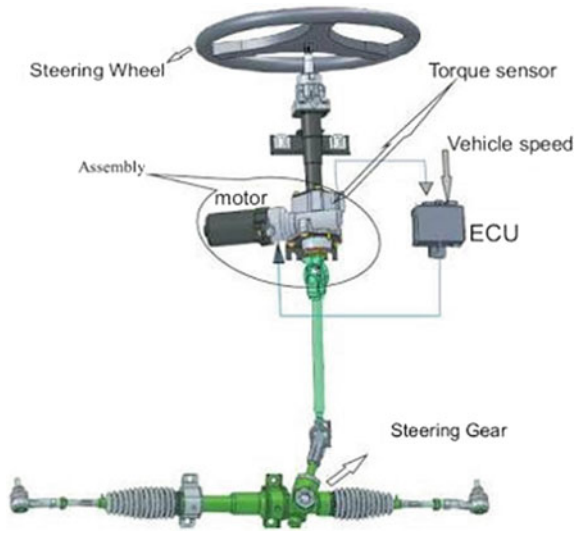
Electric power steering (EPS) is composed of a motor, steering angle/encoder, reduction gear, a rack and pinion mechanism, and power controller to drive the motor as shown in Fig. 12.2 [18]. When operated, the electric motor can turn the wheel in the direction of left, right, clockwise, or counterclockwise, causing the vehicle to turn left and or right [18].

The mathematical model for the DC motor for power steering can be summarised as:

$$I_m = \frac{V_{batt} - I_m(R_m) - B_{emf}}{L_m} \tag{12.1}$$

$$B_{emf} = K_v I_m \omega \tag{12.2}$$

Fig. 12.2 Complete electrical power steering



$$T_d = K_t I_m \quad (12.3)$$

$$T_d = J \frac{d\omega}{dt} + B_w + T_L \quad (12.4)$$

The mathematical equations for EPS are:

$$T_i - K_t(\vartheta_{sw} - \vartheta_{sc}) - B_{sw}\dot{\vartheta}_{sw} = J_{sw}\ddot{\vartheta}_{sw} \quad (12.5)$$

$$T_{mn} - T_f - B_{sc}\dot{\vartheta}_{sc} + K_t(\vartheta_{sw} - \vartheta_{sc}) - K_r\left(\vartheta_{sc} - \frac{x_r}{r}\right) = J_{sc}\ddot{\vartheta}_{sc} \quad (12.6)$$

$$\frac{k_r}{r}\left(\vartheta_{sc} - \frac{x_r}{r}\right) - F_r - b_r\dot{x}_r = m_r\ddot{x}_r \quad (12.7)$$

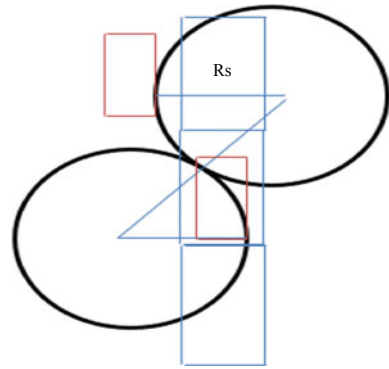
T_i is the input torque on the steering wheel, K_t is the stiffness of the torsion bar, and J_{sw} and B_{sw} are the steering wheel angle and the steering column angle, respectively.

T_{mn} and T_f are the electromagnetic drive and the friction torque on the steering column, while J_{sc} and B_{sc} are the inertia and damping constant of the steering column.

k_r is the stiffness between the rack and pinion, x_r is the displacement of the rack, and r is the stroke ratio. The angle of the pinion is equal to the column angle. F_r is the alignment force on the rack.

Once space has been identified, the minimum turning radius to fit the parking space is determined next.

Fig. 12.3 The first and second circle for the beginning and end journey of the vehicle



$$R_s = \frac{(l^2) - 2R_{min}(w) + (w)^2}{2(w)} \quad (12.8)$$

where R_s is the turning radius of the first turn, R_{min} is the minimum turning radius, L is the longitudinal length, and W is the lateral width for parking. R is also dependent on the length of the vehicle, and the width and distance of the vehicle's back tire(s) next to already parked vehicles, as shown in Fig. 12.3 [16].

12.1.4 Path Tracking

The steering turning to the left, right or centre direction determines the vehicle's turning movement. If the steering is turned to the left or right and then maintained, it causes the vehicle to move to the left or right in a circular movement. Meanwhile, the steering turned to the centre point results in the vehicle making a straight path movement. Path tracking is the process of calculating the curvature that will take the vehicle movement from its position to a goal position. A circle is defined in such a way that it passes through both the goal point and the current vehicle position. Finally, a control algorithm chooses a steering angle in relation to this circle [15, 16].

The vehicle position is calculated simply based on the accumulation of the travelled distance for wheel as per Eqs. (12.5) and (12.6).

$$X_r = X_o + l \cos(\theta) \quad (12.9)$$

$$Y_r = Y_o + l \sin(\theta) \quad (12.10)$$

where X_r and Y_r are the current positions and X_o and Y_o are the last positions. L is the distance traversed and θ is the yaw angle.

The vehicle coordinate system is defined wherein the x -axis is in a forward direction of the vehicle and the y -axis forms a right-handed coordinate system. All coordinates used must first be transformed to vehicle coordinates in order for the algorithm to work properly. The transformation involves conversion of the coordinates located in one system into its representation in another system.

Let X_r and Y_r be the current position of the vehicle, and X_g and Y_g is the goal point to be converted into vehicle coordinates. Then;

$$Y_{gv} = (X_g - X_r) \cos(-\theta) - (Y_g - Y_r) \sin(-\theta) \quad (12.11)$$

$$X_{gv} = (X_g - X_r) \cos(-\theta) + (Y_g - Y_r) \sin(-\theta) \quad (12.12)$$

where (X_{gv}, Y_{gv}) is the goal point in vehicle coordinates and θ is the current vehicle heading. In the Eq. (12.13), D is defined as to look ahead distance and Δy is the offset of the goal point from the origin. The required curvature of the vehicle is computed by:

$$\gamma_r = \frac{2\Delta y}{D^2} \quad (12.13)$$

12.2 Methodology

There are two required movements in automatic parking, which are the vehicle movement (in reverse mode) and the steering angle movement. For parallel/side and reverse automatic parking, the steering angle was controlled to a certain angle position using the two-circle turn concept. Then, the vehicle was reversed while torque and speed of the vehicle were controlled. For parallel parking, the steering angle must be turned to three positions, while for reverse parking, the steering only required two steering positions. The steering was in position zero or neutral at the beginning. This neutral position caused straight movement if the vehicle was moved by the propulsion motor. The first steering movement is shown in Fig. 12.4.

When the steering position movement was completed, the propulsion motor of the EV caused the vehicle movement to be in the position as in Fig. 12.5 with black colour line.

Once the first steering movement and vehicle movement were completed, the second steering movement or position should be undertaken as shown in Fig. 12.6. Notice the movement is moving towards the negative side.

The second steering movement, if followed by the vehicle movement, will result in the outcome as shown in Fig. 12.7.

If a combination is made, the vehicle movement is shown in Fig. 12.8.

Fig. 12.4 Steering angle during parallel parking first turn

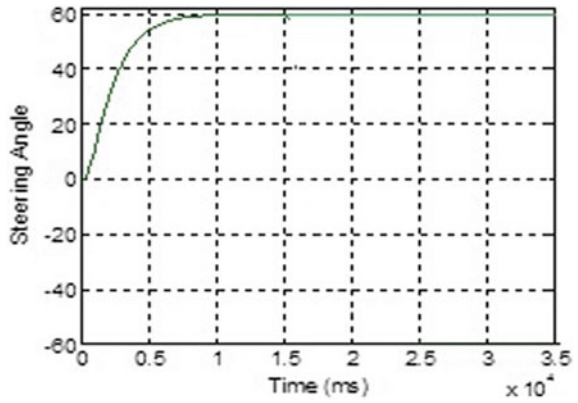


Fig. 12.5 Vehicle movement for the first steering movement

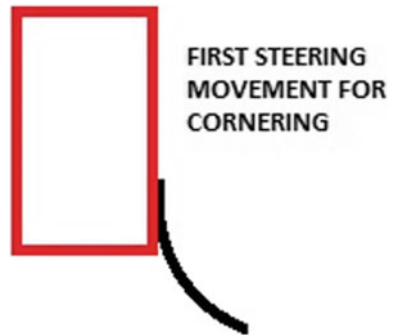


Fig. 12.6 Steering position during parallel parking

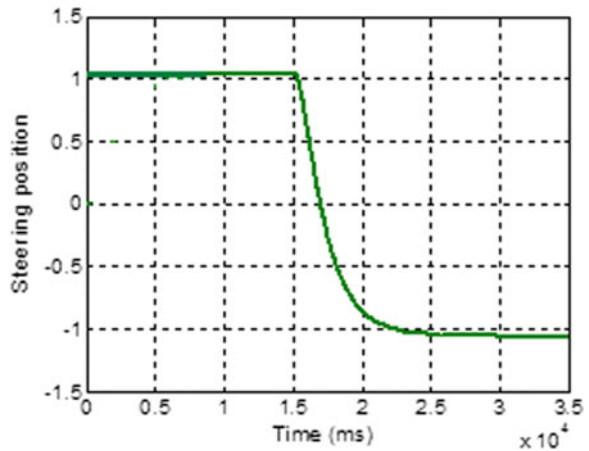
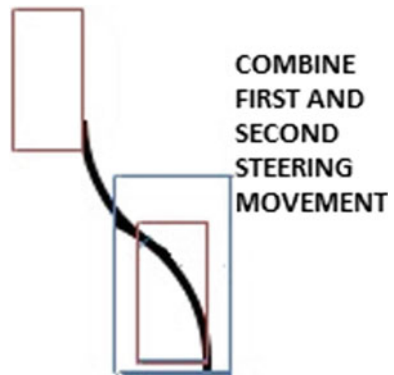


Fig. 12.7 Vehicle movement after the second steering position during parallel parking



Fig. 12.8 Combined vehicle movement



Once this movement was completed, steering was required to be placed at the neutral position identical to the beginning. Figure 12.9 demonstrates the action. No. 3 in the graph indicates the back to neutral action.

The combinations of vehicle movement and steering movement are shown in Fig. 12.10. Meanwhile, Fig. 12.11 shows a combination of steering and vehicle movement signals.

To successfully carry out automatic reverse parking, it requires a combination of steering movement, vehicle movement, and brake action. However, the vehicle movement and brake action were not discussed in detail within this paper. The overall action depicting the combinations of vehicle movement, steering movement, and brake action is shown in Fig. 12.11.

12.2.1 Position Control of Steering

The proportional integral derivate (PID) controller is used for position control of the vehicle steering. The steering angular position can be obtained by the integration of the mathematical Eq. (12.4), which results in an angular speed. To obtain the angular

Fig. 12.9 Steering movement

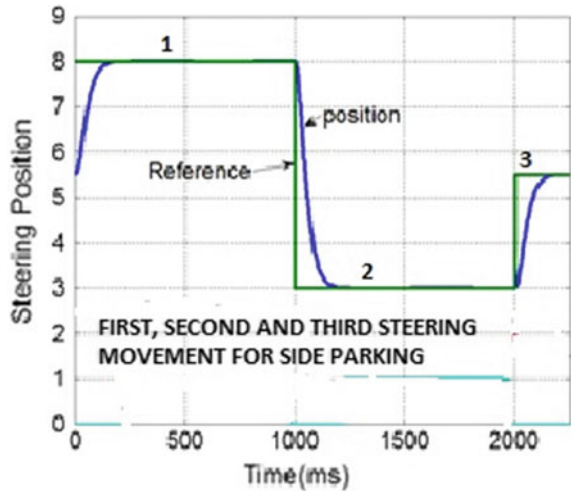
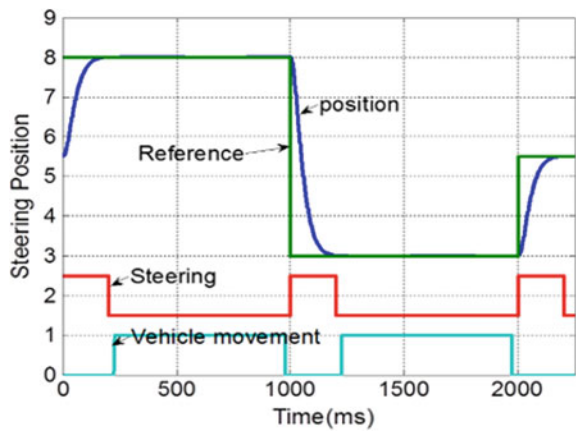


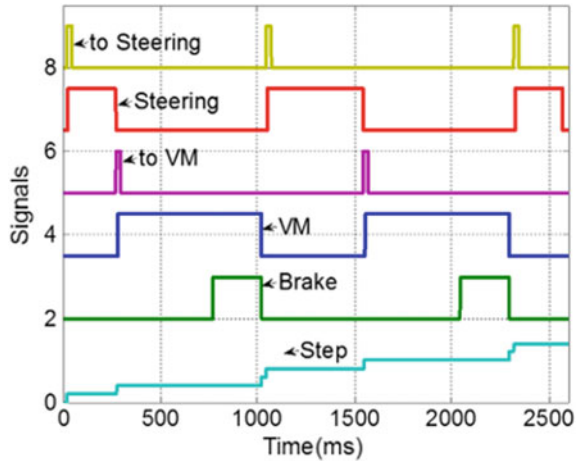
Fig. 12.10 Combination of steering and vehicle movement signals



position, the integrator was added to the output of angular speed. The steering speed was not controlled because the motor was connected to the gear, where the speed was limited for safety and convenience purposes. The position feedback sensor can serve as the potentiometer or encoder, which provides the signal feedback to the PID controller. The mathematical equation for the PID is shown in Eq. (12.10):

$$K_p + \frac{K_i}{s} + K_d s = \frac{K_p s + K_i + K_d s^2}{s} \tag{12.14}$$

Fig. 12.11 Combination of steering and vehicle movement signals



12.2.2 Tuning PID Using SISO Tool

Equations (12.1) to (12.4) can be grouped to form a physical-based model, which represents the speed. The steering angular position can be determined by adding the integrator and speed output. Meanwhile, the MATLAB/Simulink linearise tool can be used to linearise the differential equation and tune the PID. The MATLAB/Simulink PID drag-and-drop icon shows a menu, which can be clicked on to tune the PID automatically. The tuning process can be done using the MATLAB/Simulink SISOTOOL toolbox. The physical-based model must be transformed into the transfer function model first using the MATLAB/Simulink system identification toolbox. The toolbox is used to find the system order. Finally, using the SISO toolbox the transfer function for steering position system is determined, and the PID controllers gain to be obtained. The SISO tool is also used to test the system stability by using the root locus or bode plot. The PID controller gain can be obtained using the PID auto-tune function.

The SISO tool gives the compensator circuit as

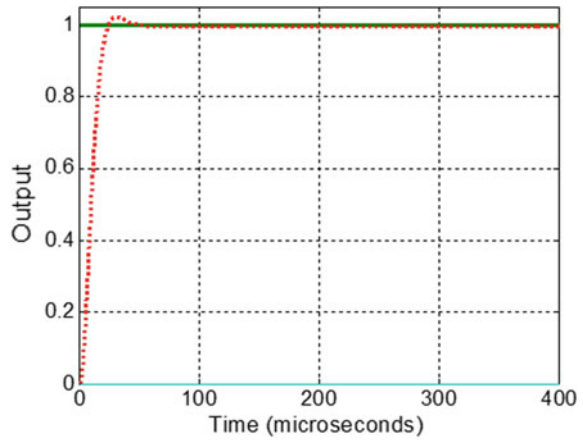
$$C = 2.6738e6x \frac{(1 + 0.38s)}{s} \tag{12.15}$$

whereby $K_p = 2.6738e6$, $z = \frac{1}{0.38}$, $z = 2.6315$, $K_i = K_pz$, $K_i = 7$.

The result of the PID controller is shown in Fig. 12.12.

The previous discussions on PID controller modelling and control have been done by using an analogue/continuous system, and with an analogue PID controller. However, in this current timeline, the analogue controller is no longer used and now replaced by the digital/discrete controller.

Fig. 12.12 Results of tuning with MATLAB/Simulink toolboxes



12.2.3 Simulation Model

A simulation model was developed to test the control technique. As the position for angular and displacement was known, the feedback control for speed and torque in regard to vehicle movement and steering position control by using a PID controller could be performed as shown in Figs. 12.13 and 12.14.

For monitoring the car trajectory, simulation models by using the mathematical equations are established, see Fig. 12.15.

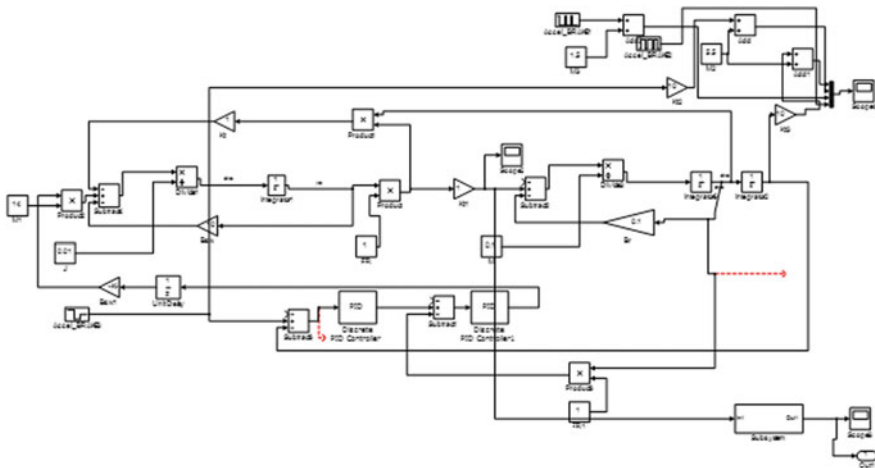


Fig. 12.13 MATLAB/Simulink physical-based model for steering motor

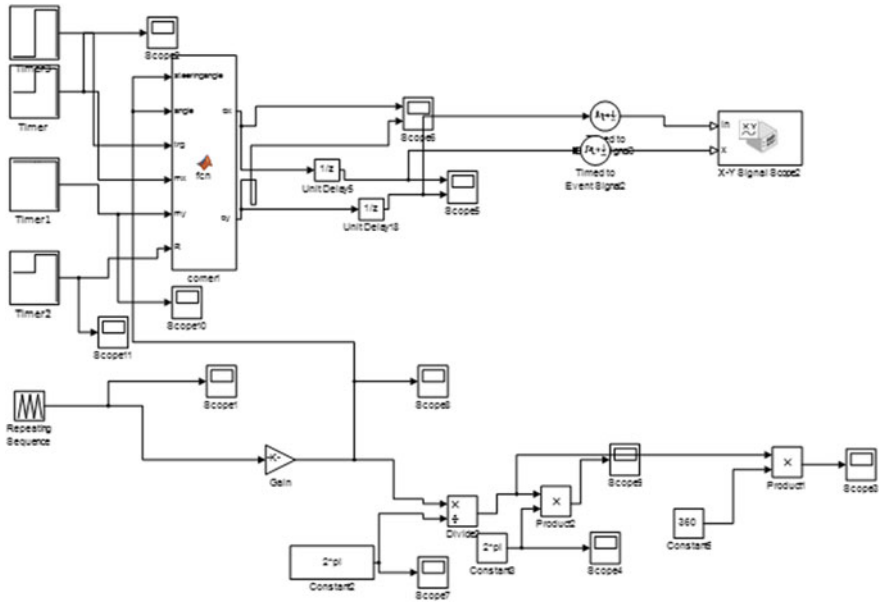


Fig. 12.14 MATLAB/Simulink simulation model for steering movement using double-circle

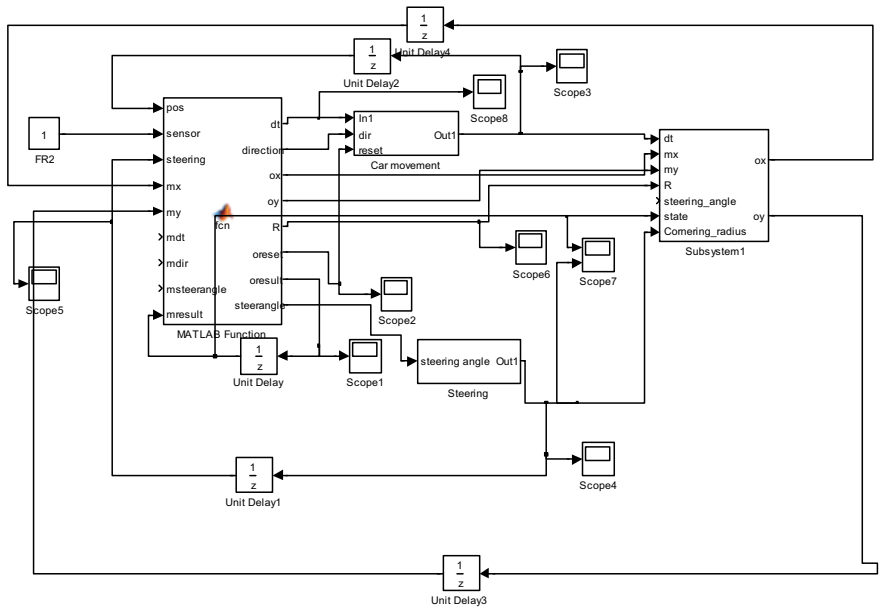
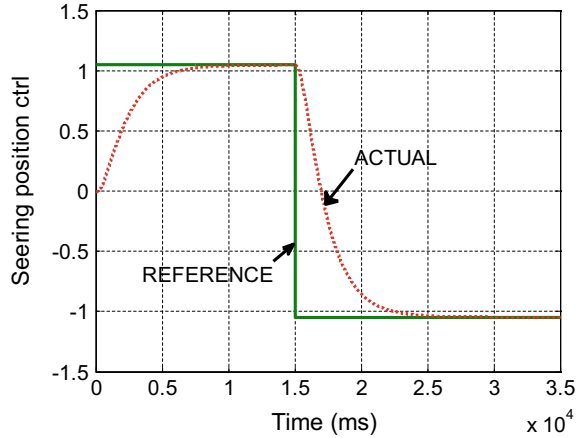


Fig. 12.15 Simulation model of auto parking

Fig. 12.16 Steering position feedback control



12.3 Results and Discussion

For parallel parking, the steering angle position control is shown in Fig. 12.16. The X-axis is the time, and Y-axis is the steering position and its reference signal. Two movements of the steering angle were shown. First, the steering was directed/moved to the right, followed by the vehicle movement. Next, the steering made a movement to the left, which was then followed by the vehicle movement.

The sequence is: first, the steering angle makes the first movement, followed by the vehicle movement. Once the vehicle movement is completed, the steering is then turned again for the second movement but at a different steering angle. Then it is followed by the vehicle movement again. When the steering is making the final movements, the vehicle is completely stopped.

Figure 12.17 shows the vehicle trajectory resulting from the combination of vehicle movement and steering movement for automatic parallel parking. In Fig. 12.18, the vehicle movement for reverse parking is shown.

Figure 12.18 shows the vehicle trajectory resulting from the combination of vehicle and steering movement for automatic reverse parking. The blue line in parallel park is measured from the right side of the back tire.

12.4 Conclusion

The control technique proposed for automatic parallel and reverse parking was successfully performed and simulated. The speed, torque, and position of steering and

Fig. 12.17 Trajectory of right side of back tire for parallel parking

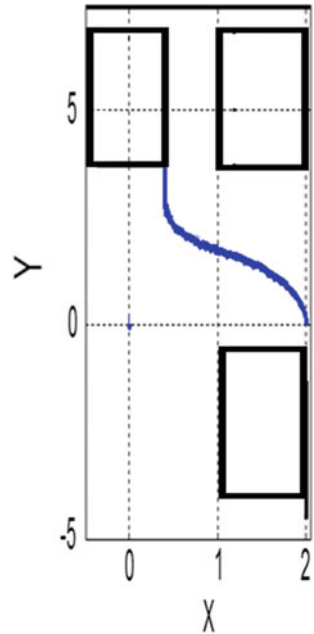
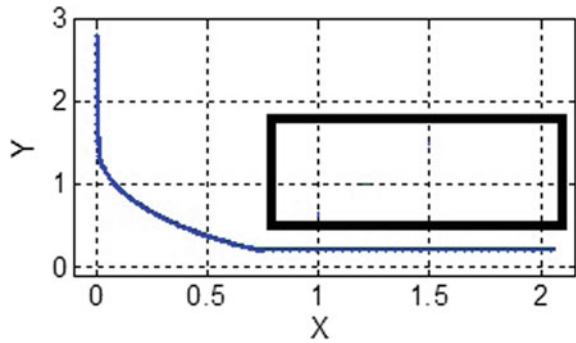


Fig. 12.18 Trajectory of right side of back tire for reverse parking



vehicle movement were successfully controlled for the application of automatic parking during reverse and parallel parking. The DC drive electric car powered by four-quadrant drive DC chopper for series motor is thus suitable for the application of DC drive electric car, which can offer automatic car parking as an extra feature.

References

1. Oak Ridge National Laboratory: Advanced brush technology for DC motors. Available: <http://peemrc.ornl.gov/projects/emdc3.jpg> (2009)
2. Arof, S., Jalil, J.A., Yaakop, N.M., Mawby, P.A., Arof, H.: Series motor four quadrants drive DC chopper part 1: overall. In: International Conference on Power Electronics (2014)
3. Arof, S., Diyanah, N.H.N., Mawby, P., Arof, H., Yaakop, N.M.: Low harmonics plug-in home charging electric vehicle battery charger utilizing multi-level rectifier, zero crossing and buck chopper: part 1: general overview. In: Progress in Engineering Technology, pp. 103–108 (2019). https://doi.org/10.1007/978-3-030-28505-0_9
4. Arof, S., Diyanah, N.H.N., Noor, N.M., Jalil, J.A., Mawby, P.A., Arof, H.: A new four quadrants drive chopper for separately excited DC motor in low cost electric vehicle. In: Progress in Engineering, pp. 119–138 (2019). http://doi.org/10.1007/978-3-030-28505-0_10
5. Arof, S., Muhd Khairulzaman, A.K., Jalil, J.A., Arof, H., Mawby, P.A.: Self tuning fuzzy logic controlling chopper operation of four quadrants drive DC chopper for low cost electric vehicle. In: 6th International Conference on Intelligent Systems, Modeling and Simulation. IEEE computer Society, pp. 40–24 (2015)
6. Arof, S., Zaman, M.K., Jalil, J.A., Mawby, P.A., Arof, H.: Artificial intelligence controlling chopper operation of four quadrants drive DC chopper for low cost electric vehicle. Int. J Simul. Syst. Sci. Technol. (2015). <http://doi.org/10.5013/IJSSST.a.16.04.03,2015>
7. Arof, S., Jalil, J.A., Kamaruddin, N.H., Yaakop, N.M., Mawby, P.A., Arof, H.: Series motor four quadrants drive DC chopper part 2: driving and reverse with direct current control. In: International Conference on Power Electronics, pp. 775–780 (2016). <https://doi.org/10.1109/pecon2016.7951663>. 978-1-5090-2547-3/16
8. Arof, S., Hassan, H., Rosyidi, M., Mawby, P.A., Arof, H.: Implementation of series motor four quadrants drive DC chopper for DC drive electric car and LRT. J. Appl. Environ. Biol. Sci. 7(3S), 73–82 (2017)
9. Arof, S., Noor, N.M., Elias, F., Mawby, P.A., Arof, H.: Investigation of chopper operation of series motor four quadrants DC chopper. J. Appl. Environ. Biol. Sci. 7(3S), 49–56 (2017)
10. Arof, S., Diyanah, N.H.N., Mawby, P.A., Arof, H.: Study on implementation of neural network controlling four quadrants direct current chopper: part 1: using single neural network controller with binary data output. In: Advanced Engineering for Processes and Technologies, pp. 37–57 (2019)
11. Arof, S., Diyanah, N.H.N., Yaakop, M., Mawby, P.A., Arof, H.: Processor in the loop for testing series motor four quadrants drive direct current chopper for series motor driven electric car: part 1: chopper operation modes testing. In: Advanced Engineering for Processes and Technologies, pp. 59–76 (2019). https://doi.org/10.1007/978-3-030-05621-6_5
12. Arof, S., Diyanah, N.H.N., Noor, N.M., Radzi, M., Jalil, J.A., Mawby, P.A., Arof, H.: Series motor four quadrants drive DC chopper: part 4: generator mode. In: Progress in Engineering, pp. 155–167 (2019). https://doi.org/10.1007/978-3-030-28505-0_12
13. Arof, S., Diyanah, N.H.N., Noor, N.M., Rosyidi, M., Mawby, P.A., Arof, H.: Genetics algorithm for setting up look up table for parallel mode of new series motor four quadrants DC chopper. In: Progress in Engineering, pp. 155–167 (2019). https://doi.org/10.1007/978-3-030-28505-0_12
14. Anwar, S.: An anti-lock braking control system for a hybrid electromagnetic/electrohydraulic brake-by-wire system. In: Proceedings of the 2004 American Control Conference (2004). <https://doi.org/10.23919/acc.2004.1383873>
15. Simonik, P., Mrovec, T., Przewczek, S., Harach, T., Klein, T.: Brake by wire for remotely controlled vehicle. In: 2018 IEEE International Conference on Electrical Systems for Aircraft, Railway, Ship Propulsion and Road Vehicles & International Transportation Electrification Conference (ESARS-ITEC) (2018) <https://doi.org/10.1109/esars-itec.2018.8607363>
16. Huang, H.-C., He, Y.-H., Lin, F.: A vehicle transverse automatic parking auxiliary system. In: 2015 International Conference on Machine Learning and Cybernetics (ICMLC) (2015). <https://doi.org/10.1109/icmlc.2015.7340654>

17. Hu, J., Duan, J.: AC electric power steering system modeling with feed-forward fuzzy control algorithm. In: Proceedings of the 10th World Congress on Intelligent Control and Automation (2012). <https://doi.org/10.1109/wcica.2012.6359030>
18. Hu, T.-H., Yeh, C.-J.: Hardware implementation of the current control using the internal model method in the electric power steering application. In: 2009 IEEE Vehicle Power and Propulsion Conference (2009). <https://doi.org/10.1109/vppc.2009.5289868>

Chapter 13

Series Motor Four-Quadrant DC Chopper: Reverse Mode, Direct Current Control, Triple Cascade PIDs, and Ascend-Descend Algorithm with Feedback Optimization for Automatic Reverse Parking



Saharul Arof, M. S. Said, N. H. N. Diyanah, N. M. Noor, J. A. Jalil, Philip Mawby, H. Arof, and Emilia Noorsal

Abstract This paper focuses on the reverse mode of a proposed series motor four-quadrant direct current chopper (FQDC). The paper proposes a control technique in controlling the acceleration and deceleration of an electric vehicle (EV) using triple cascade proportional-integral-derivative (PID) controllers with an ascend-descend algorithm for controlling speed, torque, and position. The aim is to control the electric propulsion motor powered by the FQDC for the application of automatic reverse parking of an autonomous DC drive electric car. The control technique was simulated

S. Arof (✉) · M. S. Said · N. H. N. Diyanah · N. M. Noor · J. A. Jalil
Universiti Kuala Lumpur, Malaysian Spanish Institute, Kulim Hi-Tech Park, 09000 Kulim,
Kedah, Malaysia
e-mail: saharul@unikl.edu.my

M. S. Said
e-mail: msazali@unikl.edu.my

N. H. N. Diyanah
e-mail: diyanahhisham94@gmail.com

N. M. Noor
e-mail: noramlee@unikl.edu.my

S. Arof · P. Mawby
University of Warwick School of Engineering, Coventry CV47AL, UK
e-mail: p.a.mawby@warwick.ac.uk

H. Arof
Engineering Department, Universiti Malaya, Jalan Universiti, 50603 Kuala Lumpur, Malaysia
e-mail: ahamzah@um.edu.my

E. Noorsal
Faculty of Electrical Engineering, Universiti Teknologi MARA, Cawangan Pulau Pinang, 13500
Permatang Pauh, Malaysia
e-mail: emilia.noorsal@uitm.edu.my

© The Editor(s) (if applicable) and The Author(s), under exclusive license
to Springer Nature Switzerland AG 2020
M. H. Abu Bakar et al. (eds.), *Progress in Engineering Technology II*,
Advanced Structured Materials 131,
https://doi.org/10.1007/978-3-030-46036-5_13

using MATLAB/Simulink, and the results showed that the technique has successfully met the objective of torque, current, speed, and position control for reverse and auto-reverse parking. In addition, the technique is suitable to be implemented in a DC drive electric car.

Keywords DC drive · Reverse parking · Four-quadrant DC chopper · Series motor · Torque · Position and speed · Torque control · EV

13.1 Introduction

One of the primary reasons for the introduction of electric cars into the market is the concern over greenhouse gas emissions and their contribution to global warming. The purpose of creating electric cars that reduce or eliminate exhaust emissions is to overcome this issue. Unfortunately, the price of electric vehicles (EVs) and hybrid electric vehicles (HEVs) is expensive, thus making the vehicles unattainable to many people, especially those living in poor countries. Therefore, this has led to the study on the possibility for a direct current (DC) drive EV [1] which is known to be economical.

13.1.1 Literature Review

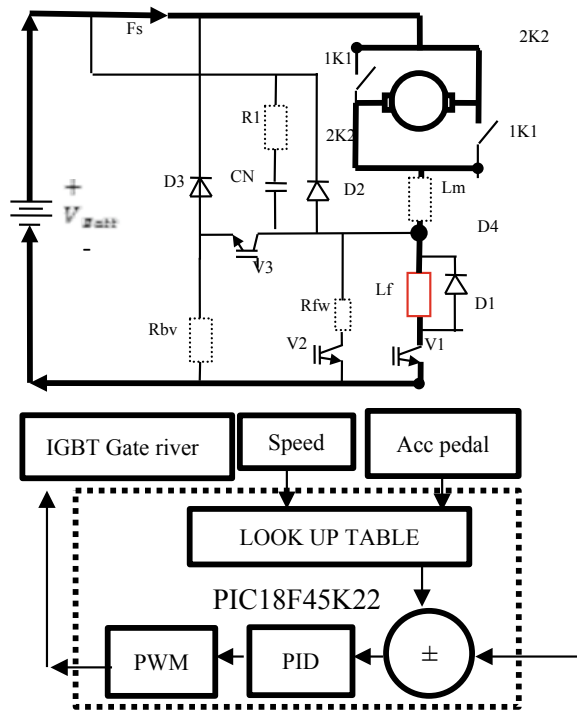
The study on DC drive EVs includes the design of new DC motors, battery charger, and four-quadrant choppers to improve the performance and extend the capability of EVs, such as adding the mode of chopper operations [1–4]. Further investigations of four-quadrant direct current chopper (FQDC) hardware and simulation model include a feedback control using DC control and optimization using artificial intelligence to optimize all operations to produce a complete EV while running in different earth profiles [5–13]. This paper further extends on the study and investigation of one of the modes of the proposed chopper operations, which is the reverse mode. The vehicle reverse mode is shown in Fig. 13.1. After releasing the pulses, a load current that corresponds to the preset control factor α (related to duty ratio) flows through the chopper. In this mode, the back electromagnetic force (EMF), armature voltage, and torque are negative. The paths of currents for reverse operation are shown in Fig. 13.1. The switching of the main IGBT V1 is determined by the control factor α .

The mathematical representations of the four-quadrant chopper in reverse mode are presented in the following equations:

$$I_a = \frac{V_{\text{batt}} - I_a(R_a + R_f) - B_{\text{emf}}}{L_a + L_f} \quad (13.1)$$

$$B_{\text{emf}} = K_v I_f \omega \quad (13.2)$$

Fig. 13.1 Current paths in reverse mode



$$T_d = K_t I_f I_a \tag{13.3}$$

$$T_d = J \frac{d\omega}{dt} + B_w + T_L \tag{13.4}$$

13.1.2 Review of Automatic Parking

Automatic parking is important when a vehicle driver is dealing with a constrained environment where much attention and skills are required. Performing automatic parking requires coordinated control of the steering angle and the surrounding to avoid collision [14]. Parking assistance systems have been developed using image assistance by Mercedes, Volvo, and BMW. Automatic parking consists of parking trajectory, vehicle location detection, parking space detection, turning, and reverse position control [15]. Parking space detection is used to check the availability of a parking space, where the details are not covered in this paper.

13.2 Methodology

13.2.1 Control Strategy During Reverse Mode

The two required movements in automatic parking are the vehicle movement (in reverse mode) and the steering angle [16]. The latter is controlled using an electric power steering as illustrated in Fig. 13.2.

Fig. 13.2 Electric power steering

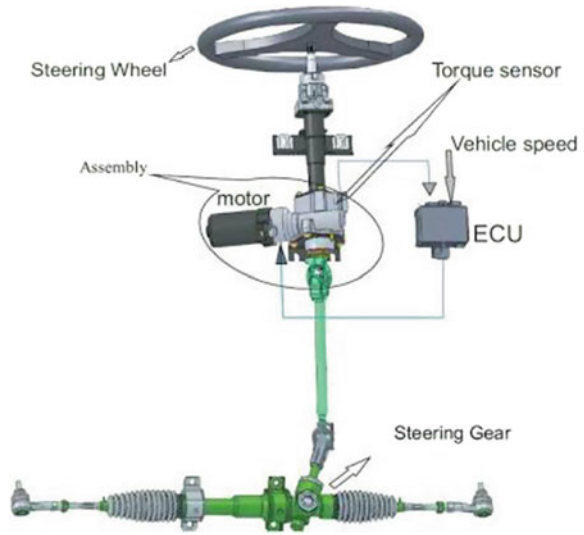


Fig. 13.3 Steering and vehicle movement

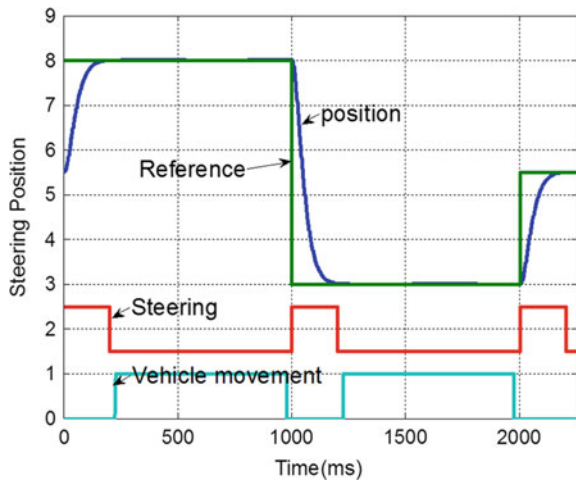


Fig. 13.4 Electrohydraulic brake system

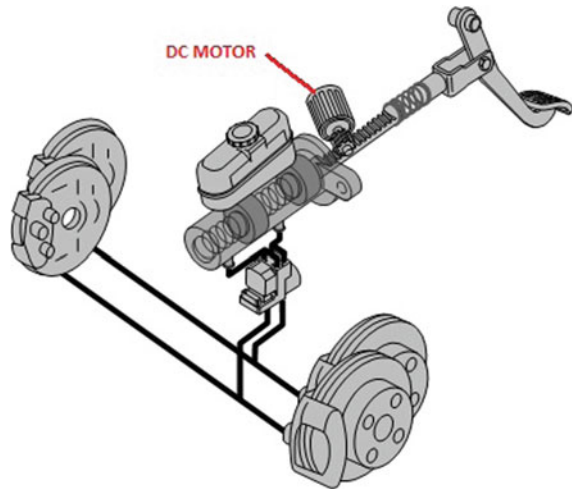
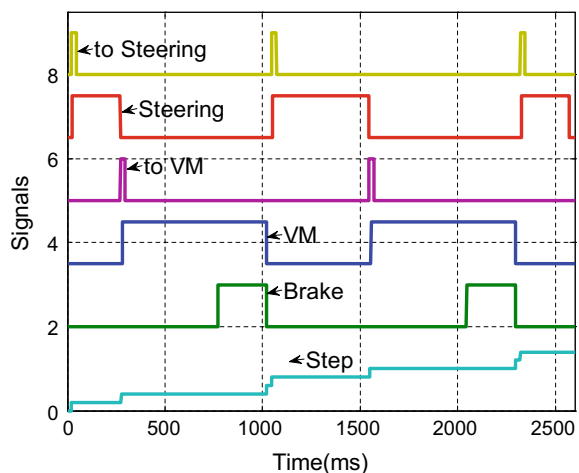


Figure 13.3 exhibits the steering and vehicle movement sequence. The *x*-axis represents time, in milliseconds, while the *y*-axis is normalized. Reference represents the desired position of the steering angle, while position is the actual steering angle movement. An FQDC operating in reverse mode provides the vehicle movement whereby the propulsion motor via FQDC provides motor torque to move an EV.

In the figure, the sequence of operation started with steering and followed by the vehicle movement. Brake control as shown in Fig. 13.4 is also important and the control is needed to create the deceleration effect and to the final stop of the EV [17]. Details regarding the brake and steering control are not covered in this paper.

Figure 13.5 shows the sequence of steering, vehicle movement, and brake. It should be noticed that brake is applied at the end session of the vehicle movement

Fig. 13.5 Steering, vehicle movement, and brake



to create the deceleration effect [18]. The overall function of an automatic reverse parking controller is to ensure that the position, acceleration, and speed are controlled according to the desired pattern for the application of automatic parking. To perform these actions, DC control, ascend-descend algorithm, and triple cascade PIDs are implemented. This is to ensure no tire slip, linear acceleration and deceleration of EV, and the final stop position are achieved.

13.2.2 Direct Current Control in Driving and Reverse Mode

DC control (DCC) is an economical way to be implemented and the approach can be used to limit excessive motor torque that causes tire slip, and consequently the EV will not be parked at the desired position [7] (Fig. 13.6).

In DCC, the motor current is set according to the speed of the motor. DCC uses the look-up table as shown in Table 13.1 and Fig. 13.7. The table represents the required

Fig. 13.6 DCC method

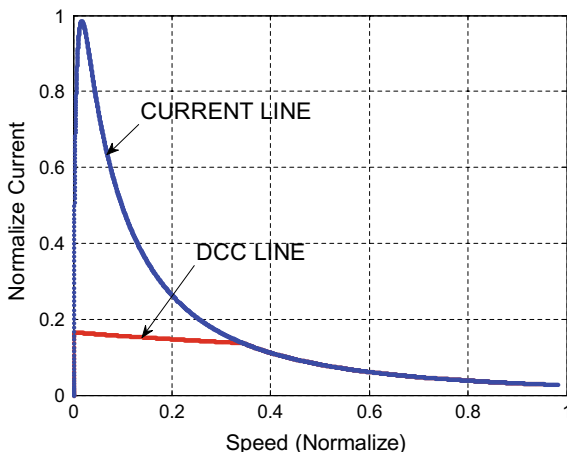


Table 13.1 Look-up table

Speed (rpm)	Current
0.00–0.34 * max speed	0.18 * max current
0.34–0.40 * max speed	0.16 * max current
0.40–0.50 * max speed	0.14 * max current
0.50–0.60 * max speed	0.12 * max current
0.60–0.70 * max speed	0.10 * max current
0.70–0.80 * max speed	0.08 * max current
0.80–0.90 * max speed	0.06 * max current
0.90–1.00 * max speed	0.06 * max current

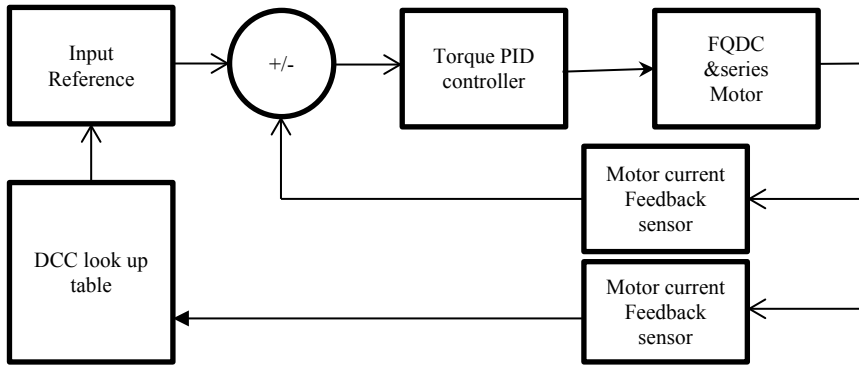


Fig. 13.7 DCC method flow

or expected current according to the motor speed. Interpolations can be made for values that are not available in the table.

13.2.3 Vehicle Movement Control with Cascade PIDs

Cascade PIDs allow several controls to be carried out in a single system. In this research, cascade PIDs were used to control the position, speed, and torque of a single propulsion motor. In a cascade PID, the output of one PID controller will be the input of the other PID controller. The most important aspect to control in this study is the position, which will be placed at the front/beginning, and followed by the least important aspects, which are speed and lastly torque. Figure 13.8 shows the PID controllers connected in cascade. The purpose of cascade PIDs is to control the system performance, such as speed and torque of the propulsion motor. The feedback

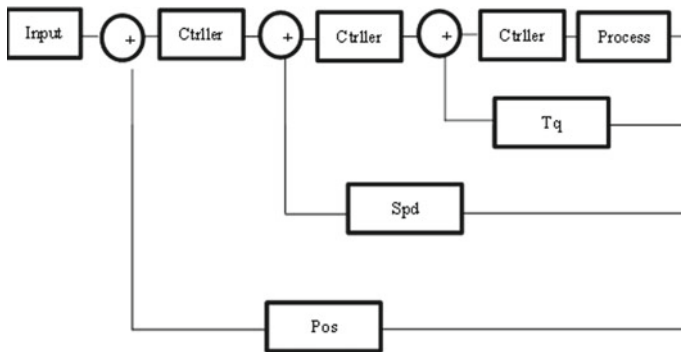


Fig. 13.8 Triple cascade PIDs

control is used to adjust the speed and torque based on the feedback gain. The DCC is controlled using current feedback gain in the cascade PIDs.

13.2.4 Ascend-Descend Algorithm

The ascend-descend algorithm is modified from the gradient descend algorithm. However, unlike the latter that is shown in Fig. 13.9, the former has no target and an error is included in the algorithm. Without error and target, the output will increase or decrease linearly.

The expected gradient effect of speed is presented in Fig. 13.10. In the figure, the speed (in rpm) increases linearly, becomes constant, and then decelerates linearly. This condition can be achieved by using the ascend-descend algorithm and applying the control algorithm output to the feedback sensor by controlling the gain of speed of the PID controller that is connected in cascade. Figure 13.11 shows the block diagram of the operation.

Fig. 13.9 Conventional gradient descend

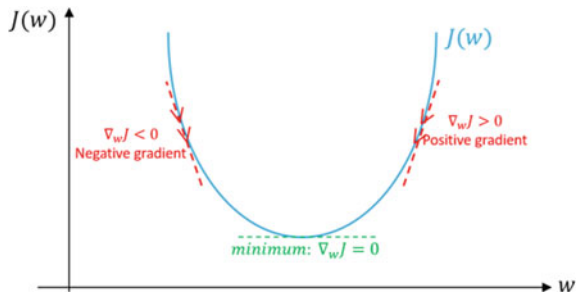


Fig. 13.10 Expected output signal of ascend-descend algorithm

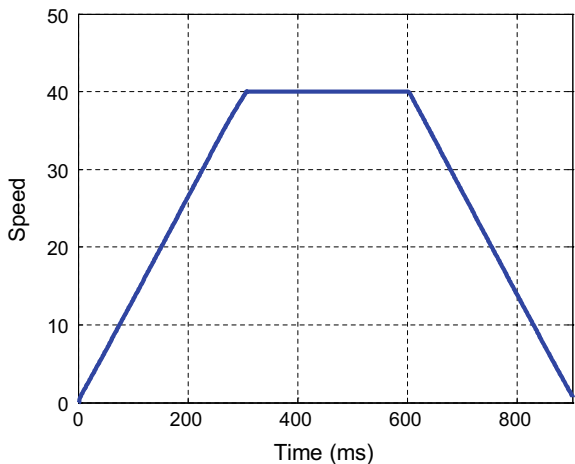
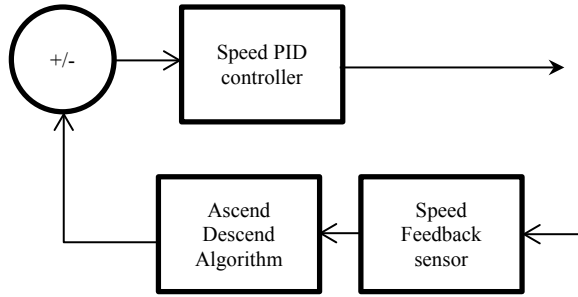


Fig. 13.11 Block diagram of ascend-descend operation



Details about DCC, cascade PIDs, and ascend-descend algorithm will be discussed in other studies.

13.2.5 Simulation Model with MATLAB/Simulink

A simulation model was developed to test the control technique. For monitoring the car trajectory, a path tacking simulation model using mathematical equations as shown in Fig. 13.12 was established.

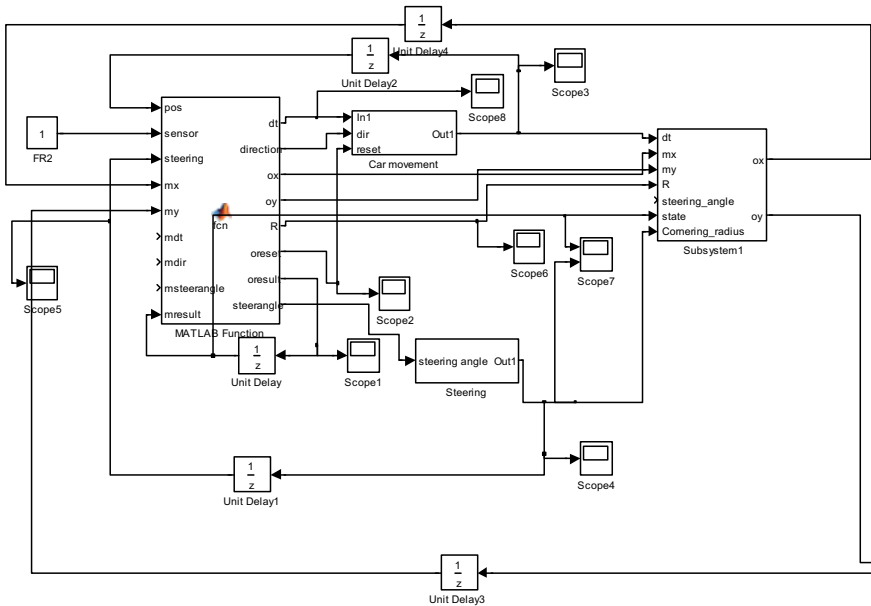


Fig. 13.12 Path trajectory simulation model

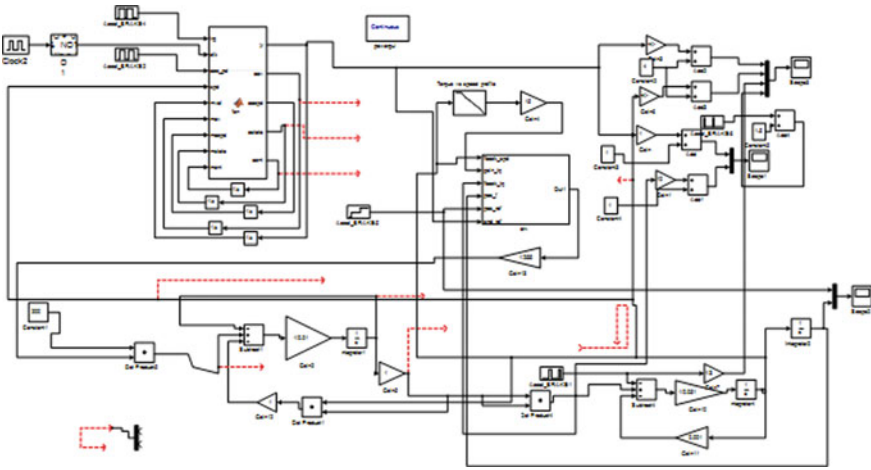


Fig. 13.13 Simulation model of vehicle movement

A simulation model of the vehicle movement for auto-parking was established as presented in Fig. 13.13. This model includes the ascend-descend algorithm controller.

Equations (13.1) to (13.4) can be grouped to form a physical-based model that represents speed. The vehicle position can be determined by adding an integrator and speed output. The MATLAB/Simulink linearize tool can be used to linearize the differential equation and finally tune the PID. MATLAB/Simulink PID drag-and-drop icon has a menu that can be clicked to tune the PID automatically. For the tuning of MATLAB/Simulink using the SISO tool, the physical-based model has to be transformed to the transfer function model using the MATLAB/Simulink system identification. The tool is used to find the system order. Finally, by using the SISO tool, the transfer function for the steering position system can be determined and the PID controller gain can be obtained. The SISO tool is also used to test system stability using root locus or Bode plot. The PID controller gain can be obtained using the PID auto-tune function.

The position, speed, and acceleration control for triple cascade PIDs are shown in Fig. 13.14.

13.3 Results and Discussion

The sequence of operations for automatic reverse parking is shown in Fig. 13.3. In the sequence, first, the steering angle makes the first movement and followed by vehicle movement. Once the vehicle movement has been completed, the steering then moves again for different steering angles and followed by vehicle movement. During steering movement, the vehicle is completely stopped.

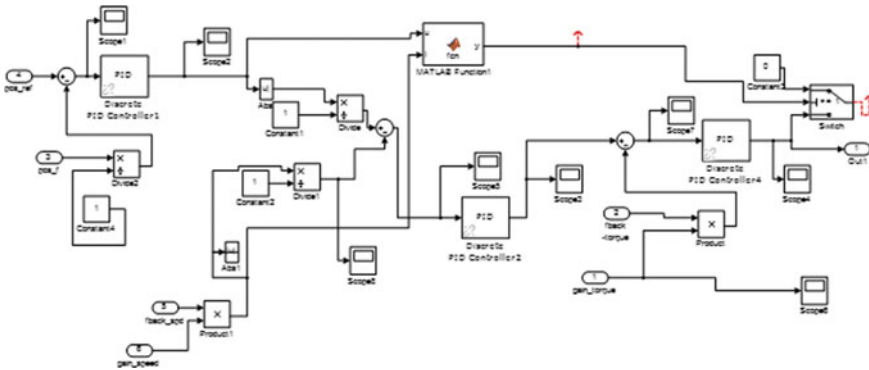


Fig. 13.14 Triple cascade PID simulation model

Figure 13.15 shows how the speed reference is applied. The speed reference is made from a small linear incremental speed value until the required speed is achieved. Once the expected speed is met, the reference speed is made constant. In the figure, the actual speed is lagging a bit from the reference speed during acceleration but once the speed is fixed, the actual speed is similar to the reference speed.

Figure 13.16 shows the vehicle movement speed and torque controlled using the cascade PIDs. The torque is constant and high at the beginning during acceleration before it decreased and increased again during acceleration. For reverse parking, the vehicle makes two movements and resulted in two similar graphs plotted. When the vehicle accelerates, the torque is maintained according to the DCC. The gap time at the beginning and between two graphs represents steering operation.

The vehicle movement position is shown in Fig. 13.17. The standstill at the beginning and middle indicates the steering turning operations.

Fig. 13.15 Speed reference with ascend-descend algorithm

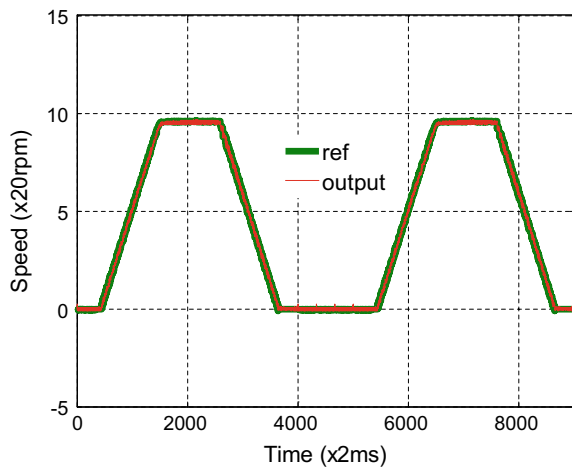


Fig. 13.16 Direct current control and vehicle speed

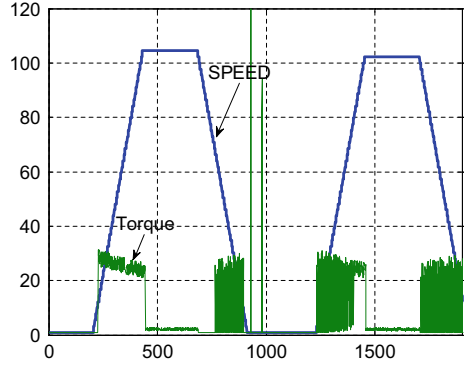


Fig. 13.17 Vehicle movement position

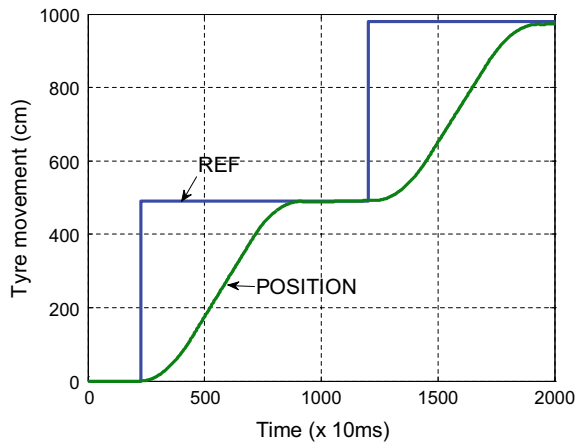


Figure 13.18 shows the vehicle trajectory resulted from the combination of vehicle movement and steering movement for automatic parallel parking. The X - and Y -axes represent the X , Y coordinates which are normalized to ease plotting.

Figure 13.19 shows the vehicle trajectory resulted from the combination of vehicle movement and steering movement for automatic reverse parking. The X - and Y -axes represent the X , Y coordinates which are normalized to ease plotting.

13.4 Conclusions

The control technique proposed for automatic parallel and reverse parking has been successfully performed and simulated. The speed, torque, steering position, and vehicle movement have been successfully controlled for the application of automatic reverse and parallel parking. Therefore, a DC drive electric car powered by FQDC

Fig. 13.18 Parallel parking measured from the rear right tire

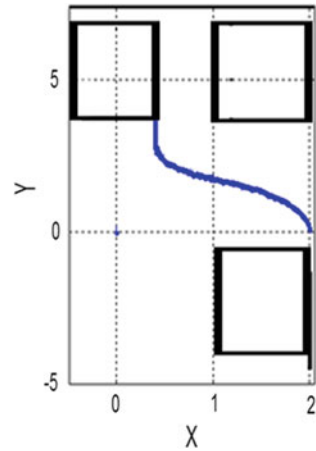
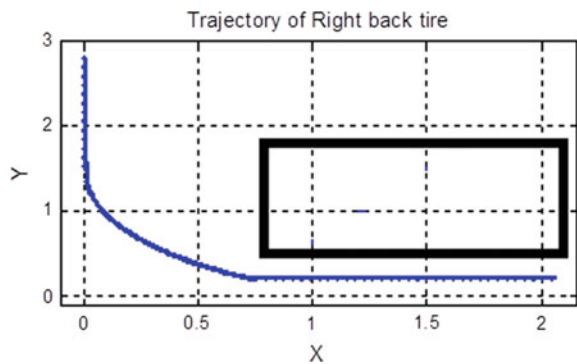


Fig. 13.19 Trajectory of the rear right tire for reverse parking



for series motor is suitable for the application of a DC drive electric car and will have automatic car parking as an extra feature.

References

1. Oak Ridge National Laboratory.: Advanced brush technology for dc motors. Available: <http://peemrc.ornl.gov/projects/emdc3.jpg> (2009)
2. Arof, S., Jalil, J.A., Yaakop, N.M., Mawby, P.A., Arof, H.: Series motor four quadrants drive DC chopper part1: overall. Int. Conf. Power Electron. (2014)
3. Arof, S., Diyanah, N.H.N., Mawby, P., Arof, H., Yaakop, N.M.: Low harmonics plug-in home charging electric vehicle battery charger utilizing multi-level rectifier, zero crossing and buck chopper: part 1: general overview. Progress Eng. Technol. 103–108 (2019) https://doi.org/10.1007/978-3-030-28505-0_9
4. Arof, S., Diyanah, N.H.N., Noor, N.M., Jalil, J.A., Mawby, P.A., Arof, H.: A new four quadrants drive chopper for separately excited DC motor in low cost electric vehicle. Progress Eng. 119–138 (2019). https://doi.org/10.1007/978-3-030-28505-0_10

5. Arof, S., Muhd Khairulzaman, A.K., Jalil, J.A., Arof, H., Mawby, P.A.: Self tuning fuzzy logic controlling chopper operation of four quadrants drive DC chopper for low cost electric vehicle. In: 6th International Conference on Intelligent Systems, Modeling and Simulation, IEEE computer Society, pp. 40–24 (2015)
6. Arof, S., Zaman, M.K., Jalil, J.A., Mawby, P.A., Arof, H.: Artificial intelligence controlling chopper operation of four quadrants drive DC chopper for low cost electric vehicle, Int. J. f Simul. Syst. Sci. Technol. <https://doi.org/10.5013/ijssst.a.16.04.03,2015>
7. Arof, S., Jalil, J.A., Kamaruddin, N.H., Yaakop, N.M., Mawby, P.A., Arof, H.: Series motor four quadrants drive DC chopper part2: driving and reverse with direct current control. Int. Conf. Power Electron. 775–780 (2016). 978-1-5090-2547-3/16. <https://doi.org/10.1109/pecon2016.7951663>
8. Arof, S., Hassan, H., Rosyidi, M., Mawby, P.A., Arof, H.: Implementation of Series motor four quadrants drive DC chopper for dc drive electric car and LRT. J. Appl. Environ. Biol. Sci. 7(3S), 73–82 (2017)
9. Arof, S., Noor, N.M., Elias, F., Mawby, P.A., Arof, H.: Investigation of chopper operation of series motor four quadrants DC chopper. J. Appl. Environ. Biol. Sci. 7(3S), 49–56 (2017)
10. Arof, S., Diyanah, N.H., Mawby, P.A., Arof, H.: Study on implementation of neural network controlling four quadrants direct current chopper: part1: using single neural network controller with binary data output. Adv. Eng. Process. Technol. 37–57 (2019)
11. Arof, S., Diyanah, N.H., Yaakop, M., Mawby, P.A., Arof, H.: Processor in the loop for testing series motor four quadrants drive direct current chopper for series motor driven electric car: part1: chopper operation modes testing. Adv. Eng. Process. Technol. 59–76 (2019). https://doi.org/10.1007/978-3-030-05621-6_5
12. Arof, S., Diyanah, N.H.N., Noor, N.M.N., Radzi, M., Jalil, J.A., Mawby, P.A., Arof, H.: Series motor four quadrants drive DC chopper: part 4: generator mode. Progress Eng. 155–167 (2019). https://doi.org/10.1007/978-3-030-28505-0_12
13. Arof, S., Diyanah, N.H.N., Rosyidi, N.M.N.M., Mawby, P.A., Arof, H.: Genetics algorithm for setting up look up table for parallel mode of new series motor four quadrants dc chopper. Progress Eng. 155–167 (2019). https://doi.org/10.1007/978-3-030-28505-0_12
14. Anwar, S.: An anti-lock braking control system for a hybrid electromagnetic/electrohydraulic brake-by-wire system. In: Proceedings of the 2004 American Control Conference. <https://doi.org/10.23919/acc.2004.1383873>
15. Castillo, J.J., Cabrera, J.A., Guerra, A.J., Simón, A.: A novel electrohydraulic brake system with tire–road friction estimation and continuous brake Pressure control. IEEE Trans. Ind. Electron. 63(3), (2016). <https://doi.org/10.1109/tie.2015.2494041>
16. Simonik, P., Mrovec, T., Przewczek, S., Harach, T., Klein, T.: Brake by wire for remotely controlled vehicle. In: 2018 IEEE International Conference on Electrical Systems for Aircraft, Railway, Ship Propulsion and Road Vehicles & International Transportation Electrification Conference (ESARS-ITEC). <https://doi.org/10.1109/esars-itec.2018.8607363>
17. Huang, H.C., He, Y.H., Lin, F.: A vehicle transverse automatic parking auxiliary system. In: 2015 International Conference on Machine Learning and Cybernetics (ICMLC). <https://doi.org/10.1109/icmlc.2015.7340654>
18. Hu, J.F., Duan, J.M.: AC electric power steering system modeling with Feed-forward fuzzy control algorithm. In: Proceedings of the 10th World Congress on Intelligent Control and Automation. <https://doi.org/10.1109/wcica.2012.6359030>

Chapter 14

The Image Processing Technique of Defect Detection in Metal Materials Using Active Infrared Thermography



Nor Liyana Maskuri, Muhamad Husaini Abu Bakar,
and Ahmad Kamal Ismail

Abstract Technology on active infrared thermography has been widely used in the field of non-destructive testing. The defects produce an uneven heat dissipation, and an infrared camera captures this thermal reaction. The phase image provides an outstanding invisible flaws description on sequences of images captured. During the data acquisition phase, the result might be affected by image noise resulting from the emissivity on the specimen surface and also by the non-uniform heating process. For this study, an infrared camera of medium wave infrared range was analysed. The heating process is done by heating the aluminium plate in an oven for 5–15 min. These specimens contain twelve numbers of flat-bottomed circular holes, from sample upper surface with different artificial depth. All of the artificial defect samples were manufactured by the milling machining process. The defect detection and characterisation used several data and different analysis methods were used in the pre-processing for quantitative analysis. The infrared test method on non-destructive thermography capability was increased since the final result appears clearer and can be used for future studies. The temperature data used the image filtering and image segmentation process for better visualisation of defects. The correlation image and the correlation image phase show promising results. The experimental setup and comparative results were analysed in detail in this document. As a conclusion, the image enhancement method has a significant influence on the defect detection result.

Keywords Non-destructive test · Active infrared thermography · Square pulse thermography · Image processing · Image segmentation

N. L. Maskuri (✉) · M. H. Abu Bakar · A. K. Ismail
System Engineering and Energy Laboratory, Universiti Kuala Lumpur-Malaysian Spanish
Institute, Kulim Hi-Tech Park, 09000 Kulim, Kedah, Malaysia
e-mail: nliyana.maskuri@s.unikl.edu.my

M. H. Abu Bakar
e-mail: muhamadhusaini@unikl.edu.my

A. K. Ismail
e-mail: ahmadkamal@unikl.edu.my

© The Editor(s) (if applicable) and The Author(s), under exclusive license
to Springer Nature Switzerland AG 2020

M. H. Abu Bakar et al. (eds.), *Progress in Engineering Technology II*,
Advanced Structured Materials 131,
https://doi.org/10.1007/978-3-030-46036-5_14

14.1 Introduction

Non-destructive evaluation of structures based on active infrared thermography is a technique widely used in the field of engineering. The current demand for non-destructive and non-contact testing assessment is slightly increasing in production lanes. Applications are in mechanical, aerospace and civil structures industries [1]. The phenomenon of material thermal convection is the driving force for the structural anomalies inspection. Any specimen item above absolute zero temperature radiates infrared radiation, and the infrared camera captures these electromagnetic radiations, and this process produces a thermogram of the test sample [2].

There are varieties of procedures in active infrared thermography. The transient thermography, square pulse thermography, and lock-in thermography are the three most commonly used methods nowadays [3, 4]. The square pulse thermography concept can be explained by short pulse, short inspection time, short duration time for heating up the specimen using a high heated source. Then, the result was recorded from the thermal response (surface) during the cooling process. The information contains defect characterisation with different size and depths. This method will give a fast analysis, but it required a high peak power for a more in-depth analysis, and they are limited on the surface on non-uniform emissivity. Detection of surface flaws depends on raw sequences of the thermal image quality. This variation in surface emissivity affects the thermogram, and there is a need for reconstruction and filtering algorithms to improve the detection of flaws [5, 6].

The thermal intensity pattern is approximately the same for all pixels in the cropped area of the sample. The temporary profile is compensated with a first-order fitting adjustment. The residue phase information of this accessory will have a prominent peak at abnormalities in the specimen surface. This article is to define the scope of image processing, analyse from the various steps and methodologies involved in image processing from thermogram images, image processing application and processes on the boundary research field.

14.2 Methodology

14.2.1 *Experimental Setup*

The experiment consisted of an aluminium alloy T6061 plate measuring 70 mm × 50 mm × 2 mm. Within the specimen subsurface, the defects were made by a milling process to produce artificial holes with various parameters. The concrete specimen consisted of twelve flaws which are artificially voids formed by the milling machine. The flaws were grouped into four different sizes. The variant size is created on 2 mm, 4 mm, 6 mm and 08 mm diameters. The defects also are located at three different depths from the top orientation, which are 1.5 mm, 1.0 m and 0.5 of the metallic surface for facing the external source of heating in this experimental process.

Fig. 14.1 Metallic specimen CAD drawing with different thickness and size

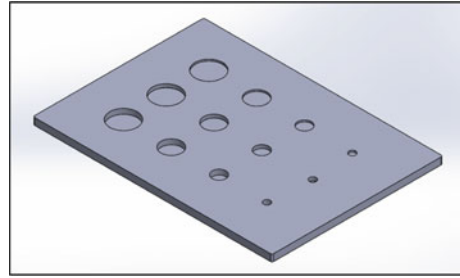


Figure 14.1 is pointing to the metallic specimen in the computer-aided design (CAD) drawing with different depths and sizes.

Figure 14.2 contains a general structure for the experiments conducted in this project. The tests were performed using heated specimens each having up to 90 °C for 15 min time duration. The heating process was conducted in a microwave oven equipment for the constant and well-maintained temperature. The infrared camera U5855A TrueIR Thermal Imager is used to capture the thermogram. The data acquisition and processing stage are done using a computer and software provided. The thermal sensitivity for this camera is 0.07 °C and the resolution is 320 × 240 (IR pixels) with eight frames per second. Each of the frames is cropped to 280 × 220 resolution as selected specimen region to reduce the time taken to process the full frames sequences. This region of interest (ROI) is the technique to define the object border consideration.

In the thermography field, the emitted radiation and released temperature from investigation surface area were interpreted. When lowering the emissivity of the surface, then the emitted radiation from the surface area will be resulting in a weaker reading. Usually, the methodology to overcome the emissivity problem is to apply

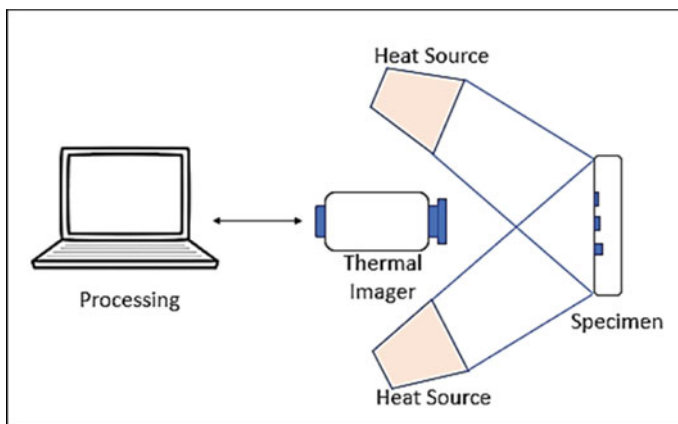


Fig. 14.2 General structure of the system for active pulse thermography

black paint with higher values of emissivity, and these techniques reduced the reflection form [7]. For detection sensitivity condition and avoiding error, the specimen surface was painted with flat black paint to achieve a stable emissivity of 0.95. This condition allowed to satisfy the requirement near at 1.0 value of black body emissivity and an excellent emissivities value of 0.95.

14.2.2 Image Acquisition and Processing

The thermographic camera device forms a video and an image from the infrared radiation that is known as the thermogram. For the first step, the camera captured an image based on the considered parameters. The thermogram is in RGB format and extracted to the others image representation. Next, pre-processed of the captured image such as RGB conversion and image enhancement process are carried out.

14.2.3 Image Representation in the Red Green Blue Scale

The red green blue (RGB) image presentation model is a primary colour unit that contains the monochrome 8-bit or pixel standard. The corresponding red green blue is a combination of 24-bit (pixel) that is referring to 8 bit for each colour band. These RGB combination colours are represented in Fig. 14.3.

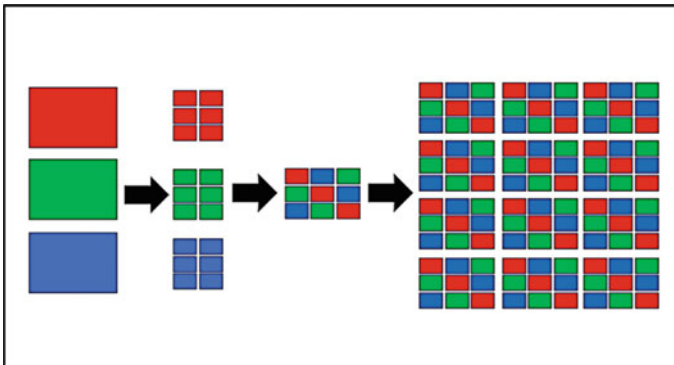
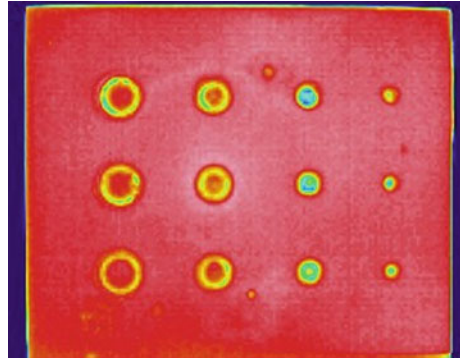


Fig. 14.3 RGB pixel representation

Fig. 14.4 Image acquisition gained from thermal camera



14.3 Results and Discussion

14.3.1 Image Data

The goal of this project phase is to concentrate on the image processing algorithm simulated in the MATLAB software available code. Images taken should be simple enough to be processed and the errors that may occur should be eliminated. The selecting thermal image sequence is cropped to the region of interest (ROI). Some selected methods of pre-processing of the data are required to compensate for the thermal effect. Figure 14.4 is the raw image captured by using a thermal imager.

14.3.2 Image Filtering and Enhancement

Image processing is the method that converts the input from original images are creates other new images as output. Image enhancement is one of the processes of adjusting selecting pictures frames, and the result will fit for display or further image analysis. The edited image has a provision on image editors to image the created histogram. The image pixels are plotted in the histogram in the vertical axis with a particular brightness value in the horizontal axis provided. These digital editor algorithms allow adjusting visually the brightness value of each pixel and the result is dynamically displayed. These improvements led to the desired contrast brightness of the image. The image of the histogram result before applying the histogram contrast method is shown in Fig. 14.5.

Contrast adjustment is the process of remapping the image intensity to the full display data type range. An excellent contrast on images has differenced sharp intensity values. Figure 14.6 is the result example with high contrast. This phenomenon will cover the poor contrast with limited intensities value towards the ranges of the

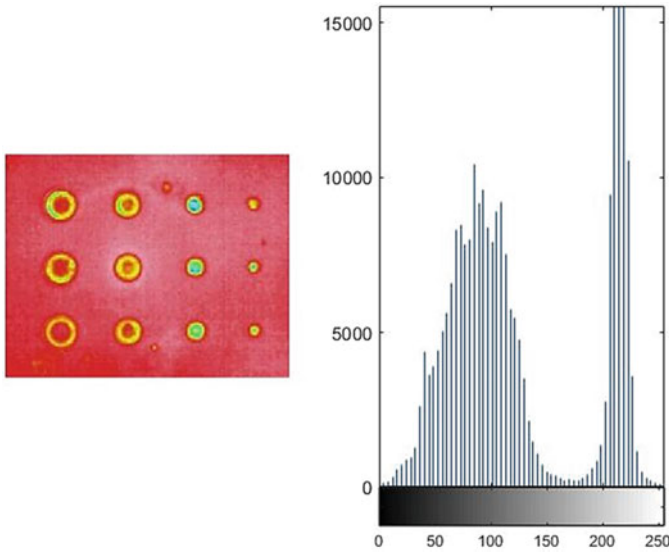
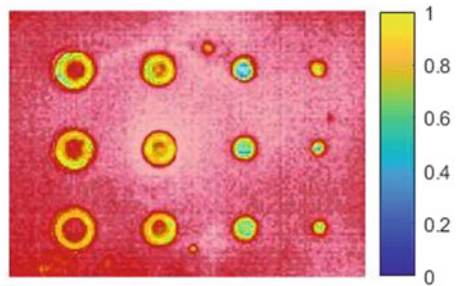


Fig. 14.5 Result in histogram before applying histogram contrast

Fig. 14.6 Result on image when applied histogram contrasts



middle portion. The contrast adjustment step will present the intensity of image values filled with wide-ranging power (0, 250). A higher image contrast level will result in a highlighted brighter look with the darkest shadow.

The histogram stretch concept is a lined normalisation which stretches to the arbitrary intensities interval of an image then fit the interval for others arbitrary intervals. This target range is the possible minimum and maximum of the image, which is 0 and 250. Figure 14.7 is the illustration of the histogram stretching concept.

The histogram equalisation contrast normalisation is non-linear. The area was stretched with high abundance intensities of the histogram, and then the area compresses with low-abundance intensities. Figure 14.8 shows the result gained at the histogram after applying the histogram contrast.

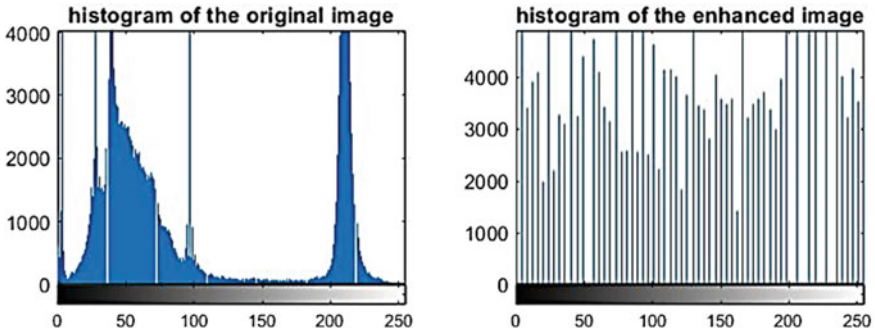


Fig. 14.7 Histogram stretching concept

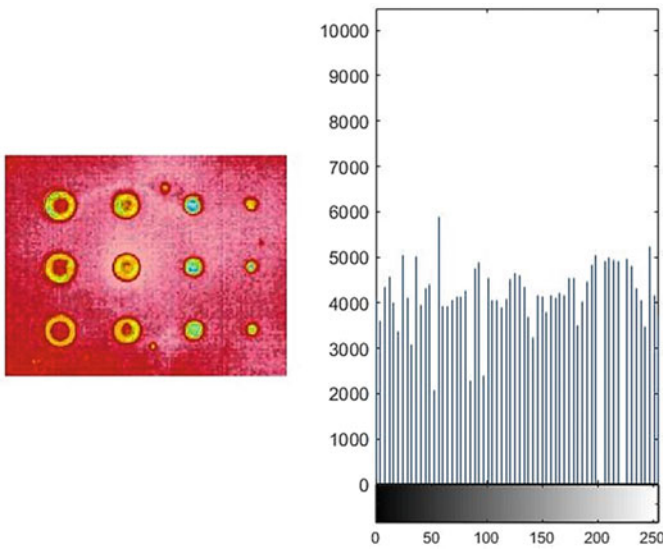
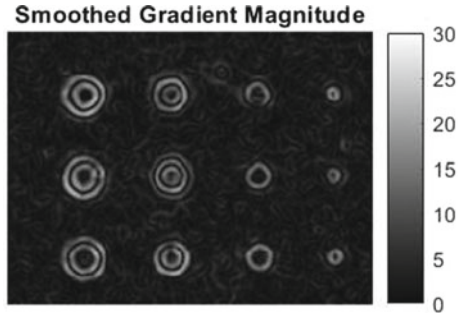


Fig. 14.8 Result in histogram after applying the histogram contrast

14.3.3 Image Segmentation and Analysis

The process on the classification of the image into different groups can be defined as the image segmentation. Plenty of researchers were focussing on the image segmentation problem solution by using the clustering method. Various methods of application are practically applied, and the K-means image segmentation algorithm is one of the most popular use methods. The K-means image segmentation algorithm is one of the unsupervised algorithm class, and from the background image, it works to segment the area of interest. The image histogram is applied to enhancement

Fig. 14.9 Smooth gradient magnitude



stretching at the picture first for improving image quality just before applying the K-means segmentation algorithm.

Figure 14.9 demonstrates how to reduce noise in the image gradient associated with the computer image gradient inclines. Features in the image were highlighted by the image gradient and this is used in many feature recognition algorithms such as a corner or edge detection. By reducing the noise gradient, calculations are important to detect the precise characteristics. This phase is to read out an image on the workspace then convert this image to greyscale form.

Object group separated is called a clustering process. The K-means segmentation algorithm detects barrier objects surrounded by each cluster as close as possible from another. The K-means segmentation algorithm specifies the cluster number for subdivided and matrix gap to measure the closeness between dual object purposes, respectively. Figure 14.10 is the result in binary image presentation. The edge pixel is represented by a white pixel and other pixels are coloured in black.

Detecting the flaws in the plate is now easier because of the noise eliminates process from the image and a smooth model is obtained for the next step. Figure 14.11 shows the result of the image segmentation. The region of the flaw is presented in colour for better defect characterisation. The defect edge is easier to recognise without distraction. Features detection and features extraction area are used in the edge detection concept. The image of the specimen part has an edge enhanced supported by automatic recognition and measurement, and the defect is detected.

Fig. 14.10 Image in binary presentation

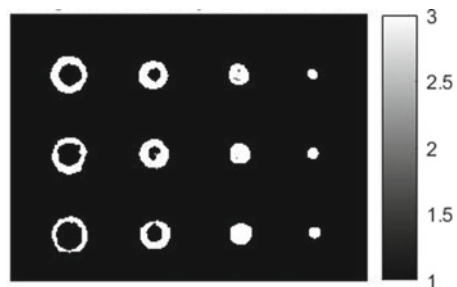
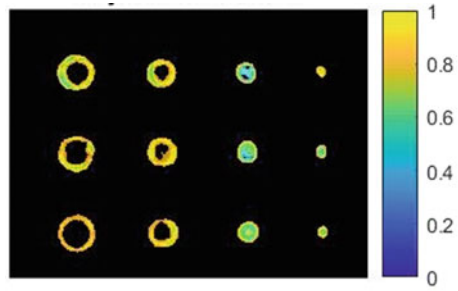


Fig. 14.11 Result of image cluster segmentation by colour



14.4 Conclusions

Every metal response to the thermal excitation is different depending on the way it has been examined. Thermography is one of the best techniques that provide excellent defect resolution based on an optical method. However, the result will strongly be affected by surface features. This paper presented the solution of the image enhancement for the thermal image. The submitted image processing is not obtaining from the raw thermogram but in the JPEG greyscale image. Such an approach enables image processing in the academic research community by using the standard MATLAB software. This method will cover the limitation of pulse thermography requirement that needs to do a repetition of the cycle and high-power pulse usage. The analysis and correlation based on pulse method have been implemented and are proven by the result shown. The image processing is able to help the researcher to visualise and carry out information for the future process and better classification. Image processing tools such as image filtering and image segmentation improve the result for enhanced thermal contrast.

Acknowledgements All of the experiment and analysis were conducted under System Engineering and Energy Laboratory (SEELab), Universiti Kuala Lumpur-Malaysian Spanish Institute and support from Yayasan Tengku Abdullah Scholarship (YTAS).

References

1. Maldague, X., et al.: Applications of infrared thermography in nondestructive evaluation. *Trends Opt Nondest. Test.* 591–609 (2000)
2. Bolleni, N.K., et al.: Environmental effects on subsurface defect detection in concrete structures using infrared thermography. *J.* (2005). <https://doi.org/10.32469/10355/5374>
3. Mulaveesala, R., et al.: Non-destructive evaluation of concrete structures by non-stationary thermal wave imaging. *Progress Electromagnet. Res. Lett.* **32**, 39–48 (2012)
4. Ghali, V.K., Mulaveesala, R.: Comparative data processing approaches for thermal wave imaging techniques for non-destructive testing. *Sens. Imaging: Int. J.* **12**, 15–33 (2011)
5. Shepard, S.M.: Enhancement and reconstruction of thermographic NDT data. *Int. Soc. Opt. Photonics* 531–535 (2002)

6. Wan, K., Qishuang, M., et al.: Data-fitting reconstruction for defect inspection of airplane aluminum structure in infrared thermographic. In: 4th IEEE Conference on Industrial Electronics and Applications. IEEE (2009)
7. Ranjit, S., Kim, W., et al.: Detection of subsurface defects in metal materials using infrared thermography. *Image Process. Finite Elem. Model.* 128–134 (2014)

Chapter 15

Alternator Performance Analysis of a Micro-Turbogenerator in Automotive Application



**Khairul Shahril, Muhammad N. A. Hamid, Mohamad Zulfikar, Adli Tajul,
and Shahril. N. Soid**

Abstract A micro-turbogenerator is a combination of an alternator and a turbocharger which is used to convert rotational mechanical energy into electrical energy. It can be configured with different prime movers such as a steam turbine, a gas turbine in single-cycle or in a combined-cycle arrangement. The primary objective of this project is to study the performance analysis of a micro-turbogenerator in automotive application and to determine the correct alternator that can supply current to generate the test rig. An experiment has been conducted to find the output current of the alternator by using an instrument and it involved certain mathematical calculations based on the output voltage and alternator power. The results show that the higher the alternator speed, the higher the output current or power produced. This concludes that with the increment of the alternator's output voltage along with the alternator's speed, the alternator is really charging up the battery. A fully charged battery should have a voltage reading above 13.7 V. Therefore, this proves that the usage of the alternator in a lower engine capacity is applicable. Besides, the higher the alternator's speed, the lower the alternator's output current. This indicates that theoretically, there are possible loads acting on the engine and the current decreased as it was consumed by the loads. In addition, the higher the alternator's output voltage, the lower the alternator's output current.

K. Shahril (✉) · M. N. A. Hamid · M. Zulfikar · A. Tajul · Shahril. N. Soid
Mechanical Section, Universiti Kuala Lumpur Malaysian Spanish Institute, 09000 Kulim, Kedah
Darul Aman, Malaysia

e-mail: khairuls@unikl.edu.my

M. N. A. Hamid

e-mail: mnajib@unikl.edu.my

M. Zulfikar

e-mail: zulfikaryusoff17@gmail.com

A. Tajul

e-mail: tajuladli@unikl.edu.my

Shahril. N. Soid

e-mail: shahrilnizam@unikl.edu.my

© The Editor(s) (if applicable) and The Author(s), under exclusive license
to Springer Nature Switzerland AG 2020

M. H. Abu Bakar et al. (eds.), *Progress in Engineering Technology II*,
Advanced Structured Materials 131,
https://doi.org/10.1007/978-3-030-46036-5_15

Keywords Alternator · Turbocharger · Micro-turbogenerator · Automotive

15.1 Introduction

A micro-turbogenerator is a combination of an alternator and a turbocharger. It is used to convert rotational mechanical energy into electrical energy. It can be configured with different prime movers such as a steam turbine, a gas turbine in single-cycle or in a combined-cycle arrangement. According to Faraday's law of induction, "An electric current is induced in a conductor in proportion to the rate of change in the lines of magnetic flux". Essentially this means that if there is relative motion between a conductor and a magnetic field, then current will be generated in the conductor. The amount of current generated is proportional to the density of the magnetic field and the speed of the relative motion between the conductor and the magnetic field.

Alternators have been applied in cars, lorries and locomotives. However, the actual performance of an alternator towards a turbocharged engine has never been tested. Thus, there was a requirement to conduct a study to find out what the actual performance of this alternator is and whether or not it boosts the turbocharger. Besides, the current produced from a micro-turbogenerator engine was never been measured. Therefore, it is important to determine the correct alternator that can supply power to the test rig so that alternator's output current can be measured. Lastly, the suitability of an alternator towards a lower engine capacity with an installed turbocharger was unsure. Therefore, by collecting data of alternator's output voltage and current can prove the suitability of an alternator towards a lower engine capacity with an installed turbocharger.

The primary objective is to study the performance of a micro-turbogenerator in automotive application. This will lead to several other objectives which are to determine the correct alternator that can supply current to generate the test rig. Besides, another objective of this project is to fabricate the position of the alternator in the test rig. Lastly, the objective of this project is to measure the current produced by the alternator.

15.2 Literature Review

For the turbocharger performance, Kusztelan [1] carried out a one-dimensional analysis using the AVL Boost software on a series of compression and spark ignition engines utilizing a manufacturer fitted single-entry turbocharger and a modified twin-entry variety, the latter adopting two turbine housing inlet ports. The model reconstruction using the AVL Boost considers parameters that accurately represent the physical engine conditions including manifold geometry, turbocharger flow maps and combustion chamber characteristics, etc. Model validations have been made for a manufacturer single-entry turbocharger configuration to predict the maximum engine

power and torque, in comparison with available manufacturer data and analytical calculations. Further studies concentrated on engine performance comparisons between single- and twin-entry turbochargers in terms of torque, shaft speed and compressor efficiency and at low engine speed conditions typically in a range of 1000–3000 rpm. It was found that on average the engine response has been increased by 27.65%, 5.5% and 5.5% in terms of turbine shaft speed, engine power and torque, respectively, which implies improved “drivability” of the vehicle. This study reveals the potential benefits of adopting a twin-entry turbocharger and the findings would be useful for both industry and academic communities [1–4].

For electric-turbocharger performance, according to An et al., Naomichi et al., engine downsizing through supercharging began to cope with the yearly enhanced improvement in fuel consumption and exhaust gas. However, the existing turbochargers face a time lag and EGR response delay while proper control is difficult. With the addition of electric power to assist the existing exhaust gas turbochargers to utilize the high-speed response of an electric motor that significantly improves fuel consumption and transient response is to be expected. In this research, an electric compressor is combined with an inverter and a high efficiency motor with a conventional 12 V electrical system, maximum power of 3 kW and maximum speed of 90,000 rpm. For evaluation, it was conducted as a two-stage turbocharging system by combining it with an existing exhaust gas turbocharger. A variety of comparison of the two-stage turbocharging system during the development of two-stage electric-turbocharging system has been made including the arrangement of the electric compressor were made. The pros and cons of it are discussed in this paper [5].

As shown in Fig. 15.1, the gasoline engine with a two-stage electric-turbocharger maintains a stable performance and improves the transient response by 42% compared to a gasoline engine with a waste turbocharger. Figure 15.2 shows that the gasoline engine with a waste gate turbocharger with no EGR as base line, in case of EGR at 10%, engine torque was decreased by 19% while it shows an improvement in fuel consumption of approximately 10%. Contrarily, the gasoline engine with a

Fig. 15.1 Engine downsizing effect (GT-Power calculation)

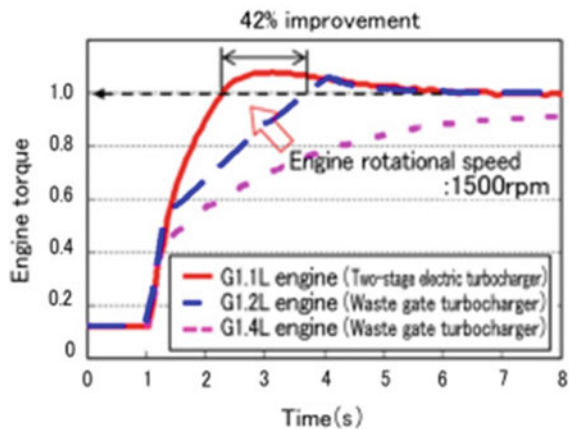
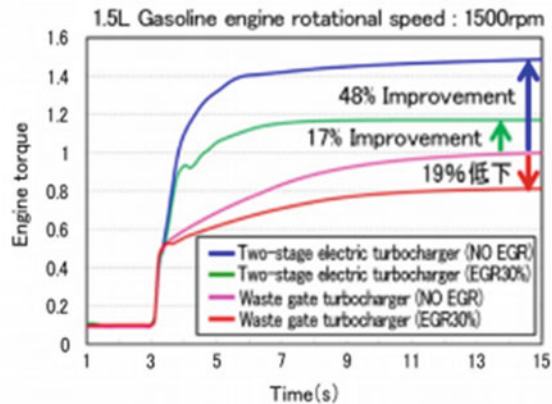


Fig. 15.2 Comparison of transient response change through EGR (GT-Power calculation)



two-stage electric-turbocharger shows 48% torque increase with no EGR and a 17% torque increase even with EGR at 30% and shows an improvement of approximately 30% compared with gasoline NA engine. The total displacement can be made smaller through the turbocharger Mitsubishi Heavy Industries Technical Review Vol. 52 No. 1 (March 2015) 76 downsizing effect, and the friction loss, heat loss, pumping loss and exhaust energy loss can be improved [5].

For the alternator performance, based on V. Hajek et al., they stated there is a reliability problem with common types of generators in hard conditions. It shows possibilities of construction changes that should increase the machine reliability. This contribution is dedicated to the study of brushless alternators for the automotive industry. There are described problems with the usage of common types of alternators and main benefits and disadvantages of several types of brushless alternators in this paper. Authors come to the conclusion that there is a requirement in making a wide research on the topic of brushless alternators. This first solution promises only a small increase of weight and axial length, but after the planned optimization is possible to remove also this minus. In terms of further development prospects of alternators this proposal represents a partial phase brushless alternator for variant liquid cooled machines. The tendency for using fluid cooling alternators is increasingly beginning to receive more concrete contours, since cooling air, when rising claims on performance and limited dimension are considered, becomes a deficient. The alternator would then be connected to the cooling system of an internal combustion engine vehicle. Liquid cooling compared to air cooling is more efficient and leads to an increase in the ratio w/kg and significantly reduce the alternator noise [6–11].

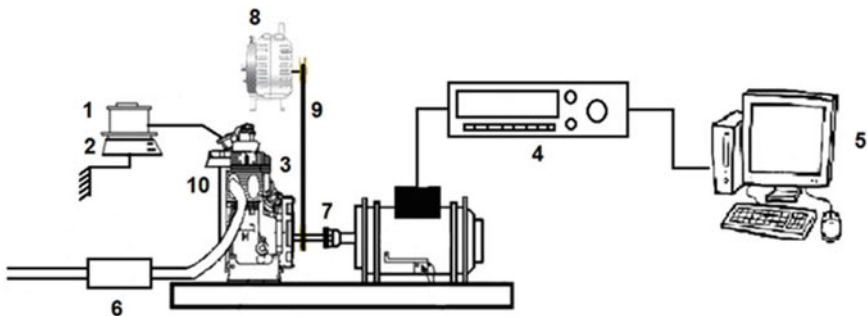
15.3 Experimental Set-Up

Figure 15.3 shows the performance analysis of the micro-turbocharger experiment layout. The alternator is connected to the engine shaft through a chain and sprocket.

15.3.1 Result Measurement

Figure 15.4 shows mechanical installation of alternator and Fig. 15.5 shows the process of alternator’s speed readings measurement. While the alternator was running, a tachometer is directed towards a reflecting tape attached to the alternator.

Figure 15.6 shows the connection of the multimeter (label M) during the reading measurement of the alternator’s output voltage. The positive terminal of the multimeter is connected with the positive terminal of the battery while the negative terminal of the multimeter is connected with the negative terminal of the battery. The negative terminal of the alternator is connected with the negative terminal of the battery. In order to take the voltage reading, the multimeter is set to voltage reading.



No.	Part Name	Quantity
1	Fuel tank	1
2	Tank Load Cell	1
3	Lifan Engine 160cc	1
4	Dynamometer Controlle	1
5	Personal Computer	1
6	Exhaust Pipe	1
7	Engine Shaft	1
8	Alternator	1
9	Motorcycle Chain	1
10	Turbocharger	1

Fig. 15.3 Schematic diagram of performance analysis of micro-turbocharger experiment

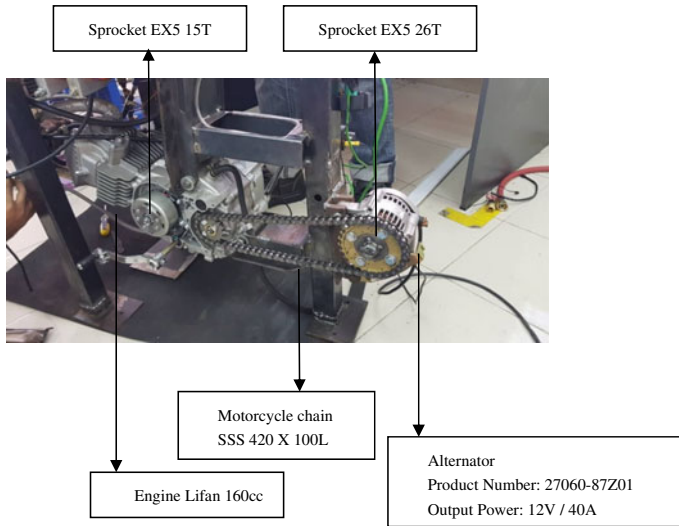
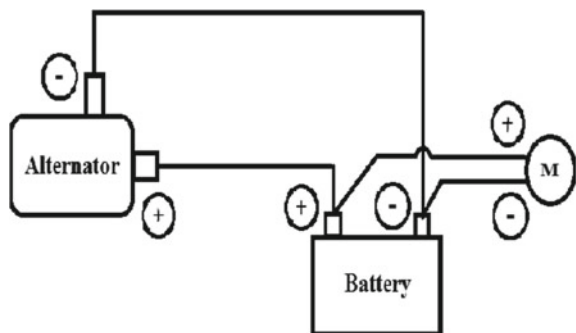


Fig. 15.4 Real mechanical installation



Fig. 15.5 Alternator's speed reading measurement

Fig. 15.6 Alternator's output voltage reading measurement layout diagram



15.4 Results and Discussion

The test rig is set up in order to measure the output voltage and rpm of the alternator by setting a different engine speed in rpm. The obtained results were tabulated and represented in line charts. Besides the mentioned data, other parameters were calculated which is the power and output current of the alternator. When the voltage causes the current to flow, energy is converted. This is described as power. The unit of power is the Watt (W). As with Ohm's law, any value can be calculated if the other two are known. Since there were no loads on the engine and in order to obtain the alternator's power, it can be calculated by multiplying the provided alternator current 40 A together with provided voltage 12 V. Below is the equation to calculate the alternator power.

$$P = IV \quad (15.1)$$

where P is alternator power (W), I is alternator output's current (A) and V is alternator output voltage (V).

Hence,

$$P = IV = (40)(12) = 480 \text{ Watts} \quad (15.2)$$

As stated above, the alternator's power was calculated and fixed as 480 Watts. Therefore, the output current can be calculated by using the same Eq. (15.1). One of the examples of the calculated output current would be obtained from Eq. (15.1);

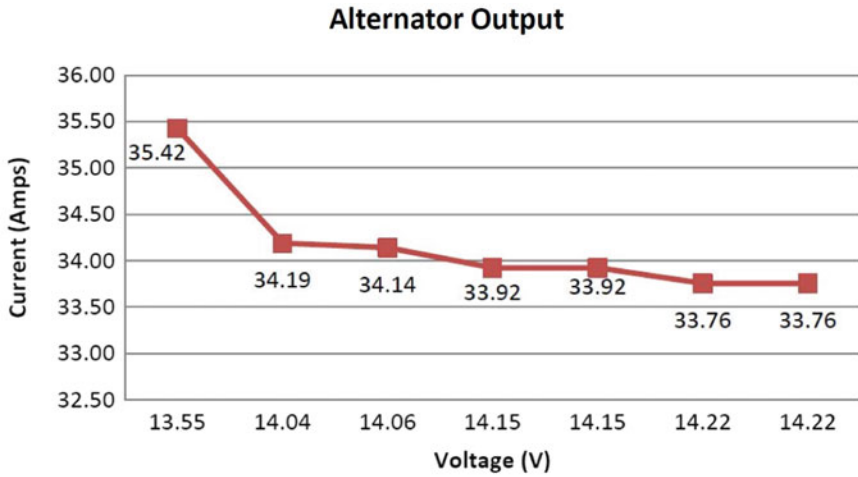
$$I = \frac{P}{V} = \frac{480}{13.55} = 35.42 \text{ A}$$

Table 15.1 shows the summary of measured and calculated data.

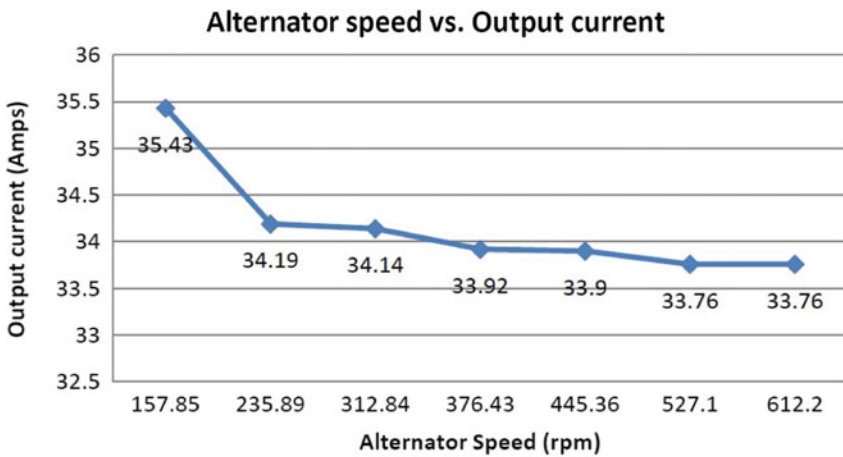
Figure 15.7a shows the relationship between the alternator's speed and the output current while Fig. 15.7b shows the relationship between alternator's outputs.

Table 15.1 Summary of result

Engine speed (RPM)	Average alternator speed (RPM)	Voltage (V)	Power (W)	Current (AMPS)
1000	157.85	13.55	480	35.42
1500	235.89	14.04	480	34.19
2000	312.84	14.06	480	34.14
2500	376.43	14.15	480	33.92
3000	445.36	14.15	480	33.92
3500	527.10	14.22	480	33.76
4000	612.20	14.22	480	33.76



(a)



(b)

Fig. 15.7 Results. **a** Graph of alternator speed versus output current. **b** Graph of alternator’s outputs

Based on Fig. 15.7a, the higher the alternator’s speed, the lower the alternator’s output current. This indicates that theoretically, there are possible loads acting on the engine and the current was consumed by the loads.

Meanwhile, Fig. 15.7b shows that the higher the alternator’s output voltage, the lower the alternator’s output current. This means that the battery charged even when theoretically there are loads acting on the engine. Thus, once again, this proves that

the usage of an alternator in a lower engine capacity is applicable as it is able to charge the battery during consumption of current by loads.

15.5 Conclusion

The primary objective of this project is to study the performance a micro-turbogenerator in automotive application and to determine the correct alternator that can supply the current to generate the test rig. To achieve this, an alternator with the smallest size was selected to match with the small motorcycle engine capacity and a test rig was set up at which the engine is connected with the alternator using a chain and sprocket.

The result shows that the faster the alternator, the more power it can produce. With the increment of the alternator's output voltage along with the alternator's speed, this indicates that the alternator really charged the battery. A fully charged battery should have a voltage reading above 13.7 V. The normal battery voltage is 12 V. The alternator's output voltage also means an input battery voltage. The alternator significantly charges the battery starting from an engine speed of 1000 rpm. In addition, this shows that there is enough power to supply load to the engine as at the engine speed of 1500 rpm, the output voltage reaches 14 V and increases along the engine speed. This also proves that the usage of an alternator in a lower engine capacity is applicable.

Besides, the higher the alternator's speed, the lower the alternator's output current. In addition, the higher the alternator's output voltage, the lower the alternator's output current. This means that the battery was charged even when theoretically there are loads acting on the engine. This proves that the usage of an alternator in a lower engine capacity is applicable as it is able to charge the battery during consumption of current by loads.

References

1. Kusztelan, A., Marchant, D.: Increases in low speed response of an IC engine using a Twin-entry turbocharger. In: *Proceedings of the World Congress on Engineering*, vol. III, p. 6 (2012)
2. Muqem, M.: Turbocharging with air conditioner assisted intercooler. *IOSR J. Mech. Civ. Eng. (IOSRJMCE)* 2(3), 38–44 (2012)
3. Shaaban, S., Seume, J.: Impact of turbocharger non-adiabatic operation on engine volumetric efficiency and turbo lag. In: Han, J.C. (ed) *International Journal of Rotating Machinery*. p 11 (2012)
4. Serrano, J.R., Olmeda, P., Arnau, F.J., Dombrovsky, A., Smith, L.: Turbocharger heat transfer and mechanical losses influence in predicting engines performance by using one-dimensional engines performance simulation codes. *Energy* 204–218 (2015)
5. Byeongil, A.N., Naomichi, S.: Development of two-stage electric turbocharging system for automobiles. *Mitsubishi Heavy Ind. Tech. Rev.* 52(1), 71–76 (2015)

6. Spinner, G., Dahinten, F.: Electrified boosting systems in today's and future. In: 2018 Thirteenth International Conference on Ecological Vehicles and Renewable Energies (EVER), p. 5 (2018)
7. Katsanos, C.O., Hountalas, D.T.: Simulation of a heavy-duty diesel engine with electrical turbocompounding system using operating charts for turbocharger components and power turbine. *Energy Convers. Manage.* 712–724 (2013)
8. Pasini, G., Lutzemberger, G.: Evaluation of an electric turbo compound system for SI engines: a numerical approach. *Appl. Energy* 527–540 (2016)
9. Van Arsie, Cricchio, A.: Evaluation of CO₂ reduction in SI engines with electric turbo-compound by dynamic powertrain modelling. *IFAC-PapersOnLine* 93–100 (2015)
10. Arsie, I., Cricchio, A.: Modeling analysis of waste heat recovery via thermo-electric generator and electric turbo-compound for CO₂ reduction in automotive SI engines. *Energy Procedia* 81–88 (2015)
11. Hajek, V., Hajek, V., Vitek, O., Mach, M.: Brushless alternator in automotive applications. In: 2013 Eighth International Conference and Exhibition on Ecological Vehicles and Renewable Energies (EVER) (2013)

Chapter 16

Experimental Study of the Engine Performance Enhancement by Using a Micro-turbocharger System



Khairul Shahril, S. N. Soid, Khairul Akmal, Muhammad N. A. Hamid, and W. Faradiana

Abstract This project deals with an experimental study of a micro-turbocharger test rig for engine performance with and without a turbocharger system. In order to achieve higher performance, bigger engines are needed. With the turbocharger, the performance of the engine can be increased without the need of a bigger engine. This is called a downsize. Therefore, the objective of this research work is to develop a micro-turbocharger test rig using a motorcycle engine for laboratory usage to evaluate the performance of the motorcycle engine with and without turbocharger system. In order to fabricate the test rig, the finite element method (FEM) was chosen as the method to study the stress and displacement of the structure before performing an action for the fabrication. Moreover, in this project, the turbo IHi RHF3 and Lifan 160 cc motorcycle engine was selected according to the required specification. The engine performance such as torque, brake power, mean effective pressure, fuel consumption, specific fuel consumption and brake thermal efficiency was measured. The test data were collected by using a dynamometer controller. All the data of the engine performance were collected, and some calculations were made to obtain the resulting power after installing the turbocharger.

Keywords Single-Cylinder petrol engine · Turbocharger · Engine performance · Dynamometer testing · Test rig

K. Shahril (✉) · S. N. Soid · K. Akmal · M. N. A. Hamid · W. Faradiana
Mechanical Section, Universiti Kuala Lumpur Malaysian Spanish Institute, Kulim Hi-Tech Park,
09000 Kulim, Kedah, Malaysia
e-mail: khairuls@unikl.edu.my

S. N. Soid
e-mail: shahrilnizam@unikl.edu.my

K. Akmal
e-mail: khairulakmal@unikl.edu.my

M. N. A. Hamid
e-mail: mnajib@unikl.edu.my

W. Faradiana
e-mail: wfaradiana@unikl.edu.my

16.1 Introduction

The most common internal combustion engines (ICE) use fossil fuel such as gasoline or diesel. In the ICE system, the compression stroke of the engine is the main compression that every engine performs an additional compressor feeding into the intake of the engine, will increase the total compression ratio of the engine system. This is called a pressure boost. The combustion process will produce heat and is capable of transforming the heat into useful work. The engine power is proportional to the amount of air and fuel that can get into the cylinders. All things being equal, larger engines flow more air and as such will produce more power [1, 2]. In this project, the four-stroke horizontal motorcycle engine with 160-centimeter cubic has been used in order to analyze the performance of the engine with and without the turbocharger. By installing a turbocharger, the small engine can produce more power like a big engine performance [3, 4]. By using a turbocharger, the energy recovery systems harvest waste from the exhaust system and boost up the engine performance and simultaneously increase compression for the engine. This is called downsizing. Higher compression engines need a higher density of the intake gas. Therefore, by increasing the density of the intake gas, it will allow more power per cycle of the engine. The current test rig for the micro-turbocharger engine performance is developed for vehicles mainly used in a car engines. The existing test rig is not capable of measuring the performance of the micro-turbocharger. By developing the micro-turbocharger test rig, it can measure the performance of the engine with and without the turbocharger. In order to achieve a higher performance, bigger engines are needed. With the turbocharger, the performance of the engine can be increased without the need for a bigger engine. It will bring a great benefit for the future study in order to study the engine performance with the turbocharger. There is a method for increasing the engine power performance which is by increasing the volume of air entering into the cylinder and increasing the fuel intake proportionately. This is exactly what the turbocharger does where it increases the volumetric efficiency of an engine in a naturally aspirated engine [5].

16.2 Literature Review

The aim using of micro-turbocharger is to increase the air: fuel ratio by increasing the power using the exhaust gas of the engine passing through the turbine compressor arrangement. This compressor compresses the fresh air and sends it to the carburetor [6]. Based on the experiment, the characteristic curve for Suzuki engine with and without turbocharger for improving efficiency is shown in Fig. 16.1.

The petrol consumption and emission rate have been increased day by day due to the increased number of motorcycles. In addition, an experimental study has been performed to investigate the used of the exhaust gas to rotate a turbine thus rotating a compressor for supplying compressed air to the inlet. The turbocharger increases

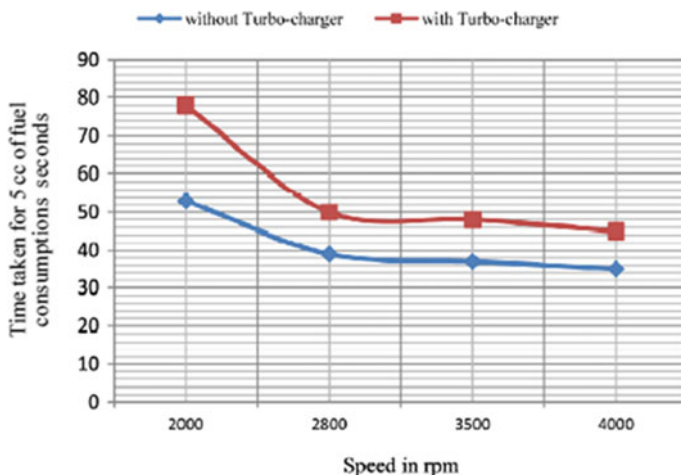


Fig. 16.1 Characteristic curve for Suzuki engine with and without turbocharger (improving efficiency). Adapted from [6]

the pressure at the point where air enters the cylinder, thereby increasing the pressure gradient across the intake valves and thus more air enters the combustion chamber [6, 7].

There is a large volume of published studies describing turbochargers. Reviewing the available literature on the fabrication of turbocharger for two-wheeler, it is which stated that a turbocharger is a device that increases the overall performance of the engine by reusing the exhaust heat to drive the turbine [8, 9]. The power of the engine will increase by the installation of a turbocharger that is reusing the exhaust gas which results in less fuel consumption. The present finding also supports the conclusion that the brake specific emissions of the turbocharged engine are all lower than those of the naturally aspirated engine [10]. However, emission concentrations in the turbocharged engine are higher, except for HC concentrations. This suggests that the increase in power will compensate for the increase in emissions. In addition, the peak torque and power are boosted by roughly 97% and 95%, respectively. Their increase in other points of the engine speed range is lower, especially in low-end speeds. This is due to the policy in choosing the turbocharger which has been focused on boosting the maximum power. This policy leads to larger turbochargers which operate well in high-end speeds. Figures 16.2 and 16.3 show the increasing trend between brake power and brake torque in the case of turbocharged against naturally aspirated engines.

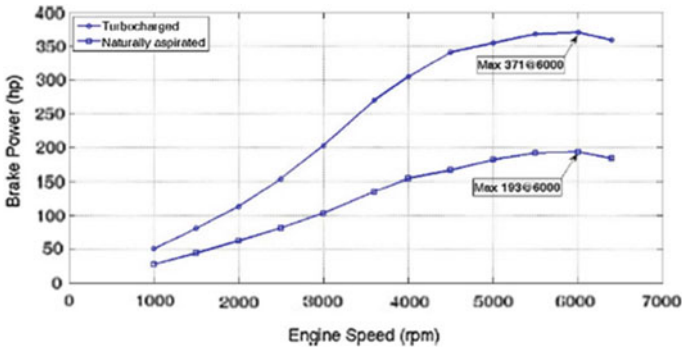


Fig. 16.2 Brake power in turbocharger and naturally aspirated engine. Adapted from [10]

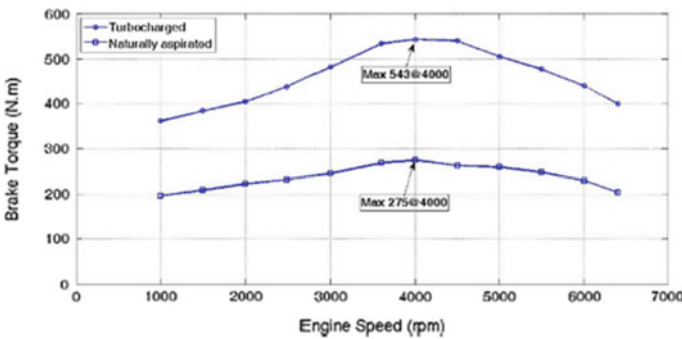


Fig. 16.3 Brake torque in turbocharger and naturally aspirated engine. Adapted from [10]

16.3 Experimental Setup

16.3.1 Motorcycle Engine

An engine or motor is a machine designed to convert one form of energy into chemical or heat energy, which is exhaust gas. In this project, a new Lifan engine with 160 cc was selected according to the specification needed. Table 16.1 shows the specification of the engine.

16.3.2 Turbocharger (Spinning Turbine)

As the turbocharger, the model Kubota Excavator Various RHF3 Turbo VE410128 CK30 from IHi Japan was chosen as a device that converts chemical or heat energy to the kinetic energy. Table 16.2 shows the specification of this turbocharger.

Table 16.1 Engine Lifan specification

Parameter	Specification
Type	Single-cylinder; four-stroke; oil-cooled
Bore and stroke	60 mm × 57 mm
Engine displacement	161.2 ml
Compression ratio	9.5:1
Primary reduction	3.722
Max power & rotating speed	10.3 kW/9500 r/min
Max net power & rotating speed	10 kW/9500 r/min
Rated power & rotating speed	9.5 kW/9000 r/min
Max torque & rotating speed	11.5 Nm/7000 r/min
Idling speed	1500 r/min
Ignition	CDI
Clutch	Hand-clutched start at any gear 160 cc
Exhaust	One-into one
Starter	Kick start
Lubrication	Pressure or splash
Transmission	Four-speed continuous

Table 16.2 Turbo IHi RHF3 specification

Parameter	Specification
Part number	VB410088
V-SPEC	VQ38
Turbo model	RHF3-44001P7NRBRL2616CDZ
kW	63HP
Angle α (compressor housing)	240°
Angle β (turbine housing)	331°
Turbine housing AR	7
Inducer diameter (<i>A</i>)	32.9 mm
Exducer diameter (<i>B</i>)	29.5 mm
Tip height (<i>C</i>)	4.6 mm
Journal bearing diameter (<i>D</i>)	6.3 mm
Compressor Wheel Bore	4.4 mm

16.3.3 Test Rig

The test rig is an apparatus used for assessing the performance of a piece of mechanical equipment. For the test rig, the finite element method (FEM) has been used in order to test the structure of the test rig strength and displacement when some loads

have been applied. The fabrication of the test rig is manually fabricated in order to suit with the dynamometer and also the engine position.

16.3.4 Project Setup Overview

Figure 16.4 shows the experimental setup in which the turbocharger is installed. The turbine inlet of the turbocharger is connected with engine exhaust manifold with the help of stud nut and welding. The turbine shaft is coupled to a compressor, which draws in atmospheric air, compresses it, and then supplies it to the engine. The turbocharger compressor outlet is connected with a hosepipe to the carburetor air. An air filter is connected with the carburetor inlet section to prevent other foreign particles from entering the intake system. The parameter of the engine performance will be analyzed and measured by using the dynamometer. Firstly, the engine with the turbo IHi RHF3 will be mounted to the test rig. Then, the engine with test rig will be assembled with the dynamometer, and the performance of the engine will be analyzed. After that, the engine performance will be tested without the turbocharger in order to compare the result with and without the turbocharger system. All the data shown on the computer will be used for the analyses. The fuel also will be measured by the fuel load tank, and the data will be generated on the computer to see the fuel consumption of the engine with and without the turbocharger system. In this set up the output of the engine exhaust gas is given to the input of the turbine blades where the turbine shaft is coupled to the compressor. The compressor draws in ambient air and pumps it into the intake manifold at increased pressure, resulting in an excess amount of air entering the cylinders on each intake stroke thereby producing proper combustion.

Fig. 16.4 Experimental Setup



16.4 Results and Discussion

The performance test is done on the four-stroke, single-cylinder petrol engine in order to study and compare its performance under various engine speeds with and without the turbocharger system. The test rig consists of a 160 cc SI engine which is fitted on a dynamometer shaft by using a sprocket 14-T. There are four important performance parameters of the engine represented in this section such as the fuel consumption, specific fuel consumption, brake thermal efficiency, brake power and torque. The educational test rig is set up in order to calculate the motorcycle engine performance with and without the turbocharger system by using a dynamometer. The speeds of the motorcycle engine for fuel consumption are set up from 2500 to 5000 revolution per minute (rpm) by an increment of 500 for each stage. Meanwhile, the speeds for engine performance are set up from 3000 until 6500 revolutions per minute. The results are represented in Tables 16.3, 16.4, 16.5 and 16.6. All the data are acquired by using a dynamometer controller. The outcome of this study will be more explained below.

Table 16.3 Fuel consumption of turbocharger system for RON 95

Revolution Per Minute (rpm)	RON 95 Turbocharger		
	W1 (kg)	W2 (kg)	mf (kg)
2500	0.127	0.122	0.000167
3000	0.12	0.114	0.0002
3500	0.112	0.105	0.000233
4000	0.106	0.1	0.0002
4500	0.098	0.092	0.0002
5000	0.091	0.08	0.000367

Table 16.4 Fuel consumption of turbocharger system for RON97 and RON 100

Revolution per minute (rpm)	RON 97 Turbocharger			RON 100 Turbocharger		
	W1 (kg)	W2 (kg)	mf (kg)	W1 (kg)	W2 (kg)	mf (kg)
2500	0.205	0.202	1.00E-04	0.31	0.308	6.66667E-05
3000	0.197	0.193	0.000133	0.299	0.296	0.0001
3500	0.188	0.184	0.000133	0.292	0.289	0.0001
4000	0.176	0.171	0.000167	0.287	0.284	0.0001
4500	0.167	0.16	0.000233	0.282	0.278	0.000133333
5000	0.154	0.147	0.000233	0.275	0.27	0.000166667

Table 16.5 Fuel consumption by using RON 95 for without turbocharger system

Revolution per minute (rpm)	RON 95 W/O Turbocharger		
	W1 (kg)	W2 (kg)	mf (kg)
2500	0.079	0.078	3.3333E-05
3000	0.073	0.071	6.6667E-05
3500	0.067	0.064	6.6667E-05
4000	0.064	0.061	0.0001
4500	0.06	0.055	0.00016667
5000	0.056	0.05	0.0002

Table 16.6 Fuel consumption by using RON 97 and RON 100 for without turbocharger system

Revolution Per Minute (rpm)	RON 97 W/O Turbocharger			RON 100 W/O Turbocharger		
	W1 (kg)	W2 (kg)	mf (kg)	W1 (kg)	W2 (kg)	mf (kg)
2500	0.144	0.143	3.33E-05	0.172	0.171	3.33333E-05
3000	0.142	0.14	6.67E-05	0.165	0.164	3.33333E-05
3500	0.138	0.136	6.67E-05	0.162	0.16	6.66667E-05
4000	0.137	0.134	0.0001	0.158	0.157	3.33333E-05
4500	0.133	0.13	0.0001	0.152	0.15	6.66667E-05
5000	0.128	0.123	0.000167	0.149	0.144	0.000166667

16.4.1 Fuel Consumption

By investigating the graph, the minimum fuel consumption takes place at 4000 rpm for RON 100 without a turbocharger, and the maximum fuel consumption takes place at 5000 rpm for RON 95 without turbocharger. Between RON 95 and RON 97, it is proven that RON 100 is the most suitable fuel to be used for naturally aspirated engines. This statement can be supported by the result that has been gained from the analysis that has been done. The result can be seen clearly from the graph in Fig. 16.5. Based on the conducted study, RON 100 also has the highest dosage of additives compared to other brands of gasoline. The higher dose of additives also means more effective cleaning power, better combustion enhancement and less friction compared to RON 95 and RON 97. Even by using the turbocharger system, the fuel consumption for RON 100 is lower compared to the others RON without the turbocharger system. Therefore, by adding a turbocharger in-vehicle system, it can be concluded that the fuel consumption has higher usage compared to the system without the turbocharger. But, there is some fuel that helps to reduce the fuel consumption when using a turbocharger system such as RON 97 that seems much better compared to RON 95. Overall, there are advantages and disadvantages using a turbocharger system in vehicle nowadays (Tables 16.7, 16.8, 16.9 and 16.10).

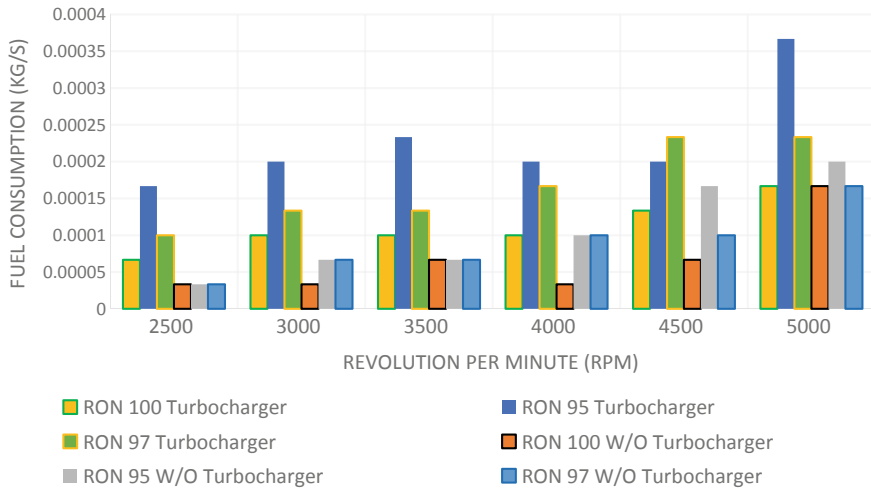


Fig. 16.5 Overall fuel consumption

Table 16.7 Data collection for the system without turbocharger

No.	Dynamometer speed w/o turbocharger (rpm)	WOT torque w/o turbocharger (Nm)	Engine speed w/o turbocharger (rpm)	Engine torque w/o turbocharger (Nm)	Brake power w/o turbocharger (W)
1	808.63	25.06	2990.26	6.755	2115.1723
2	943.4	24.77	3487.4	6.677	2438.2795
3	1078.17	23.53	4021.64	6.342	2671.0428
4	1212.94	22.45	4503.94	6.051	2854.0703
5	1347.7	21.69	5004.79	5.846	3064.0873
6	1482.48	20.11	5498.22	5.42	3120.9723
7	1617.25	19.53	5980.52	5.264	3296.8327
8	1752.02	17.57	6529.6	4.736	3238.2775

16.4.2 Engine Power, Torque and Brake Mean Effective Pressure

Figures 16.6 and 16.7 show typical power and torque versus engine speed curves. As seen on the graph, the power of the engine slightly increases as the engine speed increases. This is because if the throttle setting is higher, it means that the engine speed is also higher. However, the graph also shows that the maximum power and torque that the engine yields is located at a certain point and then drops back down as the speed increases further. Figures 16.6 and 16.7 reveal the brake power and brake torque in

Table 16.8 Data collection for the system with turbocharger

No.	Dynamometer Speed with turbocharger (rpm)	WOT Torque with turbocharger (Nm)	Engine Speed with turbocharger (rpm)	Engine Torque with turbocharger (Nm)	Brake Power with turbocharger (W)
1	808.63	30.19	3005.1	8.137	2560.81
2	943.4	29.71	3498.53	8.008	2933.89
3	1078.17	28.95	3999.38	7.803	3268.11
4	1212.94	27.39	4518.78	7.383	3493.57
5	1347.7	26.87	4989.95	7.243	3784.6
6	1482.48	25.56	5513.06	6.889	3977.49
7	1617.25	24.16	6010.2	6.512	4098.66
8	1752.02	23.43	6451.69	6.315	4266.79

Table 16.9 Specific fuel consumption without turbocharger data

Revolution per minute (rpm)	mf w/o Turbocharger (kg/s)	Brake power w/o turbocharger (W)	SFC w/o turbocharger (kg/Wh)
3000	6.66667E-05	2115.172	0.000113466
3500	6.66667E-05	2438.28	9.84301E-05
4000	0.0001	2671.043	0.000134779
4500	0.0001	2854.07	0.000126136
5000	0.000166667	3064.087	0.000195817

Table 16.10 Specific fuel consumption with turbocharger data

Revolution per minute (rpm)	mf with Turbocharger (kg/s)	Brake power with turbocharger (W)	SFC with turbocharger (kg/Wh)
3000	0.000133333	2560.81	0.000187441
3500	0.000133333	2933.89	0.000163605
4000	0.000166667	3268.11	0.000183592
4500	0.000233333	3493.57	0.000240442
5000	0.000233333	3784.60	0.000221952

the turbocharged engine increase substantially compared to the engine without the turbocharger system. The maximum power in the turbocharger condition is 7.76 HP at 6451.69 rpm, while the maximum power in the engine without the turbocharger system is 5.89 HP at 6529.6 rpm. The maximum brake torque in the turbocharged engine is 8.137 Nm at 3000 rpm, while the naturally aspirated engine is 6.755 Nm at

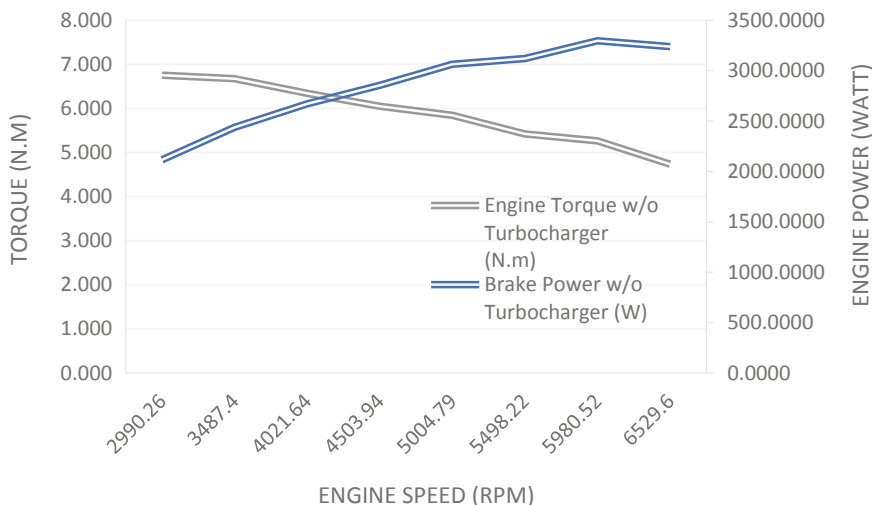


Fig. 16.6 Engine power and torque curve without turbocharger system

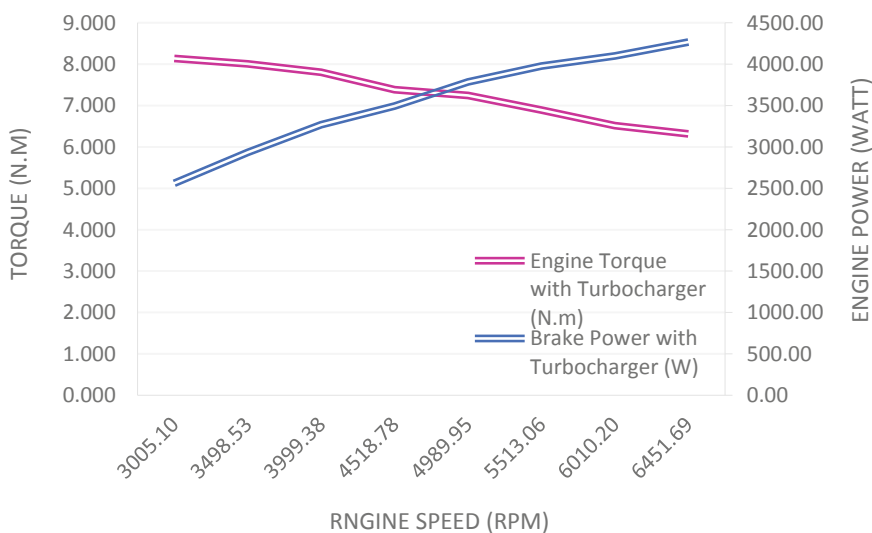


Fig. 16.7 Engine power and torque curve with turbocharger system

3000 rpm. In addition, it is interpreted from these figures that higher ranges of brake power and torque are accessible with the turbocharged engine.

By plotting the graphs between brake mean effective pressure with and without turbocharger system versus engine speed in rpm, it is clear that the brake mean effective pressure has improved significantly for all speeds right from 3000 rpm until 6500 rpm. The brake mean effective pressure for the turbocharger system was

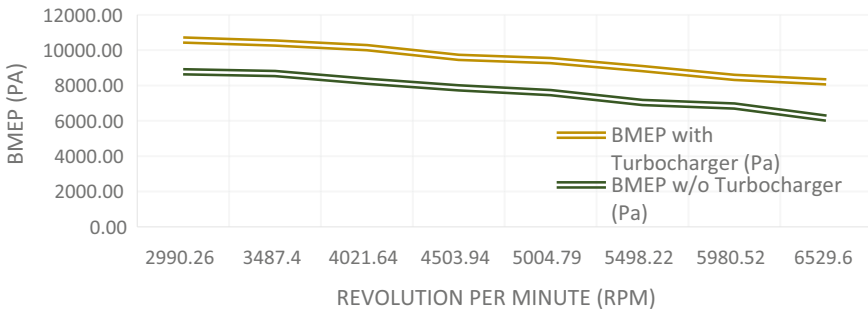


Fig. 16.8 Brake mean effective pressure with and without turbocharger system

slowly decreased when the engine speed increased while the brake mean effective without turbocharger system was gradually decreased as seen in Fig. 16.8. The brake mean effective pressure was improved by 25.01% at the maximum engine speed of 6500 rpm. The BMEP is purely theoretically and has nothing to do with the actual cylinder pressure.

16.4.3 Specific Fuel Consumption

While measuring the specific fuel consumption, it was observed that the brake specific fuel consumption decreased in these experimental conditions with an increase in engine speed. However, it is slightly increased up to 4000 rpm as the engine speed increased. From the graph shown in Fig. 16.9, both the graphs for the naturally aspirated and turbocharger increased and decreased from 3000 to 3999 rpm but started to change at 4000 rpm. For the turbocharger, the graph started to increase at 4000 rpm



Fig. 16.9 Specific fuel consumption

while the naturally aspirated decreased at 4000 rpm. This change continues up to 5000 rpm. From the result analysis, it is shown that the specific difference between the naturally aspirated and turbocharger at the initial speed is around 39.47% and 11.78% at the final speed. It is being recorded a 27.70% difference of specific fuel consumption between the initial and final speed at the range of 3000 rpm (initial) to 5000 rpm (final). Furthermore, the results obtained from the experiment conclude that the lowest specific fuel consumption with and without turbocharger for the entire engine speed was observed at 3500 rpm. From this experimental result, it can be concluded that, the higher the specific fuel consumption, the more power it will produce, which leads to less efficiency.

16.5 Conclusions

In order to accomplish this goal, a model of the test rig with motorcycle engine was built and dynamometer as the testing machine in order to get the experimental data. The most important conclusions of this research are as follows. For comparison between turbocharged and naturally aspirated:

1. The minimum fuel consumption takes place at 4000 rpm for RON 100 without a turbocharger, and the maximum fuel consumption takes place at 5000 rpm for RON 95 without turbocharger (Fig. 16.5).
2. By using the turbocharger system, the fuel consumption for RON 100 is lower compared to the others RON without the turbocharger system (Fig. 16.5).
3. The peak torque is boosted roughly 17%, respectively, of the engine with turbocharger compared to the without turbocharger system.
4. The brake power for the turbocharger system gradually increased when the engine speed increased while the brake power without the turbocharger system slowly increased. The brake power was improved 24.10% at the maximum engine speed of 6500 rpm.
5. The brake mean effective pressure for the turbocharger system was slowly decreased when the engine speed increased while the brake mean effective without turbocharger system was gradually decreased. The brake mean effective pressure was improved 25.01% at the maximum engine speed of 6500 rpm (Fig. 16.7).
6. The difference of specific fuel between the naturally aspirated and turbocharger at the initial speed is around 39.47% and 11.78% at the final speed. It is being recorded that 27.70% difference of specific fuel consumption between the initial and final speed at the range of 3000 rpm (initial) to 5000 rpm (final) (Fig. 16.9).

References

1. Vishwakarma, M., Kumar, R.P.: Internal combustion engine. *Int. Res. J. Eng. Technol.* **21**, 1–19 (1985). e-ISSN
2. Pulkrabek, W.W.: *Engineering Fundamentals of the Internal Combustion Engine*. Prentice Hall, Upper Saddle River (2004)
3. Saini, A., Shakti, P., Kulshrestha, H.: Turbocharged single cylinder SI engine. *Int. J. Adv. Technol. Eng. Res.* **1** (2014)
4. Israr, M., Tiwari, A., Labana, M., Gangele, A.: Performance analysis and fabrication on a turbocharger in two stroke single cylinder petrol engine. *Int. J. Eng. Technol. Innov.* **2**(2), 14–21 (2015)
5. Mathanraj, S.P.V.: Performance analysis of variable geometry turbocharged CI engine. *Perform. Anal. Var. Geom.* (2018)
6. Balashanmugam, P., Elakiya, E., Sharma, S.: Performance analysis on a turbocharger two wheeler engine. *Int. J. Innov. Res. Sci. Eng. Technol.* (2013)
7. Sujith, G., Nair, J.S., Faruq, M.J., Muhammad Ameer, M., Nair, N.P.: Modification and analysis of 125 cc petrol engine with turbocharger. *Int. J. Innov. Res. Sci. Eng. Technol.* **5**, 4968–4977 (2016)
8. Shah, D.S., Prajapati, S.R.: Fabrication of turbocharger for two wheeler. *Int. J. Sci. Res. Eng.* **1**(3), 254–261 (2017)
9. Salazar, F.: *Internal Combustion Engines*. Department of Aerospace and Mechanical Engineering University of Notre Dame Notre Notre Dame, IN 46556 (1998)
10. Mahmoudi, A.R., Khazaei, I., Ghazikhani, M.: Simulating the effects of turbocharging on the emission levels of a gasoline engine. *Alexandria Eng. J.* **56**(4), 737–748 (2017)

Chapter 17

Solving the Production Bottleneck Through Minimizing the Waste of Motion for Manual Assembly Processes



Mohd Norzaimi Che Ani and Ishak Abdul Azid

Abstract In this paper, the application of the waste elimination technique in solving the waste of motion for manual assembly processes has been studied, analyzed, and implemented. The waste of motion is one of the seven wastes as highlighted in the lean manufacturing system (LMS), where it can happen at any time and workers are required to make movements that do not add any value to the overall production processes. A poor designed manual assembly processes can cause low productivity and inefficiency of the production system due to excessive motions. An excessive motion will cause the production bottleneck process and production delinquency, increase inventory, encourage waste of waiting, and unable to smoothing the production flow. In minimizing the waste of motion, the step-by-step of manual assembly processes needs to be studied and observed to ensure fully understanding of the process requirement. Then, each step of the manual assembly process needs to be analyzed to identify the waste of motion which is affecting the productivity and efficiency of the production systems. Once the waste of motion has been identified, the steps of manual assembly processes are required to be re-visited and re-designed to achieve optimum efficiency of the production process flow. Some of the unwanted processes might be eliminated or integrated to ensure minimum motions during the manual assembly process. This research has been conducted by analyzing the manual assembly processes in selected case study in industry and implementation the improvement process to solve the waste of motion. The result of this study shows that the process cycle time has been drastically improved by 60% and at the same time this improvement had increased the production output and solved the worker fatigue

M. N. Che Ani (✉)

Manufacturing Section, Malaysian Spanish Institute, Universiti Kuala Lumpur, 09000 Kulim, Kedah, Malaysia

e-mail: mnorzaimi@unikl.edu.my

I. Abdul Azid

Mechanical Section, Malaysian Spanish Institute, Universiti Kuala Lumpur, 09000 Kulim, Kedah, Malaysia

e-mail: ishak.abdulazid@unikl.edu.my

© The Editor(s) (if applicable) and The Author(s), under exclusive license to Springer Nature Switzerland AG 2020

M. H. Abu Bakar et al. (eds.), *Progress in Engineering Technology II*, Advanced Structured Materials 131,

https://doi.org/10.1007/978-3-030-46036-5_17

issue due to the overburden tasks. Through an effective analysis and implementation, the waste of motion for production process had been identified and successfully minimized.

Keywords Waste · Motion · Manual assembly · Bottleneck · Efficiency

17.1 Introduction

In the production system, a bottleneck is one of the processes in a chain of process flow where the bottleneck process will define the capacity of the production system. A bottleneck in a production system is the process that requires the longest time in operations of the production system [1]. The process bottlenecks occur when demand is higher than the production capability and also happen for other reasons such as out-of-date equipment, inefficient labor, or scarce resources [2]. The results of having a bottleneck in the process flow causes increased inventory, waiting time for the next process, and unbalanced processes.

The current main challenging situation in manufacturing processes is not only to satisfy the needs of customers but process optimization through minimizing the production wastes and minimum operation costs are prioritized [3]. The production process flow requires five sub-processes for the completion of the finished good product and one of the sub-processes records the highest time a during time study analysis. This identified sub-process is considered as the bottleneck process. Possible root-cause of the bottleneck may be contributed from non-value added activities such as waiting time and handling time [4].

The production capacity will be determined through motion time study analysis for the entire processes of the production system and the highest process time will be defined as the bottleneck workstation which is that this process would affect the production output. In solving the bottleneck issue in the production system, several approaches have been implemented such as adding resources at the bottleneck operation [5], ensuring that the bottleneck process only produces quality parts [6], increasing the time of operation for the bottleneck process [7], and avoiding from production downtime [8]. But, implementation of the mentioned approaches requires investment in terms of equipment, skilled workers, and extra expenses for the increased operation times.

Thus, this research has been conducted to solve the process bottleneck of production systems, focusing on the manual assembly process in selected case study industries by minimizing the investment costs. The first objective is to determine the process cycle time required for completion of the process. The second objective is to identify the waste of motions in performing the manual assembly process through observation. Then, the primary objective is to minimize the identified waste of motion to ensure increased production capacity.

This chapter has been divided into six main sections to elaborate the findings of this research. This research will start with the elaborations on the production

bottleneck process in the first section, and then the following section will present the techniques employed to solve the bottleneck process based on the findings from several published literatures. Completion of the both sections, then it was driven into next section which is the discussion on the research design in solving the production bottleneck process. From the developed research design, then data collection, results analysis, and discussions will be discussed in the next two sections which are the fourth and fifth sections. The conclusion of the overall achievement of this research chapter will be concluded in the last section of this chapter.

17.2 A Review of Solving the Production Bottleneck

The production bottleneck is considered as a critical process in the production system because it will define the constraints of the production system. This concept has been developed and applied through the years and it initially focused only on selected functional areas of the production. However, presently it is widely used for the purpose of managing the production system [9, 10]. Basic assumptions using the theory of constraints (TOC) in managing the production bottleneck require critical thinking to improve the production system regarding the production output and managing the customer's order [9].

Normally, a simple bar chart based on a work breakdown sheet is usually the most adapted tool to identify the bottleneck process [11] as illustrated in Fig. 17.1. Each related process in the production floor will be studied in terms of process cycle time, and the results will be plotted into a bar chart. In the bar chart, the horizontal axis or x-axis represents a process sequence, the vertical axis or y-axis represents the process cycle time and each bar represents a different process based on a certain sequence. Based on the result of plotting such a bar chart, the tallest bar will be considered as bottleneck process. By using this bar chart, the bottleneck can be easily detected and the production personnel can then be alerted.

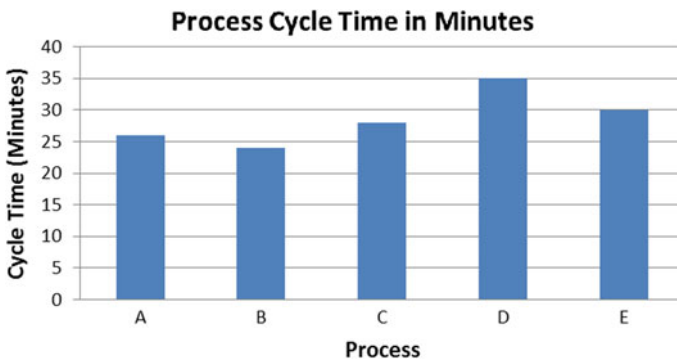


Fig. 17.1 The bar chart for bottleneck identification

Currently, various approaches have been implemented in industries to solve the bottleneck process in order to increase the production capacity. The bottleneck is identified by using time study analysis and the identified wastes are eliminated or minimized. Time study analysis is widely applied in any manufacturing industries to monitor the performance of the production processes in terms of production cycle time and production planning. Normally, during planning of the production capacity, the bottleneck process time will be considered as a constraint of the production system, and it will be improved according to the increasing of the demands. This activity is well-known as continuous improvement activity or most of the industries are familiar with the Japanese words, Kaizen. The term “Kaizen” means an incremental improvement of the production processes as defined goals of reducing wastes to improve performance, availability, and quality as demanded by customers [12].

As an outcome from the literature review of published articles, we found several case studies that have applied the motion time study analysis in optimizing the productivity, process improvement, and production optimization. Based on the thoroughly reviewed articles, the results show that the waste of motion for the manual assembly process highly contributes to the bottleneck process.

Saito [13] evaluated the case study production situation by using the time study analysis and proceeded with the improvement through better methods of motion elements, and successfully increased the production output. Ani et al. [4] used the time study approach to reduce or minimize “non-value added activities” or wastes of motions in the process cycle time which contributed to the bottleneck time. Gupta and Chandrawat [14] had also successfully implemented continuous improvement in two case study industries by minimizing the motion elements and they found some percentage increase in workforce productivity. The results from all these articles proved that the motion elements played a main role contributing to the highest time of the production process.

In modern continuous improvement programs, most of the industries executed the elimination of the wastes by implementing the lean manufacturing system (LMS). Currently, the LMS is widely applied in various industries with the purpose of eliminating the production wastes and fastening the production lead time. The LMS is founded on the concept of continuous and incremental improvements on product and process while eliminating redundant activities [15]. In LMS, two activities are identified in the production floor known as the value added process and the non-value added process, where the value added means any process that changes the physical state of the part, while non-value added is considered as wastes [16]. Seven types of non-value added processes or production wastes were identified by Ohno [15] during the development of the Toyota production system (TPS). These production wastes were known as transportation, inventory, motions, waiting, over-processing, over-production, and defects [15]. Furthermore, Chen and Meng [17] interpreted the value added process as those things the customer is willing to pay for, everything else is waste, and should be eliminated, simplified, reduced, or integrated.

Based on the enhancement of the continuous improvement of the bottleneck processes, a few research articles have been found using the LMS methodology to eliminate the wastes on motion in the production floor. Ani et al. [18] have compared

Table 17.1 The approach on minimizing waste of motions from published literature

Researcher	Year	Reference	Approach	Achievement
Saito	2001	[13]	Time study analysis	Increased output
Ani et al.	2014	[4]	Time study analysis	Minimizing wastes
Gupta and Chandrawat	2012	[14]	Time study analysis	Minimizing motions
Ani et al.	2013	[18]	Comparison analysis	Better method
Rane et al.	2015	[19]	LMS	Minimizing motions
Kolińska and Domański	2017	[20]	LMS	Improved cycle time

the effectiveness between two methods of assembly processes based on motion elements and they found motion elements which contribute to the production efficiency. Same results were found in the study by Rane and Sudhakar [19], where they found minimizing the motion elements could potentially improve some percentage of process cycle time. This situation supported the significance of focusing on the waste of motions in the production floor during performing the continuous improvement activities. The purpose of reducing the impact of bottlenecks is to minimize entailed independence from constraints [20].

The results of reviewing several articles from published literature found that the motion elements in the production processes are one of the main factors contributing to the shortage of the production capacity. Even though several approaches were introduced and implemented, there is still room of improvement. This motion element is identified as a production waste but it is still required in order to assemble the finished good product. It means the motion element is a waste or non-value added process but it is necessary. The role of researchers is to think alternatively how to minimize the motion elements in production processes. As a result from the published literature, the approaches and outcome of the elimination of the motion elements are summarized in Table 17.1.

17.3 Research Framework

This section presents and discusses the application framework in solving the production bottleneck for manual assembly processes. In order to determine the potential wastes of motion to be eliminated for bottleneck process, it requires familiarization in each motion step while performing the assembly processes. The result of the developed framework in this study derived three main phases which were the identification of the selected processes to conduct a motion time study in the first phase, and then followed by the bottleneck analysis and proposed countermeasures of the identified waste in the second phase. And then, the proposed solution was implemented in the selected process to validate and verify the proposed solution in

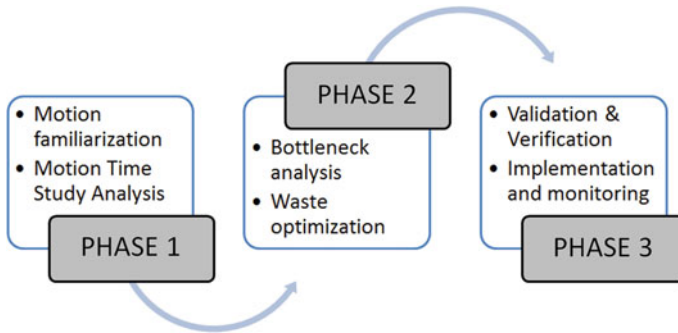


Fig. 17.2 The research framework for solving the production bottleneck for manual assembly process

the last phase. The application of the research framework in solving the production bottleneck for manual assembly processes is summarized in Fig. 17.2.

17.4 Data Collection and Analysis

The selected case study of this research is a company that is operating the refurbishes cylinders for liquefied petroleum gas (LPG). The selected company provides refurbishment services for LPG cylinders as demanded by customers. In overall of the production floor, the machinery and workstation setting is based on a single line or known as a product-based production system. The processes depend on the sequence of the process activity. The process sequence is connected as production chain and the semi-finished good material flows from one workstation to another workstation using a gravity conveyor system. The production system of this selected company is human dependent and requires numerous manual work in the production floor such as transferring the material between workstations, material lifting, production labeling, inspection, and finished good crating.

17.4.1 Phase 1: Process Familiarization and Time Study Analysis

The production processes were observed and the feedback from the management of the case study industry was investigated in this phase. Based on the observation and feedback results, one of the required manual processes caused unsmoothness of the production processes which was identified as the painting process. This process required hanging of the LPG cylinder into an overhead conveyor before transferring

it into the painting room and the process of hanging was fully human dependent as illustrated in Fig. 17.3.

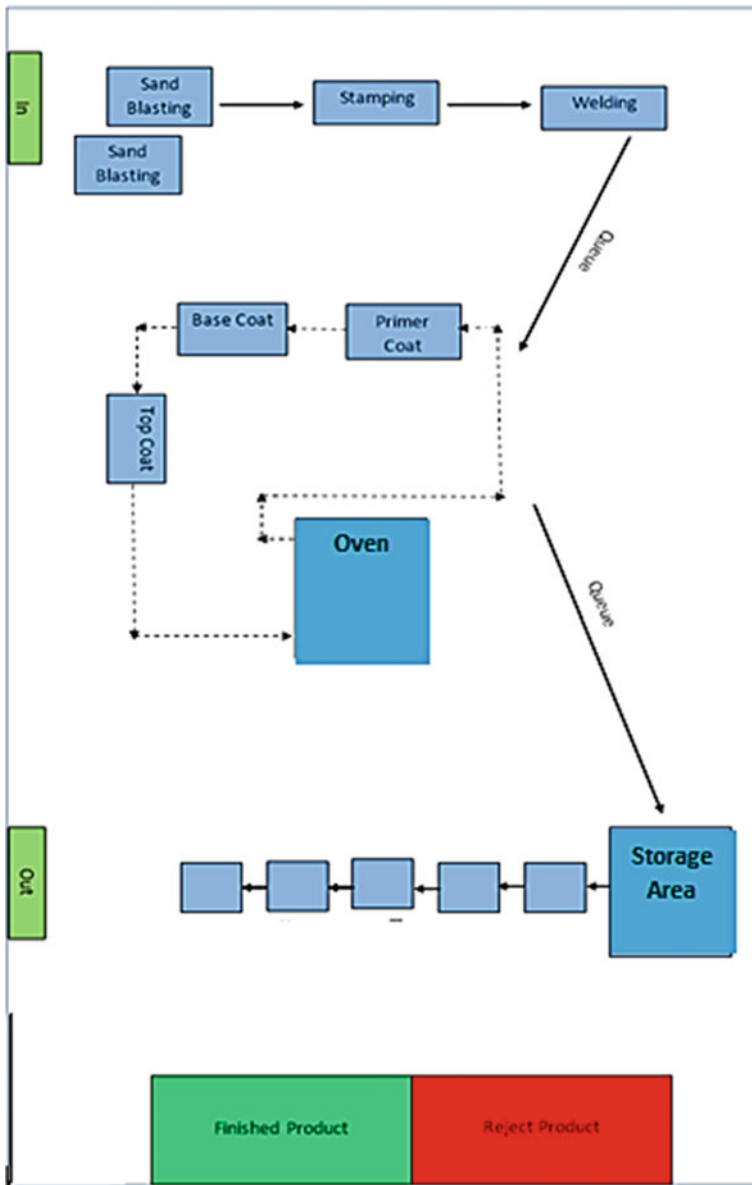


Fig. 17.3 The production floor of the selected process

Based on the observation results, the hanging process required three manual steps, which were placing the hanger, twisting, and lifting the LPG cylinder to hang into the overhead conveyor as illustrated in Fig. 17.4.

The twisting process in the second step was required because the process of locking the hanger into the LPG cylinder in which the outside tread was designed and applied into the hanger. The hanger's tread is illustrated in Fig. 17.5.

From the study of the selected process, the process cycle time was captured and recorded as performed by workers in the production floor. The selection of workers was chosen from the experienced team and new workers in same production floor to ensure the stability and accuracy of the process cycle time. The stopwatch was used in capturing the motion study to record the actual cycle time based on detailed motions of the workers as observed. The results of the recorded time study as captured production floor are presented in Table 17.2.

Once the detailed analysis of the cycle time for motion elements was carried out, solutions to the problematic motion issues were identified and analyzed in the next phase.

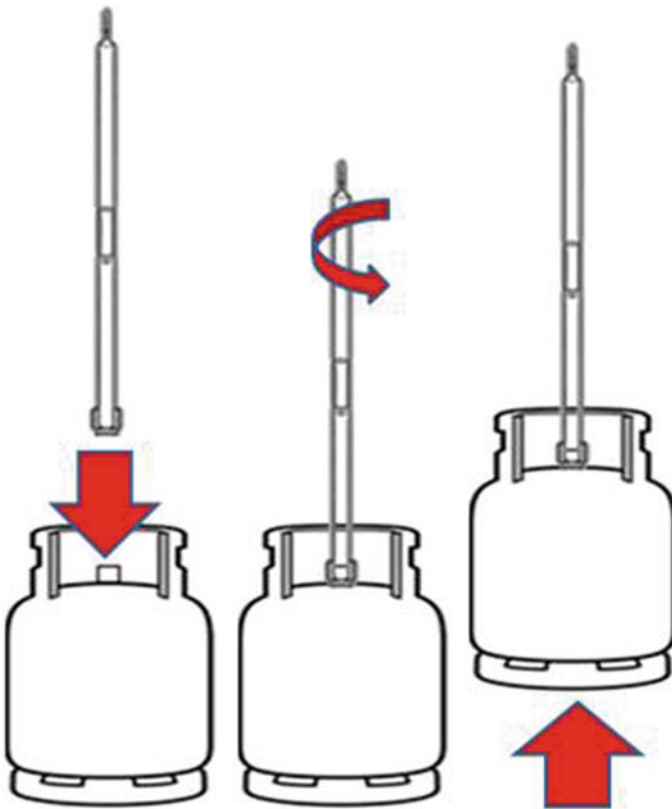


Fig. 17.4 The manual handling process

Fig. 17.5 The cylinder hanger



Table 17.2 The cycle time for the motion elements

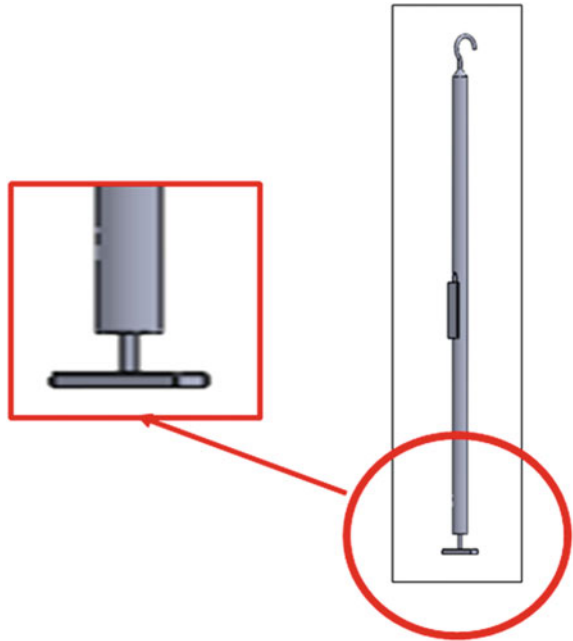
Motion elements	Time (seconds)	Total time (seconds)
Placing the hanger	3.0	
Twisting the hanger	12.0	
Lifting up and hang into conveyor	5.00	20.0

17.4.2 Phase 2: Bottleneck Analysis and Waste Optimization

The results from the previous phase (Table 17.2) showed that twisting was the bottleneck process from the selected case study. This process required averagely 12.0 s per cycle for the completion of twisting. The twisting process did not only require a high process cycle time, but also identified other potential risks. Firstly, untighten the hanger into the LPG cylinder would cause the cylinder falling down from the overhead conveyor and this would create a serious safety issue. Secondly, an improper twisting process would cause the worn out of the cylinder’s tread and would defect the LPG cylinder. Thirdly, the twisting process exposed to the ergonomic hazards in which the workers are required to twists 2000 times per day based on the customer demands. This would create the risks of musculoskeletal disorder (MSD) to the workers since the process was fully depending on human skills.

Based on the results of the analysis, the hanger had been re-designed to minimize the potential hazards and risks. The main objective of re-designing the hanger was to

Fig. 17.6 The re-designed cylinder hanger



ensure that the process required only minimum cycle time of manual handling. The result of the re-designed hanger is illustrated in Fig. 17.6.

From Fig. 17.6, after re-designing the hanger, the assigned workers only needed to press the button for activation of the hook as illustrated in Fig. 17.7. This process eliminated the twisting and solved the potential risks as discussed in the previous section.

17.4.3 Phase 3: Validation, Verification, and Implementation

From the results of Phase 2, and after identifying the highest cycle time element contributing to the bottleneck process, a new design of the LPG cylinder hanger was implemented in the selected case study to validate, verify, and monitor the improvement activity. The analysis of the new process cycle time based on the new design of the hanger was captured and monitored similar to phase 1. From the captured time study, the time saving gained from this improvement activity was five seconds. This was due to the elimination of the twisting process and the impacts of saving five seconds per cycle enabled the production system to increase their capacity by 11.5% per day. As presented in Table 17.3, the new process time for the selected manual handling process is 15.0 s instead of 20.0 s from the previous activity.

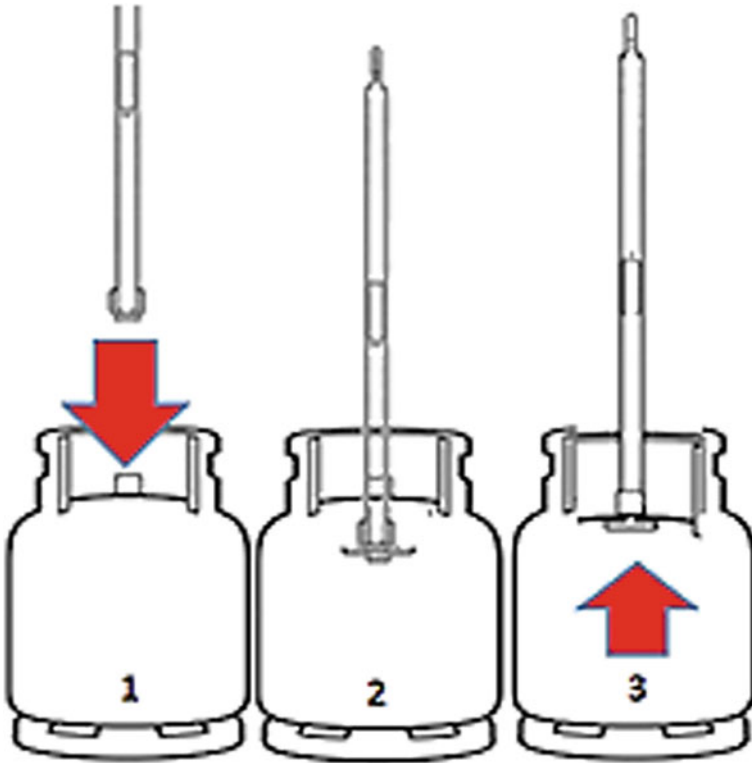


Fig. 17.7 The process required for re-designed cylinder hanger

Table 17.3 The cycle time for the motion elements

Motion elements	Time (seconds)	Total time (seconds)
Placing the hanger	3.0	
Twisting the hanger	7.0	
Lifting up and hang into conveyor	5.00	15.0

17.5 Discussions

From the results obtained during the validation, verification, and implementation of the developed framework, the motion elements were minimized to increase the production capacity. The benefit gained from the implementation was five seconds eliminated in case study industry by minimizing the waste of motion. This cycle time improvement was equivalent to 2.77 h because the production capacity required 2000 units of LPG cylinders per day as calculated in Table 17.4. Overall, 11.5% in terms of time usage per day had been improved.

Table 17.4 The comparison result between before and after improvement activity

When	Cycle time (s)	Daily capacity (units)	Time saving per cycle (seconds)	Time saving per day
Before	20.0			5 s × 2000 cycle = 10,000 s @ 2.78 h
After	15.0	2000	5 s	

The obtained results proved that the small continuous improvement activity or Kaizen had drastically optimized the production. The selected research framework had solved the production system by tackling the waste of motion which would have been obtained through daily operation activities. By forming a systematic approach of waste prevention as the developed framework, the industry will minimize the potential wastes of investment and indirectly minimize the operation costs. Through the results of implementation, the possibility of the production system without wastes will be achieved.

17.6 Conclusions

In this paper, the waste of motion for a manual assembly process was minimized through the continuous improvement approach. Overall, the results of this research met the objectives as defined prior to conducting this research. The defined objectives are to determine the cycle time required for completion of the production process, to identify the wastes of motions related to manual assembly process through the observation and monitoring, and to minimize the identified waste of motion in the production floor toward maximizing the production capacity. As implemented the developed research design in the selected case study industry, some percentage on the waste of motion from the process cycle time was eliminated. This was obtained through successful elimination of five seconds per cycle, which was equivalent to 2.78 h per day. The future research will focus on other potential processes in the selected case study industry which affect the production output.

Acknowledgements The authors of this chapter acknowledge the Malaysian Spanish Institute, Universiti Kuala Lumpur (UniKL MSI) for funding this research that resulted in publishing of this chapter. Also supported from selected case study industry and anonymous reviewers to improve the quality of this research chapter are highly appreciated.

References

1. Karvonen, S., Rämö, J., Leijala, M., Holmström, J.: Productivity improvement in heart surgery—a case study on care process development. *Prod. Plann. Control* **15**(3), 238–246 (2004)
2. Karkkainen, B.C.: Bottlenecks and baselines: tackling information deficits in environmental regulation. *Tex L Rev.* **86**, 1409 (2007)
3. Gunasekaran, A., Spalanzani, A.: Sustainability of manufacturing and services: investigations for research and applications. *Int. J. Prod. Econ.* **140**(1), 35–47 (2012)
4. Ani, C., Bin, M.N., Hamid, A., Binti, S.A.: Analysis and reduction of the waste in the work process using time study analysis: a case study. *Appl. Mech. Mater.* (660) (2014)
5. Uzsoy, R., Wang, C.-S.: Performance of decomposition procedures for job shop scheduling problems with bottleneck machines. *Int. J. Prod. Res.* **38**(6), 1271–1286 (2000)
6. Melton, T.: The benefits of lean manufacturing: what lean thinking has to offer the process industries. *Chem. Eng. Res. Des.* **83**(6), 662–673 (2005)
7. Ruthruff, E., Pashler, H.: Mental Timing and the Central Attentional Bottleneck. *Attention and Time*, pp. 123–135 (2010)
8. Akcalt, E., Nemoto, K., Uzsoy, R.: Cycle-time improvements for photolithography process in semiconductor manufacturing. *IEEE Trans. Semiconductor Manuf.* **14**(1), 48–56 (2001)
9. Cyplik, P., Hadas, L., Adamczak, M., Domanski, R., Kupczyk, M., Pruska, Z.: Measuring the level of integration in a sustainable supply chain. *IFAC Proc. Volumes* **47**(3), 4465–4470 (2014)
10. Cyplik, P., Domański, R.: Implementation of the theory of constraints in the area of stock management within the supply chain—a case study. *LogForum* **5**(3), 1–12 (2009)
11. Brown, A., Amundson, J., Badurdeen, F.: Sustainable value stream mapping (Sus-VSM) in different manufacturing system configurations: application case studies. *J. Cleaner Prod.* **85**, 164–179 (2014)
12. Imai, M.: *Gemba Kaizen: A Commonsense, Low-Cost Approach to Management: A Commonsense, Low-Cost Approach to Management*. McGraw Hill Professional (1997)
13. Saito, S.: Case study: reducing labor cost using industrial engineering techniques. *Maynard's Ind. Eng. Handbook* **2**(151-2), 64 (2001)
14. Gupta, M.P.K., Chandrawat, M.S.S.: To improve work force productivity in a medium size manufacturing enterprise by MOST Technique. *IOSR J. Eng.* **2**(10), 8–15 (2012)
15. Ohno, T.: *Toyota Production System: Beyond Large-Scale Production*. CRC Press (1988)
16. Liker, J.K., Morgan, J.M.: The Toyota way in services: the case of lean product development. *Acad. Manage. Perspect.* **20**(2), 5–20 (2006)
17. Chen, L., Meng, B.: The application of value stream mapping based lean production system. *Int. J. Business Manage.* **5**(6), 203 (2010)
18. Ani, B.C., Norzaimi, M., Ismail, A.B., Mustafa, S.A., Feng, C.J. (eds.): *Simulation Analysis of Rabbit Chase Models on a Cellular Manufacturing System*. Applied Mechanics and Materials. Trans Tech Publ (2013)
19. Rane, A.B., Sudhakar, D., Rane, S. (eds.): *Improving the performance of assembly line: review with case study*. In: 2015 International Conference on Nascent Technologies in the Engineering Field (ICNTE), IEEE (2015)
20. Kolińska, J., Domański, R.: The analysis of production lines bottlenecks—identification and ways of management. In: *Business Logistics in Modern Management* (2017)

Chapter 18

Investigation the Impact of 5S Implementation Toward Accident-Free Manufacturing Industries



**Muhammad Syafiq Ridha Mutaza, Mohd Norzaimi Che Ani,
and Azmi Hassan**

Abstract In this paper, the impact of 5S implementation toward accident-free manufacturing industries was reviewed and investigated. The 5S method is a standardized process that when systematically implemented creates and maintains an organized, safe, clean, and efficient workplace. The 5S also implemented and improved the visual controls to make any process non-conformance's obvious and easily detectable. The 5S is a systematic housekeeping technique used by organizations initiated from Japanese words; Seiri (sort), Seiton (set in order), Seiso (shine), Seiketsu (standardize), and Shitsuke (sustain). The implementation of a 5S environment in a workplace requires employee motivation and good management. All the different levels of an organization need to put their best efforts on a day-to-day basis and work together toward achieving improved performance and reducing waste. The 5S is the most effective tool and widely applied worldwide in any organization to improve the workplace. However, industrial accidents still occurred and increased. Based on current data, the Department of Safety and Health (DOSH, Malaysia) in their Web site stated an increase of accidents by 107% (January to June 2018–2019) and it is a long journey before an accident-free industry can be achieved. Hence, in this research, the impact of 5S implementation toward accident-free manufacturing industries was investigated. The literature of the 5S implementation was thoroughly reviewed through searching from published literature from the Emerald Insight, Elsevier, Google Scholar, and other databases. The data captured from this published

M. S. R. Mutaza (✉)

Manufacturing Section, Universiti Kuala Lumpur—Malaysia Italy Design Institute, Cheras,
56100 Kuala Lumpur, Malaysia

e-mail: msyafiq.mustaza@s.unikl.edu.my

M. N. Che Ani

Manufacturing Section, Universiti Kuala Lumpur—Malaysian Spanish Institute, 09000 Kulim,
Kedah, Malaysia

e-mail: mnorzaimi@unikl.edu.my

A. Hassan

Electrical & Electronics Section, Universiti Kuala Lumpur—Malaysian Spanish Institute,
09000 Kulim, Kedah, Malaysia

e-mail: azmi.hassan@unikl.edu.my

© The Editor(s) (if applicable) and The Author(s), under exclusive license
to Springer Nature Switzerland AG 2020

M. H. Abu Bakar et al. (eds.), *Progress in Engineering Technology II*,

Advanced Structured Materials 131,

https://doi.org/10.1007/978-3-030-46036-5_18

literature was analyzed to study the impact of the 5S implementation. The result of this research shows based on the theoretical implementation, the 5S implementation potentially helps the organization to reduce the industrial accident but it requires systematic monitoring plans such as an internal audit. Through an effective investigation in this paper, the impact of 5S implementation on accident-free manufacturing industries was successfully carried out.

Keywords 5S · Accident-Free · Industrial accident · Manufacturing industries

18.1 Introduction

5S is a systematic process of workplace housekeeping methods to achieve a tranquil environment in the workplace involving all the employees, with a commitment to sincerely implement and practice housekeeping. “Japanese have immaculately practiced these principles of housekeeping from a small retail shop to major industries” [1]. The abbreviation 5S is derived from the Japanese words Seiri (sort), Seiton (set in order), Seiso (shine), Seiketsu (standardize) and Shinsuke (sustain) Hirano Hiroyuki in his book argues that this method is frequently viewed as a visual control or visual work place [2]. Along with standard work and total productive maintenance, 5S is regarded as the most widely adopted technique from the lean manufacturing toolbox.

An industrial accident refers to something unexpected, random even in the sequence of incidents that occurred through a combination of courses that resulted in injury or illness to a person or damage to assets and the environment [3]. According to National Institute of Safety and Health (NIOSH) from their official Web site, it is stated that environment, design, system or procedure, and human behavior are the main contributing factors to industrial accident [3], environmental factor referred for accidents that is not attributed to human conduct includes both natural or manmade environment. Common example is poor visibility which includes poor light situation or heavy rain, ambient temperature, sound pollution, or bad weather. The other contributors are the design and this happens when the worksite layout is poorly designed or tools and equipment are not designed to follow safety rules and regulations.

This paper aims to investigate the implementation of 5S in the manufacturing industry from a previous study [1] to understand more about the implementation of 5S itself and to study the 5S effect to safety performance.

The structure of this paper starts with an introduction to overview 5S implementation and industrial accident. Then, the paper more focuses on literature review of 5S implementation and its effect on safety in the industry. This paper then discusses the research approach from collecting a paper until the result and analysis stage. Then paper will discuss the findings and concludes the result of this paper.

18.2 5S Review

Hirano states that the 5S measure is designed to enhance efficiency, strengthen the performance, and provide continuous improvement in almost every segment of the organization [2]. These steps involve a structured improvement program with progressively identified steps that relate to each other. According to the Japanese organization system, 5S has two components, a high level of management and organizational system with complex meanings and it translates to perfect performance and the other is the provision of management tools [4].

The Toyota production system provides a well-known example of the 5S principles in practice. In Japan, the 5S practice started in the making sector and then expanded to other industries and services sector. Early versions of the 5S were based on the 3S, and then developed into the 4S [5]. Western countries like Europe and American industry getting benefit in productivity, profit, and employees behavior from implementing the 5S in the manufacturing sector then the 5S were adopted in the healthcare service [6].

18.3 Research Approach

The review relies on three major stages see Fig. 18.1, the first stage is the paper extraction process which is the process to select paper from reputable database. The literature on the 5S implementation was thoroughly searched in the Scopus, Emerald Insight, Elsevier, Google Scholar, and other databases by using the keyword 5S, safety, an industrial accident. The second stage is the paper selection. In this stage, papers that have strong integration between 5S and safety are only selected for further study.

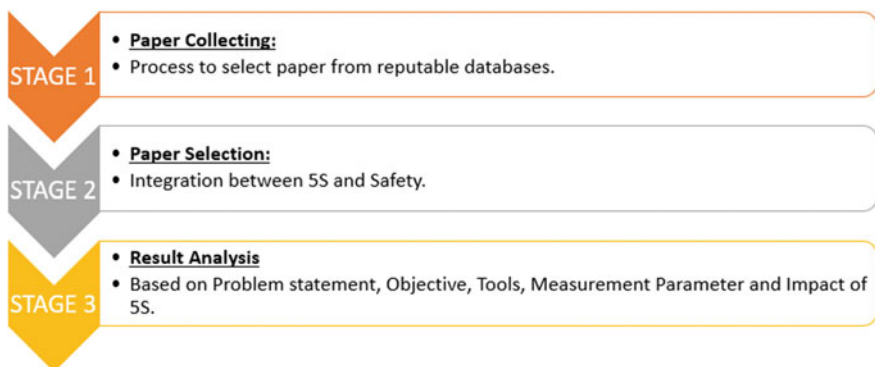


Fig. 18.1 Research approach

In the last stage, i.e., the results analysis, data captured from this published literature were analyzed to study the impact of the 5S implementation base on the problem statement, objective, tools, measurement parameter, and impact of 5S.

The first stage is the literature finding using keywords for all the database and this process resulted in the initial identification of 49 publications in the second stage 33 of the publication were removed because of the integration between 5S and safety were not strong and did not meet the criteria. Only four publications from recent years were selected for the last stage and four of this paper were reviewed again for analysis summary and write-up.

18.4 Result and Discussion

The process of identifying and selecting articles, after considering the exclusion criteria, produced four best papers. The earliest published articles were recorded in 2014, and the most recent is in 2019. The findings below are the result of the analysis and are presented in Table 18.1.

Fernandes et al. [7] in his research to study the 5S contribution to occupational safety performance by implementing 5S in an automotive production line, the author used risk assessment tools to find that the 2S (set in order) gives the significant impact to safety. The advantage of this paper is that the researcher analyzed all the “S” one by one to find the most significant stage in 5S practice but the last “S” (sustain) was not much discussed by the author.

Lamprea et al. [8] in his effort to study whether the 5S methodology could be considered as an effective tool to improve manufacturing companies by implementing 5S in a metalwork company and then measuring the takeout before, during and after implementation of 5S unlike Sharma [9] Vipulkumar [10] that just analyzed 5S before and after implementation. Lamprea [8] found that 5S shows a positive result in decrease in the risk identified in the workshop plan. This research was implemented in SMEs and was easy to monitor but this research relies on visual inspection to collect data unlike Fernandes [7] who used risk assessment method can be used to precisely measure safety.

18.5 Conclusion

The paper intention was to focus on the implementation of 5S in the manufacturing industry. This may contribute preliminary work related to the implementation of 5S in small- and medium-sized enterprises (SMEs) to increase the safety and performance.

The most important barrier in implementing 5S is human behavior to maintain the practice in workplace because of poor communication or lower employee morale [11].

Table 18.1 Result

Researcher	Year	Methodology	Finding	Remarks
Fernandes et al.	2019	Implement 5S in the automotive production line, use risk assessment tools to monitor safety condition	The result shows that “set in order” gives a significant impact on safety	Pro: analyze all the “S” one by one Con: The last S is not so much discussed Comment: implement 6S to integrate with occupational safety. Using a risk assessment method to measure safety
Lamprea et al.	2015	Implement 5S in the metal company, measurement take out before, during and after implementation of 5S	Shows positive result as a decrease of the risk identified in the workshop	Pros: implement in SME easy to monitor Con: Generally does not discuss how safety was analyzed in detail Comment: Paper focuses on all of 5S. using questionnaire and visual inspection to assist the safety
Sharma et al.	2015	Measure organization performance before and after 5S practice	5S is effective tools which strongly supports the objective of TPM that improves safety performance	Con: Do not measure org performance during implement of 5S Comment: integrate 5S with safety. safety measured using questionnaire
Vipullkumar et al.	2014	Implement 5S to a ceramic manufacturing company	Show improvement in space, safety, inventory, and machine efficiency	Pro: focus more on 5S in terms of efficiency Con: Safety effect not much covered in this research Comment: Author do not specify how safety was measured, integrate 5S

The 5S implementation potentially helps the organization to reduce industrial accident [1, 7, 8] but it requires a systematic monitoring plans such as an internal audit. Through an effective investigation in this paper, the impact of 5S implementation toward accident-free industries in the manufacturing sector was successfully carried out.

References

1. Ramesh, N., Ravi, A.: 5S route for safety management. *Int. J. Bus. Excell.* **10**(3), 283–300 (2016)
2. Hirano, H.: *5S for Operators: 5 Pillars of the Visual Workplace*. Productivity Press, New York (1996)
3. NIOSH: *Workplace Accident, Malaysia*, p. 2 (2018)
4. Gapp, R., Fisher, R., Kobayashi, K.: Implementing 5S within a Japanese context: an integrated management system. *Manag. Decis.* **46**(4), 565–579 (2008)
5. Ohno, T.: *The Toyota Production System: Beyond Large-Scale Production*. Portland, Oregon (1988)
6. Young, F.: The use of 5S in healthcare services: a literature review. *Int. J. Bus. Soc. Sci.* **5**(10), 240–248 (2014)
7. Jiménez, M., Romero, L., Fernández, J., Espinosa, M., et al.: Extension of the Lean 5S methodology to 6S with an additional layer to ensure occupational safety and health levels. *Sustain* **11**(14), 1–18 (2019)
8. Lamprea, E.J.H., Carreño, Z.M.C., Sánchez, P.M.T.M.: Impact of 5S on productivity, quality, organizational climate and industrial safety in Caucho Metal Ltda./Impacto de las 5S en la productividad, calidad, clima organizacional y seguridad industrial en la empresa Cauchometal Ltda. *Ingeniare Rev. Chil. Ing.*, vol. 23, no. 1, pp. 107–117 (2015)
9. Sharma, R., Singh, J.: Impact of implementing Japanese 5S practices on total productive maintenance. *Int. J. Curr. Eng. Technol.* **55**(22), 2277–4106 (2015)
10. Patel, V.C., Thakkar, H.: A case study: 5S implementation in ceramics manufacturing company. *Bonfring Int. J. Ind. Eng. Manag. Sci.* **4**(3), 132–139 (2014)
11. Singh, J., Rastogi, V., Sharma, R.: Implementation of 5S practices: a review. *Uncertain Supply Chain Manag.* **2**(3), 155–162 (2014)

Chapter 19

Effect of Maleic Anhydride Polypropylene on the Properties of Spear Grass Fiber in Reinforced Polypropylene and Ethylene Propylene Diene Monomer Composites



Muhammad Azree Ifwat Adnan, Faizatul Azwa Zamri,
Mohamad Sabri Mohamad Sidik, and Siti Rohana Ahmad

Abstract Polypropylene ethylene propylene diene monomer (PP/EPDM) polymer composites reinforced by spear grass (10, 20, 30, 40, and 50 wt%) were prepared with and without compatibilizer. The maleic anhydride polypropylene (MAPP) was applied as compatibilizer to the composites. The water absorption test and tensile test were conducted according to the ASTM570 and ASTM638, respectively. The percentage of water absorption, and elongation at break, was reduced with the increment of spear grass content. In contrast, tensile strength increased from 10 to 20 wt% and then reduced thereafter. Besides, the MAPP enhanced the water absorption, tensile strength, tensile modulus and elongation at break properties of the composites. In conclusion, the 20 wt% reinforcement of spear grass in the polypropylene ethylene propylene diene monomer polymer composites and MAPP as compatibilizer agent results in good properties.

Keywords Spear grass · Polypropylene · Ethylene propylene diene monomer · Spear grass · Mechanical properties

M. A. I. Adnan · F. A. Zamri · M. S. Mohamad Sidik (✉) · S. R. Ahmad
System Engineering and Energy Laboratory, Universiti Kuala Lumpur Malaysian Spanish
Institute, Kulim Hi-Tech Park, 09000 Kulim, Kedah, Malaysia
e-mail: msabri@unikl.edu.my

M. A. I. Adnan
e-mail: azree.adnan@s.unikl.edu.my

F. A. Zamri
e-mail: faizatul.zamri08@s.unikl.edu.my

S. R. Ahmad
e-mail: sitirohana@unikl.edu.my

19.1 Introduction

The development of new materials has a huge impact nowadays to the automotive industry. The usage of polymer materials as car parts is expected to reduce the car's weight and fuel consumption. Polymers are ideal for certain car parts due to their low density and flexible characteristics. However, improper recycle management of polymers may result in environmental pollution due to their non-biodegradability properties. Thus, the usage of biodegradable polymers filled with natural fibers is an alternative for environmental-friendly composites. Polypropylene (PP) is a thermoplastic polymer used in various applications such as in packaging, labeling, textiles, and stationary. In the automotive field, PP is commonly used as bumper, side cladding, interior parts, etc. Besides PP, ethylene propylene diene monomer (EPDM), an elastomer has an excellent heat, aging, and oxidation resistance which is mostly used for automotive sealings [1–3].

Spear grass (*Imperata cylindrica*) is the most dominant, competitive, and difficult weed to control in Asia, West Africa, and Latin America. In recent research, spear grass fiber (SGF) has been extracted and filled in the low-density polyethylene/thermoplastic powder composites as a reinforced filler [4, 5]. The tensile properties including tensile strength, tensile modulus, and elongation at break of the composites with varying composition were determined. The certain amount of spear grass reinforcement has enhanced the properties.

Maleic anhydride polypropylene (MAPP) was widely used as compatibilizer. Its function is to strengthen the composite containing fillers and/or fiber reinforcements and to improve the tensile properties. In recent study, it was shown that MAPP improves the storage modulus of the oil palm fiber composites when added [6]. This is because the compatibilizer modified the polymer matrix by graft copolymerization, thus resulting in strong adhesion at the interface. However, it remained question for SGF reinforcement and MAPP as compatibilizer in the PP/EPDM polymer composites.

In this paper, the MAPP was used as compatibilizer in PP/EPDM/SGF composites. The composites were prepared at 10, 20, 30, 40, and 50 wt% spear grass loading. The water absorption and tensile test were conducted to study the effect of MAPP in the PP/EPDM/SGF composites.

19.2 Methodology

19.2.1 Preparation of PP/EPDM/SGF Composites

Figure 19.1a shows the materials (PP, EPDM, MAPP, and SGF) and Fig. 19.1b shows the sample of composite specimen in dumbbell shape. The matrix of the composites consists of PP and EPDM with the composition ratio 70 wt% and 30 wt% by the weight percentage, respectively. The short discontinuous SGF varied its composition

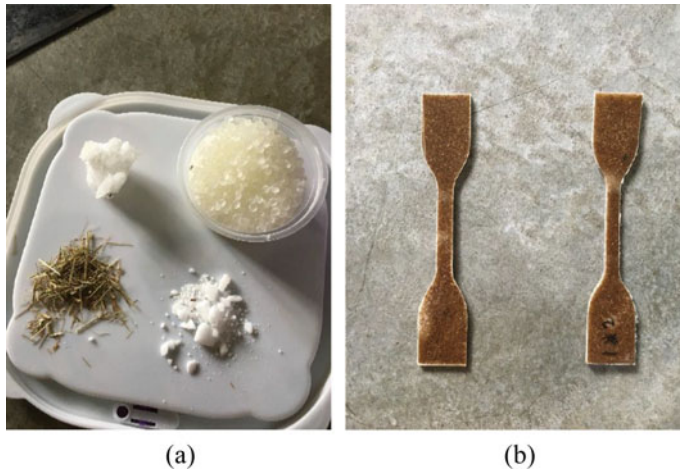


Fig. 19.1 a Raw materials; b dumbbell shape of the composites

by 10, 20, 30, 40, and 50 wt% from the total mass of the matrix which is 45 g. In order to study the effect of the compatibilizer, the maleic anhydride grafted polypropylene, MAPP was added in the composition by 3 wt% from the total mass of the filler prior the mixing process. The summary of the composition ratio used in this research is shown in Table 19.1. A total 100 pieces of composite specimens with 10 different composition ratios were produced using the fabrication process steps as shown in Fig. 19.2.

Table 19.1 Composition ratio of composites

Sample/materials	Matrix (wt%)		Filler (wt%)	Compatibilizer (wt%)
	PP	EPDM	SGF	MAPP
1	70	30	10	-
2			20	
3			30	
4			40	
5			50	
6	70	30	10	3
7			20	
8			30	
9			40	
10			50	

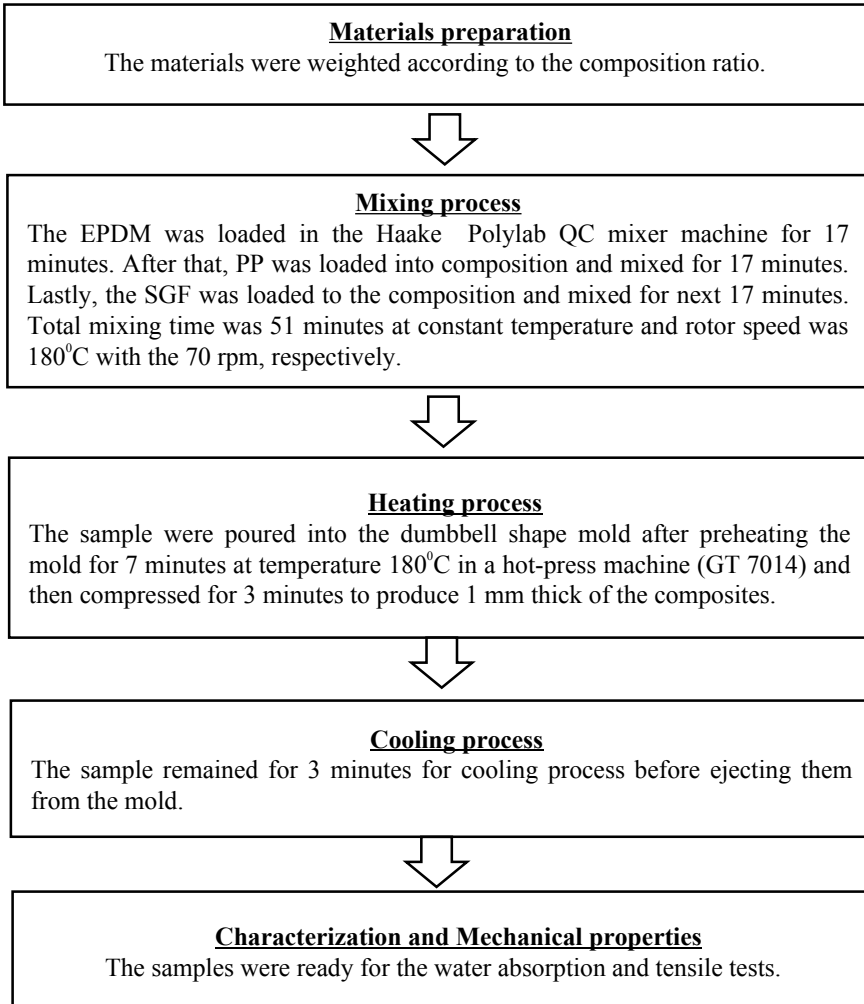


Fig. 19.2 shows the fabrication process flow of the composites

19.2.2 Water Absorption Test

The water absorption test was performed according to the ASTM D570. Prior testing, the specimens were dried in the oven for 24 h at 80 °C and the initial weight, W_d was recorded. The percentage of water absorption M_t was calculated using Eq. (19.1) where W_n is the equilibrium weight after immersing in the water. The dimensions of specimen used in this test were 2.5 cm × 1.5 cm and 1.0 cm for their length, width, and thickness, respectively.

$$M_t = \frac{W_n - W_d}{W_d} \times 100 \quad (19.1)$$

where M_t is the water absorption percentage, W_n is the weight after immersion, and W_d is the initial dry weight.

19.2.3 Tensile Test

The tensile test was performed according to the ASTM D638 using a universal testing machine model QUASAR 100 from Galdabini with a cross-head speed of 10 mm/min. The testing was done in standard laboratory atmosphere of $23 \text{ }^\circ\text{C} \pm 2 \text{ }^\circ\text{C}$ and $50 \pm 5\%$ relative humidity. The specimens were positioned vertically in the grips of the testing machine. The grips were then tightened evenly and firmly to prevent any slippage with gauge length kept at 50 mm. The test was carried out on the 10 specimens for each composition in order to determine the tensile strength, tensile modulus, and elongation at point break of the composites.

19.3 Result and Discussion

19.3.1 Water Absorption

Figure 19.3 shows that the 10 wt% of filler content has the lowest percentage of water absorption and this significantly increased with filler content for MAPP and without MAPP. The MAPP used in the composite has reduced the percentage of water absorption at 20–50 wt% of filler content. In agreement with reference [7],

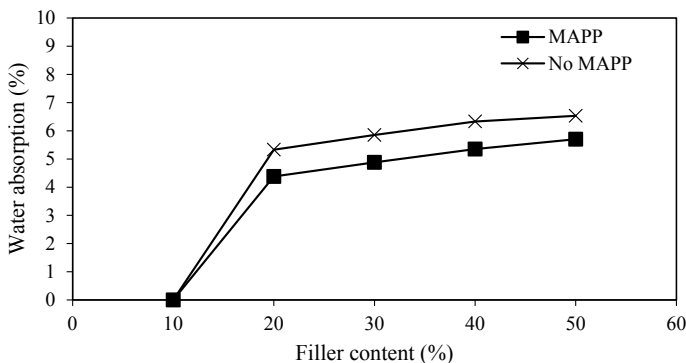


Fig. 19.3 Percentage of water absorption with different filler content with MAPP and without MAPP, respectively

where it was found that the presence of MAPP indicates that the composites with MAPP have better water resistance. The range of water absorption for MAPP was observed within 0–5.7% meanwhile 0–6.53% for composites without MAPP.

19.3.2 Tensile Properties

The tensile properties including tensile strength, tensile modulus, and elongation at break were determined for PP/EDPM/SGF with and without MAPP composites. From Fig. 19.4, the highest tensile strength at 20 wt% of filler content in the composites for MAPP and without MAPP with 7.5 MPa and 6.5 MPa, respectively. Any further increment of the filler content results in lowering the tensile strength of the composites probably due to the weak interfacial area between the fiber and matrix when increasing the filler content [8, 9].

Meanwhile, the trend for the tensile modulus of the composite was increased with the increased filler content for MAPP and without MAPP as shown in Fig. 19.5. However, the increment was not significantly different for 10 wt% to 50 wt% of filler content since the range of tensile modulus for the composites with and without MAPP was within 0.57 GPa to 0.82 GPa and 0.50 GPa to 0.70 GPa, respectively. This trend is similar and the tensile modulus properties are comparable with other work using PP/EPDM and MAPP as compatibilizer [8, 9].

The elongation at break is decreased due to the fact that the fillers had hardened the composites and reduced their ductility. This is observed in the spear grass fiber reinforced PP/EDPM polymer composites as shown in Fig. 19.6. Besides that, the MAPP compatibilizer reduced the percentage of elongation of the composites.

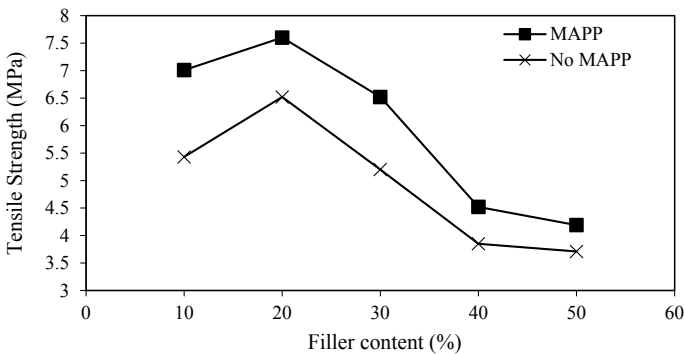


Fig. 19.4 Tensile strength with different filler content for MAPP and without MAPP, respectively

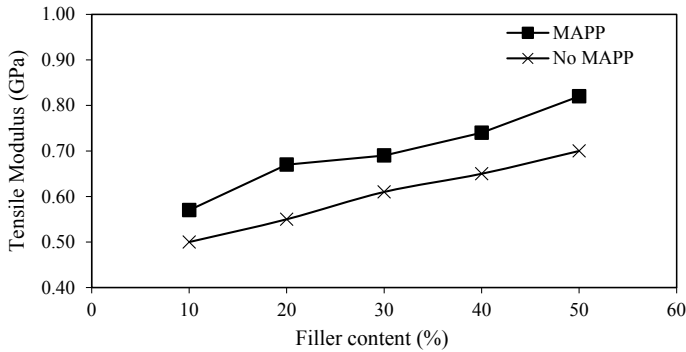


Fig. 19.5 Tensile modulus with different filler content with MAPP and without MAPP, respectively

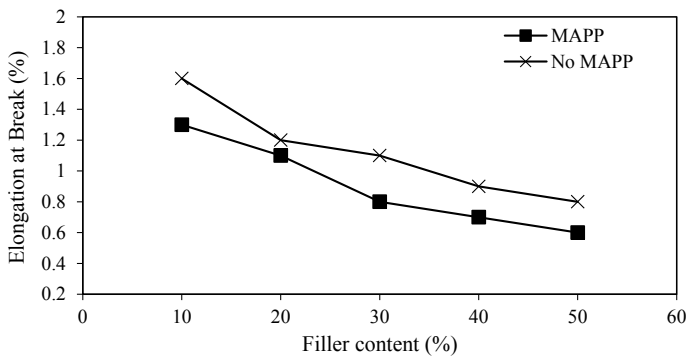


Fig. 19.6 Elongation at point break with different filler content for MAPP and without MAPP, respectively

19.4 Conclusion

The spear grass filled PP/EPDM composites with the 10, 20, 30, 40, and 50 weight percentage (wt%) were prepared and tested with the MAPP and without MAPP as compatibilizer. The presence of MAPP enhanced 15% of the water absorption at maximum SGF loading. Besides, the optimum tensile strength (7.5 MPa) occurred at 20 wt% of SGF loading. The maximum value of tensile modulus is 0.82 GPa. Thus, this study proved the SGF reinforced with MAPP treatment has better mechanical properties and applicable to be used as a substitute to reduce the plastics usage.

Acknowledgements The authors would like to thank the Universiti Kuala Lumpur Short Term Research Grant (UniKLSTRG str17043) for financial funding and System Engineering and Energy Laboratory (SEELab) for guidance of this project.

References

1. Zinkweg, D.: Not reinventing the wheel: the importance of rubber components in automotive applications. *Rubber World Mag.* **256**(1), 20–21 (2017)
2. Shanks, R.A., Kong, I.: General purpose elastomers: structure, chemistry, physics and performance. In: Visakh, P.M., Thomas, S., Chandra, A., Mathew, A.P. (eds.) *Advances in Elastomers: Blends and Interpenetrating Networks*. Springer-Verlag, Berlin (2013)
3. Franta, I.: *Elastomers and Rubber Compounding Materials*. Elsevier Science Publishers Company, New York (2012)
4. Nuradibah, M.A., Halim, N.A., Kasim, K.F., Sam, S.T., Zulhaimi, H.I., Uda, M.N.A.: Extraction of spear grass (*Imperata Cylindrica*) as pro-oxidant in polymer blends. In: *MATEC Web of Conferences*, vol. 150, p. 06015. EDP Sciences (2018)
5. Sam, S.T., Santhiya, P., Ragunathan, S., Noriman, N.Z., Ismail, H.: Tensile and morphological properties of low-density polyethylene/spear grass composites. *Key Eng. Mater.* **594–595**:715–719 (2014) (Trans Tech Publications)
6. Simão, J.A., Marconcini, J.M., CapparelliMattoso, L.H., Sanadi, A.R.: Effect of SEBS-MA and MAPP as coupling agent on the thermal and mechanical properties in highly filled composites of oil palm fiber/PP. *Compos. Interfaces* **26**(8), 699–709 (2019)
7. Pasbakhsh, P., Ismail, H., Fauzi, M.A., Bakar, A.A.: Influence of maleic anhydride grafted ethylene propylene diene monomer (MAH-g-EPDM) on the properties of EPDM nanocomposites reinforced by halloysite nanotubes. *Polym. Test.* **28**(5), 548–559 (2009)
8. Sabri, M., Hafiz, F., Shahril, K., Rohana, A.S., Husseinsyah, S.: Effects of silane coupling agent on mechanical properties and swelling behaviour of coconut fiber filled polypropylene composite. *Adv. Mater. Res.* **626**, 657–661 (2013) (Trans Tech Publications)
9. Salmah, H., Rohana, A.S., Kamarudin, H.: Effect maleic anhydride polypropylene on properties of calcium carbonate filled polypropylene/ethylene propylene diene terpolymer composites. *Key Eng. Mater.* **594**, 770–774 (2014) (Trans Tech Publications)

Chapter 20

Effect of Acid Acrylic on Mechanical Properties and Swelling Behavior of Spear Grass Fiber Filled Polypropylene Composites



Nuramalena Abdul Latif, Muhammad Afiq Mohd Nabin, Mohamad Sabri Mohamad Sidik, and Nurashikin Sawal

Abstract In recent years, polypropylene (PP) is an ideal choice for automotive components due to its lightweight and the flexibility in the manufacturing process. However, due to the environmental effect, the usage of PP has been reduced by reinforced green materials such as spear grass fiber (SGF). In this study, acrylic acid (AA) has been used as a compatibilizer between the matrix and fiber. The composite mixture was prepared in the formulation of 5, 10, 15 and 20 wt% of treated and untreated composites. The tensile test suggests the composite with 5 wt% for treated and untreated composite have the highest value of tensile strength. The modulus of elasticity increased with the increasing in filler loading. In contrast, the elongation at break decreased with the increasing in filler loading. Moreover, the swelling test discerned that the increase in filler loading has increased the water absorption of composites. The presence of AA reduced the equilibrium water absorption percentage.

Keywords Spear grass fiber · Composite · Polypropylene · Acrylic acid · Compatibilizer

N. Abdul Latif · M. A. Mohd Nabin · M. S. Mohamad Sidik (✉) · N. Sawal
System Engineering and Energy Laboratory, Universiti Kuala Lumpur Malaysian Spanish Institute, Kulim Hi-Tech Park, 09000 Kulim, Kedah, Malaysia
e-mail: msabri@unikl.edu.my

N. Abdul Latif
e-mail: nuramalena.latif@s.unikl.edu.my

M. A. Mohd Nabin
e-mail: afiq.nabin@s.unikl.edu.my

N. Sawal
e-mail: nurashikins@unikl.edu.my

© The Editor(s) (if applicable) and The Author(s), under exclusive license to Springer Nature Switzerland AG 2020
M. H. Abu Bakar et al. (eds.), *Progress in Engineering Technology II*, Advanced Structured Materials 131,
https://doi.org/10.1007/978-3-030-46036-5_20

20.1 Introduction

The leap in automotive ground had been a huge impact on research and development of new materials. In the present days, where the crude oil price is hiking, the urge of producing fuel-efficient and eco-friendly car is demanding. This brings engineers to the usage of polymer materials as car parts to reduce the weight for better fuel consumption. Polymers are ideal for certain car parts due to their low density making it lightweight, ease of manufacturing process, and in addition, it can serve as a method to increase pedestrian safety. The drawbacks of polymers are the non-biodegradability that makes them one of the pollutant sources. Although recycling may be one of the solutions, the use of biodegradable polymers and natural fibers is deemed as a good alternative for environmentally friendly composites [1].

In the present day, in Peninsular Malaysia alone, a total of 4.2 million tons of crop residue and 2.3 million tons of livestock waste were produced, which mostly consists of grass. Therefore, the spear grass (*Imperata cylindrica*) offers a fiber source with excellent commercial value. The spear grass fiber (SGF) is renewable, biodegradable, environment-friendly, lightweight material compared to the synthetic fiber reinforced composites.

Acrylic acid (AA) is used as the compatibilizer for the composites. Compatibilizer has been added to improve the dispersion, adhesion and compatibility between the two dissimilar materials [2]. In addition, the compatibilizer is used to modify the polymer matrix by graft co-polymerization, thus resulting in strong adhesion, even cross-linking at the interface.

20.2 Experimental

20.2.1 Materials

A composite made of spear grass fiber reinforced polypropylene (PP) was investigated in this study. The polypropylene grade S12232 G112 was supplied by Polypropylene Malaysia Sdn Bhd in the form of pellets. The properties of polypropylene are shown in Table 20.1. The spear grass was obtained from several unoccupied fields in Kulim, Malaysia. The process of obtaining the SGF is presented in Fig. 20.1. The AA compatibilizer was supplied by Modern-Lab Chemicals Sdn Bhd.

20.2.2 Mixing Procedure

The mixing of composites was prepared in the Haake PolyLab QC mixer machine for 17 minutes at the temperature of 180 °C and the rotor speed of 70 rpm. The mixer allowed to have a maximum volume of up to 45 g. The mixing has been repeated

Table 20.1 General properties of polypropylene [3]

Typical resin properties	Values
Melt flow rate, at 230 °C (g/10 min)	14
Density (g/cm ³)	0.9
Tensile strength at yield (kg/cm ²)	360
Elongation at yield (%)	10
Flexural modulus (kg/cm ²)	17,500
Notched Izod impact strength at 23 °C (kg cm/cm)	2.6
Heat deflection temperature at 4.6 kg/cm ² (°C)	99
Rockwell hardness (R scale)	97
Water absorption after 24 h (%)	0.02

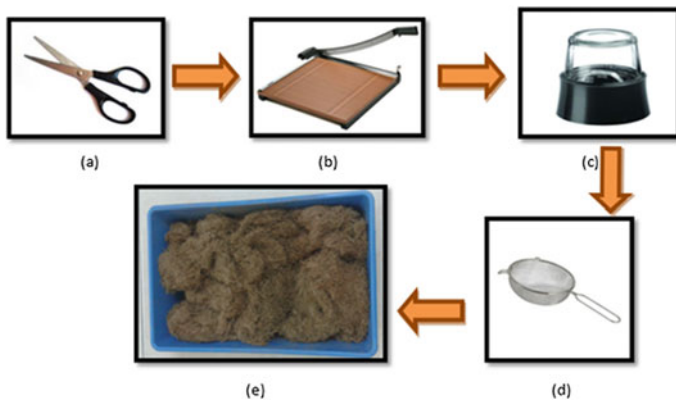


Fig. 20.1 Process flow of producing short discontinuous spear grass fiber. **a** Cut into small section, **b** cut to more refined pieces, **c** blend the balance fiber, **d** straining process and **e** obtained filler fibers

several times in order to prepare 90 samples (10 samples for each composition with and without treatment including the control sample). Firstly, the PP pellets were mixed and melted in the mixer chamber. Specifically, after 12 minutes, the SGF was added into the mixer. The mixing process was continued for another 5 minutes until the 17 minutes were reached. Table 20.2 shows the mixture composition in wt% for each sample with different loads of SGF (treated and without treated).

Table 20.2 Composition ratio of composites

Materials	PP/SGF (untreated) (wt%)	PP/SGF (treated with AA) (wt%)
Polypropylene (PP)	100, 95, 90, 85, 80	100, 95, 90, 85, 80
Spear grass fiber (SGF)	0, 5, 10, 15, 20	0, 5, 10, 15, 20
Acid acrylic (AA)	–	3*

*wt% of filler

20.2.3 Filler Treatment

PP pellets were added into the mixer chamber simultaneously with AA to treat the SGF. Then, the SGF was mixed into the chamber 12 minutes later, and the mixing was continued for another 5 minutes. The mixing completed at 17 minutes for each 45 g of composite mixture.

20.2.4 Compression Molding

The composite mixtures were transferred into a dumbbell shape fabricated mold and then compressed using a hot-press machine (GT 7014) to form a dumbbell shape using a fabricated mold. The hot press needs to preheat for 6 min at 180 °C, the compressing for another 4 minutes at the same temperature and subsequent slow cooling for another 4 minutes before the pressure can be released.

20.2.5 Mechanical Tensile Test

The tensile tests were carried out using a Galdabini Quasar 100 tensile testing machine. A dumbbell shape according to ASTM D638 (Type IV) specimen size was selected for this test. The testing was performed at standard laboratory room temperature with a crosshead displacement rate of 50 mm/min and a gauge length of 50 mm. For statistical purpose, 10 samples were tested to obtain sufficient accuracy of the results.

20.2.6 Water Absorption Test

The water absorption tests were carried out according to ASTM D570. The samples with dimensions 25 mm × 15 mm × 1.0 mm were dried in the oven at 80 °C for 24 h. The specimens were weighted to measure the original dry weight using an electrical digital balance. The specimens were immersed in distilled water at room temperature and were weighted at regular predetermined intervals. The percentage of water absorption, M_t , is calculated by Eq. (20.1) below.

$$M_t = \frac{W_n - W_d}{W_d} \times 100 \quad (20.1)$$

where W_n is the weight after immersion, and W_d is the initial dry weight.

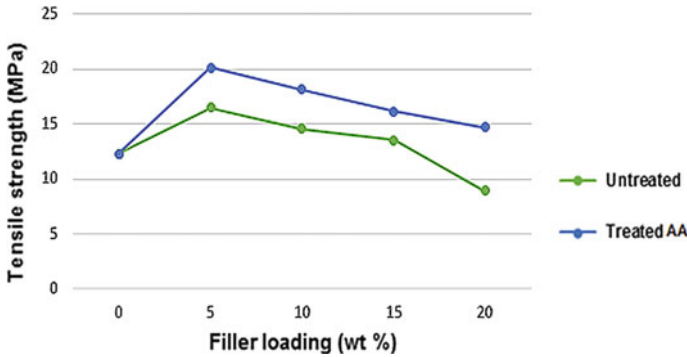


Fig. 20.2 Effect of untreated and treated filler loading to tensile strength of PP/SGF composite

20.3 Results and Discussion

20.3.1 Tensile Strength

Figure 20.2 shows the tensile strength versus SGF filler loading of the untreated and treated composite. The result shows that the highest strength is obtained for the 5 wt% treated and the lowest is 20 wt% untreated composites. Both treated and untreated composites show a similar pattern when the tensile strength value was increased when the filler is adding up to 5 wt%. Same goes for both composites, when more than 5 wt% filler were added, the tensile strength decreased. At this point, the weak interfacial area between the SGF (reinforced filler) and the PP (polypropylene matrix) occurs when the filler loading is increased [4, 5]. Moreover, treated composites have better results of tensile strength compared to untreated composites. PP/SGF with the existence of AA contributes to the better dispersion and adhesion of SGF and PP.

20.3.2 Young's Modulus

Figure 20.3 shows Young's modulus versus SGF filler loading for untreated and treated composites. It clearly shows that Young's modulus is increased for both composites. High amount of filler has increased the stiffness of the composites [6, 7]. Young's modulus of the treated composite is higher than for the composite without treatment.

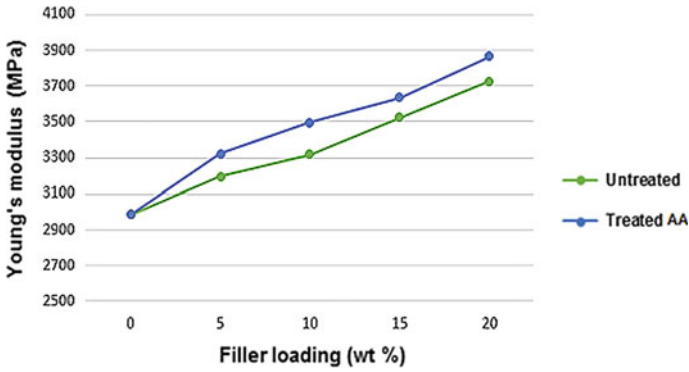


Fig. 20.3 Effect of treated and untreated filler loading on Young's modulus of PP/SGF composites

20.3.3 Elongation at Break

Figure 20.4 shows the elongation at break percentage versus filler loading for untreated and treated composites. It shows that the elongation at break was decreased as the filler loading increased. This is due to the deformability of the rigid interface between the SGF and PP matrix that has reduced proportionally to the fiber concentration. The fillers had hardened the composites and reduced their ductility [8–10].

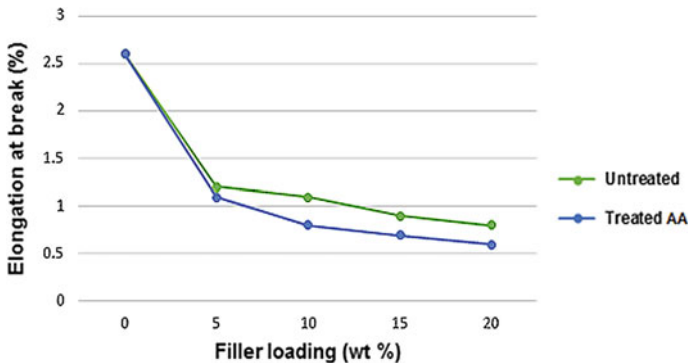


Fig. 20.4 Effect of untreated and treated filler loading on elongation at break percentage of PP/SGF composite

20.3.4 Water Absorption

Figure 20.5 shows the water absorption percentage of different filler loadings versus time. The untreated composite absorbs more compared with treated composite. The highest water absorption is at 20 wt% composite without treatment, while the lowest water absorption is at 5 wt% composite with treatment. The presence of AA indicates that the composite has a better water resistance [7, 8]. The compatibility between PP and SGF was improved because the anhydride groups in AA form a strong interaction with the matrix.

Figure 20.6 shows the equilibrium water absorption versus different filler loading for treated and untreated composites. The increases in filler loading in the composites have increased the number of hydrogen bonds between SGF with water molecules [8, 10, 11]. The lower rate of water absorption of treated PP/SGF composites indicates

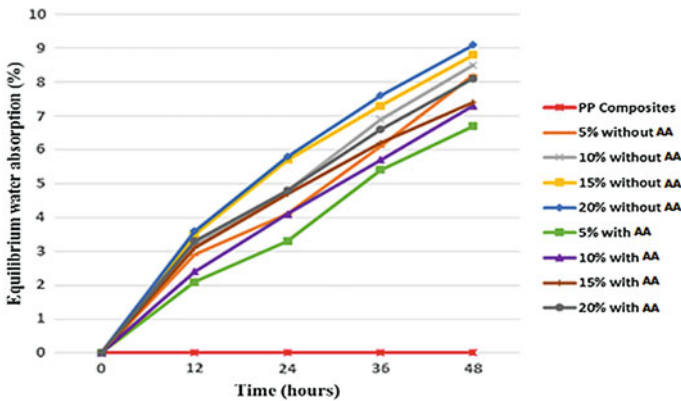


Fig. 20.5 Comparison of treated and untreated PP/SGF composites in regard to water absorption

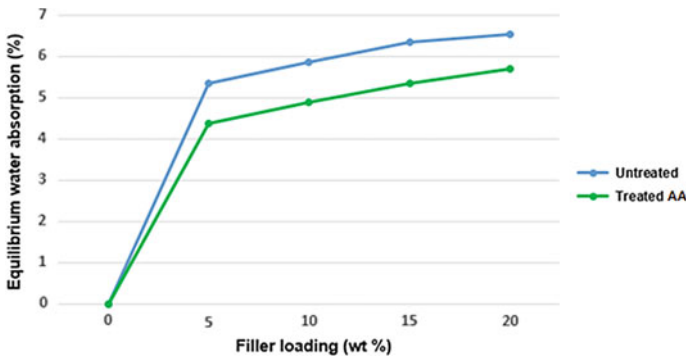


Fig. 20.6 Effect of filler loading on equilibrium water absorption percentage of treated and untreated PP/SGF composite

a better water resistance property. Number of gaps and flaws exist at the composite interface, were decreased and thus reduced the number of possible water path which penetrates the composites.

20.4 Conclusion

In conclusion, the presence of AA has improved the fiber and matrix adhesion. It leads to an increased tensile strength and modulus of elasticity of the composite. The elongation at break decreased due to the increased bonding strength which gave to the composites more stiffness and lower resistance to break. Compatibilizer treatment also decreases the hydrophilic characteristic of SGF by forming a protective chemical layer which protects the bonds between the SGF filler and PP matrix from water attacks. This reduced the water absorption and prevents deterioration of filler–matrix bonding, protecting the mechanical properties from degrading.

Acknowledgements The authors would like to thank the Universiti Kuala Lumpur Short-Term Research Grant (UniKLSTRG str17043) for financial funding and System Engineering and Energy Laboratory (SEELab) for the guidance of this project.

References

1. AL-Oqla, F.M., Sapuan, S.M., Ishak, M.R., Nuraini, A.A.: Predicting the potential of agro waste fibers for sustainable automotive industry using a decisionmaking model. *Comput. Electron. Agric.* **113**, 116–127 (2015)
2. Sabri, M., Mukhtar, A., Shahril, K., Siti Rohana and Husseinsyah Salmah, A.: Effect of compatibilizer on mechanical properties and water absorption behaviour of coconut fiber filled polypropylene composite. *Adv. Mater. Res.* **795**, 313–317 (2013)
3. Properties of polypropylene, the source obtained from Polypropylene Malaysia Sdn. Bhd
4. Hatta, N.: Mechanical properties of polystyrene/polypropylene reinforced coconut and jute fibers, 24–26 (2008)
5. Bhoopathi, R., Ramesh, M., Deepa, C.: Fabrication and property evaluation of grass-hemp-glass fiber reinforced composites. *Procedia Eng.* **97**, 2032–2041 (2014)
6. Prasad, V., Joy, A., Venkatachalam, G., Narayanan, S., Rajakumar, S.: Finite element analysis of jute and grass fibre reinforced hybrid polymer matrix composite and optimization of design parameters using ANOVA technique. *Procedia Eng.* **97**, 1116–1125 (2014)
7. Annie Paul, S., Boudenne, A., Ibos, L., Candau, Y., Joseph, K., Thomas, S.: Effect of fiber loading and chemical treatments on thermophysical properties of grass fiber/polypropylene commingled composite materials. *Compos. Part A Appl. Sci. Manuf.* **39**(9), 1582–1588 (2008)
8. Li, M, Wen, X, Liu, J., Tang, T.: Composites: part a synergetic effect of epoxy resin and acid acrylic on improving mechanical properties of polypropylene/short carbon fiber composites. *Compos. Part a*, **67**, 212–220 (2014)
9. Supri, A.G., Lim, B.Y.: Effect of treated and untreated filler loading on the mechanical, morphological, and water absorption properties of water hyacinth fibers-low density polyethylene composites. *J. Phys. Sci.* **20**(2), 85–96 (2009)

10. Yang, H.S., Kim, H.J., Lee, B.J., Hwang, T.S.: Effect of compatibilizing agent on rice husk flour reinforced polypropylene composites. *Compos. Struct.* **77**, 45–55 (2007)
11. Bettini, S.H.P., Bicudo A.B.L.C., Augusto, I.A., Antunes, L.A., Morassi, P.L., Condotta, R. Bonse, B.C.: Investigation on the use of coir fiber as alternative reinforcement in polypropylene. *J. Appl. Polym. Sci.* **118**, 2841–2848 (2010). ISSN 1359-835X

Chapter 21

Parametric Optimization of Electrical Discharge Machining of SiSiC Ceramic Through the Taguchi Design Approach



Abdul’Azeez A. Aliyu, Ahmad Majdi Abdul Rani,
Muhammad Al’Hapis Abdul Razak, and Sadaqat Ali

Abstract The evolution of silicon carbide (SiC) ceramics has recently attracted the interest of several researchers due to their industrial applications. Nonetheless, the shaping of SiC is quite challenging using conventional techniques due to its extreme hardness, high thermal stability and high brittleness characteristics. This study attempts to shape a modified SiC called siliconized SiC (SiSiC) by the electrical discharge process (EDM). Moreover, the effective utilization of the Taguchi approach to study the EDM parameters and optimize the responses has been reported. The responses to be studied include material removal rate (MRR), electrode wear (EW) and surface roughness (SR). The Taguchi methodology using L9 orthogonal arrays was employed to plan the experiment, and the signal-to-noise (S/N) ratio was used to predict the optimum parameter settings. The experimental results were analyzed using S/N and ANOVA. The results reveal that the peak current (I) and on-time (ON) were the main significant parameters on MRR and SR whereas EW was influenced mainly by the peak current. The off-time was found to be insignificant in all the selected responses. The results obtained were justified by conducting the verification runs.

Keywords EDM · SiSiC · S/N · Taguchi · Parameters · Optimization · Responses

A. A. Aliyu (✉)
Mechanical Engineering Department, Bayero University Kano, Kano, Nigeria
e-mail: aaaliyu.mec@buk.edu.ng

A. M. Abdul Rani
Mechanical Engineering Department, Universiti Teknologi Petronas, 32610 Bandar Seri Iskandar,
Perak, Malaysia
e-mail: majdi@utp.edu.my

M. A. Abdul Razak
Manufacturing Section, Universiti Kuala Lumpur Malaysian Spanish Institute, Kulim Hi-Tech
Park, 09000 Kedah, Malaysia
e-mail: alhapis@unikl.edu.my

S. Ali
National University of Sciences and Technology (NUST), Islamabad, Pakistan
e-mail: engineersadaqat@gmail.com

21.1 Introduction

In recent years, there has been uprising demand for silicon carbide (SiC) especially for producing aerospace components, cutting tools, nuclear reactors, dies, bearing parts and engine parts [1, 2]. SiC have unique and excellent mechanical properties like extreme hardness, good thermal stability, low density and high compressive strength [3]. However, its high hardness and brittleness makes it difficult to machine using traditional processes such as grinding and lapping [4, 5].

Recently, electrical discharge machining (EDM) emerges as an alternative to the conventional techniques for shaping SiC ceramics. The EDM is an electrothermal process which erodes material through series of repetitive sparks thereby leading to erosion of both electrodes in form of craters by melting and vaporization. It can produce any complex shape with good surface quality and low tool wear. The EDM remained the most efficient process in manufacturing of dies, molds and finishing parts of aerospace, medical implants and automotive applications [6–10]. Although EDM process was proven as the most efficient and economical technique to machine ceramic materials, the main hindrance is its very low electrical resistivity of SiC (10^3 – 10^5 Ω cm). To enhance the electrical conductivity of SiC, liquid silicon (Si) is normally infiltrated into green SiC-C thereby producing new form of SiC called siliconized silicon carbide (SiSiC) or reaction bonded silicon carbide (RBSiC) [11]. The strategies for machining SiC were developed and compared to the industries, which resulted in time reduction of about 50% [12]. Aliyu, Hamidon [13] studied machining performance of SiSiC by EDM process using copper electrode. The parameters for machining SiSiC were fully studied and optimized through response surface methodology [14]. A large surface area was successfully achieved during electric discharge milling process milling of SiSiC [15].

In this paper, aluminum powder mixed EDM (PMEDM) was used to machine SiSiC using copper electrode. The experiment was planned and analyzed using Minitab software. The Taguchi technique was employed to analyze and optimize the responses (material removal rate (MRR), electrode wear (EW) and surface roughness (SR)). The Taguchi is an efficient design approach used to achieve low cost, less production time and improved production rate of the final component in sinking EDM of SiSiC. The responses MRR, EW and SR were successfully optimized to achieve higher MRR with lower EW and SR.

21.2 Experimentation

21.2.1 Materials

A Sodik-AG40L die-sinking EDM machine was employed in this study to machine a solid block of SiSiC with dimensions of 12 by 50 by 50 mm. A solid cylindrical shape copper electrode with 21.8 mm tip surface area and 50 mm length was chosen to be

Table 21.1 Physical and mechanical properties of SiSiC

Properties	Data
SiC content (%)	88
Melting point (°C)	2600
Density (g/cm ³)	3.05
Maximum service temperature (°C)	1380
Hardness (GPa)	25–35
Thermal conductivity (W/(m K))	36
Electrical resistivity (Ω cm)	36
Young modulus (GPa)	10 ² –10 ³

Source Manufacturer's data

the tool to erode the work material. PGM white 3 aluminum powder was added to the Sythen SEM 212 dielectric fluid. Table 21.1 displays the physical and mechanical properties of the work material used in this study.

21.2.2 Procedure and Methods

Both the electrode and workpiece were fully immersed in the dielectric fluid as displayed in Fig. 21.1. The EDM machine was run after setting the selected and constant parameters. The work material was eroded, and the machine stopped automatically



Fig. 21.1 Photograph of the sinking EDM machine

Table 21.2 Parameters and levels

Parameter	Level		
	1	2	3
Peak current (A)	4.4	8.8	13.2
On-time (μ s)	10	20	30
Off-time (μ s)	200	500	800
Servo voltage (V)	40	60	80

when the machining was completed. The machining time, weight of both the workpiece and the electrode were recorded before and after machining. MRR and EW were calculated. The SR was measured using a Mitutoyoformtracer CS-5000. The experiment was planned by the Minitab 16 design software. Three level L9 orthogonal arrays of the Taguchi technique consisting of 4 columns and 9 runs were designed. Thus, 9 experimental runs were conducted. The parameters selected and the levels of each parameter are depicted in Table 21.2. The significant parameters that affect the machining performance characteristics were determined by means of analysis of variance (ANOVA).

21.2.2.1 Design Parameters

Several EDM parameters which demonstrated great influence on the EDM machining performance have been identified by many researchers. These parameters were mainly classified into *electrical* and *non-electrical* parameters. Electrical parameters such as peak current (I), on-time (ON), off-time (OFF) and servo voltage (Sv) were selected in this study. Thus, they are the most essential and generally used by many researchers [16].

21.2.2.2 Response Variables

The selected responses in this study were defined in the following equations:

$$\text{MRR (mm}^3/\text{min)} = (\text{workpiece weight difference before and after machining}) \\ \times 1000 / (\text{machining time} \times \text{workpiece density})$$

$$\text{EW (\%)} = (\text{electrode weight difference before and after machining}) \\ \times 100 / (\text{workpiece weight difference})$$

whereby the weight is expressed in grams, machining time in minutes and density in gram/centimeter cube.

21.2.3 Taguchi Approach

The Taguchi method was named after the Japanese Dr. Genichi Taguchi who developed the method. The Taguchi approach has been widely applied in several European and US industries, as far long as 1980s. In contrast to classical techniques, the Taguchi method is mainly focused on design for quality characteristics and to achieve low cost of the final product. A Large number of experiments are needed to be carried out in classical methods especially when a high number of process parameters are involved. Thus, classical methods are considered complex and difficult to execute. The Taguchi method utilizes an exceptional design of orthogonal array to examine the influence of process parameters by conducting only few numbers of experiments. For example, 4 factors would require about 20 experiments in classical method which can produce almost the same as with 9 experimental runs when the Taguchi method is used. Thus, the Taguchi technique can increase the production rate, minimize cost, reduce production time and increase profit. Moreover, the Taguchi method can consider both control and uncontrol (noise) factors whereby classical methods deal only with control factors. The Taguchi method is considered more effective than the factorial method as it tests only pair (orthogonal) combinations. Factorial design requires to test all possible combinations [16].

21.2.3.1 Signal-to-Noise Ratio

Taguchi developed the signal-to-noise (S/N) ratio to reduce the variation from the value of the target response. After the required number of experiments has been conducted according to the designed orthogonal arrays, the experimental results are then converted to the S/N ratio. S/N ratio serves as a measure of the machining characteristics that deviate from the desired value. The determination of the S/N ratio depends on the required condition of the machining performance characteristics and the objectives of the experiment. Generally, three categories in the analysis of the S/N ratio have been identified. These categories are defined in Eqs. (21.1), (21.2) and (21.3).

- The bigger is the best

$$S/N \text{ (max)} = -10 \log \left((1/n) \left(\sum (1/y^2) \right) \right) \quad (21.1)$$

- The smaller is the best

$$S/N \text{ (min)} = -10 \log \left((1/n) \left(\sum (y^2) \right) \right) \quad (21.2)$$

- The nominal is the best

$$S/N \text{ (min)} = 10 \log \left(\bar{y}/s y^2 \right) \quad (21.3)$$

where y is the observed data of the responses, \bar{y} is the mean of observed data of the responses, sy is the variance of y and n is the number of the experimental observation.

The responses with higher S/N ratio are considered the best irrespective of the category of S/N ratio. Thus, a higher value of the S/N ratio determines the optimum parameter settings and the corresponding response value.

21.3 Results and Analysis

Table 21.3 shows the L9 designed experimental results corresponding to each parameter settings. The S/N ratio for the responses was calculated using Eqs. (21.1) and (21.2) as displayed in Table 21.4. Since there is the need to maximize the MRR, the

Table 21.3 Parameter settings and experimental results

Exp No.	Ip (A)	ON (μ s)	OFF (μ s)	Sv (V)	MRR (mm^3/min)	EW (%)	SR (μm)
1	4.4	10	200	40	0.3293	17.88	1.407
2	4.4	20	500	60	0.5907	12.85	1.227
3	4.4	30	800	80	0.2742	13.02	1.544
4	8.8	10	500	80	0.6529	31.18	1.258
5	8.8	20	800	40	1.7468	35.32	1.441
6	8.8	30	200	60	1.6485	36.17	1.595
7	13.2	10	800	60	1.2190	42.40	1.375
8	13.2	20	200	80	2.5188	41.23	1.644
9	13.2	30	500	40	2.4227	41.87	2.031

Table 21.4 Signal-to-noise ratio for the responses

Exp. No.	Signal-to-noise ratio		
	MRR	EW	SR
1	-9.6482	-25.0474	-2.9659
2	-4.5727	-22.1780	-1.7769
3	-11.2387	-22.2922	-3.7730
4	-3.7031	-29.8775	-1.9936
5	4.8449	-30.9604	-3.1733
6	4.3418	-31.1669	-4.0552
7	1.7201	-32.5473	-2.7660
8	8.0239	-32.3043	-4.3180
9	7.6860	-32.4380	-6.1542

bigger the better (Eq. 21.1) was applied. To minimize EW and SR, the smaller the better (Eq. 21.2) was considered.

Tables 21.5, 21.6, 21.7 and 7 display the response table for the S/N ratio and ANOVA for MRR, EW and SR. For quality characteristics the best response variable is obtained at larger value of the S/N ratio. It can be seen from the ANOVA shown in Table 21.6 that process parameters I and ON with percentage contribution of 69.1% and 22.1%, respectively, are the main significant factors for MRR. Following similar analysis, it was found that *I* is the main significant parameter on EW whereby I, ON and Sv are the significant factors on SR.

Figures 21.2, 21.3, 21.4, 21.5, 21.6 and 21.7 show the main effect plots for the S/N ratio and the corresponding plots for means of MRR, EW and SR, respectively. The total mean of the S/N ratio is represented by the horizontal line in the plots. The higher value of S/N ratio indicates the best response value for quality measures. Thus, maximum MRR was achieved at high current (level 3) of 13.2 and ON-time of 20 μm (level 2) as displayed in Fig. 21.2. EW is mainly affected by the current whereby low

Table 21.5 Response table for S/N ratio of MRR

Level	I	ON	OFF	Sv
1	-8.4865	-3.8771	0.9058	0.9609
2	1.8279	2.7654	-0.1966	0.4964
3	5.8100	0.2630	-1.5579	-2.3059
Delta	14.2965	6.6424	2.4637	3.2668
Rank	1	2	4	3

Table 21.6 ANOVA for MRR

Source	DF	SS	MS	% Contribution
I	2	4.14125	2.07063	69.1
ON	2	1.32313	0.66156	22.1
OFF	2	0.27224	0.13612	4.6
Sv	2	0.24351	0.12175	4.2
Total	8	5.98013		

Table 21.7 Response table for S/N ratio of EW

Level	I	ON	OFF	Sv
1	-23.17	-29.16	-29.51	-29.48
2	-30.67	-28.48	-28.16	-28.63
3	-32.43	-28.63	-28.68	-28.16
Delta	9.26	0.68	1.34	1.32
Rank	1	4	2	3

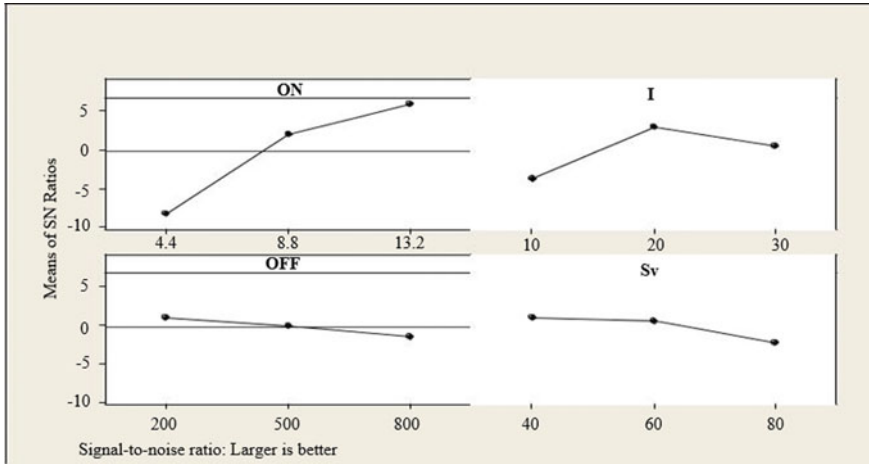


Fig. 21.2 Main effects plot for S/N ratios of MRR

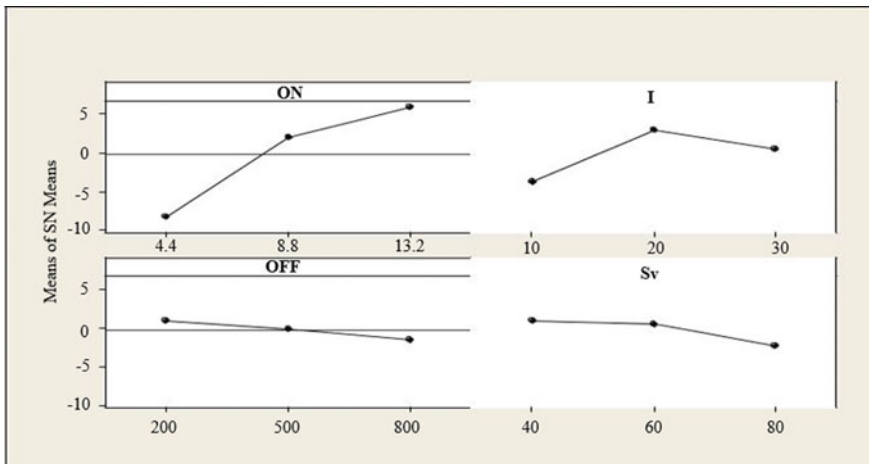


Fig. 21.3 Main effects plot for means of MRR

EW is achieved at low current of 4.4A (level 1) as shown in Fig. 21.4. Figure 21.6 indicates that SR was significantly affected by I, ON and Sv. Thus, improved SR was obtained at low I, low ON and mid-level of Sv. The results achieved in this study (9 experimental runs) agree with several researches made using factorial design techniques which required at least 16 experimental runs [17]. This justified that the Taguchi approach is the most cost-effective technique in achieving the quality of the manufacturing product.

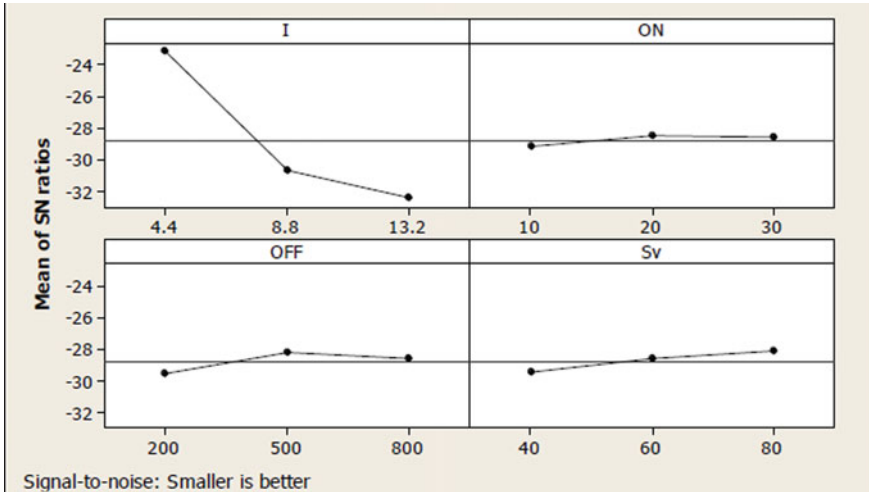


Fig. 21.4 Main effects plot for S/N ratios of EW

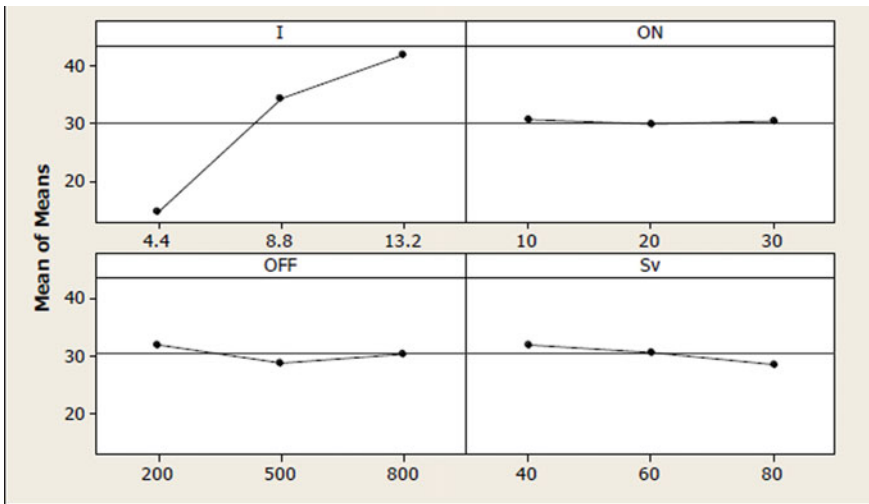


Fig. 21.5 Main effects plot for means of EW

21.4 Verification Runs

To validate the experimental results, three experimental runs were carried out using the optimum parameter settings. The optimum parameters were obtained from the main effect plots for S/N ratio values. As earlier stated, the higher the S/N ratio the better is the response value. Thus, the optimum setting for each response was taken

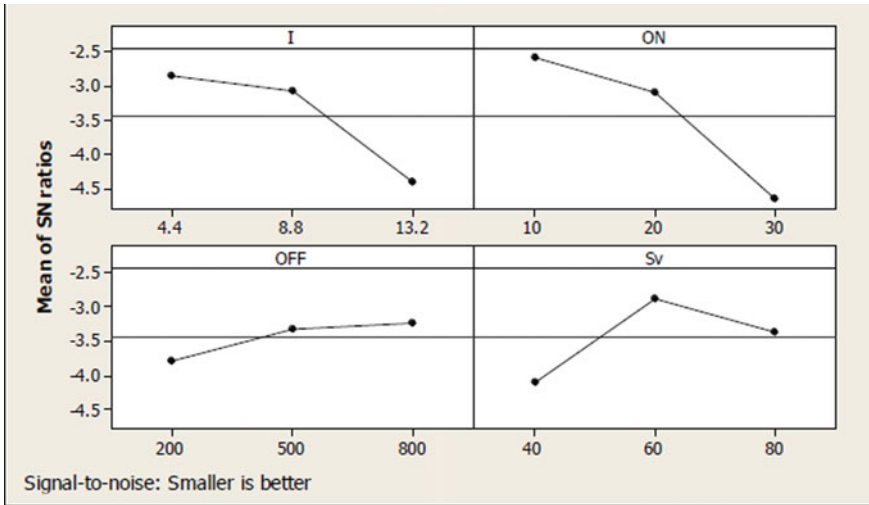


Fig. 21.6 Main effects plot for S/N ratios of SR

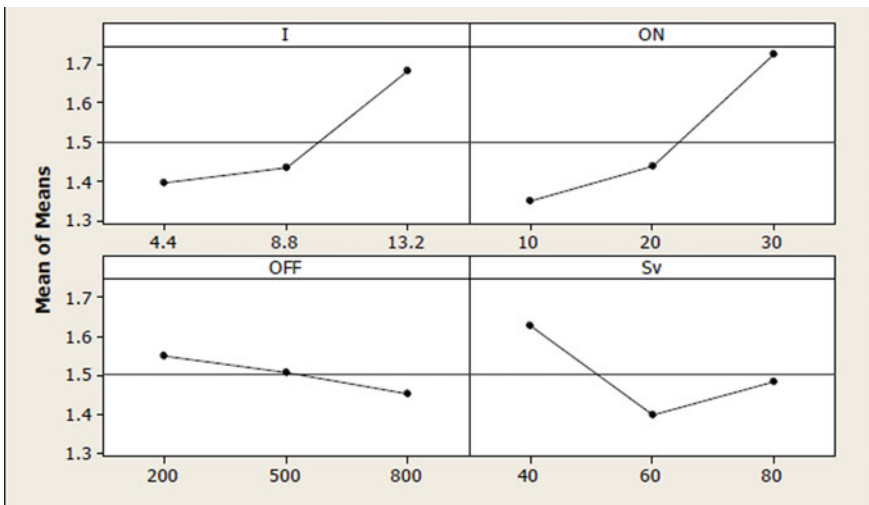


Fig. 21.7 Main effects plot for means of SR

from the highest level of the S/N ratio in the corresponding main effect plots of each response. The quality characteristics responses requirement and the optimum parameter settings are displayed in Table 21.8 and the corresponding verification experimental results are depicted in Table 21.9. The verification experimental results reveal that MRR of 3.12 mm³/min, EW of 12.93% and SR of 1.084 μm was achieved.

Table 21.8 Quality responses and optimum parameter settings

Quality characteristics requirement	Optimum parameter settings			
	I	ON	OFF	Sv
Maximize MRR	13.2	20	200	40
Minimize EW	4.4	20	500	80
Minimize SR	4.4	10	800	60

Table 21.9 Confirmation experimental results for the selected responses

Experimental runs for validation	MRR (mm ³ /min)	ER (%)	SR (μm)
Maximum MRR	3.1186	41.14	1.696
Minimum EW	0.2049	12.93	1.287
Minimum SR	0.1380	13.73	1.084

21.5 Conclusions

The following conclusions were made after the experimental study:

- The current was found to be the most influential parameter on all the selected responses.
- On-time is also significant on MRR whereby ER was also influenced by the on-time and servo voltage.
- Optimum responses (maximum MRR, minimum EW and minimum SR) were achieved through optimum parameter settings.

References

1. Okada, A.: Automotive and industrial applications of structural ceramics in Japan. *J. Eur. Ceram. Soc.* **28**(5), 1097–1104 (2008)
2. Katoh, Y., Kondo, S., Snead, L.L.: DC electrical conductivity of silicon carbide ceramics and composites for flow channel insert applications. *J. Nucl. Mater.* **386–388**, 639–642 (2009)
3. Zhang, N.-L., et al.: Preparation and properties of reaction bonded silicon carbide (RB-SiC) ceramics with high SiC percentage by two-step sintering using compound carbon sources. *Ceram. Int.* **45**(12), 15715–15719 (2019)
4. Yang, X.H., Zhang, Y.M., Han, J.C.: High speed lapping of SiC ceramic material with fixed abrasive. *Key Eng. Mater.* (2007) (Trans Tech Publ)
5. Shumyacher, V., Dushko, O., Pushkarev, D.: Predicting the grinding efficiency of hard ceramics in terms of surface brittleness. *Russ. Eng. Resear.* **29**(6), 623–624 (2009)
6. Yadav, U.S., Yadava, V.: Experimental modeling and multiobjective optimization of electrical discharge drilling of aerospace superalloy material. *Proceed. Inst. Mech. Engineers, Part B: J. Eng. Manuf.* **229**(10):1764–1780 (2015)
7. Aliyu, A.A.A., et al.: Characterization, adhesion strength and in-vitro cytotoxicity investigation of hydroxyapatite coating synthesized on Zr-based BMG by electro discharge process. *Surf. Coat. Tech.* **370**, 213–226 (2019)

8. Aliyu, A.A.A., et al.: Hydroxyapatite mixed-electro discharge formation of bioceramic Lakargite (CaZrO_3) on Zr–Cu–Ni–Ti–Be for orthopedic application. *Mater. Manuf. Proc.*, pp. 1–11 (2018)
9. Abdul-Rani, A.M., et al.: Enhancing surface quality of Zr-Cu-Ni-Ti-Be through hydroxyapatite mixed EDM for potential orthopedic application. In: *AIP Conference Proceeding*. AIP Publishing (2018)
10. Aliyu, A.A.A., et al.: A Review of additive mixed-electric discharge machining: current status and future perspectives for surface modification of biomedical implants. *Adv. Mater. Sci. Eng.* **2017** (2017)
11. Clijsters, S., et al.: EDM technology and strategy development for the manufacturing of complex parts in SiSiC. *J. Mater. Proc. Tech.* **210**(4), 631–641 (2010)
12. Lauwers, B., Kruth, J.P., Brans, K.: Development of technology and strategies for the machining of ceramic components by sinking and milling EDM. *CIRP Ann.* **56**(1), 225–228 (2007)
13. Aliyu, A.A., Hamidon, M., Rohani, J.M.: Parametric study of powder mixed electrical discharge machining and mathematical modeling of SiSiC using copper electrode. *Adv. Mater. Res.* (2014) (*Trans Tech Publ*)
14. Aliyu, A.A.A., et al.: Optimization of electrical discharge machining parameters of SiSiC through response surface methodology. *J. Tek.* **79**(1), 119–129 (2017)
15. Liu, Y., et al.: Electric discharge milling of silicon carbide ceramic with high electrical resistivity. *Int. J. Mach. Tools Manuf.* **48**(12), 1504–1508 (2008)
16. Montgomery, D.C.: *Design and analysis of experiments*. Wiley (2017)
17. Habib, S.S.: Study of the parameters in electrical discharge machining through response surface methodology approach. *Appl. Math. Model.* **33**(12), 4397–4407 (2009)

Chapter 22

The Impact of Sintering Dwell Time on Nitrogen Absorption, Densification and Microhardness of 316L Stainless Steel Using Powder Metallurgy



Sadaqat Ali, Ahmad Majdi Abdul Rani, Muhammad Al'Hapis Abdul Razak, Abdul Azeez Abdu Aliyu, and Krishnan Subramaniam

Abstract Powder metallurgy is one of the promising techniques for producing different metals and their alloys. The uniqueness of this technique owes to its processing parameters that can be optimized to produce a desired material with tailored physical and mechanical properties. Among the available biomaterials, the austenitic stainless steel 316L has been used for some time for manufacturing implants and other surgical devices. However, this material is prone to localized corrosion attacks. It corrodes in human physiological conditions in long-term applications and releases metal ions. The corrosion products include ions of nickel, chromium and iron that accumulate in the tissues surrounding the implant limiting its usage as a biomaterial. This research work aims diffusing a sintering gas (nitrogen) into the matrix of stainless steel by increasing the dwell time. The results of the study show that the increased dwell time

S. Ali (✉) · A. M. Abdul Rani
School of Mechanical and Manufacturing Engineering, National University of Sciences & Technology (NUST), H-12, Islamabad, Pakistan
e-mail: engineersadaqat@gmail.com

A. M. Abdul Rani
e-mail: majdi@utp.edu.my

A. A. Abdu Aliyu
Mechanical Engineering Department, Universiti Teknologi PETRONAS, 32610 Bandar Seri Iskandar, Perak, Malaysia
e-mail: garoabdul@gmail.com

M. A. Abdul Razak
Manufacturing Section, Universiti Kuala Lumpur Malaysian Spanish Institute, Kulim Hi-Tech Park, 09000 Kulim, Kedah, Malaysia
e-mail: alhapis@unikl.edu.my

K. Subramaniam
Department of Mechanical Engineering, Manipal International University, Putra Nilai, 71800 Negeri Sembilan, Malaysia
e-mail: simmam06@yahoo.com

not only diffuses nitrogen into the matrix but also forms a protective layer of nitrogen onto the samples surface. There is also a notable effect of increased dwell time on the densification and microhardness of the sintered samples. The results indicate that this surface layer can prevent the leaching of metal ions from the stainless steel matrix.

Keywords 316L stainless steel · Sintering · Dwell time · Nitrogen diffusion · Leaching

22.1 Introduction

Metals are extensively used as biomaterials in the medical field for joint replacements, orthopaedic fixation, stents and dental restorations including tooth roots and denture bases [1]. All biomaterials are required to be highly biocompatible to the physiological and biological condition of the human body [2]. Biocompatibility is considered as the crucial element in long-term success of an implant within the healthcare disciplines.

Among commercially available biomaterials, austenitic 316L stainless steel has been the widely acceptable biomaterial in producing implants due to its low cost, reasonable corrosion resistance and ease of fabrication [3, 4]. However, this material is prone to localized corrosion attacks. It corrodes in human physiological conditions in long-term applications limiting its use as an implant material [5]. It has been reported that in vitro corrosion of stainless steel results in the release of metal ions. This release of ions inhibits the immune response and alters the expression of lymphocyte-surface antigens [6, 7]. The corrosion products include ions of nickel, iron and chromium that accumulate in tissues surrounding the implant [8]. The patient is thus exposed to these corrosion products resulting in the initiation of reactions in the tissues. These include irritation, unpleasant taste, allergy, eczematous rash and many other reactions. These factors affect the life of implants, erosion of implants weakens them and the patients have to go for repeated surgery [9].

Therefore, to cater these issues and to obtain the desired response of 316L stainless steel material as an implant material, a number of surface coating techniques have been developed to improve the biocompatibility of this material. These techniques are being explored to develop the desired biological response between the implant material and human tissue. However, these surface modification techniques owe certain limitations including expensive raw materials, non-uniform crystallinity, line of sight, time consuming, low deposition rate and difficult to produce crack-free coatings [10–12]. These limitations necessitate the development of an efficient approach to enhance the corrosion resistance of this material and minimize the leaching of metal ions [13].

Powder metallurgy (P/M) is evaluated as the most common and successful technique for producing implant materials. This technique dates back to the 1960s when a porous hip prosthesis implant was produced by the P/M method [14, 15]. Powder

metallurgy is preferred in dentistry and orthopaedic cases where a load bearing capacity with a reliable implant-bone connection is needed [15–17]. Therefore, to solve the above-mentioned issue, implant materials with an inherent protective surface layer are required [18, 19]. It is hypothesized that sintering of samples in nitrogen atmosphere with increased dwell time can develop a surface nitride layer along with diffusion of nitrogen into the matrix. This approach can increase the corrosion resistance and minimize the leaching of metal ions.

22.2 Materials and Methods

In this research work, samples from pure 316L stainless steel powder were produced by the powder metallurgy method. The chemical composition of the powder used in the study is specified in Table 22.1.

The SEM and XRD of the powder used are shown in Figs. 22.1 and 22.2, respectively.

Table 22.1 Chemical composition of the powder used in this study

Element	Cr	Ni	Mo	O	Si	C	Mn	Fe
wt%	17.04	12.01	2.4	0.068	0.9	0.028	1.5	Balance

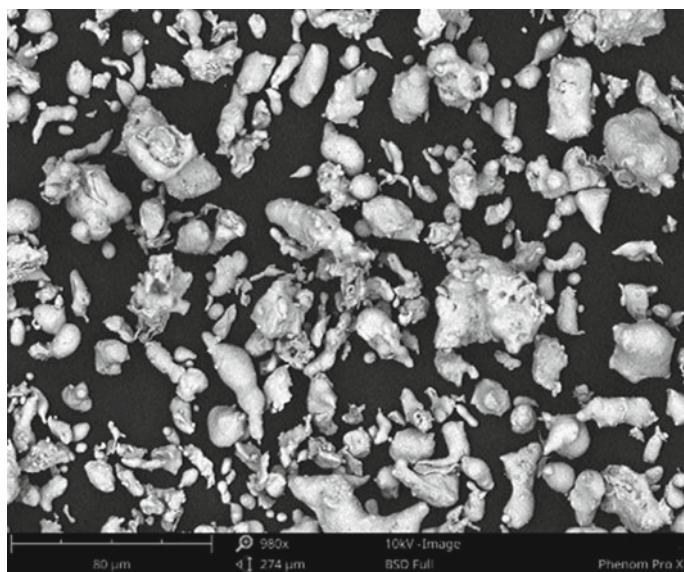


Fig. 22.1 SEM image of 316L stainless steel powder

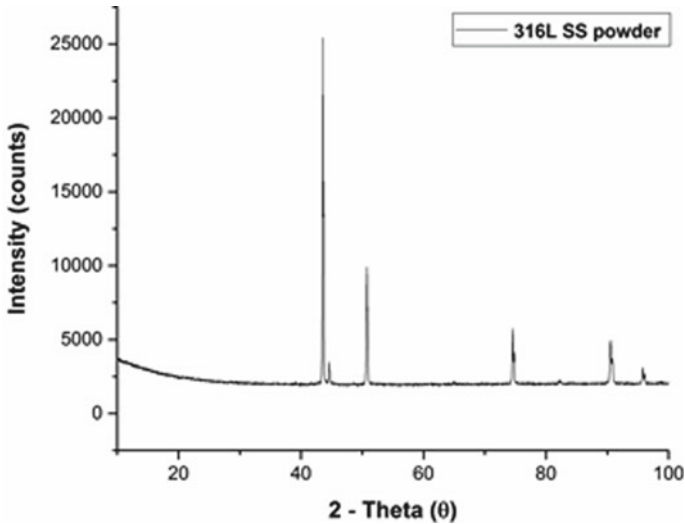


Fig. 22.2 XRD pattern of 316L stainless steel powder

The samples of 30 mm diameter and ~5 mm thickness were made from powder using the cold compaction process. The powder was compressed in a die at a pressure of 800 MPa to prepare pellet shape samples followed by sintering in nitrogen atmosphere in a tube furnace at a temperature of 1200 °C. The green compact samples were sintered with varying dwell time of 1, 3, 5 and 8 h.

The green density of the samples was determined by geometrical method, whereas the sintered density was calculated using Archimedes' principle. The hardness of the sintered samples was measured using a Vickers hardness tester and XRD analysis was carried out to compute the formation of compounds during sintering. The XPS analysis was done to see the effect of dwell time on the formation of the nitride layer. Finally, the weight loss measurements were carried out to determine the corrosion resistance of the sintered samples. The samples were immersed in an artificial saliva solution for 28 days and the weight before and after immersion was calculated.

22.3 Results and Discussion

Firstly, the green density of the compacted samples after the cold compaction process was calculated by the geometrical method. It involved the measurement of mass and geometrical dimensions of the compacted sample. The green density was then calculated by dividing the mass of the sample by its volume. The green density for the compacted sample was found to be 6.5 g/cm³. The impact of sintering parameters on the densification of the sintered samples was calculated by measuring the sintered density. The sintered density was found by Archimedes' principle. The densification

results indicate that the dwell time has a notable effect on densification and the sintered density values increased by increasing dwell time. The sintered density for 1 h dwell time was found to be 7.35 g/cm³ and its value increased to 7.57 g/cm³ for 8 h dwell time. The green and sintered density values for all the samples are given in Table 22.2.

The effect of sintering parameters on the microhardness of the sintered samples was obtained by conducting Vickers hardness testing. The testing was done by applying 200 gf on the sintered samples for 15 s. The results of microhardness are shown in Fig. 22.3. The results indicated that the microhardness values increase by increasing the dwell time. A microhardness of 185 HV was observed for samples sintered with a dwell time of 1 h, whereas the hardness value increased to 235 HV for 8 h dwell time sintered samples. The increase in microhardness with increasing dwell time can be indebted to the increase of nitrogen diffusion at higher dwell times.

The XRD analysis for all the sintered samples was carried out for the confirmation of nitrogen diffusion. The XRD patterns of all the sintered samples revealed the nitrogen diffusion. The nitrogen diffused into the matrix of stainless steel and reacted

Table 22.2 Green and sintered densities of samples at different dwell times

S. No.	Dwell time (h)	Green density (g/cm ³)	Sintered density (g/cm ³)	Densification (%)
1	1	6.5	7.35	92.45
2	3	6.5	7.38	92.83
3	5	6.5	7.46	93.83
4	8	6.5	7.57	95.22

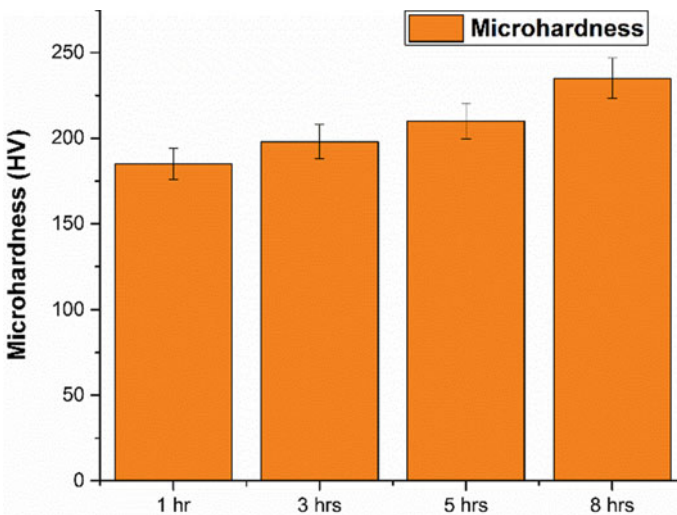


Fig. 22.3 Microhardness of samples at different dwell times

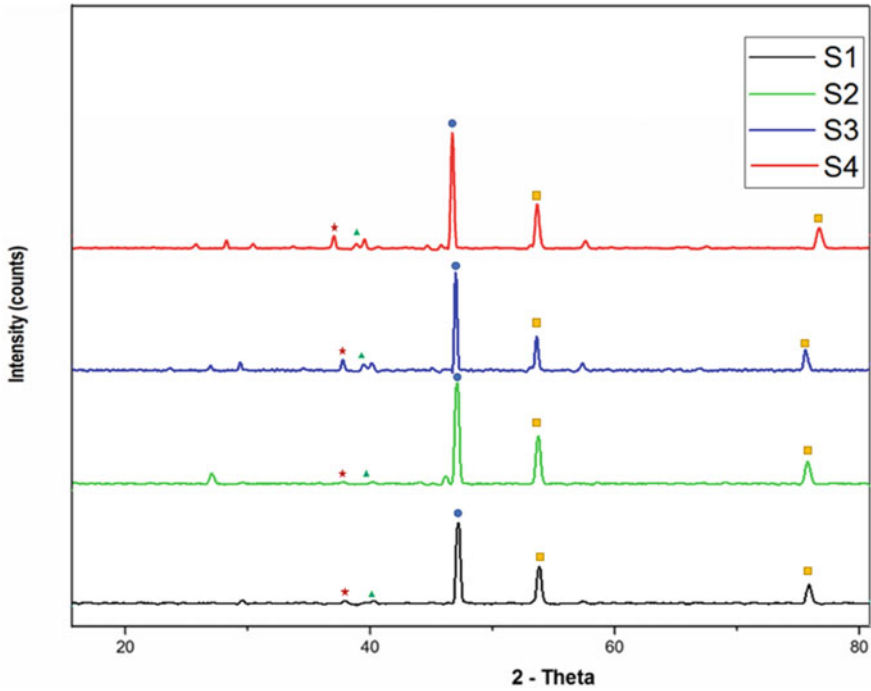


Fig. 22.4 XRD patterns of sintered samples at different dwell times

with the constituents of the stainless steel resulting in the formation of their respective nitrides. The XRD patterns of all the samples are presented in Fig. 22.4. The results indicate the formation of C_3N_4 at a d spacing of 2.51960 \AA , $FeN_{0.324}$ at a d spacing of 2.07500 \AA , Cr_2O_3 at a d spacing of 2.66348 \AA and $Ni(Cr_2O_4)$ at a d spacing of 2.49354 \AA . The nitrogen did form bonds with carbon and iron in the stainless steel and their peaks increased with increasing the dwell time. Thus, it clearly shows that due to increased amount of nitrides in the matrix, the overall mechanical properties of the material are improved. The notable results were found in the increased microhardness of the sintered samples.

The XPS analysis of sintered samples with different dwell times was carried out to investigate the existence of nitrogen and other elements at the surface of the samples. The results indicated the presence of nitrogen on each sample surface. The amount of nitrogen present on the sintered sample for 1 h dwell time was found to be 1.04% and the amount of nitrogen for 3, 5 and 8 h dwell time sintered samples was found to be 1.32%, 1.93% and 2.82%, respectively. These results indicate that a surface nitride layer was formed on the surface of the sintered samples and its value increased with increasing dwell time. There were other elements found on the sample surface. The notable elements were oxygen, carbon, iron and chromium. The oxygen reacts with iron to form iron oxide and with chromium, it forms chromium oxide. These oxide layers along with the nitride layer make the surface of the sintered sample stable and

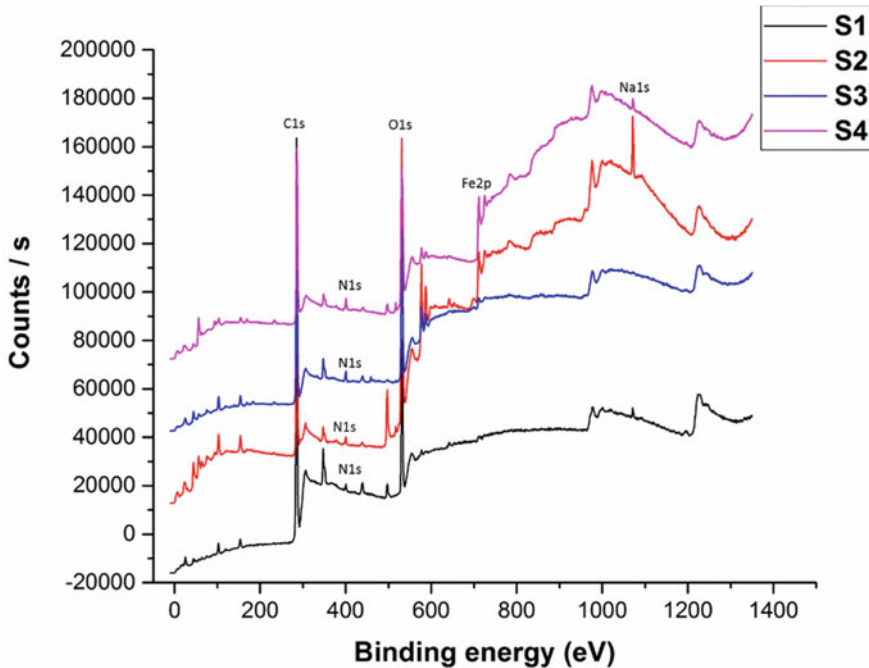


Fig. 22.5 XPS spectra of sintered samples at different dwell times

resistant against leaching of ions when subjected to saline solution. The XPS spectra for all the samples are shown in Fig. 22.5.

22.4 Conclusion

The key points from this research work can be concluded as:

1. Austenitic 316L stainless steel sintered in nitrogen atmosphere has better results in terms of densification and microhardness.
2. The sintering dwell time plays an important role in the diffusion of nitrogen into the matrix of stainless steel.
3. There is a surface nitriding of material with increasing dwell times and a dwell time of 8 h seems to be better among others due to its increased nitrogen absorption, densification and microhardness.
4. This efficient approach for nitrogen diffusion and surface nitriding can reduce the leaching of nickel and other metal ions.

Acknowledgements The authors would like to thank Universiti Teknologi PETRONAS (UTP), Malaysia for their resources.

References

1. Hussein, M.A., Mohammed, A.S., Al-Aqeeli, N.: Wear characteristics of metallic biomaterials: a review. *Materials* **8**(5), 2749–2768 (2015)
2. Wilson, J.: *Metallic biomaterials: state of the art and new challenges*. In: *Fundamental Biomaterials: Metals*, pp. 1–33. Woodhead Publishing (2018)
3. Ali, S., Rani, A.M. A., Altaf, K., Baig, Z.: Investigation of Boron addition and compaction pressure on the compactibility, densification and microhardness of 316L Stainless Steel. *IOP Conf. Ser. Mater. Sci. Eng.* **344**(1), 012023 (2018)
4. Jacobs, J.J., Gilbert, J.L., Urban, R.M.: Current concepts review-corrosion of metal orthopaedic implants. *Jbjs* **80**(2), 268–282 (1998)
5. Fathi, M.H., Salehi, M., Saatchi, A., Mortazavi, V., Moosavi, S.B.: In vitro corrosion behavior of bioceramic, metallic, and bioceramic–metallic coated stainless steel dental implants. *Dent. Mater.* **19**(3), 188–198 (2003)
6. Tracana, R.B., Sousa, J.P., Carvalho, G.S.: Mouse inflammatory response to stainless steel corrosion products. *J. Mater. Sci.-Mater. Med.* **5**(9–10), 596–600 (1994)
7. Fellah, M., Labaiz, M., Assala, O., Iost, A., Dekhil, L.: Tribological behaviour of AISI 316L stainless steel for biomedical applications. *Tribol. Mater. Surf. Interf.* **7**(3), 135–149 (2013)
8. Lei, M.K., Zhu, X.M.: In vitro corrosion resistance of plasma source ion nitrided austenitic stainless steels. *Biomaterials* **22**(7), 641–647 (2001)
9. Powers, J.M., Wataha, J.C.: *Dental Materials-E-Book: Properties and Manipulation*. Elsevier Health Sciences (2015)
10. Dudek, A.: Investigations of microstructure and properties in bioceramic coatings used in medicine. *Arch. Metall. Mater.* **56**(1), 135–140 (2011)
11. Huang, Y., Qu, Y., Yang, B., Li, W., Zhang, B., Zhang, X.: In vivo biological responses of plasma sprayed hydroxyapatite coatings with an electric polarized treatment in alkaline solution. *Mater. Sci. Eng., C* **29**(8), 2411–2416 (2009)
12. Dayss, E., Leps, G., Meinhardt, J.: Surface modification for improved adhesion of a polymer-metal compound. *Surf. Coat. Technol.* **116**, 986–990 (1999)
13. Ali, S., Rani, A. M. A., Altaf, K., Hussain, P., Prakash, C., Hastuty, S., Rao, T.V.V.L.N., Subramaniam, K.: Investigation of alloy composition and sintering parameters on the corrosion resistance and microhardness of 316L Stainless Steel alloy. In: *International Scientific-Technical Conference Manufacturing*, pp. 532–541. Springer, Cham (2019)
14. Dabrowski, J.D., Oksiuta, Z.: Porous implantation material from Vitalium alloy powder. *Inzynieria Materialowa* **21**(4), 174–178 (2000)
15. Kurgan, N., Sun, Y., Cicek, B., Ahlatci, H.: Production of 316L stainless steel implant materials by powder metallurgy and investigation of their wear properties. *Chin. Sci. Bull.* **57**(15), 1873–1878 (2012)
16. Kurgan, N.: Effects of sintering atmosphere on microstructure and mechanical property of sintered powder metallurgy 316L stainless steel. *Mater. Des.* **1980–2015**(52), 995–998 (2013)
17. Pilliar, R.M.: P/M processing of surgical sintered porous surfaces for tissue-to-implant fixation. *Int. J. Powder Metall.* **34**(8), 33–45 (1998)
18. Ali, S., Rani, A., Majdi, A., Mufti, R.A., Azam, F.I., Hastuty, S., Hussain, M., Shehzad, N.: The influence of nitrogen absorption on microstructure, properties and Cytotoxicity assessment of 316L Stainless steel alloy reinforced with boron and niobium. *Processes* **7**(8), 506 (2019)
19. Ali, S., Rani, A., Majdi, A., Mufti, R.A., Hastuty, S., Hussain, M., Shehzad, N., Baig, Z., Aliyu, A., Azeez, A.: An efficient approach for nitrogen diffusion and Surface nitriding of boron-titanium modified stainless steel alloy for biomedical applications. *Metals* **9**(7), 755 (2019)

Chapter 23

Kinematic and Dynamic Analysis of a Stephenson III Six-Bar Linkage for Amplified Rectilinear Motion: Application to Globe Valve Control Mechanism



Farooq I. Azam, Haizum Aimi Zaharin, Ahmad Majdi Abdul Rani, and Muhammad Al'Hapis Abdul Razak

Abstract This paper presents the kinematics of a six-bar linkage which magnifies the magnitude of linear motion. A designed mechanism eliminates the problem of long bellow lengths in bellow valves which makes the valve design aesthetically more suitable for industrial applications. The mechanism is a planer linkage with a single degree of freedom where a straight-line motion at input is converted to an extended perpendicular translatory motion at output. The amplification obtained at output can be increased by addition of a link. The mechanism is based on a Stephenson III six-bar linkage. Graphical synthesis of the mechanism is attained through qualitative design process. Analyses on the proposed solutions are performed to determine their viability. Iteration between the synthesis and analysis is done until the desirable results are achieved. The paper uses the vector closed loop equations method for kinematic analysis, and later, the results are also verified by a numerical example. After the geometry and motion for the task is achieved, as an application of the mechanism, the mechanism is applied to a bellow globe valve as its opening and closing mechanism. Force analysis is carried out to study the force propagation in the mechanism and actuation of the valve. The synthesized linkage application in

F. I. Azam (✉)

Mechanical Engineering Department, Universiti Teknologi PETRONAS, Perak, Malaysia
e-mail: farooq.i_g03648@utp.edu.my

H. A. Zaharin · A. M. Abdul Rani

Faculty of Engineering and Built Environment, Universiti Kebangsaan Malaysia, Selangor, Malaysia
e-mail: p100279@siswa.ukm.edu.my

A. M. Abdul Rani

e-mail: majdi@utp.edu.my

M. A. Abdul Razak

Manufacturing Section, Universiti Kuala Lumpur Malaysian Spanish Institute, Kedah, Malaysia
e-mail: alhapis@unikl.edu.my

© The Editor(s) (if applicable) and The Author(s), under exclusive license to Springer Nature Switzerland AG 2020

M. H. Abu Bakar et al. (eds.), *Progress in Engineering Technology II*, Advanced Structured Materials 131, https://doi.org/10.1007/978-3-030-46036-5_23

the globe valve reduces the length of bellow required up to 75% which as a result reduces the height of the valve significantly.

Keywords Extended motion · Six-bar · Linkage synthesis · Position analysis · Force analysis · Bellow valve · Control mechanism

23.1 Introduction

The focus of this study is on the kinematics and design of a six-bar linkage for magnified motion and its application in globe valve design. Six-bar linkages are typically used to create the required complex motion which is not possible using four-bar linkages. A six-bar linkage is basically a combination of a four-bar linkage on another four-bar linkage with some joints and links shared [1]. Several standard six-bar linkages, such as Watt and Stephenson, are available which forms the basis of various complex mechanisms with interesting outputs. Examples of such mechanisms include excavator buckets, concrete pump booms, etc. A common application of six-bar linkages is their use in extending linkages. These linkages are used to magnify displacements, which convert small displacements to large displacements. Some commonly encountered extending linkages include: scissor linkages based on Watt I linkage are used in scissor cranes [2], folding linkages used in concrete pump trucks [3], telescoping booms used in portable lifts [4]. Extending linkages are of great importance in industry as they are compact, easy to setup and have long reach in their use. The extending linkage designed in this study is for the opening and closing mechanism of globe valves.

The control valves usage varies from petrochemical industries to common household taps to control fluid flow. These valves are responsible for the major proportion of unwanted emissions from industries. As per European Sealing Association (ESA) statistics, valves account for up to 60% emissions from any plant. Most probable cause of this leakage is the valve's frequent operation, causing the stem and seals to wear thus, allowing fugitive emissions [5]. Environment protection agency (EPA) standards limits the leakage to 100 ppm as acceptable [6].

Bellow sealed valves are used in industry to achieve zero leakage from any fluid system [7]. Metal bellow has the characteristic of zero emission sealing by compressing or extending within the elastic limit while allowing the required motion to operate the valve. To limit the motion in the elastic limit during compression or extension, an extended bellow length is required, which in return increases the height of the valve due to increase in shaft length. The increased height makes the bellow valve usage restricted, especially for large sizes [8]. This study introduces a six-bar linkage to globe valve operating mechanism to reduce overall valve height [9]. The mechanism reduces the input displacement while delivering same motion at output. Six-bar linkages form the origin of various mechanisms [10], including the Watt II linkage-based hand rehabilitation robot [11], Stephenson III-based leg mechanism [12], Watt I-based body guidance mechanism [13] and furniture hinge mechanism

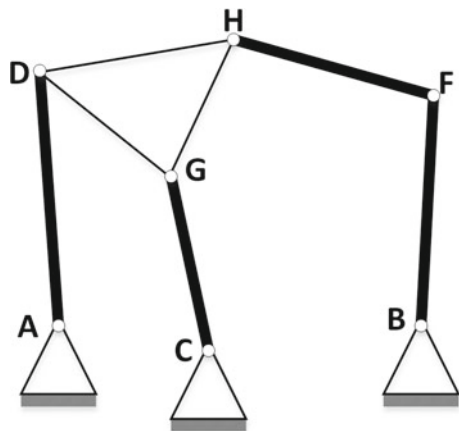
[14]. The following sections present the kinematic synthesis of linkage for the mechanism, followed by an analysis of the linkage to check its viability and in the end the simulation study of the application of the mechanism in the globe valve as its control mechanism.

23.2 Kinematic Synthesis

This study uses the method of qualitative synthesis/type synthesis to create the potential solution of the problem [15]. The synthesized linkage is based on Stephenson III six-bar linkage. Stephenson III six-bar linkage, as shown in Fig. 23.1, is a combination of two four-bar linkages where one four-bar linkage drives the second four-bar linkage. The six-bar linkage forms the basis of various modern applications. Figure 23.1 shows the links and joints connected to form the Stephenson III linkage. The linkage consists of one ternary link, four binary links and one ternary ground link, and all the links are joined by pin joints. The link AD, also called crank, is usually the input of the linkage, whereas our desired output is produced at joint F.

In the problem under consideration here, the input is a straight-line motion and the output is also a straight-line motion but with different magnitude. To get our desired motion, we consider the length of link AD and link BF equals to infinity. This will cause the motion generated by joint D and F to follow the circular path with infinite radius, which is a straight line. The resulting linkage is illustrated in Fig. 23.2. The motion of joint D is now in straight line along the Y direction and motion of joint F is in straight line along the X direction. Now we take the ternary link DGH as straight link in which joints D and H are at the end points of ternary link, whereas the joint G is at the centre. To convert the motion of joint G in a straight line along the X direction, we also consider the length of link CG equals to infinity, as shown in Fig. 23.2.

Fig. 23.1 Stephenson III six-bar linkage



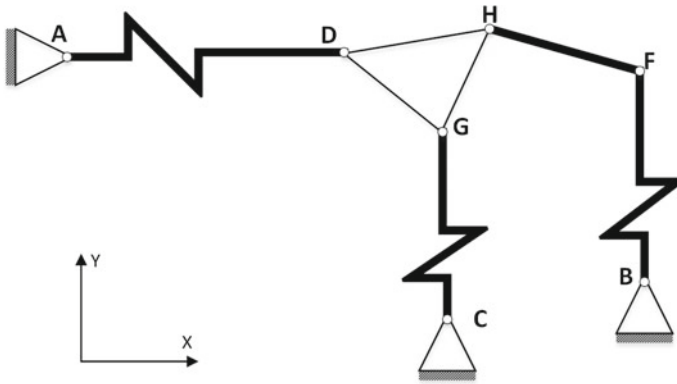


Fig. 23.2 Stephenson III linkage with ground link at infinity

Figure 23.3 shows the synthesized linkage after modifications in the Stephenson III six-bar linkage. The linkage forms three slider joints at point D, G and F allowing a straight-line motion only. When the input motion is applied at point D, it moves along in the Y direction, causing the link DGH to rotate at point G and also to move the joint G along the X direction. This movement will also create the same kind of motion in link HF, causing it to rotate and slide at joint F in the X direction, thus producing a magnified motion at point F. The magnitude of motion produced at joint F can be increased by adding more links between link DGH and link HF with the constraints to produce the same motion as of link DGH.

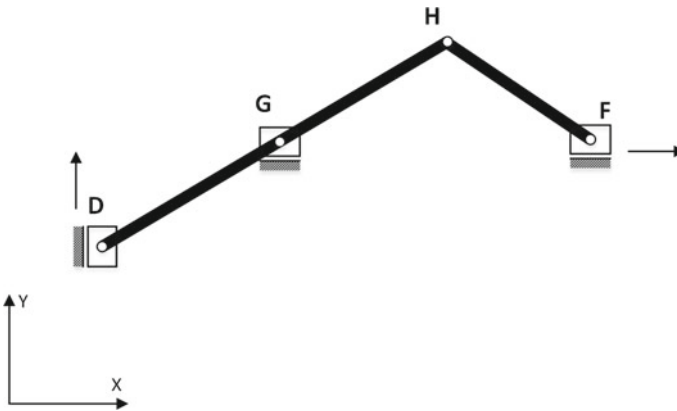


Fig. 23.3 Synthesized linkage

23.3 Kinematic Analysis

After the synthesis of a tentative linkage design, the linkage is analysed to determine the position of our points of interest in the linkage, which are the input and output of mechanism. The analysis validates the linkage design and aids determining dynamic forces in the linkage which are then used to calculate stresses in the mechanism. For the analysis, the closed loop vector method by Raven is used. In this method, all the links in a linkage are represented by position vectors that form a closed vector loop. The magnitude of the vectors represents the length of a link, whereas the angle represents the position. For the linkage synthesized above, the closed loop vector representation is shown in Fig. 23.4.

For the six-bar linkage, the method is used by solving two sets of four-bar loops and then combining their equations to achieve the results. Figure 23.4 illustrates the two four-bar loops, DGC and GHF, formed by the linkage. As the slider crank forms the non-offset slider crank, the loops can be represented by three position vectors. Vector R_{DC} , R_{DG} and R_{CG} make the loop DGC, whereas vectors R_{GH} , R_{GF} and R_{FH} forms the loop GHF. The magnitude of vector R_{CG} represents the input displacement, since it is a straight-line motion along the Y axis the angle θ_{CG} will always be 90° . The vector R_{DC} represents the motion of joint G along the X axis and the angle θ_{DC} will always be zero. The vector R_{GF} shows the displacement due to link FH. The total output displacement will be the sum of vectors R_{DC} and R_{GF} represented by d . Magnitudes and angles of vectors R_{DG} and R_{GH} are the same as they are part of same link. To achieve the final relations, equations for both loops are solved separately.

The vector loop equation for loop DGC is:

$$R_{DC} + R_{CG} - R_{DG} = 0 \tag{23.1}$$

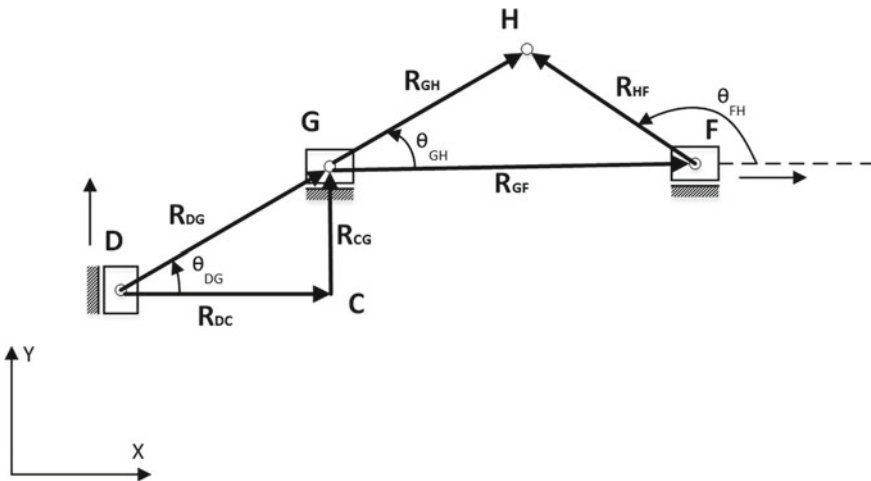


Fig. 23.4 Vector loop diagram

Let the magnitude of links be represented by R_{DC} , R_{CG} , R_{DG} . Writing vectors in complex number notation:

$$R_{DC}e^{j\theta_{DC}} + R_{CG}e^{j\theta_{CG}} - R_{DG}e^{j\theta_{DG}} = 0 \quad (23.2)$$

By Euler substitution

$$\begin{aligned} R_{DC}(\cos \theta_{DC} + j \sin \theta_{DC}) + R_{CG}(\cos \theta_{CG} + j \sin \theta_{CG}) \\ - R_{DG}(\cos \theta_{DG} + j \sin \theta_{DG}) = 0 \end{aligned} \quad (23.3)$$

Separating components

$$R_{DC} \cos \theta_{DC} + R_{CG} \cos \theta_{CG} - R_{DG} \cos \theta_{DG} = 0 \quad (23.4)$$

$$j R_{DC} \sin \theta_{DC} + j R_{CG} \sin \theta_{CG} - j R_{DG} \sin \theta_{DG} = 0 \quad (23.5)$$

$$\theta_{DC} = 0, \theta_{CG} = 90^\circ$$

$$R_{DC} - R_{DG} \cos \theta_{DG} = 0 \quad (23.6)$$

$$R_{CG} - R_{DG} \sin \theta_{DG} = 0 \quad (23.7)$$

Applying the same procedure to loop GHF

$$\mathbf{R}_{GF} + \mathbf{R}_{FH} - \mathbf{R}_{GH} = 0 \quad (23.8)$$

Let the magnitude of links be represented by R_{GF} , R_{FH} , R_{GH} . Writing vectors in complex number notation:

$$R_{GF}e^{j\theta_{GF}} + R_{FHE}^{j\theta_{FH}} - R_{GHE}^{j\theta_{GH}} = 0 \quad (23.9)$$

By Euler substitution

$$\begin{aligned} R_{GF}(\cos \theta_{GF} + j \sin \theta_{GF}) + R_{FH}(\cos \theta_{FH} + j \sin \theta_{FH}) \\ - R_{GH}(\cos \theta_{GH} + j \sin \theta_{GH}) = 0 \end{aligned} \quad (23.10)$$

Separating components

$$R_{GF} \cos \theta_{GF} + R_{FH} \cos \theta_{FH} - R_{GH} \cos \theta_{GH} = 0 \quad (23.11)$$

$$j R_{GF} \sin \theta_{GF} + j R_{FH} \sin \theta_{FH} - j R_{GH} \sin \theta_{GH} = 0 \quad (23.12)$$

$$\theta_{GF} = 0, \theta_{GH} = \theta_{DG}, R_{GH} = R_{DG}$$

$$R_{GF} + R_{FH} \cos \theta_{FH} - R_{DG} \cos \theta_{DG} = 0 \quad (23.13)$$

$$R_{FH} \sin \theta_{FH} - R_{DG} \sin \theta_{DG} = 0 \quad (23.14)$$

R_{CG} is the magnitude of input which is known, R_{DG} is half the length of link DH that is also known and the length of link R_{FH} is also available. Now we are left with four unknown variables R_{DC} , R_{GF} , θ_{DG} and θ_{FH} which can be determined by solving Eqs. (23.6), (23.7), (23.13) and (23.14) simultaneously.

Solving

$$R_{DC} = R_{CG} \quad (23.15)$$

$$\theta_{DG} = \sin^{-1} \left(\frac{R_{CG}}{R_{DG}} \right) \quad (23.16)$$

$$R_{GF} = R_{DG} \cos \theta_{DG} - \frac{R_{DG} \sin \theta_{DG} \cos \theta_{FH}}{\sin \theta_{FH}} \quad (23.17)$$

$$\theta_{FH} = \sin^{-1} \left(\frac{R_{DG} \sin \theta_{DG}}{R_{FH}} \right) \quad (23.18)$$

The resulting equations show the behaviour of the linkage at every position and the output, when an input is applied. As a numerical example, let us take the length of link DH equal to 10 unit and length of link FH as 5 units. The input displacement at point D is 1 unit. So, from Eqs. (23.15)–(23.18) above, R_{DC} is 1 unit, θ_{DG} is 36.8° , R_{GF} is 2 and θ_{FH} is 143.2° . The total output displacement d at point F is the sum of R_{DC} and R_{GF} , that is 3 units. Figure 23.5 illustrates the initial and final position of the linkage in our example.

The position analysis of the synthesized linkage depicts the magnified motion and validates the synthesis. The desired output can be achieved from a certain input by choosing suitable dimensions of links and vice versa. The output can also be increased by addition of a ternary link depending upon the constraints of the application. Adding another link will create two more four-bar link loops that will have the same motion characteristics. The designed mechanism is applied to a potential application of the globe valve, as illustrated in Figs. 23.6 and 23.7, to help solve the large displacement problem. The DN 25 bellow globe valve is used as a case study. The required input displacement to operate the valve is 25 mm to fully open or close the valve. This requires the bellow length of 305 mm to keep the motion in the elastic limit. By applying the synthesized linkage and replacing shaft mechanism, the input motion can be reduced to 10 mm while delivering the same output motion. This in return will reduce the bellow length needed to 50 mm thus, reducing the overall height of the valve significantly.

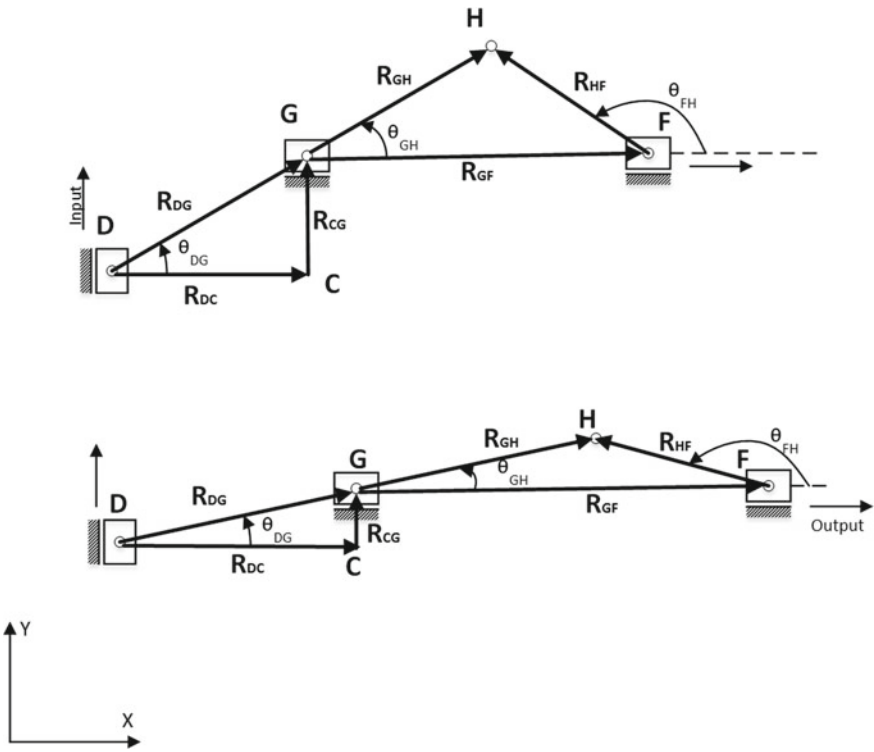


Fig. 23.5 Initial and final position of example linkage

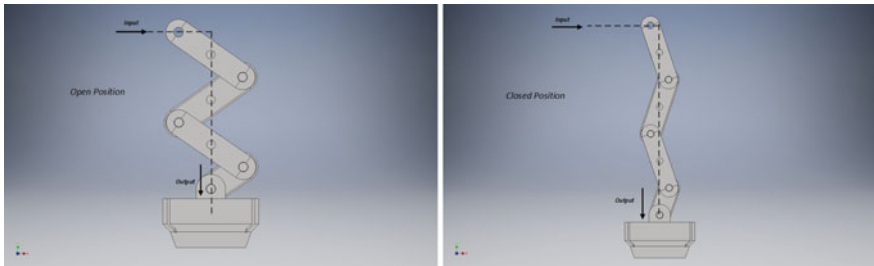


Fig. 23.6 CAD model of control mechanism at opened- and closed position

23.4 Force Analysis

The extending mechanism produces the magnified motion, as it is obvious from the name, but it comes at a price. The extending mechanism also reduces the force at the output as compared to the force applied at the input. So, the next step is to perform the force analysis on the designed mechanism to calculate the force required to actuate

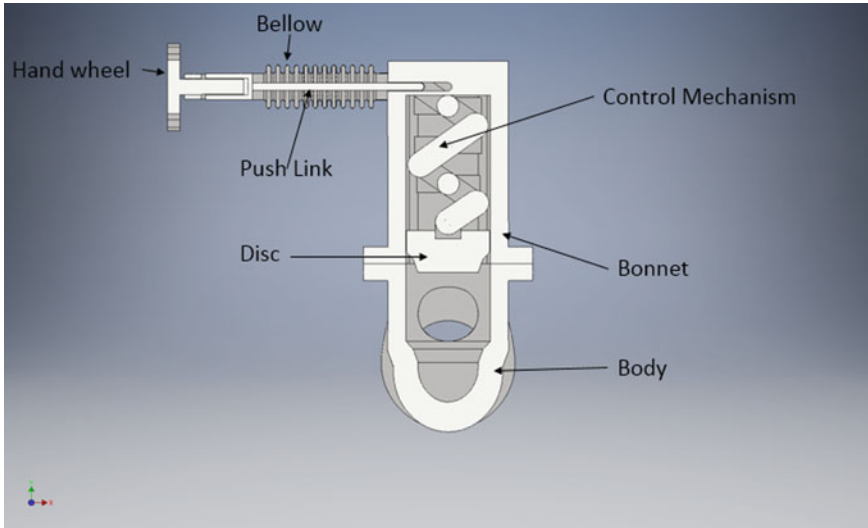


Fig. 23.7 Globe valve with designed mechanism

the mechanism. For this purpose, the valve design with the applied mechanism is subjected to a rigid dynamics analysis. Boundary conditions are applied to represent the real-life conditions which includes the fluid pressure in the valve acting on the disc and the input force required to move the disc. Figure 23.8 shows the applied conditions. We assume that the fluid pressure through the valve is 5 units, which is also acting on the disc and resisting its motion to close the valve, as represented by point C. We need to determine the force required at input to overcome the fluid resistance in order to produce the motion in the valve disc. The input force is represented by point B.

The model is solved using a rigid dynamics solver to calculate required input force. Figure 23.9 shows the input force and displacement produced at the disc. Approximately 40 units force is required to overcome the 5 unit by fluid pressure.

To validate the calculated force, the same force is applied at the input and the reaction force is calculated at disc by keeping the disc at a fixed position. The reaction force is approximately equal to the force applied by the fluid. Figure 23.10 shows the reaction force representation.

23.5 Conclusion and Future Implications

This study presents a kinematic synthesis and analysis of a six-bar linkage, based on the Stephenson III six-bar linkage, that magnifies the linear motion. The displacement at the input is converted into an extended motion at the output. The paper then shows the application of the developed linkage by making the opening and closing

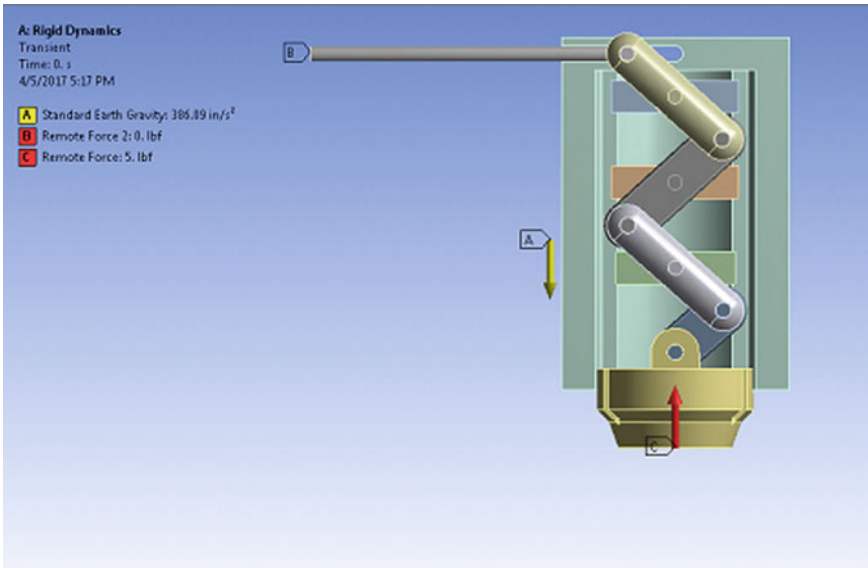


Fig. 23.8 Forces acting on mechanism

mechanism of the globe valve. The new design of the globe valve reduces the bellow length as well as valve height which make the design of valve more suitable for industrial applications. This makes the valve design a step further towards reduced fugitive emissions from industries. The application of the linkage is not only limited to the globe valve. The linkage can be used in other valves as well with little modifications. Further study includes the analysis of dynamic forces in the linkage to study the behaviour of forces in the mechanism and the actuation of the valve. The bellow valve with the designed mechanism solves the problem of long valve heights and makes the design more suitable for use in industry. Future studies will include the development of a prototype to experimentally validate the mechanism and to provide an insight towards commercialization of the product.

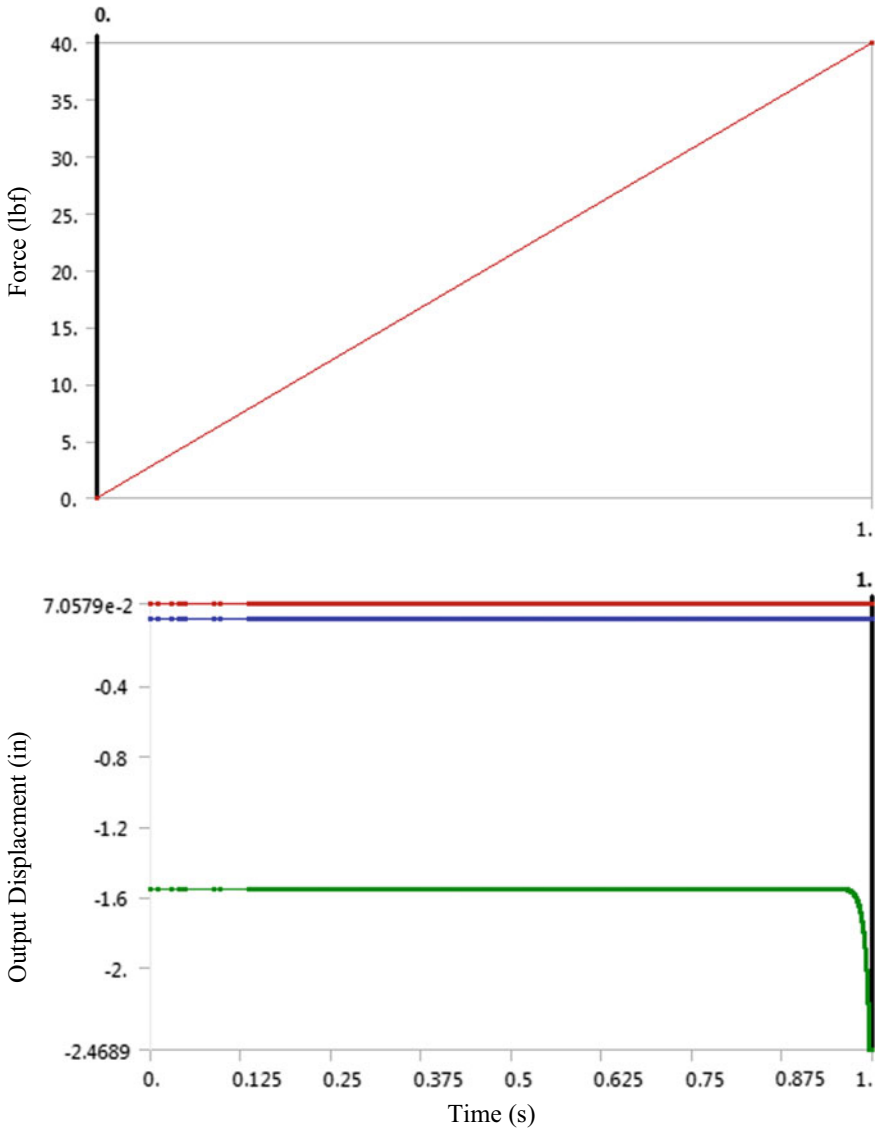


Fig. 23.9 Force analysis on mechanism

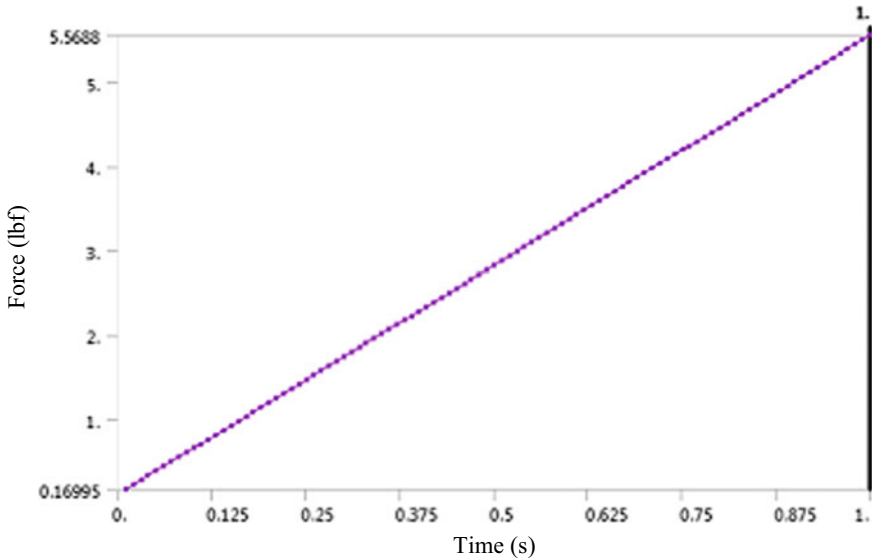


Fig. 23.10 Reaction force analysis

References

1. Shigley, J.E.: Theory of Machines and Mechanisms, 5th edn. Oxford University Press (2016)
2. Schaeffer, O., Vogt, M.-M.: Move: Architecture in Motion—Dynamic Components and Elements. Birkhauser Verlag AG (2010)
3. Schlecht, K.: Movable concrete pump comprising a distribution boom (2009)
4. Magni, R.: High lift truck with telescoping boom assemblies (1985)
5. Ippc, E.U., Esa, D.: Sealing Technology—BAT guidance notes (2009)
6. Khiani, G.: The Hidden Cost. The Valve's Role in Fugitive Emissions Compliance (2014). <https://www.flowcontrolnetwork.com/industry-applications/oil-gas/article/15561005/the-valves-role-in-fugitive-emissions-compliance> (Accessed: 19 October 2018).
7. Smith, P., Zappe, R.W.: Valve Selection Handbook, Gulf. Professional Publishing (2004)
8. Flitney, R.: Seals and Sealing Handbook, 6th edn. Butterworth-Heinemann (2014)
9. Pennock, G.R., Kassner, D.J.: Kinematic analysis of a planar eight-bar linkage: application to a platform-type robot. ASME J. Mech. Des. **114**(1), 87–95 (1992)
10. Erdman, A.G., Sandor, G.N., Kota, S.: Mechanism Design: Analysis and Synthesis, 4th Edition, Pearson (2001)
11. Gezgin, E., Chang, P., Faruk, A.: Synthesis of a Watt II six-bar linkage in the design of a hand rehabilitation robot. MAMT **104**, 177–189 (2016)
12. Batayneh, W., Al-araidah, O., Malkawi, S.: Biomimetic design of a single DOF Stephenson III leg mechanism. Mechanical Engineering Research **3**(2), 43–50, (2013)
13. Plecnik, M., McCarthy, J.M., Wampler, C.W.: Kinematic synthesis of a Watt I Six-bar linkage for body guidance. In: Advances in Robot Kinematic, pp. 317–225 (2014)
14. Chen, F.-C.: Analysis and verification of a Watt I six-bar furniture hinge mechanism. Proc. Inst. Mech. Eng. Part C J. Mech. Eng. Sci. **219**(10), 1107–1117 (2009)
15. Norton, R.L.: Design of Machinery: An Introduction to the Synthesis and Analysis of Mechanisms and Machines, 3rd edn. Mcgraw-Hill College (2003)

Chapter 24

Influence of Porous Designs on Mechanical Properties of Ti6Al4V for Biomedical Applications



Haizum Aimi Zaharin, Farooq I. Azam, Ahmad Majdi Abdul Rani, and Muhammad Al'Hapis Abdul Razak

Abstract Aseptic loosening and stress shielding are the most common causes of implant failure after total knee and hip arthroplasty. Failure is due to difference in mechanical properties of natural bone and artificial implants. Porous structures provide the solution to this problem and are being used in implants to avoid failure. The purpose of this research is to determine an optimum porous structure that gives similar mechanical properties as natural bone and can be used in implants. Four different structures have been analyzed for their mechanical properties at different pore sizes and orientation. Finite element analysis is performed in all designs using the ANSYS structural module mimicking ISO standard testing (ISO 13314). All of the structures give optimum porosity to be used as implants, but only some instances show similar Young's modulus and yield strength to mimic bone's mechanical properties. The analysis of the porous structures gives promising results for application in orthopedic implants. Application of optimum structure to implants can reduce the premature failure of implants and increase the reliability.

Keywords Aseptic loosening · Porous structure · Ti6Al4V alloy · Stress shielding · Selective laser melting

H. A. Zaharin

Centre for Materials Engineering and Smart Manufacturing, Faculty of Engineering and Built Environment, Universiti Kebangsaan Malaysia, 43600 UKM Bangi, Selangor, Malaysia
e-mail: p100279@siswa.ukm.edu.my

F. I. Azam · A. M. Abdul Rani

Mechanical Engineering Department, Universiti Teknologi PETRONAS, 32610, Seri Iskandar, Perak, Malaysia
e-mail: farooq.i_g03648@utp.edu.my

A. M. Abdul Rani

e-mail: majdi@utp.edu.my

M. A. Abdul Razak (✉)

SEELAB, Manufacturing Section, Universiti Kuala Lumpur Malaysian Spanish Institute, Kulim Hi-Tech Park, 09000 Kulim, Kedah, Malaysia
e-mail: alhapis@unikl.edu.my

© The Editor(s) (if applicable) and The Author(s), under exclusive license to Springer Nature Switzerland AG 2020

M. H. Abu Bakar et al. (eds.), *Progress in Engineering Technology II*, Advanced Structured Materials 131,
https://doi.org/10.1007/978-3-030-46036-5_24

24.1 Introduction

By 2030, the early failure of total knee and hip arthroplasties (TKA resp. THA), that requires revision surgery, is reported and predicted to increase by more than half million for THA and over 3 million for TKA [1]. Revision surgery is an undesirable procedure as the additional cost and the risk is higher, while the recovery rate is limited to around 69–76% only [2]. The main cause that leads to unsuccessful implant surgery is aseptic loosening as reported by many studies [2–9].

Lately, metallic porous structures have been an attractive solution for applications in orthopedic bone prosthesis, a favorite solution to constrain the effect of stress shielding, when metal components that are being used for THA and TKA procedure are too dense. Since the components used are too stiff and shield most of the stress given onto the bone, this has resulted to a phenomenon known as stress shielding. The effect of stress shielding causes the bone to lose its density, triggering the implant to loosen without the interfering of infection, known as aseptic loosening [10]. Based on computer aided design (CAD), porous structures can easily be designed and the selective laser melting (SLM) technology is able to manufacture desirable metal porous scaffolds in layers. This is a solution that can easily reduce the stiffness of the prosthesis which can improve the effect of stress shielding, significantly avoid aseptic loosening of artificial implants.

The selection of suitable material is also a crucial factor that needs to be considered in reducing the rate of implant loosening [4]. Various biocompatible materials have been used for joint replacement surgeries such as stainless steel, Co–Cr–Mo alloys, titanium alloys and others. Among the materials available for biomedical implant application, Ti-based alloys remain as the best choice for hard tissue replacement due to their excellent mechanical, physical and biological performance [11]. In collation with other biocompatible materials for the artificial implant on Young's modulus, Co–Cr alloy and 316L stainless steel show 210–253 GPa and 190–210 GPa, respectively, whereas Young's modulus of Ti-based alloys is only 100–140 GPa. At the same time, it is also reported that elements such as Co and Cr have toxic effects from the artificial implant to the human body [11], whereas, Ti-based alloys have many beneficial advantages that include lower elastic modulus, excellent corrosion resistance and enhanced biocompatibility [12]. Although Ti alloys offer low elastic modulus for implant application, the value is still much higher than Young's modulus of human's porous tissues been replaced (4–30 GPa) [10]. As a solution to overcome aseptic loosening, various porous scaffold structures have been designed and studied by many researchers to mimic the mechanical properties of natural human bone [13–16].

24.2 Literature Review

Total knee arthroplasty is a common surgery procedure to treat a diseased knee joint and revive its normal function by replacing the defected joint with the artificial

implant. While total hip arthroplasty is one of the successful reconstructive procedure, that replaces hip joint with prostheses, to restore its health and purpose. Both surgical procedures are mainly depending on the surgeon’s technical expertise and mostly on the used orthopedic implants. Successful artificial implants should have criteria like long life span, biocompatible and function comparable to the original bone tissues [1, 2].

24.2.1 Bone Mechanical Properties

Bone is built up from a combination of cortical bone tissues, the compact external side of the bone and trabecular bone (cancellous bone), the spongy internal structure of bone (see Fig. 24.1). In a simple cross section of a bone in Fig. 24.1, it is shown that there is no sudden crossing point between compact cortical bone and spongy trabecular bone. The regular pore distribution of this natural structure changes from cortical bone tissue to cancellous bone tissue, showing that the mechanical properties such as tensile strength and elasticity change steadily. However, data available in the literature is unlike. A steady decrease in mechanical properties from one tissue region to another tissue region can clearly be observed in Table 24.1 [17, 18].

Bone mechanical properties and composition change with aging process. The elasticity, plasticity, strength and hardness of a child’s bone are less compared to adults. On the other hand, mechanical properties deteriorate from adult to senior adult [11]. Based on human bone mechanical properties, the decision of material to

Fig. 24.1 Bone tissue structure [19, 20]

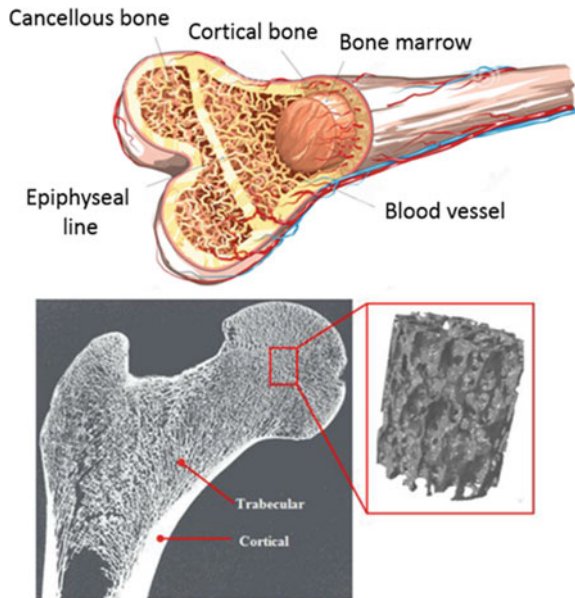


Table 24.1 Mechanical properties of natural bone

Properties	Cortical bone		Cancellous bone
	Longitudinal	Transverse	
Strength, tension (MPa)	79–151	51–56	2–5
Strength, compression (MPa)	131–224	106–133	
Elastic modulus (GPa)	17–30	6–13	0.76–4

be used for a biomedical implant should meet the requirements of human hard tissues. In this study, Ti6Al4V is selected to fulfill these requirements by manipulating the design of the porous structure and its mechanical properties.

24.2.2 Aseptic Loosening and Stress Shielding

The aseptic loosening of an implant can be defined as the weakening of the bond between the bone and the prosthetic through factors that is unrelated to infection. There are three major causes of aseptic loosening in THA and TKA which include stress shielding of the prosthetic to the bone, micro-motion and excessive wear between the implant and bone interface [21].

Stress shielding is a term used to describe a phenomenon that causes bone resorption due to insufficient stress distribution from the artificial implant to natural bone. A femoral bone in its natural state carries the majority of the body weight itself, while in the case of an implantation joint, the same load is shared between prosthesis and bone. Prosthesis with higher Young's modulus value compared to natural bone stiffness will hold most of the load, leaving the bone to carry only the remaining load. When this happens, according to Wolff's law, bone mass will slowly depreciate as the build-up structure of bone depends on the stress acting on it [22]. Zhang et al. [18] reported that stiffness of an implant made of titanium alloy, represented by elastic modulus, is about ten times greater than that of cortical bone which is 110–120 GPa > 10–30 GPa. The surrounding bone to implant suffers from the stress shielding effect due to a very high elastic modulus of implant. Insufficient stress on bone and artificial implant speeds up the implant loosening process which has become the cause of arthroplasty failure (see Fig. 24.2).

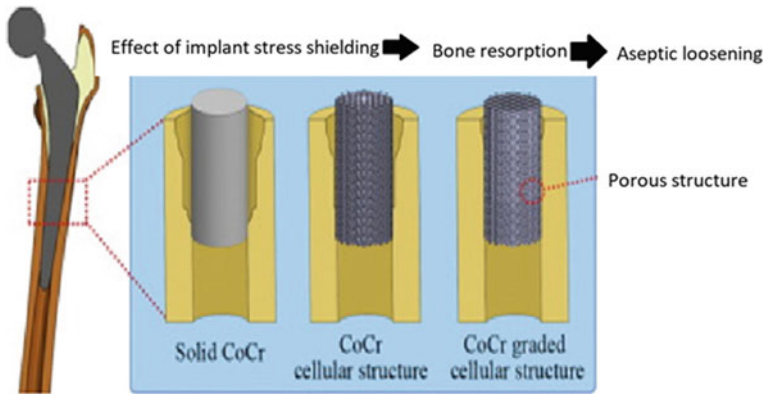


Fig. 24.2 Stress shielding effect on dense implant and porous implant [10]

24.2.3 Scaffold Porous Structures

In response to the aseptic loosening problem, the selection of the optimum design parameter for a porous geometry structure plays a significant role in reducing the aseptic loosening of the artificial joint since a higher Young's modulus of the implant material can be adjusted to imitate the elastic modulus of natural bone. The porous implant architecture influences the implant performance in terms of mechanical and biological properties [15]. Furthermore, a porous structure for implant application offers open space for tissue bone ingrowth, hence, accelerating the osseointegration process. With the enhancement of the additive manufacturing technology, the modeling and manufacturing of the porous structure design have been extensively explored over the past decade to remove limitations of conventional manufacturing techniques.

Designing the internal architecture of porous structure is crucial as different designs will result to dissimilar mechanical properties. The fundamental approach modeling the porous structure of metallic implants involves the thorough process of selection criteria including porosity, pore size and pore interconnectivity with the goal to achieve a satisfactory clinical outcome. An increasing percentage of porosity may facilitate and benefit bone tissue to grow. For example, more bone ingrowth was observed in the case of a titanium scaffold specimen implanted into a beagle of higher porosity [23]. While the impact of pore size on bone tissues regeneration is still controversial, the optimal pore for mineralized bone ingrowth is claimed to be around 100–1000 μm from various references [11, 24–26]. Too small pores will hinder bone ingrowth by promoting pore occlusion. Whereas, too large of pore size will reduce the surface area for cell adhesion, additionally, lessen the load capacity of weight bearing [26]. Thus, the choice of selection for porosity which is more than 50% and pore size should be within the optimal range to sustain good cell migration, reliable mass transportation and safe vascularization besides facilitating sufficient surface area for cell adherence as well as maintaining the mechanical stability.

24.3 Methodology

The study was based on finite element analysis of porous samples to determine mechanical properties. Autodesk Inventor 2017 was used to model unit cells and scaffold porous structures for all designs. Four different porous designs, cube, gyroid, triangle A and triangle B were selected for this study as these structures are easily to manufacture using additive manufacturing, without the requirement of any support structure. In accordance with biophysical and biological constraints, porous samples with a pore size of 300, 400, 500 and 600 μm were designed. The strut thickness was kept constant at 200 μm for all designs and sizes, corresponding to the minimum requirement by the SLM process. Scaffolding designs were dimensioned to $10 \times 10 \times 10$ mm in cube to replicate the standard compression test (ISO 13314) for porous metals. The sample models were saved in STEP file format and imported to ANSYS for further analysis. The general porosity of the porous structures, ε , was calculated using the following formula [27]:

$$\varepsilon = \left(1 - \frac{\rho}{\rho_s}\right) \times 100, \quad (24.1)$$

where ρ and ρ_s are the density of the porous structure and its theoretical density of the solid part, respectively. The density of the porous structure was measured from its weight and dimensional measurements. The theoretical density of the solid part was 4.37 g/cm^3 for the Ti–6Al–4V alloys. Based on static structural analysis, ANSYS Workbench 16.1 was used to analyze the mechanical properties for each design. The material properties of the Ti6Al4V alloy are manufactured by the SLM process, taken from the literature [28], and are applied on each sample, as presented in Table 24.2. Two plates, on top and bottom of samples, were created to mimic the experimental test following ISO 13314:2011 standard. For boundary conditions, both top and bottom plates were assumed as rigid bodies, while the sample was considered flexible. A remote force on the top plate was applied to each sample

Table 24.2 Mechanical properties of Ti6Al4V

Mechanical properties	
Material	Ti6Al4V alloys
Manufacturing process	Selective laser melting
Density	4.41 g/cm^3
Young's modulus	$109 \pm 2.1 \text{ GPa}$
Poisson's ratio	0.3
Strain life parameter	$8.8 \pm 0.6\%$
Tensile yield strength	$1098 \pm 15 \text{ MPa}$
Ultimate tensile strength	$1237 \pm 13 \text{ MPa}$
Compressive yield strength	960 MPa
Ultimate compressive strength	1000 MPa

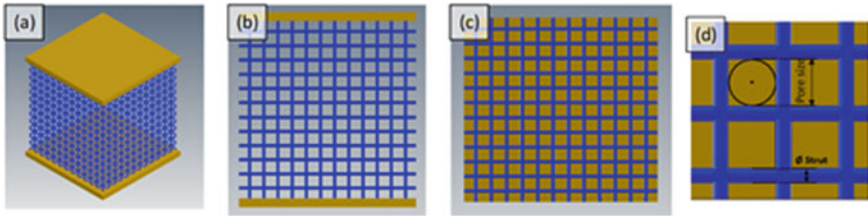


Fig. 24.3 **a** Cube sample with plates on top and bottom, **b** front view of cube sample, **c** top view of cube porous structure without top plate and **d** pore size and strut diameter for cube sample

which latter was converted to applied stress, whereas bottom plate was fixed to ground (see Fig. 24.7). In this study, the deformation was considered only in the direction of the applied force. Directional deformation data was collected, and the strain was calculated from the deformation. From the simulation, the relationship between porosity and pore size and elastic modulus versus pore size for each sample was observed. The graph of compression stress versus strain for each sample was plotted to evaluate Young’s modulus and yield strength of the sample and compared with bone mechanical properties.

The sample models are shown in Figs. 24.3, 24.4, 24.5 and 24.6 (Fig. 24.7).

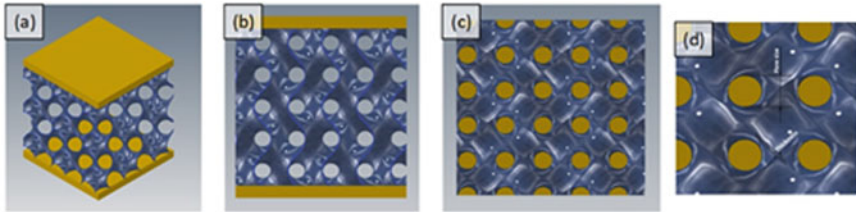


Fig. 24.4 **a** Gyroid sample with plates on top and bottom, **b** front view of gyroid sample, **c** top view of gyroid porous structure without top plate and **d** pore size and strut diameter for gyroid sample

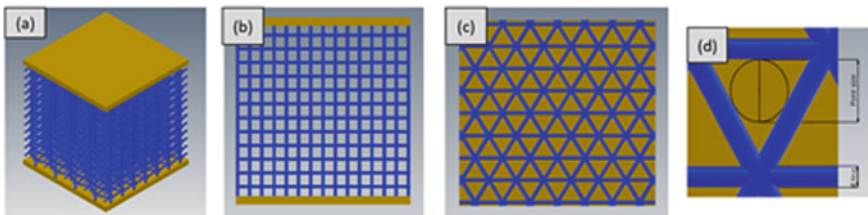


Fig. 24.5 **a** Triangle A sample with plates on top and bottom, **b** front view of triangle A sample, **c** top view of triangle A porous structure without top plate and **d** pore size and strut diameter for triangle A sample

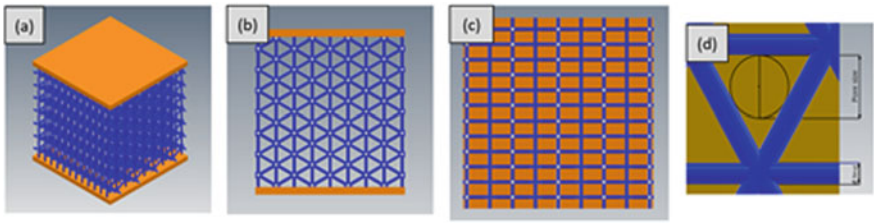


Fig. 24.6 **a** Triangle B sample with plates on top and bottom, **b** front view of triangle B sample, **c** top view of triangle B porous structure without top plate and **d** pore size and strut diameter for triangle B sample

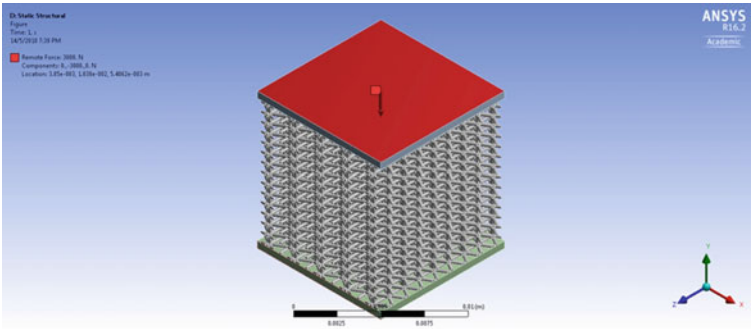


Fig. 24.7 Application of remote force to sample in Y-direction

24.4 Results

The resulting porosity of different porous structures depending on the pore size is shown in Figs. 24.8, 24.9 and 24.10. The porosity of samples was calculated using Eq. (24.1). As mentioned in the literature review section above, the optimum

Fig. 24.8 Porosity versus pore size for cube porous structure

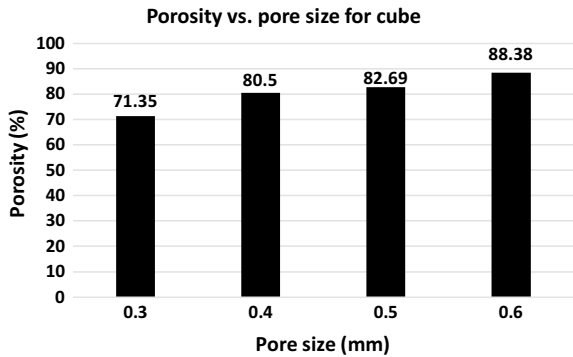


Fig. 24.9 Porosity versus pore size for gyroid porous structure

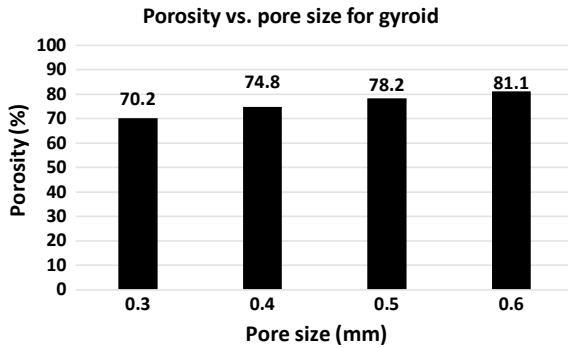
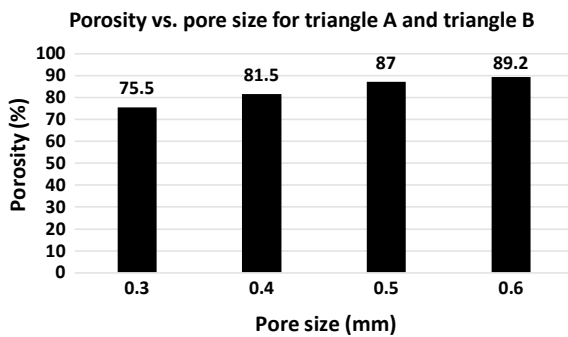


Fig. 24.10 Porosity versus pore size for triangle porous structure



porosity of a structure must be more than 50% to avoid pore occlusion and permit good permeability. Figures 24.8, 24.9 and 24.10 show the comparison between pore size and porosity for all designs.

Figures 24.8, 24.9 and 24.10 show, for all designs, the percentage of porosity increases with increase in pore size. For instance, for the cube design, from range 0.3–0.6 mm pore size, the porosity percentages are 71.35%, 80.5%, 82.69% and 88.38%, respectively. While for gyroid the design, the porosity increases from 70.2%, 74.8%, 78.2% to 81.1% with pore size 0.3–0.6 mm. For the triangle design, the porosity value remains the same for both orientations, triangle A and triangle B, as same design is being used with only different orientation. For a pore size 0.3 mm, the porosity is 75.5%, for a pore size 0.4 mm, the porosity is 81.5%, for a pore size 0.5 mm, the porosity is 87% and for a pore size 0.6 mm and the porosity is 89.2%, as illustrated in Fig. 24.10. Although porosity values were kept constant for both triangle designs, different orientations will result in dissimilar mechanical properties.

From the results obtained from the porosity test, in terms of porosity, all designs are suitable for implant applications.

Suitable porous samples were subjected to finite element analysis to calculate Young’s modulus and yield strength. A range of forces, from 250 N to 4 kN, was applied on each sample, and the model was solved for deformation in direction of

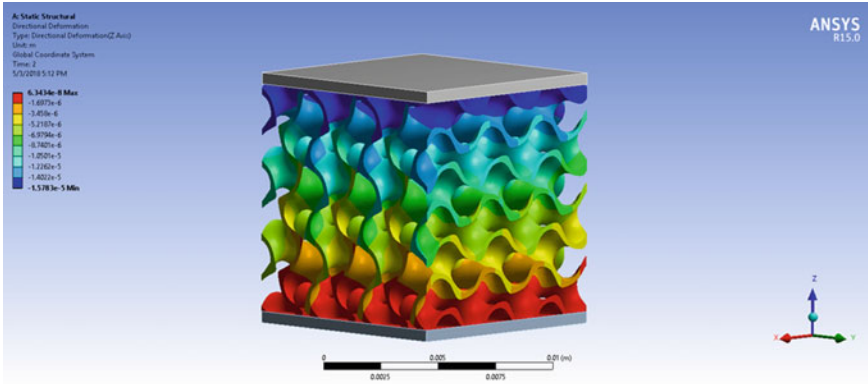


Fig. 24.11 Deformation produced in sample due to applied force

the applied force. Figure 24.11 illustrates the deformation produced in the sample due to the applied force.

The deformation data was collected from the analysis and was used to calculate the strain produced in the sample using Eq. (24.2):

$$\varepsilon = \frac{\Delta L}{L} \tag{24.2}$$

where ε is the strain, ΔL is the deformation in m and L is the original length which is 0.01 m.

The compression stress is calculated from the applied force, using Eq. (24.3):

$$\sigma = \frac{F}{A} \tag{24.3}$$

where σ is the compression stress in Pa, F is the force applied on the sample in N and A is the area of the plate, which is 0.0001 m².

The graph for compression stress versus strain is plotted for each sample to determine Young’s modulus and yield strength, as shown in Figs. 24.12, 24.13, 24.14 and 24.15.

For the cubic sample and a pore size ranging from 0.3 to 0.6 mm, Young’s modulus values are 16.3 GPa, 10 GPa, 8.9 GPa and 5.6 GPa, respectively. A decreasing trend with increase in pore size is shown by gyroid, triangle A and triangle B samples. From 0.3 to 0.6 mm pore size, Young’s modulus falls from 12.5 GPa, 9.9 GPa, 8 GPa to 6.3 GPa for gyroid sample. For the triangle A design with same pore size range, Young’s modulus is from 6.7 GPa, 5.6 GPa, 3.5 GPa to 2.9 GPa. While for the triangle B design, Young’s modulus decreases from 11.5 GPa, 8.6 GPa, 4.7 GPa to 4.4 GPa. Young’s modulus is calculated using the gradient of the plotted graphs. The yield strength is measured from the graph at a strain value of 0.02%. Based on the same pore size range, they are, 33 MPa, 20 MPa, 18 MPa and 12 MPa for the

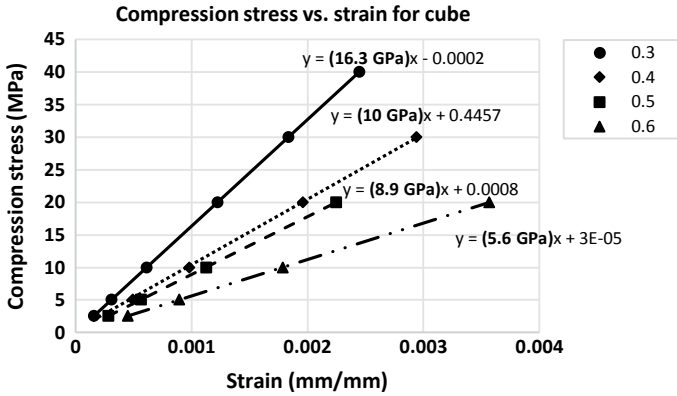


Fig. 24.12 Young’s modulus and yield strength determined from compression stress versus strain for cube porous structure

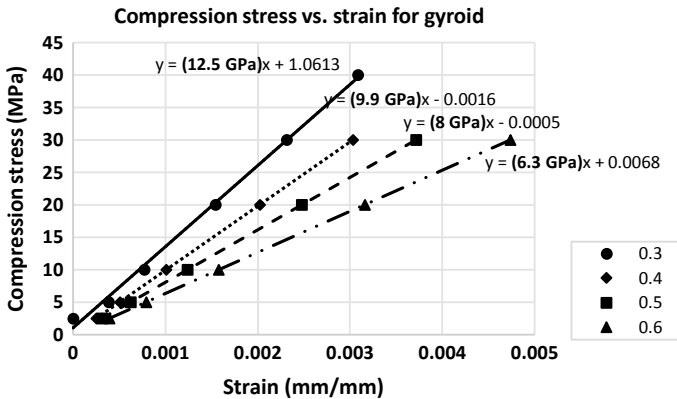


Fig. 24.13 Young’s modulus and yield strength determined from compression stress versus strain for gyroid porous structure

cube sample; 26 MPa, 20 MPa, 26 MPa and 13 MPa for the gyroid sample; 14 MPa, 11 MPa, 7 MPa and 6 MPa for the triangle A; and 23 MPa, 18 MPa, 10 MPa and 9 MPa for the triangle B. Again, the declining trend is observed for yield strength with the growth of pore size. The measured Young’s modulus and yield strength values for each design with different pore size are presented in Table 24.3.

The comparison of Young’s modulus with different pore size is shown in Figs. 24.16, 24.17, 24.18 and 24.19 for all designs.

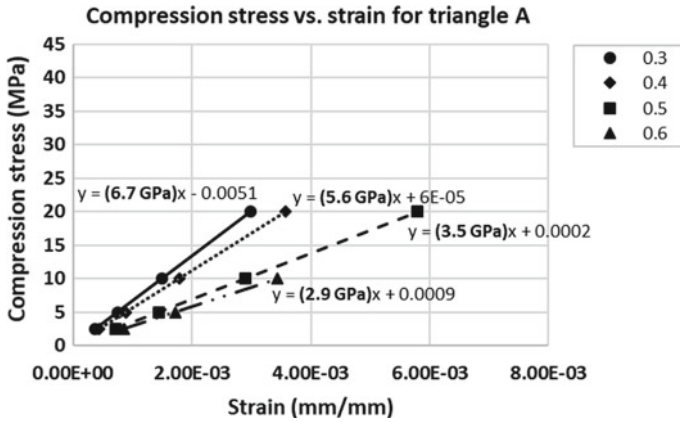


Fig. 24.14 Young’s modulus and yield strength determined from compression stress versus strain for triangle A porous structure

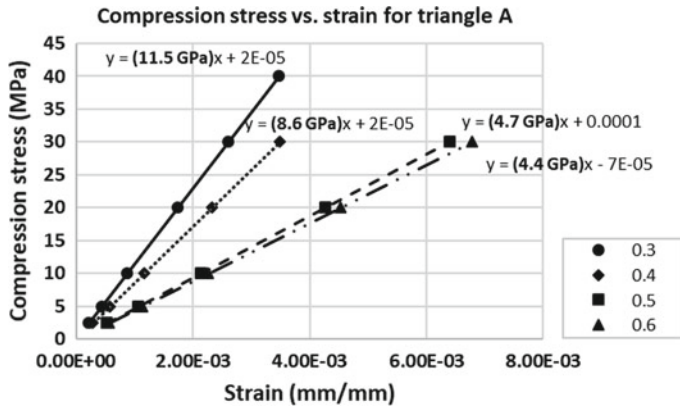


Fig. 24.15 Young’s modulus and yield strength determined from compression stress versus strain for triangle B porous structure

As described in the literature section, mechanical properties of implants must lie within the range of bone properties to avoid aseptic loosening issue. The elastic modulus and yield strength of cortical bone is between 4–30 GPa and 20–190 MPa, respectively. Whereas for trabecular bone, the range is 0.7–4 GPa and 20–40 MPa, respectively. Values of elastic modulus and yield strength, for each sample, obtained from analysis are compared with the given range for optimum structure. From Table 24.2, the elastic modulus of all samples is within the required range, but the yield strength of most of the designs is less than the recommended range. Thus, some samples are unsuitable for implant applications. Properties of the cube with a pore size of 0.3 mm and 0.4 mm, gyroid with a pore size of 0.3 mm and 0.4 mm and triangle B with a pore size of 0.3 mm are within the specified range of bone. These selections

Table 24.3 Measured Young's modulus and yield strength for all designs with different pore sizes

Design	Pore size (mm)	Yield strength (MPa)	Young's modulus (GPa)
Cube	0.3	33	16.3
	0.4	20	10.2
	0.5	18	8.9
	0.6	12	5.6
Gyroid	0.3	26	13.0
	0.4	20	9.9
	0.5	16	8.0
	0.6	13	6.3
Triangle A	0.3	14	6.7
	0.4	11	5.6
	0.5	7	3.5
	0.6	6	2.9
Triangle B	0.3	23	11.5
	0.4	18	8.6
	0.5	10	4.7
	0.6	9	4.4

Fig. 24.16 Young's modulus versus pore size for cube porous structure

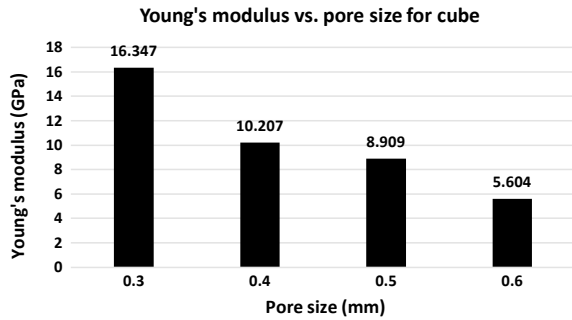


Fig. 24.17 Young's modulus versus pore size for gyroid porous structure

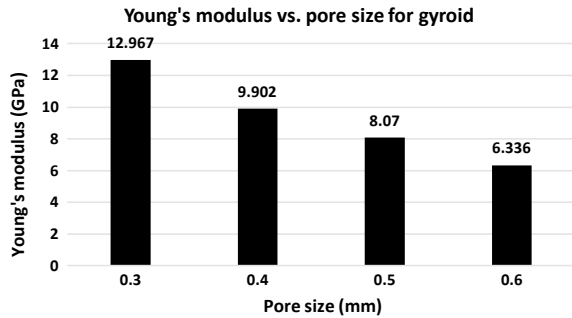


Fig. 24.18 Young's modulus versus pore size for triangle A porous structure

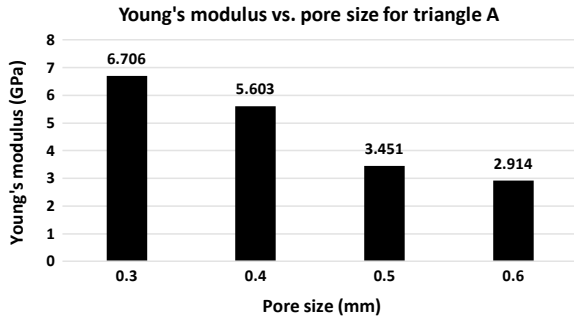
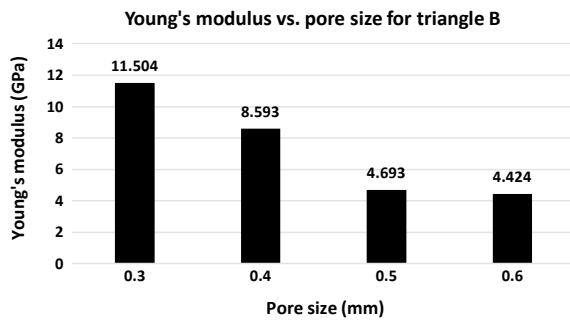


Fig. 24.19 Young's modulus versus pore size for triangle B porous structure



of sample designs are fit to be used as biomedical application. On the other hand, none of the porous properties lies within the range of trabecular bone properties. To get the properties similar to that of trabecular bone, the sample structure needs to be more porous to further reduce the elasticity and optimized design should be created to achieve the desirable trabecular yield strength.

Structural analysis of porous designs gives promising results for application in artificial implants that can achieve the properties of natural bone. Implants can be designed using optimum porous structures proposed by this study as the internal structure will be extruded to the shape of the chosen artificial implant. However, the structure of bone is not uniform and symmetric as the designed sample. The internal bone structure consists of different parts with variable mechanical properties that make the construction of bone non-uniform and asymmetric. Properties of bone vary in different orientations and parts of the bone. Therefore, to produce an implant that mimics the bone structure, implant design should consist of various structures with variable porosity. Producing such implant is impossible with conventional manufacturing processes. But with recent developments in additive manufacturing, porous implants can easily be produced. Additive manufacturing, with its capability to produce complex parts, can produce a part with variable porosity and structure. Technologies like selective laser melting (SLM) and electron beam melting (EBM)

are being used to produce metal parts for a number of applications. The same technologies can also be used to produce artificial implants that are similar to the bone structure and properties, which is still a drawback for conventional technologies.

Samples analyzed in this research are a step in the development toward producing better implants. Cube, gyroid and triangle, all of these structures can be produced by selective laser melting (SLM) without support structures, keeping in view the limitation of metal additive manufacturing. Also, these structures show optimum properties, with suitable pore size, to form the basis of porous implants. Analysis of these structure has shown a reduction in mechanical properties as well as strength which, when applied to implant application, will reduce the stress shielding effect and in return minimizes the problem of implant aseptic loosening. Use of these porous designs will increase the life of implants, making them more durable and suitable for the human body.

24.5 Conclusion and Future Implications

In this research, four different porous designs with porosities ranging from 0.3 to 0.6 mm have been analyzed for elastic modulus and yield strength, using the titanium alloy Ti6Al4V. The purpose of this analysis is to determine the optimum porous structure that has similar mechanical properties to that of natural bone. All porous structures are tested following the ISO standard (ISO 3314) to predict the mechanical properties. Instances of cube, gyroid and triangle samples have shown similar properties as of natural bone and can be used in implant applications. An implant with a porous structure can help to reduce stress shielding in implants and also aseptic loosening of implants. These porous designs can be used to produce porous artificial implants with bone properties and can be reliably manufactured by additive manufacturing. Future studies can include fabrication of these porous samples and performing experimental tests to validate the designs. The ultimate goal of this evolution is to produce better performing prostheses with increased mechanical stability and reliability.

Acknowledgements The author hereby acknowledges the financial support from Ministry of Higher Education (MOHE), Malaysia, through grant number FRGS/1/2014/TK01/UTP/02/08.

References

1. Kurtz, S., Ong, K., Lau, E., Mowat, F., Halpern, M.: Projections of primary and revision hip and knee arthroplasty in the United States from 2005 to 2030. *J. Bone Joint Surg. Am.* **89**(4), 780–785 (2007)
2. Dalury, D.F., Pomeroy, D.L., Gorab, R.S., Adams, M.J.: Why are total knee arthroplasties being revised? *J. Arthroplasty* **28**(8), 120–121 (2013)

3. Bahraminasab, M., et al.: Multi-objective design optimization of functionally graded material for the femoral component of a total knee replacement. *Mater. Des.* **53**, 159–173 (2014)
4. Bahraminasab, M., Jahan, A.: Material selection for femoral component of total knee replacement using comprehensive VIKOR. *Mater. Des.* **32**(8–9), 4471–4477 (2011)
5. Bahraminasab, M., et al.: On the influence of shape and material used for the femoral component pegs in knee prostheses for reducing the problem of aseptic loosening. *Mater. Des.* **55**, 416–428 (2014)
6. Cherian, J.J., Jauregui, J.J., Banerjee, S., Pierce, T., Mont, M.A.: What host factors affect aseptic loosening after THA and TKA? *Clin. Orthop. Relat. Res.* **473**(8), 2700–2709 (2015)
7. Sundfeldt, M., Carlsson, L.V., Johansson, C.B., Thomsen, P., Gretzer, C.: Aseptic loosening, not only a question of wear: a review of different theories. *Acta Orthop.* **77**(2), 177–197 (2006)
8. Penner, M.J., Almousa, S.A., Kolla, L.: Aseptic loosening. *Gene Ther.* **11**(4), 116–122 (2004)
9. Yunpeng, J., Tanghong, J., Paul, H.W., Shang-you, Y.: Current research in the pathogenesis of aseptic implant loosening associated with particulate wear debris. *Acta Orthop. Belg.* **79**, 1–9 (2013)
10. Limmahakhun Oloyede, S., Sittthiseripratip, K., Xiao, Y., Yan, C.: Stiffness and strength tailoring of cobalt chromium graded cellular structures for stress-shielding reduction. *Mater. Des.* **114**, 633–641 (2017)
11. Li, Y., Yang, C., Zhao, H., Qu, S., Li, X., Li, Y.: New developments of ti-based alloys for biomedical applications. *Materials (Basel)* **7**(3), 1709–1800 (2014)
12. Rack, H.J., Qazi, J.I.: Titanium alloys for biomedical applications. *Mater. Sci. Eng., C* **26**(8), 1269–1277 (2006)
13. Parthasarathy, J., Starly, B., Ramanand, S., Christensen, A.: Mechanical evaluation of porous titanium (Ti6Al4V) structures with electron beam melting (EBM). *J. Mech. Behav. Biomed. Mater.* **3**(3), 249–259 (2010)
14. Wauthle, R., et al.: Additively manufactured porous tantalum implants. *Acta Biomater.* **14**(March), 217–225 (2015)
15. Amin Yavari, S., et al.: Relationship between unit cell type and porosity and the fatigue behavior of selective laser melted meta-biomaterials. *J. Mech. Behav. Biomed. Mater.* **43**, 91–100 (2015)
16. Wieding, J., Wolf, A., Bader, R.: Numerical optimization of open-porous bone scaffold structures to match the elastic properties of human cortical bone. *J. Mech. Behav. Biomed. Mater.* **37**, 56–68 (2014)
17. Sola, A., Bellucci, D., Cannillo, V.: Functionally graded materials for orthopedic applications—an update on design and manufacturing. *Biotechnol. Adv.* **34**(5), 504–531 (2016)
18. Zhang, L.C., Klemm, D., Ecker, J., Hao, Y.L., Sercombe, T.B.: Manufacture by selective laser melting and mechanical behavior of a biomedical Ti-24Nb-4Zr-8Sn alloy. *Scr. Mater.* **65**(1), 21–24 (2011)
19. TeachPE: Bone structure (2018). [Online]. Available: <https://www.teachpe.com/anatomy-physiology/structure-of-bones>. Accessed: 19 Oct 2018
20. Billiar, K.L.: The Mechanical environment of cells in collagen gel models global and local effects in three-dimensional biological hydrogels. *Stud. Mechanobiol. Tissue Eng. Biomater.*, (November 2010), 201–245 (2011)
21. Bahraminasab, M., Sahari, B.B., Edwards, K.L., Farahmand, F., Arumugam, M., Hong, T.S.: Aseptic loosening of femoral components—a review of current and future trends in materials used. *Mater. Des.* (2012)
22. Huiskes, R., Weinans, H., van Rietbergen, B.: The relationship between stress shielding and bone resorption around total hip stems and the effects of flexible materials. *Clin. Orthop. Relat. Res.* **274**, 124–134 (1992)
23. Pei, X., et al.: Bionic mechanical design of titanium bone tissue implants and 3D printing manufacture. *Mater. Lett.* **208**, 133–137 (2017)
24. Murr, L.E., et al.: Microstructure and mechanical properties of open-cellular biomaterials prototypes for total knee replacement implants fabricated by electron beam melting. *J. Mech. Behav. Biomed. Mater.* **4**(7), 1396–1411 (2011)

25. Yan, C., Hao, L., Hussein, A., Young, P.: Ti-6Al-4V triply periodic minimal surface structures for bone implants fabricated via selective laser melting. *J. Mech. Behav. Biomed. Mater.* **51**, 61–73 (2015)
26. Kasper, C., Witte, F., Pörtner, R. (eds.): *Tissue Engineering III: Cell—Surface Interactions for Tissue Culture*, vol. 126. Springer Berlin Heidelberg (2012)
27. Gibson, I., Rosen, D., Stucker, B.: *Additive Manufacturing Technologies: 3D Printing, Rapid Prototyping, and Direct DIGITAL Manufacturing*, 2nd edn. (2015)
28. Kadhodapour, J., et al.: Failure mechanisms of additively manufactured porous biomaterials: effects of porosity and type of unit cell. *J. Mech. Behav. Biomed. Mater.* **50**, 180–191 (2015)